



UNIVERSITAT DE
BARCELONA

Investigating the role of mitochondrial dysfunction in the pathogenesis of Parkinson's disease using patient-specific derived astrocytes

Irene Fernández Carasa

ADVERTIMENT. La consulta d'aquesta tesi queda condicionada a l'acceptació de les següents condicions d'ús: La difusió d'aquesta tesi per mitjà del servei TDX (www.tdx.cat) i a través del Dipòsit Digital de la UB (diposit.ub.edu) ha estat autoritzada pels titulars dels drets de propietat intel·lectual únicament per a usos privats emmarcats en activitats d'investigació i docència. No s'autoritza la seva reproducció amb finalitats de lucre ni la seva difusió i posada a disposició des d'un lloc aliè al servei TDX ni al Dipòsit Digital de la UB. No s'autoritza la presentació del seu contingut en una finestra o marc aliè a TDX o al Dipòsit Digital de la UB (framing). Aquesta reserva de drets afecta tant al resum de presentació de la tesi com als seus continguts. En la utilització o cita de parts de la tesi és obligat indicar el nom de la persona autora.

ADVERTENCIA. La consulta de esta tesis queda condicionada a la aceptación de las siguientes condiciones de uso: La difusión de esta tesis por medio del servicio TDR (www.tdx.cat) y a través del Repositorio Digital de la UB (diposit.ub.edu) ha sido autorizada por los titulares de los derechos de propiedad intelectual únicamente para usos privados enmarcados en actividades de investigación y docencia. No se autoriza su reproducción con finalidades de lucro ni su difusión y puesta a disposición desde un sitio ajeno al servicio TDR o al Repositorio Digital de la UB. No se autoriza la presentación de su contenido en una ventana o marco ajeno a TDR o al Repositorio Digital de la UB (framing). Esta reserva de derechos afecta tanto al resumen de presentación de la tesis como a sus contenidos. En la utilización o cita de partes de la tesis es obligado indicar el nombre de la persona autora.

WARNING. On having consulted this thesis you're accepting the following use conditions: Spreading this thesis by the TDX (www.tdx.cat) service and by the UB Digital Repository (diposit.ub.edu) has been authorized by the titular of the intellectual property rights only for private uses placed in investigation and teaching activities. Reproduction with lucrative aims is not authorized nor its spreading and availability from a site foreign to the TDX service or to the UB Digital Repository. Introducing its content in a window or frame foreign to the TDX service or to the UB Digital Repository is not authorized (framing). Those rights affect to the presentation summary of the thesis as well as to its contents. In the using or citation of parts of the thesis it's obliged to indicate the name of the author.



UNIVERSITAT DE
BARCELONA

Facultat de Biologia
Programa de Doctorat de Biomedicina

Investigating the role of mitochondrial dysfunction in the pathogenesis of Parkinson's disease using patient-specific derived astrocytes

Memòria presentada per **Irene Fernández Carasa** per optar
al grau de doctora per la Universitat de Barcelona

Dra. Antonella Consiglio
Directora de la tesi

DEL RIO
FERNANDEZ
JOSE ANTONIO -
38552812M

Digitally signed by DEL
RIO FERNANDEZ JOSE
ANTONIO - 38552812M
Date: 2021.04.26
11:19:19 +02'00'

Dr. José Antonio del Río Fernández
Tutor de la tesi

Irene Fernández Carasa
Doctoranda

A mi familia

... l'èxit comença a la voluntat ...

Walter D. Wintle

ACKNOWLEDGEMENTS

Empezaré los agradecimientos por esa persona que, un viernes por la tarde sentada frente al ordenador y delante de una decena de imágenes por analizar, me dijo “Y tú, ¿por qué no haces el doctorado?”. Antonella no ha dudado ni un momento en que podía doctorarme y eso es lo que me ha transmitido, y siempre que he tenido dudas me ha animado a continuar. Ella me convenció y me matriculé, desde entonces ha dirigido mi tesis. Quiero agradecerle la confianza depositada en mí, las herramientas que me ha brindado para crecer como profesional y el tiempo invertido en este proyecto y en mi formación. Formamos un buen equipo y hemos trabajado juntas con mismo objetivo. Gracias.

Mis compañeros de laboratorio han sido una parte crucial en este camino. Hemos sabido construir un equipo unido y colaborativo en el que el éxito de cada uno de los miembros es el éxito del grupo. Este hecho nos ha ayudado a llegar cada vez más lejos y a aportar a la comunidad científica datos valiosos para el avance en la investigación sobre el Parkinson. Gracias a todos.

A Carles le agradezco su tesón y templanza, a Giulia su sonrisa permanente, a Alba su “estoy aquí”, a Meritxell sus sabios consejos, a Lucas su oreja siempre dispuesta y a Valentina el trabajo en equipo. A las nuevas incorporaciones, Arianna y Veronica, les agradezco haber traído entusiasmo renovado.

También quiero agradecer a anteriores compañeros de laboratorio, a Roger, Armida, Neus, Janani, Eugenia e Isabel, así como a todos los estudiantes que nos han acompañado, aunque fuera solo unos meses. Gracias a cada uno de ellos he mejorado profesionalmente.

Agradezco a las compañeras que han colaborado activamente en este proyecto. A Janani, Silvia, Cristina, Valentina, Alba y Meritxell, gracias por aportar vuestro tiempo, vuestras manos y vuestra cabeza.

Quiero mencionar a nuestro laboratorio hermano, con el que tanto hemos compartido, años de colaboraciones y de discusiones científicas que nos han permitido ampliar nuestros conocimientos y capacidades. Gracias a Ángel Raya por hacerlo posible con su apoyo constante, a Yvonne por su sabiduría celular y las soluciones ingeniosas, a Rubén por su compañía en las tardes de cultivos y a Francesca por su energía. Gracias a todos y también a Raquel, Yannis, Karina, Cristina, Alba, Léa, Stefano y Maria, y a todo el p-CMRC, por estar siempre disponibles y dispuestos a colaborar.

Gracias a Juan Pablo Muñoz y a Antonio Zorzano, nuestros colaboradores en el IRB, por acompañarnos en el desarrollo de este proyecto.

Agradezco a mi familia su apoyo incondicional y su confianza en mí. A mis padres, por enseñarme que una nunca debe ponerse límites, a mis hermanos, Raúl y Gabriel, por ser los únicos capaces de sacarme una sonrisa hasta en mis días más negros y a Janek por contagiarme su energía y entrega en todo lo que hace. Gracias a mis amigas del alma, Mar y Mercè, por estar siempre.

ABSTRACT

Parkinson's disease (PD) is an incurable, chronically progressive disorder of old age leading to premature invalidity and death. Clinically, PD is characterized by classical motor syndrome linked to a progressive loss of dopamine-containing neurons (DAN) in the substantia nigra pars compacta, and disabling non-motor symptoms related to extranigral lesions.

The identification of several genes associated to familiar PD have brought considerable insight into underlying pathogenic mechanisms. However, the unknown etiology of the sporadic forms (90% of patients) and the emerging view that non-neuronal cells could be also implicated in the pathophysiology of the disease, greatly impact on the development of accurate models and on the discovery of a cure. Here, I investigate the role of astrocytes in disease pathogenesis using a human iPSC-based model of Parkinson's disease.

First, I introduce Parkinson's disease, its pathological hallmarks and the progression of the symptoms, and discuss genetic and environmental influences. Then, I elaborate on the different mechanisms involved in PD including mitochondrial dysfunction, oxidative stress and autophagy as well as on the inflammatory phenotypes observed in the disease and recent work describing the role of inflammation in PD animal models and post-mortem brain tissue.

Subsequently, I examine the association of astrocytic dysfunctions with neuronal morphological and functional abnormalities that contribute to the progression of several neurodegenerative including Parkinson's disease and the recent data showing an astrocyte-autonomous process mediating PD-associated degeneration of dopaminergic neurons, mainly via intracellular accumulation of α -synuclein aggregates in astrocytes and subsequent propagation of such toxic aggregates to surrounding neurons.

In the results section, I describe the generation and characterization of iPSC-derived astrocytes of LRRK2-PD patients (LRRK2^{G2019S} PD), healthy individual (Ctrl) and CRISPR/Cas9 gene edited isogenic control. I show that LRRK2^{G2019S} PD astrocytes exhibited extensive perinuclear accumulation of fragmented mitochondria and a significant increase in DRP1 phosphorylation compared to control astrocytes. Fragmented mitochondria accumulated in LRRK2^{G2019S} PD astrocytes was due to a defective mitophagy leading to an increase in oxidative stress. I also show that oxygen consumption rate, ATP production and mitochondrial membrane potential were significantly decreased in LRRK2^{G2019S} PD astrocytes indicating altered mitochondrial function in PD astrocytes and that LRRK2^{G2019S} PD astrocytes exhibited lower expression levels of mitochondrial biogenesis-related genes compared to control astrocytes. Importantly, correction of G2019S mutation in the LRRK2 gene by CRISPR-Cas9 gene editing normalized mitochondria morphology, clearance and function to those of control astrocytes. Then, I describe the effects of Urolithin A, a mitophagy activator drug, that was able to rescue mitochondrial fragmentation and accumulation in LRRK2^{G2019S} PD astrocytes by inducing mitophagy, promoting expression of mitochondrial biogenesis-related genes and reducing ROS production in those astrocytes.

Finally, in the last chapter, I show that, in a co-culture system established between LRRK2^{G2019S} PD astrocytes and healthy DA neurons, the treatment with Urolithin A, prevented neuronal cell death, suggesting a potential astrocyte-targeted therapeutic.

In conclusion, our findings provide the advantage for using iPSC-based modeling for assessing the consequences of mitochondrial dysfunctions in astrocytes and dissecting the initial mechanisms that lead to neuronal cell loss in PD. The present modeling has uncovered mitophagy dysfunction as a relevant altered mechanism in PD astrocytes whose activation might represent an interesting therapeutic option for counteracting PD-related neurodegeneration.

TABLE OF CONTENTS

LIST OF FIGURES AND TABLES	xiii
LIST OF ACRONYMS	xv
INTRODUCTION	1
1. Parkinson’s disease	1
1.1. Neuropathology	2
1.2. Treatment	4
2. Etiology of Parkinson’s disease	6
2.1. Risk factors	6
2.2. Genetic contribution	7
2.2.1. Leucine-rich repeat kinase 2	9
3. Mechanisms involved in PD pathogenesis	11
3.1. Mitochondrial dysfunction	12
3.2. Oxidative stress	15
3.3. Dysfunctional protein degradation	16
3.4. Neuroinflammation	17
4. Astrocytes in Parkinson’s disease	18
4.1. Astrocytes’ functions in healthy brain	18
4.2. Astrocytes in response to pathology	20
4.3. Astrocytes as disease modulators in Parkinson’s disease	21
5. Modeling Parkinson’s disease	25
5.1. Induced Pluripotent Stem cells to model Parkinson’s disease	27
OBJECTIVES	31
MATERIALS AND METHODS	33

RESULTS	45
1. iPSC-derived astrocytes generation and characterization	45
2. Altered mitochondrial dynamics in PD astrocytes	47
2.1. Aberrant mitochondrial morphology and distribution in PD astrocytes	47
2.2. Imbalance of fission and fusion events in PD astrocytes	49
3. PD astrocytes display dysfunctional mitophagy	51
3.1. Mitochondrial protein accumulation in PD astrocytes	51
3.2. Blockage of mitophagy upon CCCP activation in PD astrocytes	52
3.3. Impairment in the mitolysosomes formation in PD astrocytes	55
4. Biogenesis in PD astrocytes	58
5. Dysfunctional mitochondria are present in PD astrocytes	59
6. PD astrocytes exhibit increased sensitivity to oxidative stress	61
7. Urolithin A rescues mitochondrial alterations promoting mitophagy	62
8. Contribution of astrocytic mitochondrial dysfunctional to dopaminergic degeneration	65
8.1. PD astrocytes promotes neurodegeneration in control dopaminergic neurons	65
8.2. Rescue of mitochondrial alterations in astrocytes prevents degeneration of DA neurons in co-culture	66
DISCUSSION	69
1. Characterization of iPSC-derived astrocytes	70
2. Mitochondrial dynamics in Parkinson’s disease astrocytes	70
3. Dysfunctional mitophagy as a pathogenic mechanism in Parkinson’s disease	71
4. Mitochondrial dysfunction in Parkinson’s disease astrocytes	72
5. Mitophagy as a potential therapeutic target for Parkinson’s disease	73
6. Restoration of mitostasis in PD astrocytes during co-culture of control neurons with PD astrocytes	75
CONCLUSIONS	77
REFERENCES	81
APPENDICES	95

LIST OF FIGURES AND TABLES

Figure 1. Clinical symptoms of Parkinson’s disease over time.	2
Figure 2. Pathological hallmarks of Parkinson’s disease.	3
Figure 3. Schematic representation of L-DOPA (Levodopa) site of action.	5
Figure 4. Schematic representation of the LRRK2 protein.	9
Figure 5. Molecular mechanisms involved in Parkinson’s disease.	11
Figure 6. Roles of LRRK2 in PINK1/Parkin dependent mitophagy.	15
Figure 7. Generation of iPSC for disease modeling in PD.	26
Figure 8. Morphological alterations of PD-iPSC-derived dopaminergic neurons.	28
Figure 9. Abnormal accumulation of α -synuclein in PD-iPSC-derived dopaminergic neurons.	28
Figure 10. Graphical abstract summarizing results obtained in di Domenico et al., 2019 study.	29
Figure 11. Diagram of the protocol for astrocyte generation.	34
Figure 12. Diagram of Seahorse XF Cell Mito Stress Test Profile showing different inhibitors used and key mitochondrial functional parameters measured.	41
Figure 13. iPSC-derived astrocytes express astrocytic markers and are functional.	46
Figure 14. PD astrocytes show fragmented mitochondria and abnormal mitochondrial distribution.	48
Figure 15. PD astrocytes display higher levels of fission related proteins compared to control.	50
Figure 16. PD astrocytes display increased levels of DRP1-P protein.	50
Figure 17. PD astrocytes accumulate mitochondrial proteins.	52
Figure 18. Blockage of mitochondrial clearance in PD astrocytes.	53
Figure 19. Nucleoid degradation is impaired in PD astrocytes.	54
Figure 20. Direct visualization of mitophagy impairment in PD astrocytes using mt-keima plasmid.	57
Figure 21. PD astrocytes failure to transfer mitochondria to lysosomes.	57

Figure 22. Decreased expression of mitochondrial biogenesis-related genes in PD astrocytes compared to isogenic astrocytes.	58
Figure 23. PD astrocytes present dysfunctional mitochondrial.	60
Figure 24. PD astrocytes exhibit increased oxidative stress compared to control and isogenic astrocytes.	61
Figure 25. Urolithin A rescues mitochondrial fragmentation in PD astrocytes.	63
Figure 26. Urolithin A promotes mitophagy.	63
Figure 27. Urolithin A treatment promotes mitochondrial biogenesis and prevents oxidative stress.	64
Figure 28. PD astrocytes promotes neurodegeneration when co-cultured with control DAn.	66
Figure 29. Mitophagy inducer Urolithin A rescues mitochondrial alterations in astrocytes preventing neurodegeneration in co-culture.	67
Table 1. Familial PD-related genes.	8
Table 2. iPSc lines used in this study.	33

LIST OF ACRONYMS

6-OHDA	6-hydroxydopamine
BBB	Blood brain barrier
CCCP	Carbonyl Cyanide m-Chlorophenyl hydrazone
CMA	Chaperone Mediated Autophagy
CNS	Central nervous system
CTCF	Corrected Total Cell Fluorescence
DAMPs	Damage-associated molecular patterns
DAn	Dopaminergic neurons
DCF	2',7'-dichlorofluorescein
DCF-DA	2',7'-dichlorofluorescein diacetate
DNP-hydrazone	2,4-dinitrophenylhydrazone
DRP1	Dynamamin-related Protein 1
FCCP	Carbonyl cyanide-p-trifluoromethoxyphenyl hydrazone
GABA	Gamma-Aminobutyric acid
GDNF	Glial cell-derived neurotrophic factor
GFAP	Glial fibrillary acidic protein
ID-PD	Idiopathic Parkinson's Disease
iPSC	Induced Pluripotent Stem Cells
ITPKB	Inositol-Trisphosphate 3-Kinase B
KGDHC	Alpha-ketoglutarate- dehydrogenase complex
LAMP1	Lysosomal-Associated Membrane Protein 1
LRRK2	Leucine-Rich Repeat Kinase 2
MICU3	Mitochondrial Calcium Uptake Family Member 3
MFN	Mitofusin

MPTP	1-methyl-4-phenyl-1,2,3,6-tetra hydropyridine
mtDNA	Mitochondrial DNA
NFR1	Nuclear respiratory factor 1
NG2	Neuron-glia antigen 2
OCR	Oxygen Consumption Rate
OMM	Outer membrane of mitochondria
OPA1	Optic Atrophy Gene 1
OPTN	Optineurin
PAMPs	Pathogen-Associated Molecular Patterns
PINK1	PTEN-induced putative kinase 1
PD	Parkinson's Disease
PGC1 α	PPAR (peroxisome proliferator-activated receptor)- γ coactivator-1 α
ROS	Reactive Oxygen Species
s.e.m.	Standard Error of the Mean
SNM	Spherical Neural Masses
SNpc	Substantia Nigra pars compacta
S100 β	Calcium-binding protein beta
TFAM	Mitochondrial transcription factor A
TH	Tyrosine Hydroxylase
TIM44	Mitochondrial Import Inner Membrane Translocase
TMRM	Tetramethylrhodamine, methyl ester
TUJ1	Beta-tubulin III
TOM20	Translocase of outer membrane subunit 20
UA	Urolithin A
UPS	Ubiquitin-proteasome system
VDAC1	Voltage-Dependent Anion-selective Channel 1
WB	Western Blot

INTRODUCTION

1. Parkinson's disease

Parkinson's disease was first described in 1817 by James Parkinson (Parkinson, 1817) whose description of the disease, although not complete, is still pertinent nowadays. After centuries of study, Parkinson's disease (PD) is currently known to be a chronic, progressive neurodegenerative disease characterized not only by the loss of motor functions but also by the manifestation of non-motor symptoms. It is the second most common neurodegenerative disease after Alzheimer's disease affecting more than 6,5 million people worldwide with the level of incidence in the population over the age of 65 estimated at around 3-5% (Pons-Espinal et al., 2019; Reich et al., 2019). Due to improvement of health care and increased life expectancy, it is estimated that the prevalence of Parkinson's disease will rise dramatically over the coming years, doubling the number of patients in 2030 compared to 2005 (Poewe et al., 2017).

Clinical manifestations of Parkinson's disease include motor symptoms such as bradykinesia, muscular rigidity, rest tremor and postural instability. The loss of the dopaminergic neurons (DAn) in the substantia nigra pars compacta (SNpc) and its consequent dopamine depletion in the striatum are responsible for these symptoms (Kaila et al., 2015). Non-motor symptoms are characteristic of the last stages of the disease but some can manifest themselves even years before the diagnosis. These symptoms include cognitive impairment, autonomic dysfunction, sleep disorder, depression and hyposmia (impaired smell) (see Fig. 1) (Poewe et al., 2017).

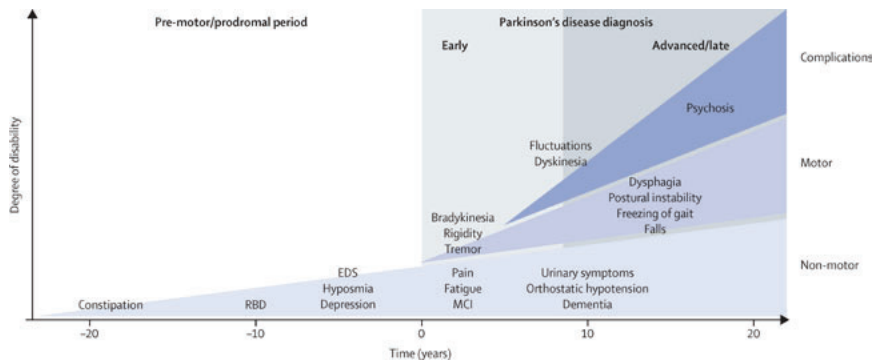


Figure 1. Clinical symptoms of Parkinson's disease over time.

Prodromal phase of PD is characterized by non-motor symptoms and can start 20 year before the diagnosis. PD is diagnosed with the onset of motor symptoms (From Kaila et al., 2015).

It is known that the loss of dopaminergic neurons and dopamine deficiency begin up to 20 years before the diagnosis (see Fig.1). Hence, the diagnosis of preclinical and prodromal Parkinson's disease focuses on the identification of non-motor and/or subtle motor symptoms to predict the diagnosis before the massive loss of dopaminergic neurons (Mahlknecht et al., 2015).

Even though there has been and incredible improvement in the quality of life of Parkinson's disease patients, there is still no definitive cure that can stop or change the course of the disease and the only available treatment is palliative. For this reason, establishing accurate models to gain insight in the molecular and cellular mechanisms underlying the dopaminergic neurodegeneration is central to discovering a definitive cure.

1.1. Neuropathology

The two main pathological hallmarks of the disease are the loss of dopaminergic neurons (DAN) from the substantia nigra pars compacta (SNpc) and the formation of protein inclusions known as Lewy bodies and Lewy neurites, mainly composed by α -synuclein (see Fig. 2) (Dickson et al., 2009).

With regard to the cell loss in Parkinson's disease, it is preferentially occurring

in the A9 subtype ventral midbrain dopaminergic neurons form the nigrostriatal pathway (see Fig. 2a). These neurons project to the striatum in the basal ganglia and release dopamine to control the initiation and execution of movements (Surmeier et al., 2017). Parkinson's disease is clinically diagnosed when more than 50% of dopaminergic neurons in the substantia nigra pars compacta are lost and there is around 80% of dopamine deficiency in the striatum, which means that the degeneration of this region starts before the onset of motor symptoms (Dijkstra et al., 2014). It is also reported that in the early stages the loss of DAN is restricted to the ventrolateral SNpc and becomes more widespread with the

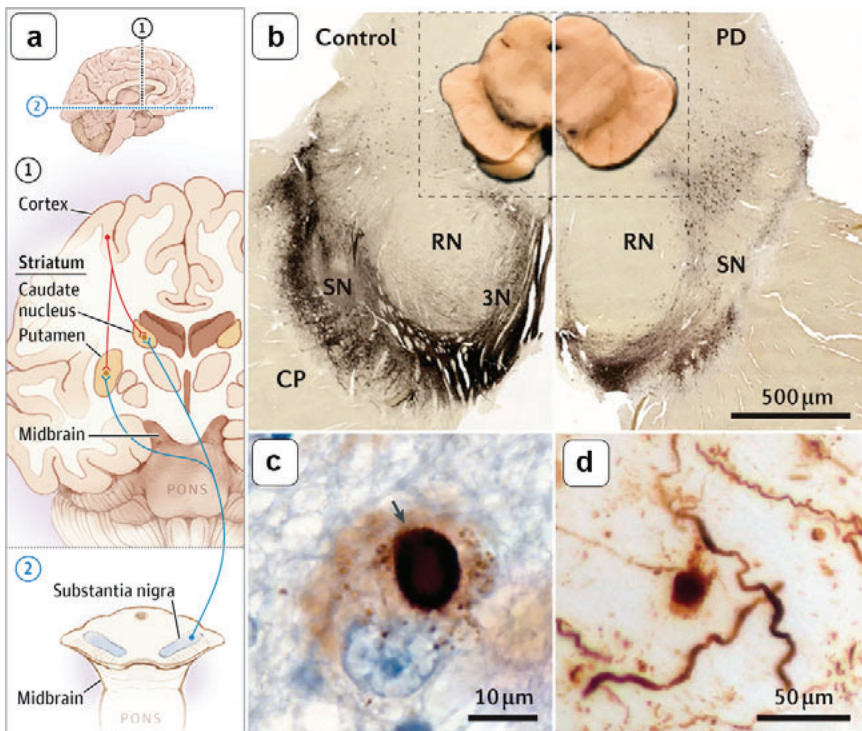


Figure 2. Pathological hallmarks of Parkinson's disease.

a. Schematic representation of the nigrostriatal pathway. B. Depigmentation of the SN is characteristic in PD as seen in right panel compared to the control in the left panel. Insets show immunohistochemical staining for tyrosine hydroxylase, gold standard marker for dopaminergic neurons, of transverse sections of the midbrain. Loss of dopaminergic neurons in the substantia nigra (SN) is evident in PD (right panel) compared to control (left panel). c-d. Immunohistochemical staining for α -synuclein shows the intracytoplasmic Lewy bodies (c, arrow) and Lewy neurites (d) (Adapted from Connolly et al., 2014 and Poewe et al., 2017).

progression of the disease (Damier et al., 1999). Along with the loss of A9 DAN, the depigmentation of SNpc occurs as these neurons display high neuromelanin pigmentation (see Fig. 2b) (Schwarz et al., 2017).

Lewy pathology is the second hallmark of PD. Lewy bodies are inclusions present in the surviving neurons composed mainly of α -synuclein but including other proteins such as ubiquitin, parkin and neurofilament. α -synuclein is normally a natively unfolded protein that plays a role in synaptic vesicle release (Spillantini et al., 1997; Goedert et al., 2013). When in a misfolded stage, α -synuclein becomes insoluble forming intracellular inclusions with aggregated proteins known as Lewy bodies, when in the cytoplasm of the cell, and the Lewy neurites, when in the processes (see Fig. 2c-d) (Kaila et al., 2015; Dickson, 2017).

Braak hypothesis of Parkinson's disease states that Lewy pathology starts in the peripheral nervous system and progresses to finally affect the central nervous system in a caudal-rostral direction (Braak et al., 2004; Dickson et al., 2009; Goedert et al., 2013). This progression has been divided into six stages, in which the stages 1 and 2 correspond to premotor symptoms, stage 3 to motor symptoms when A9 dopaminergic neurons are affected and stages 4, 5 and 6 with non-motor symptoms occurring at the later stages of the disease. Meaning that there would be a correlation between Braak hypothesis and non-motor manifestations (Kaila et al., 2015).

1.2. Treatment

So far, there has been no disease-modifying drugs available for the treatment of Parkinson's disease that could slow or stop the dopaminergic neurodegeneration. Current therapeutic treatments only ameliorate the motor symptoms for a definite period of time (Fox et al., 2011; Connolly et al., 2014; Kaila et al., 2015).

The most prevalent treatment is the administration of L-DOPA, a dopamine precursor, together with a DOPA decarboxylase inhibitor, known as carbidopa. While L-DOPA crosses the blood-brain barrier, carbidopa does not, allowing L-DOPA to be converted to dopamine preferentially in the central nervous system (see Fig. 3) (Reich et al., 2018). Even though it is the most effective therapy to alleviate motor symptoms, it has been demonstrated that it can cause dyskinesias after long-term administration (PD Med Collaborative Group et al., 2014; LeWitt et al., 2016).

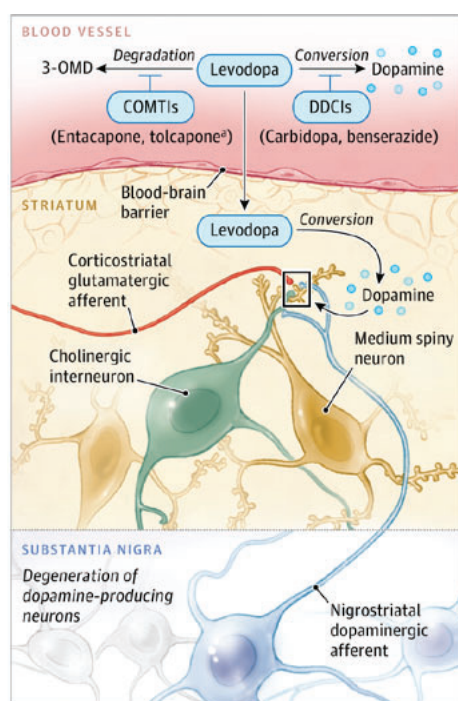


Figure 3. Schematic representation of L-DOPA (Levodopa) site of action.
 (Adapted from Connolly et al., 2014).

Alternative therapies include pharmacological treatment with the use of dopamine agonists and deep brain stimulation. Dopamine agonists can be administered at the beginning of the disease, therefore delaying the administration of L-DOPA and its side effects (Connolly et al., 2014) however it has been proven not to relieve motor symptoms to the same extent as L-DOPA. Deep

brain stimulation might compensate the motor complications secondary to a chronic treatment with L-DOPA (Perestelo-Pérez et al., 2014). Nevertheless, it is still essential to develop new treatments to stop the progression of the dopaminergic neurodegeneration and dopamine depletion.

2. Etiology of Parkinson's disease

The exact cause of Parkinson's disease is unknown although research points towards a combination of genetic and environmental factors. In fact, around 90% of PD cases are sporadic in which genetics and family history don't play a clear role in the onset of the disease. However, 10% of PD cases have a genetic basis (Tysnes et al., 2017).

2.1. Risk factors

Age is the major risk factor for developing Parkinson's disease. PD incidence is low before the age of 50 when it equals to 41 per 100.000 people, and peaks around the age of 80 when it increases to 1903 cases per 100.000 people (Delamarre et al., 2017; Ascherio et al., 2016). Gender is another risk factor for Parkinson's disease, as PD is twice as frequent in men as in women. However, women present higher mortality and faster progression of the disease (Cerri et al., 2019). There are several environmental factors considered to increase the risk of developing Parkinson's disease. After the discovery of 1-methyl-4-phenyl-1,2,3,6-tetra hydroxyridine (MPTP) as a pro-parkinsonian molecule which is similar in structure to the herbicide paraquat, it was suggested that the exposure to pesticides and other environmental chemicals could increase the risk of PD. The exposure to pesticides in the workplace has been associated with late-onset of PD in men in several studies (Cerri et al., 2019; Ascherio et al., 2016). Moreover, PD risk is increased after a traumatic brain injury. Head

injury can cause disruption of the blood-brain barrier, chronic inflammation, dysfunction of mitochondria, increase of glutamate release and α -synuclein accumulation in the brain. All these factors are potential contributors to the increased risk of suffering PD (Marras et al., 2014). Smoking and coffee have been proposed to have an inverse correlation between the exposure and PD risk. However, there are controversies whether the tobacco can really decrease the risk or if there is a change in habits of people during the prodromal stage (Cerri et al., 2019; Ascherio et al., 2016). Exercise is also a protective factor against Parkinson's disease and also prevents other disease such as diabetes and hypertension that can also increase the risk of suffering PD (Xu et al., 2019).

2.2. Genetic contribution

Familial Parkinson's disease accounts for approximately 10% of PD cases. In recent years, several genes causing monogenic forms of the disease have been identified (see table 1) (Blauwendraat et al., 2020). In addition, genome-wide association studies (GWAS) have identified single nucleotide polymorphisms (SNP) of several genes that were found to be associated with higher PD risk (Delamarre et al., 2017).

SNCA and Leucine-rich repeat kinase 2 (LRRK2) genes have been linked to autosomal dominant forms of PD. SNCA, which encodes the protein α -synuclein was the first gene identified to be associated to familial PD (Polymeropoulos et al., 1997). Several point mutations and multiplications of the gene have been associated with formation of oligomers or fibrils of α -synuclein (Lázaro et al., 2014). LRRK2 accounts for 4% (Ferreira et al., 2017) of inherited Parkinson's disease and more than 100 mutations have been already discovered. Typically, mutations in LRRK2 cause late-onset PD clinically indistinguishable from idiopathic PD (Lin et al., 2014). On the other hand, mutations in Parkin, PTEN-induced putative kinase 1 (PINK1) and DJ-1 genes cause autosomal recessive

Table 1. Familial PD-related genes.

From Blauwendraat et al., 2020.

	Mutation	Note	Year of discovery	Proposed disease mechanism	Inheritance	Frequency	Nominated by GWAS	Multiple independent families reported *	Functional evidence †	Negative reports published ‡	Confidence as actual PD gene §
SNCA	Missense or multiplication	Often with dementia	1997, 2003	Gain of function or overexpression	Dominant	Very rare	Yes	++	++	+	Very high
PRKN	Missense or loss of function	Often early onset	1998	Loss of function	Recessive	Rare	No	++	++	+	Very high
UCHL1	Missense	..	1998	Loss of function?	Dominant	Unclear	No	-	+	--	Low
PARK7	Missense	Often early onset	2003	Loss of function	Recessive	Very rare	No	++	++	+	Very high
LRRK2	Missense	..	2004	Gain of function	Dominant	Common	Yes	++	++	+	Very high
PINK1	Missense or loss of function	Often early onset	2004	Loss of function	Recessive	Rare	No	++	++	+	Very high
POLG	Missense or loss of function	Atypical PD	2004	Loss of function?	Dominant	Rare	No	++	+	+	High
HTRA2	Missense	..	2005	Unclear	Dominant	Unclear	No	-	+	--	Low
ATP13A2	Missense or loss of function	Atypical PD	2006	Loss of function	Recessive	Very rare	No	++	++	+	Very high
FBXO7	Missense	Often early onset	2008	Loss of function	Recessive	Very rare	No	++	++	+	Very high
GIGYF2	Missense	..	2008	Unclear	Dominant	Unclear	No	+	+	--	Low
GBA	Missense or loss of function	..	2009	Likely loss of function	Dominant (incomplete penetrance)	Common	Yes	++	++	+	Very high
PLA2G6	Missense or loss of function	Often early onset	2009	Loss of function	Recessive	Rare	No	++	++	+	Very high
EIF4G1	Missense	..	2011	Unclear	Dominant	Unclear	No	-	+	--	Low
VPS35	Missense	..	2011	Loss of function	Dominant	Very rare	No	++	+	+	Very high
DNAJC6	Missense or loss of function	Often early onset	2012	Loss of function	Recessive	Very rare	No	++	+	+	High
SYNJ1	Missense or loss of function	Often atypical PD	2013	Loss of function	Recessive	Very rare	No	++	+	+	High
DNAJC13	Missense	Same family as TMEM230	2014	Unclear	Dominant	Unclear	No	+	+	-	Low
TMEM230	Missense	Same family as DNAJC13	2016	Loss of function?	Dominant	Unclear	No	-	+	-	Low
VPS13C	Missense or loss of function	..	2016	Loss of function	Recessive	Rare	Yes	++	+	+	High
LRP10	Missense or loss of function	..	2018	Loss of function?	Dominant	Unclear	No	-	+	--	Low

GWAS=genome-wide association study, PD=Parkinson's disease.
 * In this column, ++ denotes ≥4 families reported; + denotes ≥2 and <4 families reported; - denotes 1 family reported; -- denotes no reported families.
 † In this column, ++ denotes ≥4 disease-related reports; + denotes ≥1 and <4 disease-related reports; - denotes no disease-related reports.
 ‡ Reports that could not replicate the finding that this gene is a PD gene. In this column, + denotes no negative reports; - denotes ≥1 and <4 negative reports; -- denotes ≥4 negative reports.
 § Sum of the scores in the three preceding columns, with each + adding 1 and each - subtracting 1; very high denotes a score of ≥5; high denotes a score of 4; medium denotes a score of 2 or 3; low denotes a score of ≤1.

forms of the disease and early-onset parkinsonism (Corti et al., 2011; Bonifati et al., 2002). Parkin and PINK1 are most frequent cause of early-onset autosomal recessive PD. They interact for the proper clearance of damaged mitochondria and mutations usually lead to loss of function. DJ-1 also interacts with Parkin

and PINK1 regulating its translocation to mitochondria. Moreover, it is involved in the prevention of aggregation of α -synuclein.

GBA gene encodes β -glucocerebrosidase, the lysosomal enzyme that is deficient in Gaucher disease. Interestingly, heterozygous mutations in GBA are known to be one of the most common genetic risk factors for developing Parkinson's disease (Billingsley et al., 2018)

2.2.1. Leucine-rich repeat kinase 2

Leucine-rich repeat kinase 2 (LRRK2) is a multidomain protein of 2.527 amino acids containing several functional domains. These include two enzymatic domains, a Ras of complex proteins (ROC)-type GTP-binding domain and a serine/threonine protein kinase domain; a carboxyl terminal of ROC (COR) domain; and a number of repeat domains (see Fig. 4) (Corti et al., 2011).

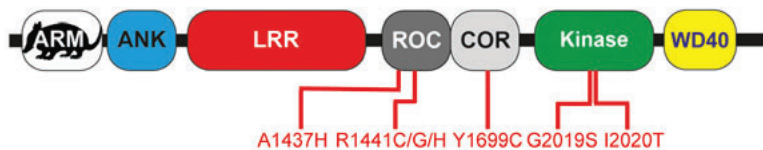


Figure 4. Schematic representation of the LRRK2 protein.

LRRK2 protein contains several conserved domains ARM (Armadillo), ANK (ankyrin repeat), LRR (leucine-rich repeat), Roc (Ras of complex proteins: GTPase), COR (COOH terminal of Roc), kinase domain, and WD40. In red, the seven pathological mutations (Adapted from Singh and Ganley, 2021).

LRRK2 is expressed in various tissues, especially in the brain, lungs and kidneys (Giasson et al., 2006). Different studies have suggested that the expression of LRRK2 in the substantia nigra and dopaminergic neurons is low (Higashi et al., 2007; Taymans et al., 2006). However, others suggested that it is preferentially expressed in A9 DA neurons of SNpc, compared to A10 DA neurons from ventral tegmental area (Han et al., 2008). At the subcellular level, it is located in the cellular cytosol and never in the nucleus. Even though the

protein does not have obvious transmembrane domains, it is also located in membranous cell structures and it has been suggested that LRRK2 can play a role in the regulation of intracellular trafficking by commuting between cytosol and membrane (Biskup et al., 2006).

Physiological functions of LRRK2 protein are not completely understood. Studies in mouse and rat *Lrrk2* KO models have demonstrated that the protein is not essential for the animal survival, but it is involved in neurogenesis as well as development of lungs and kidneys. Its role has been especially demonstrated in autophagy-lysosomal pathway and mitochondrial function (Araki et al., 2018). Through the phosphorylation of diverse substrates, including Rab family, β -tubulin or tau, LRRK2 has been suggested to have a role in several functions like autophagy, synaptic transmission, cytoskeleton remodeling and regulation of protein expression (Jeong et al., 2020)

Leucine-rich repeat kinase 2 mutations and Parkinson's disease

LRRK2 is the causative gene for PARK8-type PD with autosomal dominant inheritance. LRRK2 mutations are the most common cause of familial PD and are present in a significant fraction of sporadic PD. LRRK2 functions have even been found to be dysregulated in sporadic forms without any mutations of the gene (Pons-Espinal et al., 2019; Jeong et al., 2020).

Clinically, LRRK2 PD is a late-onset PD being similar to sporadic forms but with a slightly more benign course and less frequent dementia (Delamarre et al., 2017; Lees et al., 2009). It has been suggested that neuropathological manifestations of patients carrying mutations in LRRK2 can be modulated by genetic and environmental factors. This is due to the differences found in several histopathological studies in which only some LRRK2 PD patients present α -synuclein accumulation whereas all patients presented depletion of dopaminergic neurons (Araki et al., 2018).

Mutations in LRRK2 were discovered in 2002 and there are more than 100 mutations described to date. Only seven of them have been reported to be pathogenic with G2019S mutation being the most common (see Fig. 4) (Delamarre et al., 2017). The penetrance of the G2019S mutation is incomplete and age-dependent as it increases the risk of developing PD from 28% at the age of 60 to 74% at 79 (Lees et al., 2009; Bilingsley et al., 2018).

The G2019S mutation is believed to be responsible for an up-regulation of LRRK2 kinase activity which has been demonstrated to induce neuronal toxicity, neural shortening and cell death (Lees et al., 2009; Delamarre 2017; Jeong 2020)

3. Mechanisms involved in PD pathogenesis

The research community has made great effort to unveil the underlying mechanisms of Parkinson’s disease. Epidemiological, genetic and postmortem studies, as well as in vitro and in vivo models have helped us to better understand the molecular events leading to dopaminergic neurodegeneration.

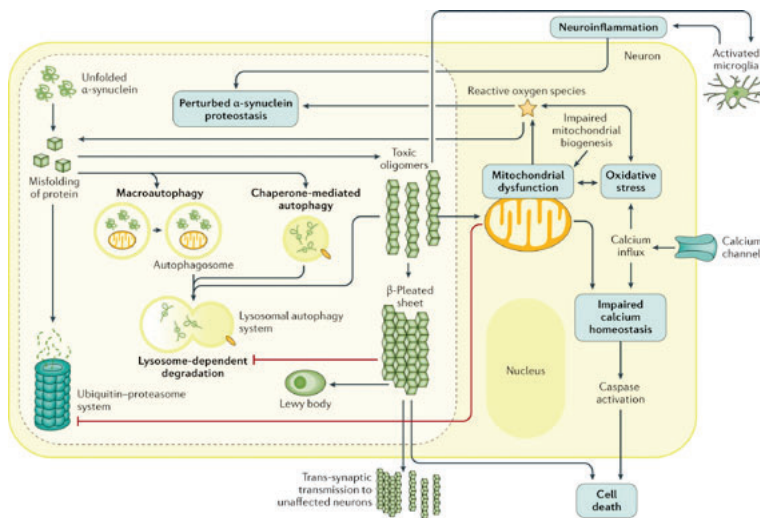


Figure 5. Molecular mechanisms involved in Parkinson’s disease. Scheme of the principal molecular pathways involved in the pathogenesis of Parkinson’s disease (From Poewe et al., 2017).

Despite the lack of understanding of the exact mechanism, it is known that mitochondrial dysfunction, oxidative stress, dysfunctional protein aggregation and degradation, and neuroinflammation play a pivotal role in the DAN loss (see Fig. 5) (Maiti et al., 2017).

3.1. Mitochondrial dysfunction

Mitochondria are called the powerhouses of the cell as they are responsible for the generation of energy in the form of ATP. These very dynamic organelles with a complex structure are involved in the regulation of calcium homeostasis and the removal of free radicals. They continuously undergo cycles of fusion and fission that determines their morphology, function and recycling (Franco-Iborra et al. 2016).

Mitochondria were first seen as important in Parkinson's disease research in the 1980s after some cases of drug abuse were link to Parkinsonian symptoms (Langston et al., 1983). It was suggested that 1-Methyl-4-phenyl-1,2,3,6-tetrahydropyridine (MPTP) after crossing the blood-brain barrier was converted to MPP⁺ by glia and internalized via the dopamine transporter (DAT) in dopaminergic neurons. In DAN, MPP⁺ inhibited respiratory chain complex I. These findings were confirmed years later with postmortem PD samples in which activity of complex I was diminished (Grunewald et al., 2018). After that, MPTP and other complex I inhibitors, such as rotenone and paraquat, have been used to generate PD animal models (Jackson-Lewis et al., 2012; (Francardo, 2018).

Reduction of complex I activity results in loss of bioenergetic function, oxidative stress and impaired calcium homeostasis (Grunewald et al., 2018). It is important to note that the deficiency of complex I has a role in loss of dopaminergic neurons, causing them to be more susceptible to neurotoxins (Perier et al., 2010).

Mitochondrial dysfunction can also alter transcription factors involved in

mitochondrial biogenesis. Both mitochondrial transcription factor A (TFAM) and proliferator-activated receptor-gamma coactivator-1 α (PGC-1 α) are dysregulated in conditions of mitochondrial dysfunction and are reported to have a protective role against neurodegeneration (Raza et al., 2019; Bose et al., 2016).

PD-related genes associated to mitochondrial dysfunction

Mutations in genes described as playing a role in familial forms of Parkinson's disease, are known to be involved in mitochondrial dysfunction. These include Parkin, PINK1, DJ-1, LRRK2 and SNCA among others.

Parkin and PINK1 have a critical role in mitophagy. Physiologically, PINK1 is located in the outer membrane of mitochondria (OMM) and it is cleaved in a voltage-dependent manner. After loss of mitochondrial membrane potential, PINK1 is accumulated in the OMM and recruits Parkin via phosphorylation of ubiquitin. Parkin, in turn, ubiquitinates OMM proteins and subsequently activates the ubiquitin-proteasome system (UPS) leading to a recruitment of autophagy machinery. At this point, mitophagosomes are formed to be removed via lysosome system (Cai and Jeong, 2020). Therefore, mutations in both Parkin and PINK1 cause defects in mitophagy.

Besides its important role in the regulation of mitophagy, lack of Parkin has been observed to promote decreased levels of proteins involved in mitochondrial function, reduced activity of complexes I and IV, lower respiratory capacity and decreased integrity of mitochondria. On the other hand, PINK1 mutations are link to decrease mitochondrial respiration and synthesis of ATP together with increased aggregation of α -synuclein and general increased of mitochondrial dysfunction (Bose et al., 2016).

Studies in human and mice models have demonstrated an impairment in mitochondrial respiration, decrease of mitochondrial membrane potential,

increased levels of ROS and altered mitochondrial morphology when DJ-1 is mutated (Bose et al., 2016).

LRRK2^{G2019S} and mitochondrial alterations

Mutations in LRRK2 have been associated equally to mitochondrial dysfunction, altered mitochondrial dynamics and dysfunctional mitophagy. In cellular models using PD patient-derived iPSCs it has been demonstrated that the G2019S mutation increases oxidative stress (Singh et al 2019) and promotes the imbalance of the fusion and fission mitochondrial events in neurons. Wang and colleagues demonstrated that R1441C and G2019S LRRK2 mutations increase fragmentation in neurons through direct interaction with DRP1, a protein that plays a critical role in mitochondrial fission (Niu et al., 2012; Wang et al., 2012). More recently, a study in microglia confirmed that LRRK2^{G2019S} promotes mitochondrial fragmentation via Drp1 and showed that it triggered a pro-inflammatory response (Ho et al. 2018).

Studies in murine primary cultures and PD patient fibroblasts carrying the LRRK2^{G2019S} mutation suggested that the increased kinase activity of the protein promotes mitophagy. However, a study from Hsieh et al. (2016) demonstrated that mitophagy is delayed in PD iPSC-derived neurons from patients harboring the G2019S mutation. Later on, Bonello et al. demonstrated that mutant LRRK2 with increased kinase activity impairs PINK1/Parkin dependent mitophagy, modulating several actors in different steps of the mitochondrial degradation, which was confirmed in another study with LRRK2^{G2019S} patient-derived fibroblasts (Bonello et al. 2019; Korecka 2019). These results were confirmed by Wauters et al. in 2020 when it was demonstrated that LRRK2^{G2019S} promotes a heightened phosphorylation of Rab10 and thus, impairment of depolarization-induced mitophagy as the interaction of Rab10 with the autophagy receptor optineurin (OPTN) is reduced (see Fig. 6).

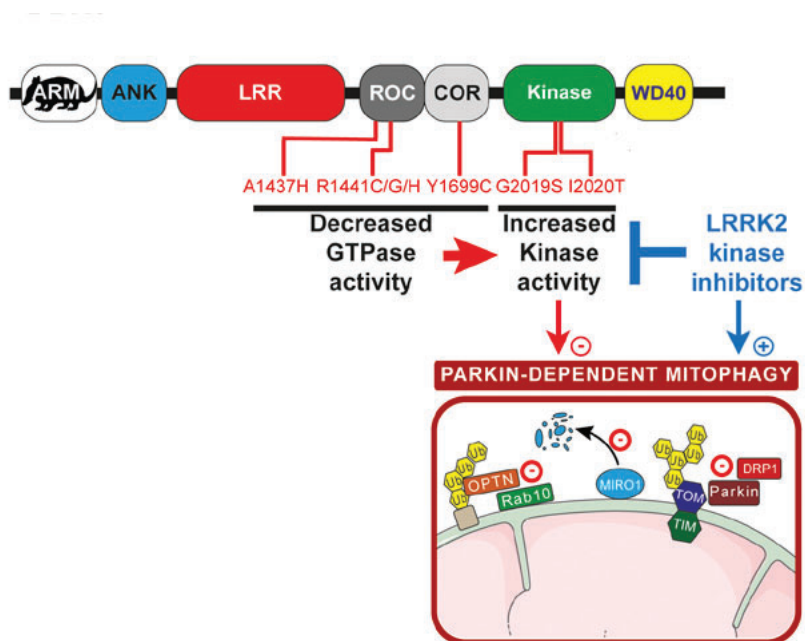


Figure 6. Roles of LRRK2 in PINK1/Parkin dependent mitophagy. Increased LRRK2 activity reduces Parkin interaction with TOM and DRP1, reduces Rab10 recruitment to mitochondria and Rab10-OPTN interaction (From Singh and Ganley, 2021).

3.2. Oxidative stress

Reactive oxygen species (ROS) are important in normal physiology. There are antioxidant proteins such as superoxide dismutase and glutathione that prevent ROS levels from getting too high (Indo et al., 2014). When the system fails, it leads to oxidative stress that have detrimental effects on cells. In fact, oxidized DNA, lipids and proteins are found in brain tissue of both sporadic and familial PD patients (Bosco et al., 2006; Nakabeppu et al., 2007).

The physiological generation of ATP in the mitochondria generates ROS as a byproduct. The process includes the transfer of electrons through a series of protein complexes via redox reactions to oxygen in the electron transfer chain. When respiratory chain complex I is altered, electrons prematurely escape from the electron transport chain causing excessive ROS production, which is detrimental to cells (Puspita et al., 2017; Grunewald et al., 2018). Dopaminergic

neurons are especially susceptible to ROS and it has been verified in the substantia nigra of postmortem PD brains because along with the decline of complex I activity it was observed the increase in intracellular ROS (Schapira et al., 1990; Parker et al., 2008).

Defective mitochondria, that exhibit high levels of oxidative stress, can also display a decreased membrane potential. As mitophagy is promoted by internalization of PINK1 in a voltage-dependent manner, damaged mitochondria can accumulate in the cell and therefore, increase ROS production (Puspita et al., 2017).

Oxidative stress can also be generated by the metabolism of dopamine itself. Dopamine can be oxidized and produce free radicals and quinones that could eventually interact with ROS scavengers, respiratory chain complexes or proteins of the mitophagy pathway (Grunewald et al., 2018).

3.3. Dysfunctional protein degradation

Protein misfolding, aggregation and accumulation are common disease mechanisms in several neurodegenerative diseases including Parkinson's disease. Accumulation of damaged or abnormal proteins may lead to perturbed cellular function and consequent cell death (Kaila et al., 2015; Raza et al., 2019). Accordingly, neurons rely on elaborated pathways of protein quality control and removal for maintaining intracellular protein homeostasis. Molecular chaperones, the ubiquitin-proteasome system (UPS) and the autophagy-lysosomal pathway (ALP) are critical degradation pathways used by a normal cell to destroy targeted abnormal proteins. The successive failure of these protein degradation pathways, as a cause or consequence of early pathological alterations in vulnerable neurons at risk, may be a crucial step in the pathological cascade that leads to spreading neurodegeneration. On this aspect, understanding how α -synuclein is degraded by neurons or even by astrocytes would be crucial in the

PD research field. Indeed, deciphering the pathway responsible for degradation of α -synuclein could impact remarkably for the development of new therapeutic approaches to facilitate clearance and to counteract α -synuclein pathology.

3.4. Neuroinflammation

For several years, Parkinson's disease research has focused on the mechanisms promoting the loss of the dopaminergic neurons and α -synuclein accumulation. However, during the last years neuroinflammation has been gaining interest of researchers and the question whether it protects or promotes neurodegeneration is to be clarified.

Inflammation aims at protecting the host from a pathogenic or damaging-causing agent and promote tissue repair. The central nervous system (CNS) has been typically seen as an immunologically privileged site as it is physically separated from the peripheral immune system by the blood-brain barrier. However, astrocytes and microglia are known to be activated with an immune response to Pathogen-Associated Molecular Patterns (PAMPs) and Damage-associated molecular patterns (DAMPs). This means that microglia and astrocytes can be recruited to create a protective environment in response to PAMPs and DAMPs such as factors secreted by damaged neurons or protein aggregates (Pajares et al., 2020). Nevertheless, recent hypothesis suggests that during the course of the disease glial cells, when activated, may switch to a toxic phenotype that can accelerate neurodegeneration. The altered responses might be influenced by aging or by the presence of specific genetic mutations associated to PD (Liddelow et al., 2017; Clarke et al., 2018).

This activation of glia in the CNS promotes persistent neuroinflammation that appears to be a contributor to disease progression (Pajares et al., 2020). There are several pathological alterations that have been described supporting the idea that neuroinflammation might sustain or exacerbate DAN degeneration.

Pro-inflammatory mediators are increased before the appearance of α -synuclein and has been correlated with a worst PD prognosis. Not only have microgliosis and reactive astrocytes been found in PD postmortem studies but also activated microglia has been detected in PET imaging in prodromal and diagnosed PD patients. Besides that, epidemiological studies have shown how PD risk is reduced with the use of anti-inflammatory medications (Kaila 2015; Pons-Espinal, 2019; Pajares, 2020).

4. Astrocytes in Parkinson's disease

Mechanisms underlying cell death that are cell autonomous to dopaminergic neurons have been widely studied and are mentioned above. Yet in recent years, non-cell autonomous mechanisms have gained interest in the field.

Astrocytes are good candidates for the study of non-cell autonomous neurodegeneration. Astrocytes are the largest glial cell population in the CNS and play a pivotal role in the maintenance of brain homeostasis. Their functions include preservation of synaptic homeostasis, trophic support to neurons and maintenance of the blood brain barrier (BBB) (Sofroniew et al., 2009). Astrocytes can respond to pathological factors and transform to reactive astrocytes which have been found in postmortem brain of PD patients. It is suggested that the disruption of the normal astrocyte functions can contribute to the pathogenesis of Parkinson's disease, not only in the later stages, but even to the initiation or progression (Pons et al., 2019).

4.1. Astrocytes' functions in healthy brain

Astrocytes make contact with blood vessels and form gap junctions between neighboring astrocytes and envelope synapses in gray matter or Ranvier nodes in white matter. It has been described that astrocytes express sodium and potassium

channels but do not propagate action potentials like neurons. However, a sign of functionality of astrocytes-astrocytes or astrocytes-neuron communication is the increase in intracellular calcium concentration. Their main functions in physiological conditions in the brain are summarized below.

Brain homeostasis

During neurodevelopment astrocytes guide both the migration of axons and some neuroblasts as well as the formation and function of synapses. They could even regulate synapsing pruning by releasing signals to tag synapses that should be engulfed by microglia (Barres, 2008).

Prostaglandins, nitric oxide and arachidonic acid are molecular mediators released by astrocytes to regulate blood flow in a coordinated manner. Locally, they can regulate blood flow in response to neuronal and synaptic activity (Koehler et al., 2009).

Synaptic maintenance

Astrocytes processes enveloping synapses are crucial for maintaining synaptic homeostasis. They express high levels of transporters for neurotransmitters such as glutamate and GABA for their rapid removal from the extracellular space to avoid detrimental accumulation and to maintain spatial and temporal encoding of synaptic transmission (Allen, 2014). Astrocytes can recycle these neurotransmitters into active transmitters such as glutamine and bring them back to the synapses (Bouzier-Sore and Pellerin, 2013).

In addition to synaptic space regulatory function, astrocytes have a direct role in synaptic transmission through the release of certain gliotransmitters. Moreover, they release growth factors, such as glial cell-derived neurotrophic factor (GDNF), that can exert powerful influence on synaptic remodeling or

pruning both in healthy or diseased CNS (Sofroniew et al., 2010).

Brain metabolism

Several studies have converged in the idea that astrocytes can also contribute to brain metabolism (Vasile et al., 2017). Due to their architecture, they can take up glucose from blood vessels and release metabolites to neurons. Additionally, astrocytic glycogen can serve as an energetic sustain to neurons in episodes of high neuronal activity or hypoglycemia (Sofroniew et al., 2010).

Blood brain barrier

Together with cerebral endothelial cells and perivascular pericytes, astrocytes are main components of the blood brain barrier (BBB), even though their role in BBB function is still to be clearly defined. Some studies sustain the idea of astrocytes inducing barrier properties in cerebral endothelial cells, but others argue that the BBB become functional before the appearance of astrocytes. In addition, other studies claim that the disruption of specific BMP signal from astrocytic endfeet can lead to BBB leaks (Sofroniew 2010).

4.2. Astrocytes in response to pathology

Almost two centuries ago, Andriezen (1983) described the hypertrophy of reactive astrocytes in a pathological brain for the first time. Since then, it has been widely accepted that morphological changes of neuroglia and astrocytes in the CNS reflects toxic or diseased state (Escartin et al., 2021).

Astrocytes reactivity is the capacity of astrocytes to adopt different states in response to diverse pathology. These different states are characterized by a specific molecular profile, functions and a distinct impact on diseases. It

is important to highlight that astrocytes also have the capacity to respond to different stimuli from the CNS in a physiological manner and are known as activated astrocytes (Escartin et al., 2021).

Reactive astrogliosis is the progressive alteration in molecular, cellular and functional aspects in astrocytes in response to pathology in the CNS. These changes can potentially result in a gain of new functions or a loss of them with a beneficial or detrimental impact in the neighboring cells (Sofroniew et al., 2010; Escartin et al., 2021). Reactive astrogliosis has been associated to neurotoxicity or inflammation. However, the function of reactive astrocytes is to protect the CNS of excitotoxicity and oxidative stress, promote blood brain barrier repair, stabilize extracellular fluids and vasogenic edema, and limit the spread of inflammatory cells by the generation of a glial scar (Sofroniew, 2009). In neurodegenerative diseases, astrocytes have been described to contribute to the progression even as not primary initiators of the disease (Escartin et al., 2021).

4.3. Astrocytes as disease modulators in Parkinson's disease

One of the key aspects of the pathogenesis of Parkinson's disease is neuroinflammation and the presence of reactive astrocytes which suggests their role in PD pathogenesis.

PD-related genes

Among the genes which are described as a cause of familial PD, some have been identified to be highly expressed in astrocytes and to have a role in its biology. Mutations in DJ-1 gene have been related to increased neuronal excitotoxicity due to a decrease in expression of the astrocytic glutamate transporter EAAT2 and a subsequent reduction in glutamate uptake (Kim et al., 2016). Since DJ-1 has a role in mitochondrial function and oxidative stress, as a result of a knockdown of

DJ-1, astrocytes have a reduced ability to protect neurons against neurotoxicity in rotenone or 6-hydroxydopamine models of PD (Booth et al., 2017). LRRK2 is also expressed in astrocytes and has been associated to the autophagy-lysosome pathway. Mutant LRRK2 has been shown to alter lysosome size and pH in primary mouse astrocytes (Manzoni et al., 2013; Henry et al., 2015).

α -synuclein accumulation

The formation of protein aggregates in neurons mainly composed of α -synuclein is one of the hallmarks of Parkinson's disease. Even though SNCA gene has low expression in astrocytes, unlike in neurons, postmortem studies demonstrated that α -synuclein inclusions are also present in astrocytes (Wakabayashi et al., 2000; Braak et al., 2007). This observation indicates that astrocytes may uptake α -synuclein secreted by neurons in order to promote a healthy environment for neurons by the removal and degradation of toxic α -synuclein. Importantly, an inflammatory response in primary astrocytes cultures with high concentrations of extracellular α -synuclein has been detected. Exceeding a certain concentration threshold, the inflammatory response starts and pathology begins to develop (Lee et al., 2010; Fellner et al., 2012; Rannikko et al., 2015). In addition, potential engulfment and accumulation of α -synuclein in astrocytes could lead to a dysregulation of physiological functions of the cell such as glutamate uptake and the integrity of the blood brain barrier. Overexpression of SNCA under astrocyte-specific promoter in a mouse model demonstrate the effect of α -synuclein in astrocytes. Apart from alteration in glutamate receptors and Aquaporin-4 channel (involved in the BBB function) in astrocytes, mice exhibited a significant loss of dopaminergic neurons (Gu et al., 2010).

Mitochondrial dysfunction

Mitochondrial function is related to key astrocytic functions such as glutamate-glutamine cycle or regulation of Ca^{2+} metabolism. As mentioned above, astrocytes are responsible for the uptake of the glutamate present in the synapses and the conversion to α -ketoglutarate and glutamine (Schousboe et al., 2013). KGDHC, enzyme responsible for the conversion of glutamate to α -ketoglutarate, is located in the mitochondria. Interestingly, PD patients present low levels of KGDHC in basal ganglia which suggest a role of this pathway in the progression of the disease. Moreover, several studies have shown that dysregulation of glutamine cycle is caused by reactive astrogliosis and that mitochondrial dysfunction in astrocytes induces alterations in glutamate metabolism and excitotoxicity. Taken together, these results suggest a common mechanism in which alterations in glutamate metabolism are a consequence of astrocytic mitochondrial dysfunction (Bantle et al., 2021).

Ca^{2+} homeostasis is a key function of mitochondria. Regulators of the Ca^{2+} flux such as ITPKB and MICU3, which are expressed in astrocytes, have been identified as risk factors for PD. Dysregulation in the turnover of Miro1, that is implicated in the localization of mitochondria close to extracellular source of Ca^{2+} , has been proposed to lead to dysbalanced Ca^{2+} signaling. Additionally, Ca^{2+} transients are involved in glucose mobilization from astrocytes to neighboring cells, response to acute injury and synaptic transmission. It can be then predicted that alteration of mitochondrial Ca^{2+} can as well contribute to PD progression (Bantle et al., 2021).

Transmitophagy

Transmitophagy is the phenomenon of transcellular mitophagy, first described in the retinal ganglion cell axons in mice in which neuronal mitochondria were

internalized and degraded by bordering astrocytes (Davis et al., 2014). More recently, it has been demonstrated in a mouse PD model that astrocytes are responsible for the clearance of damaged mitochondria transferred from DAN displaying axonal fragmentation (Morales et al., 2020). This finding is especially interesting in the context of PINK1/Parkin associated PD as PINK1 has been shown to be predominantly present in astrocytes rather than in neurons (Barodia et al., 2019). The opposite process, namely transfer of healthy mitochondria from astrocytes to neuron after an injury, has also been observed in several studies. By the usage of iPSC-derived astrocytes and neurons, transfer of astrocytic healthy mitochondria to neurons had neuroprotective effect in an in vitro PD model induced by rotenone, as it reversed DA neurodegeneration and axonal pruning (Cheng et al., 2020).

Oxidative stress

Oxidative stress is a pathogenic factor in Parkinson's disease. Astrocytes are the main actors to maintain the redox homeostasis in the brain. ROS can damage mitochondrial metabolism, DNA and mitochondrial DNA (mtDNA). mtDNA is especially susceptible to damage because, besides being close to the source of ROS, it has low repair capacity. In turn, mutations in mtDNA can cause an increase in ROS production generating a vicious cycle. In postmortem PD brains, loss of glutathione from the SNpc and the presence of oxidative stress are common features. Both are known to induce Nfr2 activity. Nfr2 is a transcription factor that regulates antioxidant genes. In overexpression experiments, Nfr2 overexpressed under the GFAP promoter prevented MPTP and 6-hydroxydopamine toxicity and mutant α -synuclein. These results indicate that astrocytes are crucial mediators of Nfr2 signaling to protect against oxidative stress (Liddell et al., 2017; Fernandez-Fernandez et al., 2012).

5. Modeling Parkinson's disease

Despite the advances in the identification of genes and proteins involved in PD, there are still considerable gaps in our understanding of the molecular and cellular mechanisms underlying the chronic neurodegenerative process in PD (Melrose et al., 2006; Dawson et al., 2010). In order to develop new treatments for the disease, it is of vital importance to gain full understanding of the mechanisms implicated in neuronal cell death and it is also required testing interventions that could have beneficial effects. Due to limited availability of living human brain tissue, experimental cellular and animal models have been developed to mimic PD pathogenesis (Booth et al., 2017; Chia et al., 2020). Nonetheless, they present some limitations.

Cellular models mainly refer to standard human tumor cell lines and therefore only partially reflect the characteristics of non-dividing human DAN, the most relevant cell type affected in PD (Lázaro et al., 2017).

Animal models include overexpression or knockdown of the gene of interest and the use of neurotoxins. Neurotoxins commonly used are 6-hydroxydopamine (6-OHDA), 1-methyl-4-phenyl-1,2,3,6-tetrahydropyridine (MPTP), paraquat, and rotenone. The addition of these molecules increases oxidative stress and consequently promote a rapid nigrostriatal dopaminergic degeneration. However, they fail to recapitulate the slow and progressive degenerative changes that occur in PD human pathology and the Lewy body formation (Tieu, 2011; Torrent et al., 2015; Chia et al., 2020). On the other hand, genetic animal models based on overexpression (driven by non-native or physiological human promoters) or knockout of the gene of interest, only partially replicated key features of neurodegeneration in PD. For instance, the significant loss of DAN neurons in the SNpc is not reproduced in most of the genetic models (Sanchez et al., 2014).

It has been difficult to replicate the overall scenario of alterations associated

with disease pathophysiology and to clarify the events that initiate and contribute to the pathologic process in PD. A breakthrough in modeling complex diseases, such as PD, overcoming the limitations mentioned above, came from the application of new technologies to reprogram fibroblasts into induced pluripotent stem cells (iPSC) (Takahashi et al., 2007; Stadtfeld and Hochedlinger, 2010). A key advantage of cell reprogramming is the possibility of generating iPSC from patients that carry the same genetic background, including precise genetic variants, which may contribute to the disease, thus providing the unprecedented opportunity to recapitulate both normal and pathologic human tissue formation in vitro, and facilitating disease investigation. It also offers the possibility of studying the interplay between different cell types, screening the patient-specific response to specific interventions in a high-throughput mode and recapitulating the time-course of the disease (see Fig. 7). In addition, the iPSC can be differentiated into disease-relevant cell types, such as dopaminergic neurons or astrocytes. It has been shown that they recapitulate some PD features that couldn't be mimic in other in vitro models (Torrent et al., 2015; Lázaro, 2017).

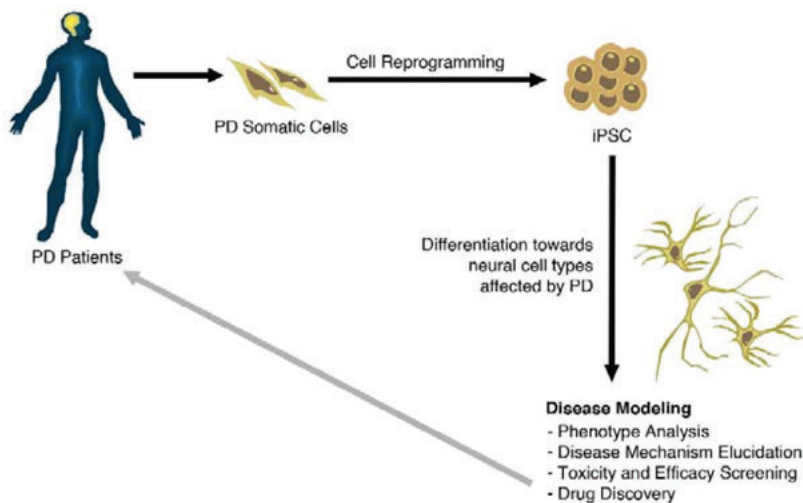


Figure 7. Generation of iPSC for disease modeling in PD.

Schematic representation of somatic cell reprogramming to iPSC and their function in disease modeling (From Torrent et al., 2015).

5.1. Induced Pluripotent Stem cells to model Parkinson's disease

For a couple of years, several laboratories have been actively investigating the development of iPSC-based technologies and disease modeling by using iPSC technology. Consiglio laboratory used an iPSC-based strategy to model not only monogenic cases of PD associated to LRRK2 mutations, but also idiopathic PD (ID-PD). Long-term cultures of iPSC-derived DAN from either ID-PD- or LRRK2-PD-iPSC showed morphological alterations which includes reduced numbers of neurites and neurite arborization (see Fig. 8), and accumulation of autophagic vacuoles which were not evident in DAN differentiated from control-iPSC (Sánchez-Danés et al., 2012). Subsequently, it has been shown that DAN from LRRK2-mutant patient-specific iPSC, but not those from idiopathic PD or control individuals, display alterations in chaperone-mediated autophagy (CMA) that are responsible for the abnormal accumulation of α -synuclein (see Fig. 9), and that they predate any morphological sign of neurodegeneration (Orestein et al., 2013). These findings demonstrated that the usage of patient-specific iPSC-derived dopaminergic neurons is very promising technique to model Parkinson's disease, as it recapitulates the key pathological hallmarks of the disease: specific dopaminergic neurodegeneration and accumulation of α -synuclein in the surviving neurons.

The experimental set up used in the present thesis was described by Di Domenico et al. (2019). We identified a novel, non-cell autonomous mechanism of neurodegeneration in PD, elicited by dysfunctional protein degradation pathways in iPSC-derived astrocytes from LRRK2-PD patients. iPSC generated from healthy donors and Parkinson's disease patients carrying the LRRK2^{G20192} mutation were differentiated towards dopaminergic neurons and astrocytes. Control DAN cultured on top of LRRK2-PD astrocytes displayed signs of neurodegeneration and abnormal accumulation of α -synuclein transferred from PD astrocytes (see Fig. 10). On the other hand, control astrocytes could partially

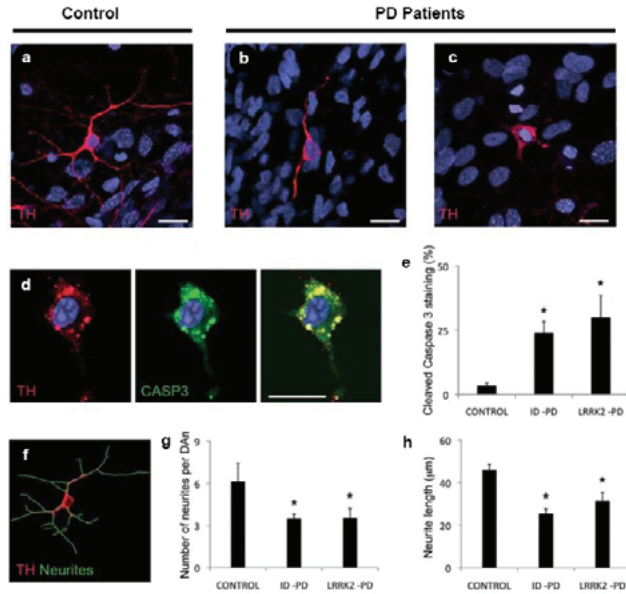


Figure 8. Morphological alterations of PD-iPSC-derived dopaminergic neurons.

a-c. Immunofluorescence staining of DAN (TH positive) after long-term culture. PD-iPSC-derived neurons display signs of neurodegeneration (neurite shortening). d. Representative image of TH and Cleaved Caspase 3 double positive DAN. e. Quantitative analysis of percentage of DAN showing cleaved caspase 3 staining representing death cells. f. Representative image of a control-iPSC-derived DAN showing a healthy morphology. g-h. Quantitative analysis of the number of neurites per DAN and the neurite length (Adapted from Sánchez-Danés et al., 2012).

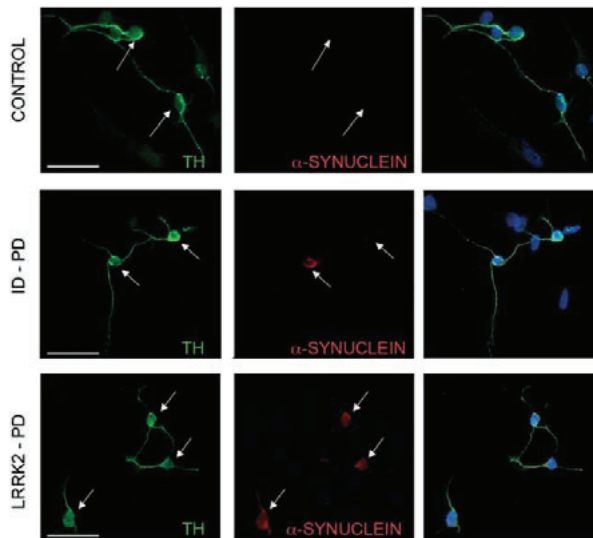


Figure 9. Abnormal accumulation of α -synuclein in PD-iPSC-derived dopaminergic neurons.

Immunofluorescence staining of DAN for TH and α -synuclein showing accumulation in ID- and LRRK2-iPSC-derived neurons (Adapted from Sánchez-Danés et al., 2012).

prevent the appearance of PD-related phenotypes in PD DA neurons. In deep study of α -synuclein clearance in the PD, astrocytes unveiled dysfunctional chaperone mediated autophagy (CMA) and macroautophagy and a progressive accumulation of α -synuclein. Induction of CMA prevented the accumulation of α -synuclein in both astrocytes and DAN and in coculture prevented the dopaminergic neurodegeneration (Di Domenico, 2019). Our study is the only analysis of the impact of LRRK2^{G20192} astrocytes on neurodegeneration in a human iPSC model.

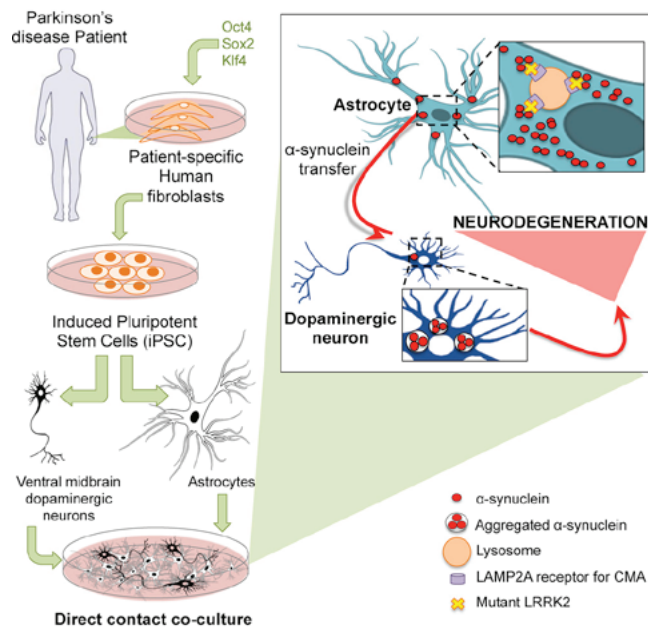


Figure 10. Graphical abstract summarizing results obtained in di Domenico et al., 2019 study.

Other groups have studied the alterations related to the LRRK2^{G20192} mutation using patient-specific iPSC-derived astrocytes. In addition to α -synuclein accumulation, Sonninen et al. (2020) described metabolic alterations in iPSC-derived LRRK2^{G20192} astrocytes. They found decreased mitochondrial respiration and increased extracellular acidification, disturbed Ca²⁺ homeostasis, and increased released of cytokines upon inflammatory stimulation in PD astrocytes.

More recently, Ramos-Gonzalez et al., 2021, found a loss of complexity and key astrocytic markers in LRRK2-PD astrocytes. In addition, astrocytes displayed aberrant mitochondrial morphology and functionality together with increased glycolysis and production of ROS.

OBJECTIVES

In our laboratory, we have developed a genuinely human PD model taking advantage of the iPSC technology that recapitulates the two pathological hallmarks of Parkinson's disease. PD iPSC-derived dopaminergic neurons (DAn) accumulate α -synuclein and degenerate after long term in culture (Sánchez-Danés et al., 2012). We also demonstrated that the LRRK2^{G2019S} inhibits chaperone-mediated autophagy (CMA) and compromises the α -synuclein clearance in dopaminergic neurons (Orestein et al., 2013). More recently, we have shown that, similarly, iPSC-derived astrocytes harboring the LRRK2^{G2019S} mutation accumulates α -synuclein secondary to a blockage of both macroautophagy and CMA. More importantly, control DAn cocultured with LRRK2-PD astrocytes displayed neurodegenerative phenotype and accumulation of astrocytic α -synuclein (di Domenico et al., 2019).

Taking advantage of our PD model, the main objectives of this thesis are to:

1. Evaluate the metabolic activity and the mitochondrial functions in control versus LRRK2-PD patient-specific iPSC derived astrocytes.

To fulfill this first objective, we will:

- a. generate an enriched population of pure astrocytes from LRRK2-PD-specific iPSC as well as from healthy and isogenic iPSC (Ctrl iPSC);
- b. characterize the newly generated LRRK2-PD and Ctrl astrocytes;

- c. carry out comparative systematic analyses of astrocytes differentiated from LRRK2-PD and Ctrl iPSC for: i) morphological alterations of mitochondrial network; and ii) metabolic activity.

2. Investigate whether mitochondrial alterations in LRRK2-PD astrocytes impact on neurodegeneration in PD.

To fulfill this second objective, we will:

- a. generate DA neurons from control iPSC;
- b. establish a co-culture between LRRK2-PD astrocytes and control dopaminergic neurons to study their possible pathological crosstalk.

MATERIALS AND METHODS

iPSC information

Six different iPSC lines were used in this study that were previously generated and characterized in the laboratory as described in Sánchez-Danés et al., 2012 and di Domenico et al., 2019 (see table 1). We used two control iPSC lines derived from fibroblasts from healthy donors and three lines generated from three LRRK2 Parkinson’s disease patients carrying the G2019S mutation (Sánchez-Danés et al., 2012). In addition, using the CRISPR/Cas9 technology an isogenic line was generated from one of the mutant lines as described in di Domenico et al., 2019.

Table 2. iPSc lines used in this study.

	Code	Sex	Age of biopsy	Age of onset	Mutation	Source
CTL	SP09	male	66			Sanchez-Danes
	SP11	female	48			Sanchez-Danes
PD	SP06	male	44	33	LRRK2-G20129S	Sánchez-Danés
	SP12	female	63	49	LRRK2-G20129S	Sánchez-Danés
	SP13	female	68	57	LRRK2-G20129S	Sánchez-Danés
ISO PD	SP13 WT/WT	female	68	57	Corrected	Di Domenico

Generation of iPSC-derived astrocytes

Astrocytes were derived from five iPSC lines as described in di Domenico et al., 2019 (see Fig. 11). Embryoid bodies (EBs) were generated from iPSC

and cultured in suspension on nonadherent plates for two days. EBs were then plated on Matrigel (Corning) coated plates for ten days in DMEM/F-12 (Gibco), 1% NEAA (Lonza), 1% UltraGlutamine (Lonza), 1% Penicillin/Streptomycin (P/S) (Lonza), 1% N2 supplement (Gibco) and supplemented with 20ng/ml b-FGF (Peprotech). Neuronal structures such as neural rosettes and neural tubes were mechanically cut and picked to culture in suspension in nonadherent plates for 4 weeks. The structures were cut every week and cysts and necrotic parts were removed until spherical neural masses (SNMs) were formed as homogenous and bright spheres of neuroectodermal progenitors.

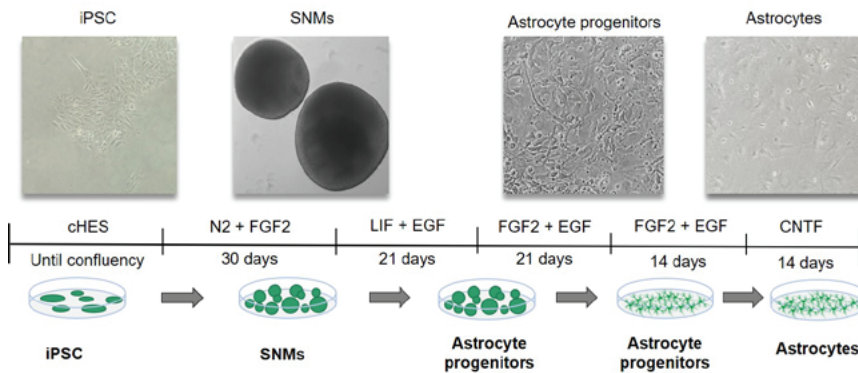


Figure 11. Diagram of the protocol for astrocyte generation.

The SNMs were kept in suspension for astrocyte progenitors induction for 3 weeks in induction medium (DMEM/F-12 (Gibco), 1% NEAA (Lonza), 1% UltraGlutamine (Lonza), 1% P/S (Lonza), 1% N2 supplement (Gibco), 0,1% B27 supplement (Gibco) supplemented with LIF (20ng/ml, Peprotech) and EGF (20ng/ml, Peprotech) and cut once every week. Then, for three more weeks in propagation medium (DMEM/F-12 (Gibco), 1% NEAA (Lonza), 1% UltraGlutamine (Lonza), 1% P/S (Lonza), 1% N2 supplement (Gibco), 0,1% B27 supplement (Gibco) supplemented with b-FGF (20ng/ml, Peprotech) and EGF (20ng/ml, Peprotech). At this point, SNMs were disaggregated to be plated as a monolayer as it follows. SNMs were cut into small pieces and

incubated with accutase (Corning) for 15 minutes at 37°C. Next, the spheres were mechanically disaggregated with the micropipette, centrifuged and plated on matrigel-coated plates in propagation medium for two weeks. The cells were passage on demand when the culture was confluent. Then, astrocyte progenitors were cultured in CNTF medium (Neurobasal (Gibco), 1% NEAA (Lonza), 1% UltraGlutamine (Lonza), 1% P/S (Lonza), 0,2% B27 supplement (Gibco) supplemented with 10ng/ul of CNTF (Peprotech)) for another 14 days. Cells were passage 0 astrocytes and could be frozen in DMSO with 10% fetal bovine serum (FBS). Astrocytes were used at passage 4 for all the experiments.

Generation of iPSC-derived dopaminergic neurons

Ventral midbrain dopaminergic neurons were generated from a control iPSC line as described in ref. Carola. The protocol was optimized in the laboratory using as references the Kriks et al. (2011) and Fedele et al. (2017) protocols. iPSCs were seeded on matrigel-coated 6-well plates at a density of 3×10^5 cells/well and the protocol started when they reached 60-70% of confluency. At this point, medium was changed to SRM medium, containing KO-DMEM (Gibco) supplemented with 15% KO-serum replacement (Gibco), 1% UltraGlutamine (Lonza), 1% NEAA (Lonza) and 55uM of mercaptoethanol (Sigma). Until day five, 10 nM of SB (Tocris) and 100nM of LDN (Sigma) were added to the culture. From day one to seven, 1uM of SAG (Millipore), 2 uM of Purmorphamine (Tocris) and 100ng/ml of FGF8 (Peprotech) were added to the medium. 3uM of CHIR (Miltenyi Biotec) was added from day three until day 13. On day five, SRM was gradually changed to N2 medium containing Neurobasal (Gibco), supplemented with 1x N2 (Gibco), 1% P/S (Lonza) and 1% Ultraglutamine (Lonza). Cells were maintained with 100nM of LDN (Sigma) and 3uM of CHIR (Miltenyi Biotec) from day seven until day 11. Next, the maturation phase included medium change to B27 medium, containing Neurobasal (Gibco),

supplemented with 2x B27 (Gibco), 1% UltraGlutamine (Lonza), 1% P/S (Lonza) plus the maturation factors BDNF (20ng/ml, Peprotech), GDNF (20ng/ml, Peprotech), TGF-beta3 (1ng/ml, Peprotech), AA (200uM), dcAMP (500uM, Sigma) and DAPT (10uM, Calbiochem). Finally, at day 20 DA progenitors were passage to 24-well plates coated with poly-L-ornithine (Sigma), laminin (Sigma) and fibronectin (Sigma) at a concentration of 105 cells/well. Half of the B27 medium was changed every two days until day 35 when the DA neurons were fully mature.

Neuron-Astrocyte co-culture system

PD astrocytes (SP13) and isogenic astrocytes (SP13 wt/wt) were plated on matrigel coated 24-well plates at a concentration of 2×10^4 cells/well. After one week of astrocyte culture, mature control DAn (SP11) that were 35-day-old, were detached using diluted accutase (Corning) and plated on top of astrocytes at a concentration of $50 \cdot 10^4$ cells/well. Co-cultures were maintained for four weeks in B27 medium without maturation factors with medium changes twice per week.

Inmunofluorescence

Cells were fixed in 4% paraformaldehyde for 20 minutes and washed with PBS (Lonza) for 15 minutes, three times. Cells were blocked in blocking solution consisting of TBS1x with 3% of normal donkey serum (Millipore) and 0,01% triton X-100 (Sigma) for 2 hours. Primary antibodies were incubated for 48 hours in the same blocking solution and then washed three times for 15 minutes. Cells were blocked again for one hour and secondary antibodies were incubated for two hours using the same blocking solution. Cells were washed and DAPI was incubated for 10 minutes. After washing the cells, the samples

were mounted with 2,5% PVA/DABCO mounting solution (Poly (vynil alcohol) and 1,4 diazabicyclo [2.2.2.] octane botch from Sigma). Primary antibodies used CD44 m (1:100, Abcam), S100 β rb (1:250, Dako), TUJ1 m (1:500, Biolegend), GFAP gp (1:1000, synaptic Systems), GFAP rb (1:1000, Dako), TOM20 m (1:1000, BD Bioscience), TOM20 rb (1:125, Santa Cruz), dsDNA m (1:250, Progen), DRP1-PS616 rb (1:400, Cell Signaling), LAMP1 (1:100, Hybridoma Bank Iowa University), LC3B (1:100, Cell Signaling), TH rb (1:1000, Sigma). All secondary antibodies were acquired at Jackson ImmunoResearch and used at 1:200.

Protein extraction

Astrocytes were culture for 72 hours on matrigel-coated 6-well-plates at a concentration of 2×10^5 cells/well in CNTF medium. Cells were washed twice with PBS and accutase (Corning) was added to detach the cells. After 6 minutes of incubation at 37°C, cells were harvested with DMEM/F-12 with 10% of fetal bovine serum (FBS). Astrocytes were centrifuged at 4000 rpm for 5 minutes and the supernatant discarded. Pellet was then washed with PBS and cells were again centrifuged at 4000 rpm for 5 minutes. After discarding the supernatant, pellet was kept at -80°C until use.

Astrocyte pellets were resuspended in RIPA protein extraction buffer (Sigma) supplemented with protease inhibitor (Roche). Supernatants containing the proteins were kept at -80°C until use. Protein quantification was done using Bradford (Bio-Rad) and a plate reader at 594 nm.

Western blot

Samples were diluted to the desired concentration in Laemmli Sampe Buffer (LSB) and 4% Dithiothreitol (DTT) (Bio-Rad) and then boiled at 95°C for five

minutes. At this point, 15 µg per sample were charged in 7-15% acrylamide gels for electrophoresis at 120V for 1 hour. Next, cell extracts were transferred to a nitrocellulose membrane (Sigma) in ice at 350A for 120 minutes. Membranes were then submerged in Ponceau solution to detect the presence of proteins and washed right after with TBS with 0,1% tween 15 minutes for three times. Samples were then blocked with 5% milk or 3-5% BSA and primary antibody incubated overnight at 4°C. Membranes were washed again in TBS-0,1% tween and incubated with peroxidase-conjugated secondary antibody (1:2000, Amersham) 1 hour at room temperature. After revealing using ECL (Amersham) in a Chemidoc (Bio-Rad), alpha-tubulin (1:1000, Sigma) as a loading control was incubated for 1 hour at room temperature and washed with TBS-0,1% tween. Finally, and after peroxidase-conjugated secondary antibody incubation, the membrane was revealed using a ECL in a Chemidoc. Protein levels were quantified using FIJI as for the band intensity for each protein and normalized by alpha-tubulin expression. Primary antibodies used DRP1-PS616 rb (1:1000, Cell Signaling), DRP1 m (1:2000, BD Bioscience), MFN1 rb (1:1000, Cell Signaling), MFN2 rb (1:1000, Cell Signaling), OPA1 m (1:1000, BD Bioscience), TIM44 rb (1:1000, Abcam), VDAC (1:1000, Abcam), and TOM20 rb (1:1000, Santa Cruz Technologies).

RNA extraction and gene expression analysis

The isolation of total mRNA was performed with the RNeasy Mini Kit and treated with RNase free DNase I (Qiagen). 500ng were used to synthesize cDNA with the SuperScript III Reverse Transcriptase Synthesis Kit (Invitrogen). Quantitative RT-PCR analyzes were done in triplicate using 2ng/ul cDNA with Platinum SYBR Green qPCR Super Mix (Invitrogen) in an ABI Prism 7000 thermocycler (Applied Biosystems). All results were normalized to β -actin. Primers used were for PGC-1 α gene Fw 5' GGCAGAAGGCAATTGAAGAG

3' and Rv 5' TCAAAACGGTCCCTCAGTTC 3'; TFAM gene Fw 5' CCGAGGTGGTTTTTCATCTGT 3' and Rv 5' GCATCTGGGTTCTGAGCTTT 3'; Nrf1 gene Fw 5' TGAGAGGGCCAAGCAAAG 3' and Rv 5' ATAAATCACACGGCGCTCTT 3'; and β -actin gene Fw 5' GATCATTGCTCCTCCTGAGC 3' and Rv 5' ACATCTGCTGGAAGGTGGAC 3'.

Mitochondrial DNA quantification

DNA was extracted with the GeneJET Genomic DNA Purification Kit (ThermoFisher Scientific) following the manufacturer's instructions. mtDNA was measured by quantitative real-time PCR approach using SybrGreen and specific qPCR primers for mitochondrial tRNA^{Leu(UUR)} gene (mtDNA tRNA^{Leu(UUR)} Fw 5' CACCCAAGAACAGGGTTTTGT 3' and Rv 5' TGGCCATGGGTATGTTGTTA 3') and nuclear β -2-microglobulin (β 2M) (nDNA β 2-microglobulin Fw 5' TGCTGTCTCCATGTTTGATGTATCT 3' and Rv 5' TCTCTGCTCCCCACCTCTAAGT 3').

Flow cytometry

The mitochondrial membrane potential was measured using the TMRM probe (Life Technologies). Astrocytes were tested by plating 5x10⁴ cells per well of a 12-well plate in CNTF medium three days before the assay. As a control for non-specific fluorescence astrocytes were incubated with CCCP at 50mM for 30 minutes. Then, astrocytes were incubated with 200nM of TMRM for 30 minutes. As a negative control, astrocytes were not incubated with TMRM. Cells were washed with PBS, incubated with trypsin without phenol red for 5 minutes at 37°C and neutralize with medium without phenol red with 10% FBS. Fluorescence was measure with a MoFlo Astrios (Beckman Coulter)

using the 561nm laser. The decrease in fluorescence was calculated as a percentage of the control line.

Mitophagy events quantification using mt-Keima plasmid

Direct detection of mitophagy events was done using the mt-Keima plasmid (56108, Addgene). Control, PD and isogenic astrocytes were seeded on μ -Slide 4 Well ibiTreat (IDIDI) at a density of 3×10^4 cells/well in CNTF medium. After three days of culture, the mt-Keima plasmid was transfected using the Lipofectamine Stem Transfection Reagent (Life Technologies) following manufacturer's instructions. After 24 hours medium was changed. The following day, astrocytes were treated with 50 μ M of Urolithin A 24 hours before the imaging and with 5 μ M of CCCP 16 hours prior the imaging. Live astrocytes were imaged using the confocal microscope Zeiss LSM880. Mitophagy events were analyzed using the mito-QC Counter plugin from Fiji. Among all the results obtained, information about mitolysosomes area relative to astrocytes area was used to compare the mitophagy efficiency among lines.

Glutamate uptake assay

To quantify the glutamate uptake of the astrocytes the glutamate assay kit (ab138883, Abcam) was used. 2×10^5 astrocytes were plated in each well of 6-well plate in CNTF medium three days before the assay was performed. After washing with PBS, astrocytes were incubated with Buffered Salt Solution (BSS) with 1 μ M glutamic acid for 10 minutes at 37°C. Then, medium at time 10 and at time 0 (BSS with 1 μ M glutamic acid) were analyzed with the glutamate assay kit used according to the manufacturer's instructions. As a negative control BSS without glutamic acid was used.

Agilent Seahorse XF Cell Mito Stress Test

The Agilent Seahorse XF Cell Mito Stress Test (103015-100, Agilent) measures the oxygen consumption rate (OCR) and the extracellular acidification rate (ECAR) being OCR proportional to mitochondrial respiration and ECAR glycolysis. During the assay, different compounds are added sequentially to the medium to measure different parameters related to mitochondrial function (see Fig. 12). After the basal OCR is measured, the inhibitor of the ATP synthase (complex V) oligomycin is added to the medium. It is used to determine to ATP production link to respiration. The FCCCP is next added as an uncoupler that disrupts the mitochondrial membrane potential. As the proton gradient is collapsed the electron flow through the electron transport chain is uninhibited and the oxygen consumption rate by complex IV reaches its maximum. Apart from the maximal OCR, the spare respiratory capacity is also measured calculated as the difference between maximal and basal respiration. It is a sign of the ability of the cell to respond to an energy challenge. Finally, rotenone, inhibitor of complex I; and antimycin A, inhibitor of complex III, are added. At this point the mitochondrial respiration is completely inhibited and it is measured the nonmitochondrial respiration.

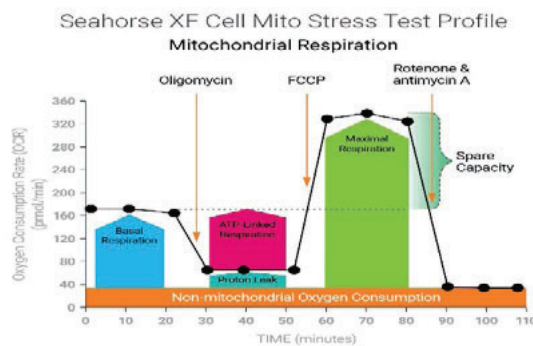


Figure 12. Diagram of Seahorse XF Cell Mito Stress Test Profile showing different inhibitors used and key mitochondrial functional parameters measured.

From Agilent Seahorse XF Cell Mito Stress Test Kit User Guide.

For the measurement of the OCR of PD and isogenic astrocytes, the 24-well format of the Agilent Seahorse XF Cell Mito Stress Test was used and 4.5×10^4 astrocytes per well were seeded. Concentration of the inhibitors were the following: Oligomycin, $3 \mu\text{M}$; FCCCP, $2 \mu\text{M}$; Rotenone, $1 \mu\text{M}$; and Antimycin, $2 \mu\text{M}$.

ROS production measurement

Astrocytes were seeded on Matrigel coated 12-well plates for two weeks in CNTF medium at a density of 5×10^4 cells/well. For treated astrocytes Urolithin A was added at $50 \mu\text{M}$ for the last three days of culture. Hydrogen peroxide was added diluted 1:25 for 10 minutes. Next, $500 \mu\text{M}$ of DCFH2-DA (Sigma) diluted in ethanol was added to each well. Absolut ethanol was used as a negative control. After one hour of incubation at 37°C , cells were harvested using 200ul of cold PBS with 1% triton. Samples were placed in 96 well-plates and the fluorescence was measured in a plate reader at 485nm/530nm. Results were normalized by protein concentration measured using the BCA kit.

OxyBlot assay

In order to quantify the protein oxidation in our astrocytes, 5×10^5 control, PD and isogenic astrocytes were plated on Matrigel-coated 12-well-plates for two weeks in CNTF medium. Before collecting the cells, hydrogen peroxide was added to one well as a positive control. Pellets were performed as explained earlier and protein quantification was done using the BCA kit (Thermo Fisher). Detection of protein oxidation was performed using the OxyBlot Protein Oxidation Detection Kit (S7150, Sigma) following the manufacturer's instructions. In short, first carbonyl groups were derivatize to 2,4-dinitrophenylhydrazone (DNP-hydrazone) by reaction with 2,4-dinitrophenylhydrazine (DNPH). Then

proteins were separated using a 12% acrylamide gel and a western blot was performed using anti-DNP antibody.

Image acquisition and analysis

All images were acquired using a Zeiss LSM880 confocal microscope using 40x and 63x objectives. Images were analyzed using Fiji - Image J software (Schindelin et al., 2009). Mitochondrial classification as fragmented and elongated was done manually using cell counter plugin in Fiji. Perinuclear localization of mitochondria was quantified segmenting the cytoplasm of astrocytes with two concentric circles and measuring the corrected total cell fluorescence in the Tom20 channel in both circles. A ratio between perinuclear and cytoplasmic Tom20 intensity was calculated. Nucleoids' area was calculated selecting dsDNA staining channel and measuring it's area that was normalized by GFAP staining area. Colocalization for Tom20 and Lamp1 was quantified using Mander's coefficients plugin (Dunn et al., 2011) using as a ROI the GFAP staining of astrocytes. Neurite length for dopaminergic neurons in co-culture experiments was calculated using the Simple Neurite Tracer Fiji plugin. Number of terminals were manually counted for each neuron.

RESULTS

1. iPSC-derived astrocytes generation and characterization

Using a previously published protocol optimized in the lab (Serio et al., 2013; di Domenico et al., 2019) astrocyte cultures were established from iPSC lines derived from LRRK2-G2019S PD patients (PD-SP06, PD-SP12 and PD-SP13) and a healthy control (CTL-SP09). An isogenic iPSC line, in which the mutation had been corrected in the original PD iPSC line, was also generated (ISO PD - SP13 WT/WT) using the CRISPR/Cas9 technology (See table 2 in Materials and Methods). Briefly, iPSCs were differentiated into spherical neural masses (SNM) containing neuroectodermal progenitors. The SNMs were cultured in suspension and induced towards astrocytic fate. Next, SNMs were desegregated and plated as a monolayer for the last step of astrocyte differentiation. As a monolayer, astrocytes were passaged to reach maturation stage and the purity of the culture was near to 100% of astrocytes (see Materials and Methods). At this point, a full characterization of the culture was done to confirm their astrocytic identity.

For this purpose, immunocytochemistry detection of CD44 as marker for astrocyte progenitors was done at first place. Immunodetection of the astrocytic markers glial fibrillary acidic protein (GFAP) and calcium-binding protein beta (S100 β) confirmed that the culture was mainly composed by mature astrocytes. In addition, no staining for the oligodendrocyte marker neuron-glia antigen

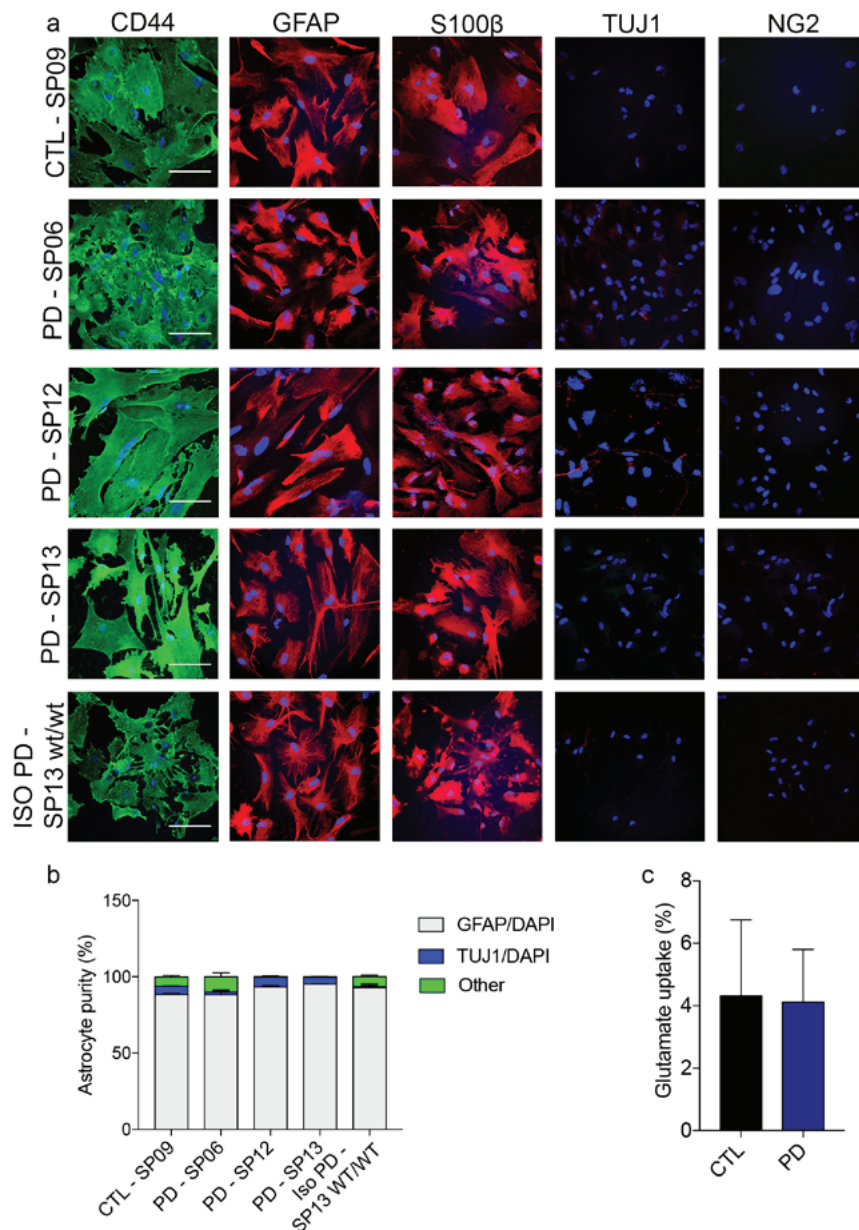


Figure 13. iPSC-derived astrocytes express astrocytic markers and are functional.
a. Representative images of astrocytes from one control line (SP09), three PD lines (SP06, SP12, SP13) and one isogenic line (SP13 wt/wt) stained positive for the astrocyte markers CD44, GFAP and S100 β , negative for oligodendrocyte marker NG2 and some cells expressing neuronal marker TUJ1. Scale bar, 100 μ m. **b.** Astrocyte cultures are composed by around 90% of astrocytes and 10% by neurons and other cell types. Data are averages \pm s.e.m. of at least three independent experiments. **c.** Glutamate uptake capacity of astrocytes. No significant differences were found in the ability of the different iPSC-derived astrocyte lines to uptake glutamate. Data are averages \pm s.e.m. of two independent experiments.

2 (NG2) was detected and only few cells were positive for the neuron marker beta-tubulin III (TUJ1) (see Fig. 13a). Quantification of these images confirmed that 90% of the cells expressed the astrocytic marker GFAP, that less than 5% expressed the neuronal marker TUJ1 and the absence of oligodendrocytes (see Fig. 13b). Along with the characterization by immunocytochemistry detection, a functional analysis, to test whether the PD and CTL iPSC derived astrocytes were able to uptake of the cytotoxic neurotransmitter glutamate (Mahmoud et al., 2019), was performed. The results showed no evident differences in glutamate uptake between CTL, ISO and PD astrocytes lines (see Fig. 13c), confirming that all iPSC derived astrocytes were similar in their ability to generate comparable and functional astrocytes.

Altogether, these data support the successful generation of pure, mature and functionally astrocyte cultures from both groups.

2. Altered mitochondrial dynamics in PD astrocytes

2.1. Aberrant mitochondrial morphology and distribution in PD astrocytes

After performing the qualitative and functional characterization of the CTL and PD astrocytes, we carried out a detailed morphological analysis of their mitochondrial component (see Fig. 14a). For this purpose, immunostaining for translocase of outer membrane (TOM20), a marker for the mitochondrial external membrane, was carried out followed by manual mitochondria counting. Interestingly, 73% of the PD astrocytes presented mainly fragmented mitochondria compared to only 18% of control astrocytes and 10% of the isogenic astrocytes (see Fig. 14b).

We also noted that mitochondria in PD astrocytes were accumulated

preferentially in the perinuclear area of the cell (see Fig. 14a). In order to quantify this observation, the following analysis was performed (see Fig. 14c). First, we set a diameter for the perinuclear area that was equal for all lines. The corrected total cell fluorescence (CTCF) for TOM20 staining was measured for both, perinuclear area and whole cytoplasm of the cell. Finally, a ratio between CTCF in the perinuclear area and the CTCF in the cytoplasm was calculated. The results confirmed our observation since the ratio in PD astrocytes was two

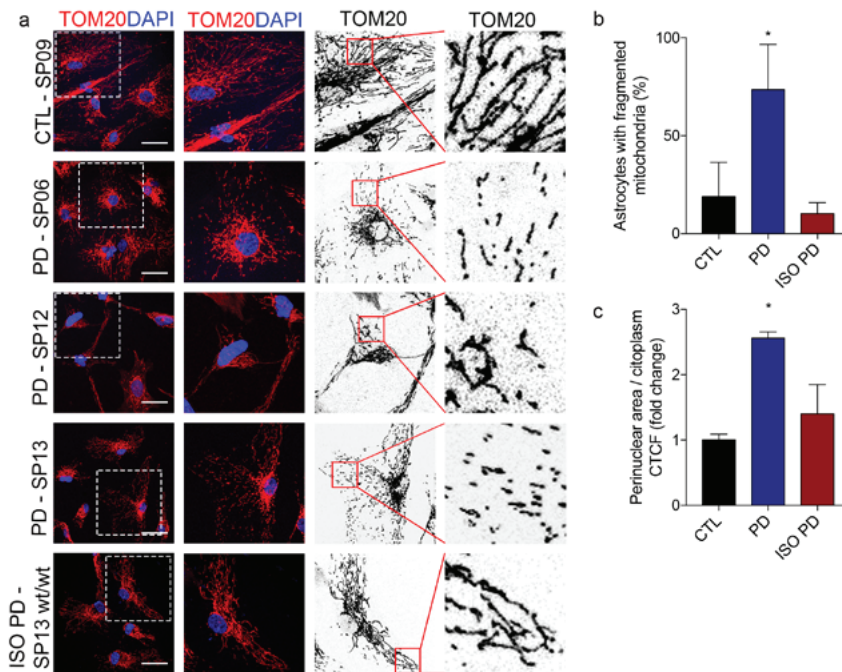


Figure 14. PD astrocytes show fragmented mitochondria and abnormal mitochondrial distribution.

a. Representative ICC images of astrocytes stained for mitochondrial marker TOM20 showing fragmented mitochondria and accumulation of mitochondria in the perinuclear area. Second and fourth columns are insets of images from their left. Scale bar, 50 μ m. **b.** 73% of PD astrocytes present majority of mitochondria that are fragmented compared to less than 20% of control and isogenic astrocytes. Data are averages \pm s.e.m. of at least three independent experiments. Unpaired t-test, asterisks denote statistically significant differences (* p <0,05). **c.** The ratio of intensity of TOM20 staining in the perinuclear area over the cytoplasm illustrates the accumulation of mitochondria in the perinuclear area preferably in PD astrocytes. Data are averages \pm s.e.m. of at least three independent experiments. Unpaired t-test, asterisks denote statistically significant differences (* p <0,05).

times higher compared to both control and isogenic astrocytes.

The fact that this aberrant distribution was not observed in the control astrocytes and more importantly in the isogenic one, indicates that this defect together with the increased mitochondrial fragmentation are directly caused by the LRRK2 mutation.

2.2. Imbalance of fission and fusion events in PD astrocytes

The increase in mitochondrial fragmentation observed in PD astrocytes compared to healthy and isogenic controls suggested that mitochondrial dynamics was altered in the diseased astrocytes. Mitochondrial dynamics refers to the fusion and fission events that undergo mitochondria and creates as a result elongated and interconnected mitochondria or fragmented mitochondria (Sebastián and Zorzano, 2018; Xie et al., 2018). To further determine whether in PD astrocytes there was an excessive fission events or an inhibition of fusion episodes, we proceeded to determine the levels of fusion and fission related proteins in both groups.

The dynamin-related protein 1 (DRP1) is a fundamental component of mitochondrial fission. Upon phosphorylation cytosolic DRP1 is activated and translocated to the outer mitochondrial membrane promoting mitochondrial fission (Smirnova et al., 2001). A western blot (WB) against the phosphorylated or active form of the protein revealed increased levels of DPR1-P in PD astrocytes compared to control and isogenic lines (see Fig. 15a-b) confirming the mitochondrial fragmentation observed in PD astrocytes by immunocytochemistry. Levels of total DRP1 showed no differences between control and PD astrocytes (see Fig. 15a and 15c).

Three GTPases regulate fusion events, being these mitofusin 1 (MFN1), mitofusin 2 (MFN2) and optic atrophy gene 1 (OPA1). MFN1 and MFN2 are located in the outer mitochondrial membrane while OPA1 is located in the

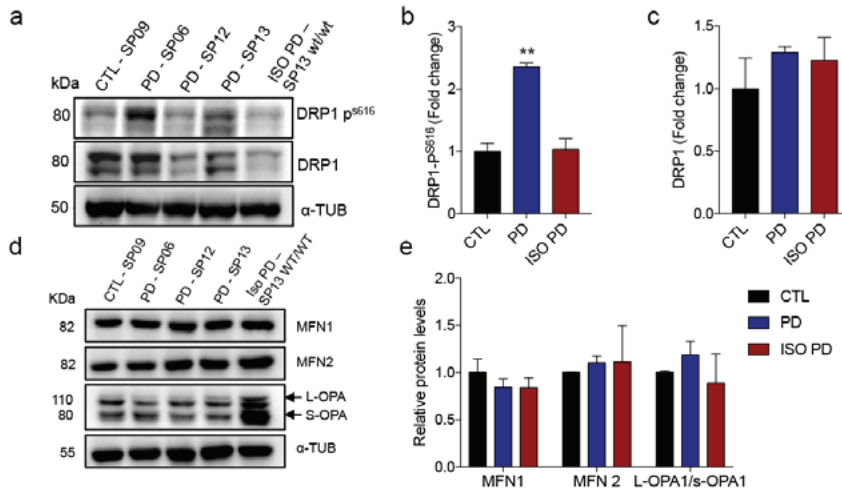


Figure 15. PD astrocytes display higher levels of fission related proteins compared to control.

a. Western blot of DRP1-P, total DRP1 and alpha-tubulin as a loading control. **b.** Quantification of DRP1-P levels in control, PD and isogenic astrocytes. Data are averages \pm s.e.m. of at least three independent experiments. Unpaired t-test, asterisks denote statistically significant differences (** $p < 0.01$). **c.** Quantification of DRP1 total levels in control, PD and isogenic astrocytes. Data are averages \pm s.e.m. of at least three independent experiments. **d** and **e.** **d.** Western Blot of mitochondrial fusion related proteins MFN1, MFN2 and OPA1 with corresponding quantification. **e.** showing no differences between control and PD astrocytes. Data are averages \pm s.e.m. of two independent experiments.

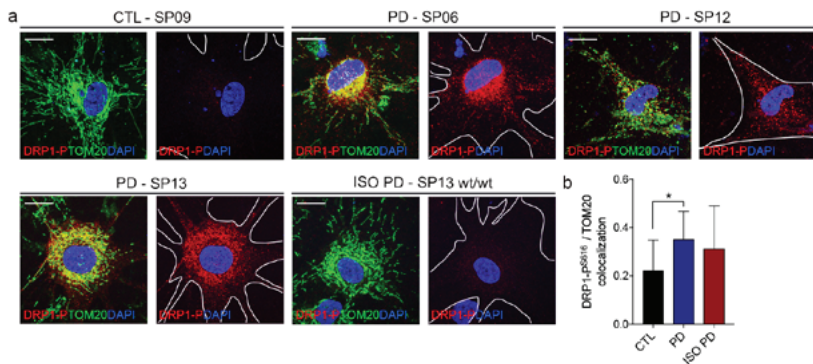


Figure 16. PD astrocytes display increased levels of DRP1-P protein.

a. Representative images of control, PD and isogenic astrocytes for mitochondrial marker TOM20 and DRP1-P protein. Scale bar, 50 μ m. **b.** DRP1-P and TOM20 colocalization Pearson's coefficient quantification. Data are averages \pm s.e.m. of at least three independent experiments. Unpaired t-test, asterisks denote statistically significant differences (* $p < 0.05$).

inner mitochondrial membrane, promoting the fusion of both outer and inner membrane sequentially (Sebastián and Zorzano, 2018; Xie et al., 2018). Results of measuring levels of fusion proteins MFN1, MFN2 and OPA1 revealed no differences between control, mutant and isogenic astrocytes (see Fig. 15d-e). These results suggested that the increase in DRP1 phosphorylation is responsible for the increase in fragmentation on the mitochondria in PD lines.

To further confirm this result, mitochondrial marker TOM20 was used together with DRP1-P marker to label the mitochondria of iPSC derived astrocytes (see Fig. 16a). After 72 h in culture, PD astrocytes showed expression of DRP1-P localized in the mitochondrial membrane. After analysing the images, the PD astrocytes shown higher colocalization of TOM20 and DRP1-P than control astrocytes (see Fig. 16b). Overall, these findings suggest that the abnormal fragmentation observed in PD astrocytes is related to an increase in mitochondrial fission events as demonstrated by the heightened activation of DRP1 protein localized specifically in mitochondria. In contrast, no differences were detected in levels of fusion-related proteins.

3. PD astrocytes display dysfunctional mitophagy

3.1. Mitochondrial protein accumulation in PD astrocytes

Morphological analysis of mitochondria by immunofluorescence in PD astrocytes showed that mitochondria were accumulated in the perinuclear area. To confirm this observation, we analyzed mitochondrial protein levels within our cells. We found that TOM20, voltage-dependent anion-selective channel 1 (VDAC1) and mitochondrial import inner membrane translocase (TIM44) proteins were increased in mutant astrocytes (see Fig. 17a) compared to control and isogenic astrocytes (see Fig. 17b).

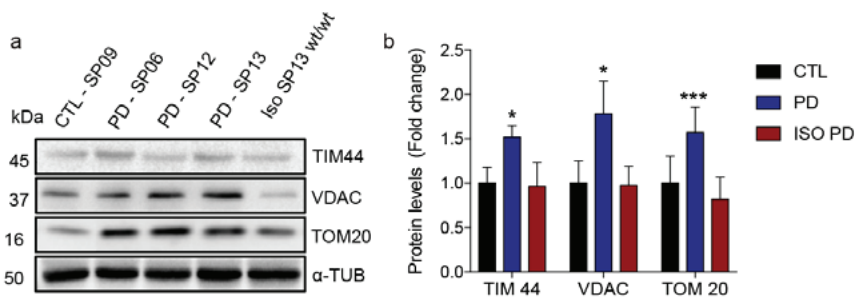


Figure 17. PD astrocytes accumulate mitochondrial proteins.

a. Western Blot of mitochondrial proteins TIM44, VDAC and TOM20 and α -tubulin as a loading control. **b.** Western blot quantification of control, PD and isogenic astrocytes. Data are averages \pm s.e.m. of at least three independent experiments. Unpaired t-test, asterisks denote statistically significant differences (* p <0,05, *** p <0,001).

3.2. Blockage of mitophagy upon CCCP activation in PD astrocytes

The aggregation of mitochondria, as we observed in our PD astrocytes, is an early phenomenon in mitophagy occurring before mitochondrial clearance. To determine whether the mitochondrial accumulation found in our PD astrocytes was due to an impaired mitophagy, cells were treated or not treated with carbonyl cyanide *m*-chlorophenyl hydrazone (CCCP), a mitochondrial uncoupler for 24 hours. After the CCCP treatment, astrocytes were collected to quantify levels of the mitochondrial protein TIM44 by WB (see Fig. 18a).

TIM44 levels were decreased in PD as well as control and isogenic astrocytes (see Fig. 18b). However, whereas levels of TIM44 in PD astrocytes decreased by 20%, in control and isogenic astrocytes it decreased up to a 50% and a 40%, respectively (see Fig. 18c). This decreased mitophagy flux suggested an impairment of the mitophagy machinery in PD astrocytes.

Mitochondrial DNA is packed by many proteins to form a nucleoid that uniformly distributes within the mitochondrial matrix. Measuring nucleoids is as well reported to be a test for the clearance capacity of the cell. Previous results measuring TIM44 protein levels were followed up by immunostaining of dsDNA to label nucleoids before and after CCCP addition (see Fig. 19a).

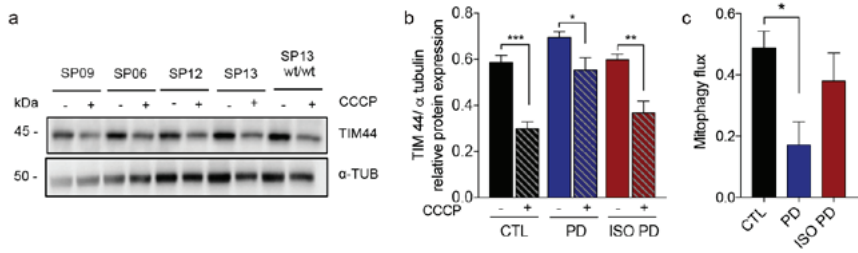


Figure 18. Blockage of mitochondrial clearance in PD astrocytes.

a. Western Blot of TIM44 protein and α-tubulin as a loading control after the addition of CCCP. **b.** Quantification of TIM44 levels in control, PD and isogenic astrocytes with or without the addition of CCCP. Data are averages ± s.e.m. of at least three independent experiments. Unpaired t-test, asterisks denote statistically significant differences (* $p < 0,05$, ** $p < 0,01$, *** $p < 0,001$). **c.** Quantification of mitophagy flux ratio in control, PD and isogenic astrocytes after the addition of CCCP. Data are averages ± s.e.m. of at least three independent experiments. Unpaired t-test, asterisks denote statistically significant differences (* $p < 0,05$).

At basal levels, the area occupied by nucleoids in PD astrocytes compared to control and isogenic astrocytes is almost half indicating that mutant astrocytes display lower mtDNA copy number at basal levels. After CCCP addition, we found that nucleoid area significantly diminished in control and isogenic astrocytes. However, no differences were found in nucleoid area in PD astrocytes before or after CCCP treatment (see Fig. 19b).

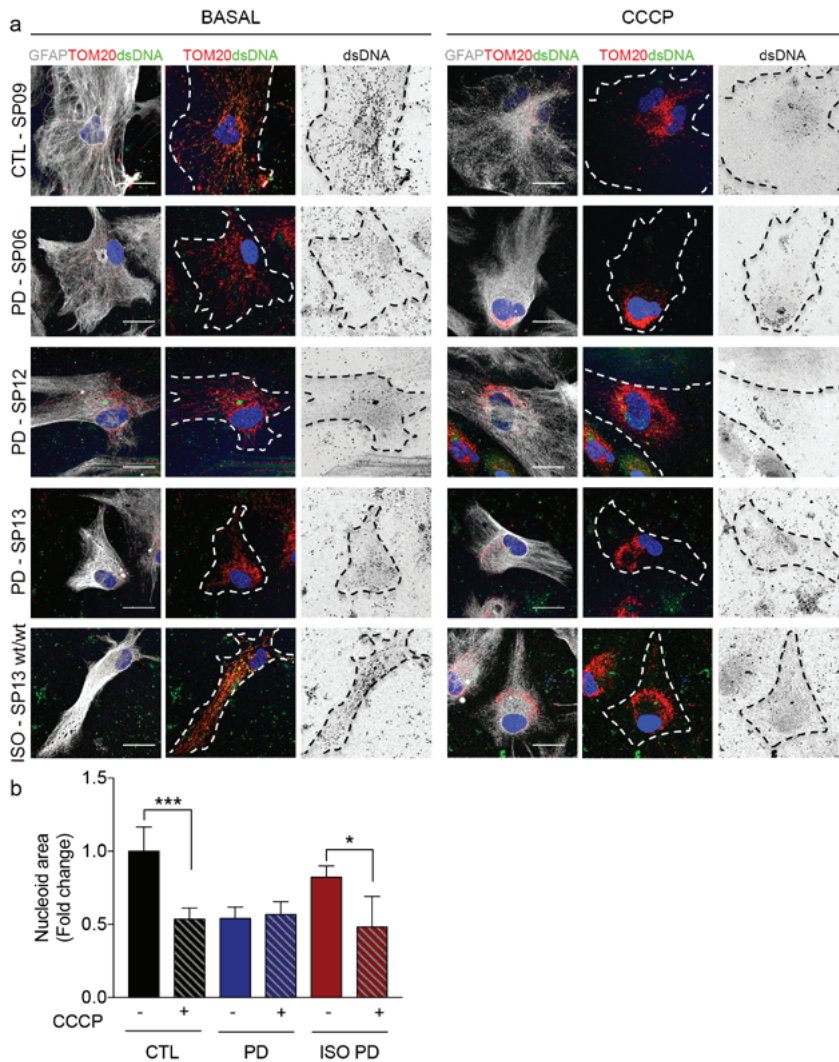


Figure 19. Nucleoid degradation is impaired in PD astrocytes.

a. Representatives ICC images of GFAP, TOM20 and dsDNA as a nucleoid marker in control, PD and isogenic astrocytes. Nuclei are stained with DAPI. Scale bar, 25 μ m **b.** Quantification of nucleoid area in control, PD and isogenic astrocytes before and after the addition of CCCP. Data are averages \pm s.e.m. of at least three independent experiments. Unpaired t-test, asterisks denote statistically significant differences (* p <0,05, *** p <0,001)

3.3. Impairment in the mitolysosomes formation in PD astrocytes

Mitophagy impairment was confirmed in live astrocytes by taking advantage of the mKeima-Red-Mito-7 (mt-keima) plasmid (Information added in Material and Methods chapter). This plasmid fuses the Keima protein with the mitochondrial protein Cox8 to be targeted to the mitochondrial matrix. The keima protein is a coral-derived fluorescent molecule that shifts its emission peak from 440 nm in neutral pH environment (pH 8,00) to 586 nm in acidic pH environment (pH 4,50). In addition, it is resistant to lysosomal degradation (Katayama et al., 2011; Sun et al., 2015; Williams et al., 2017). This allows the direct detection of mitophagy events, as mitochondria labelled with mt-Keima will turn red when undergoing degradation and therefore, transferred to a lysosome. Green signal will show the intact mitochondria (see Fig. 20a).

Control and PD astrocytes were transfected with mt-keima and imaged live in basal state or after 16 hours of incubation with CCCP. After CCCP treatment, it was clear the increase in the number of mitochondria undergoing degradation on the bases of an increase in the number of red dots, represented as a mitophagy mask (see Fig. 20b, left panels). On the contrary, PD astrocytes showed the same number of mitolysosomes before and after the cells were incubated with CCCP (see Fig. 20b). Quantification of this observation using the mito-QC counter from Fiji revealed that control astrocytes and isogenic astrocytes almost double the area occupied by mitolysosomes after adding CCCP, while no change is appreciated in PD astrocytes (see Fig. 20c-d). These results, being in line with the precedent analysis, confirmed the mitophagy impairment in PD astrocytes.

Next, we did a colocalization analysis of TOM20 and the lysosome marker

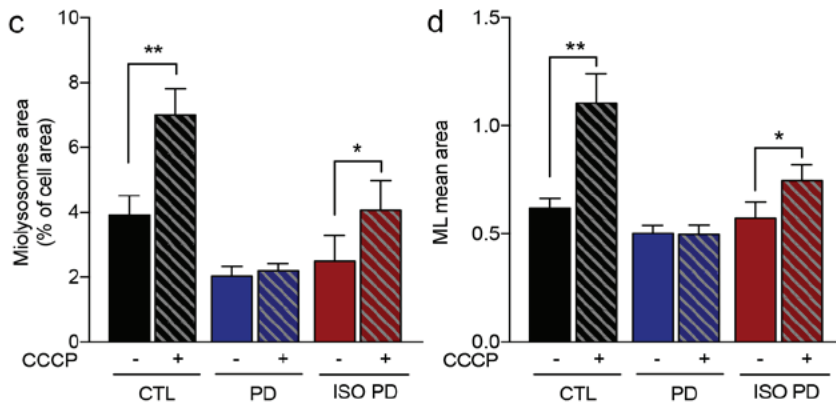
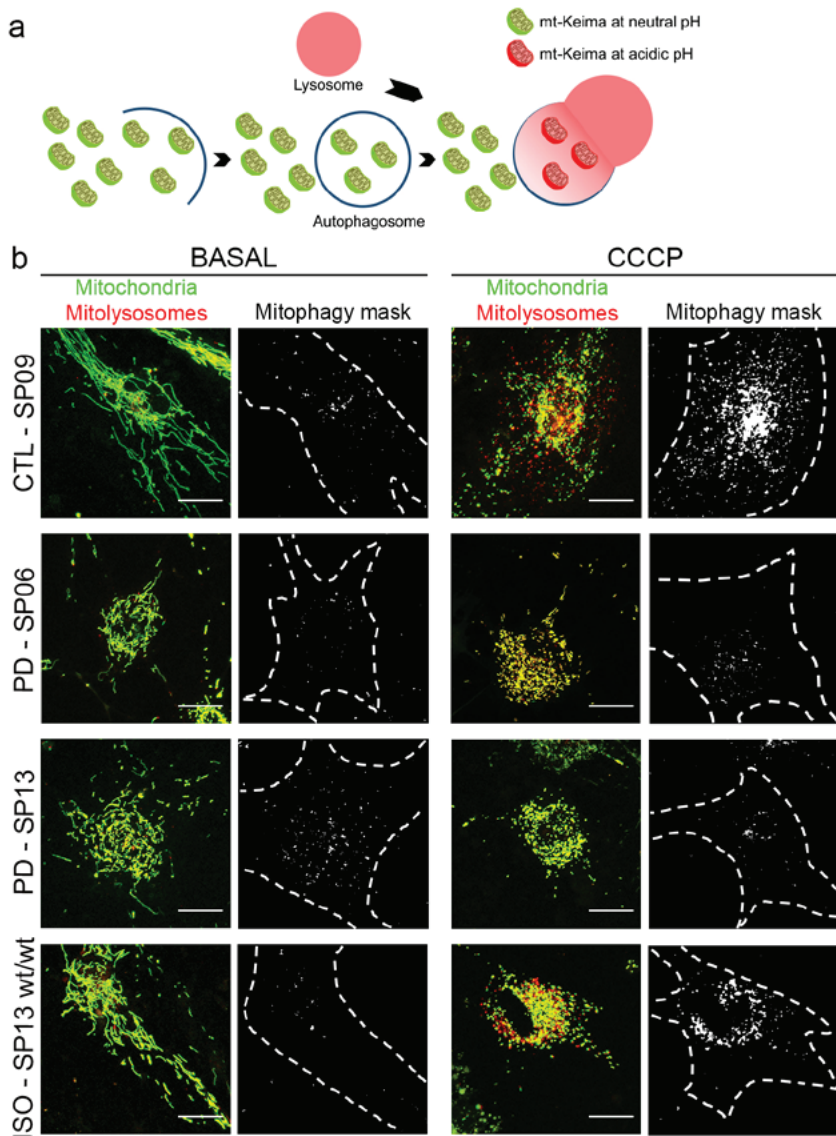


Figure 20. Direct visualization of mitophagy impairment in PD astrocytes using mt-keima plasmid.

a. Scheme of mt-Keima plasmid functionality. **b.** Representative live images of the mitophagy events measured using mt-Keima plasmid in control, PD and isogenic astrocytes in basal conditions and after the addition of CCCP. Scale bar, 25 μ m. **c and d.** Quantification of the percentage of the cell occupied by mitolysosomes (**c**) and the mitolysosomes mean area (**d**). Data are averages \pm s.e.m. of at least three independent experiments. Unpaired t-test, asterisks denote statistically significant differences (* p <0,05, ** p <0,01).

lysosomal-associated membrane protein 1 (LAMP1) by immunofluorescence (see Fig. 21a). Results were in line with the previous reported data as we found a lower colocalization between both markers in the PD astrocytes than in control and isogenic astrocytes (see Fig. 21b).

4. Biogenesis in PD astrocytes

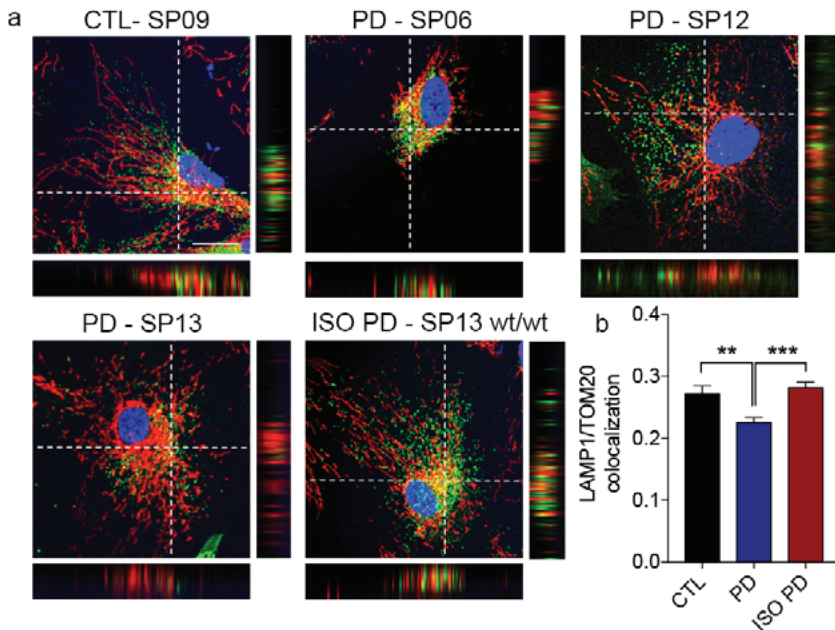


Figure 21. PD astrocytes failure to transfer mitochondria to lysosomes.

a. Representatives ICC images of the colocalization of lysosomal marker LAMP1 and mitochondrial marker TOM20 in control, PD and isogenic astrocytes. Orthogonal views of each image denote yellow dots of colocalization. Scale bar, 25 μ m. **b.** Quantification of colocalization analysis between LAMP1 and TOM20 show a higher Pearson's coefficient in control and isogenic astrocytes compared to PD. Data are averages \pm s.e.m. of at least three independent experiments. Unpaired t-test, asterisks denote statistically significant differences (** p <0,01, *** p <0,001)

Taking into consideration the fact that both mitophagy and mitochondrial biogenesis are crucial for the proper mitochondrial health, we next investigated whether our PD astrocytes present not only a blockage in mitophagy but also an alteration in mitochondrial biogenesis.

To this end, the expression of genes related to mitochondrial biogenesis, such as PPAR (peroxisome proliferator-activated receptor)- γ coactivator-1 α (PGC1 α), mitochondrial transcription factor A (TFAM) and nuclear respiratory factor 1 (NRF1) were measured). Levels of the expression of the three genes were reduced in PD astrocytes compared to isogenic, being significant in PGC1 α and TFAM (see Fig. 22).

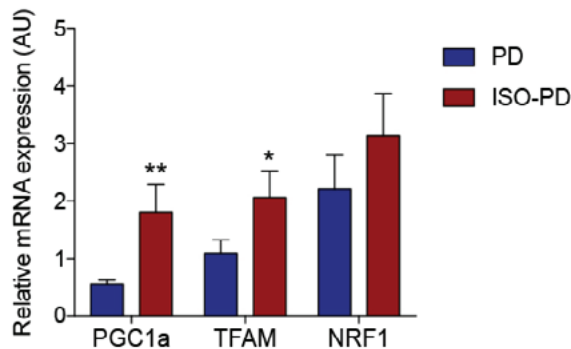


Figure 22. Decreased expression of mitochondrial biogenesis-related genes in PD astrocytes compared to isogenic astrocytes.

Profile of expression of mitochondrial biogenesis related genes PGC1 α , TFAM and NRF1. Data are averages \pm s.e.m. of at least three independent experiments. Unpaired t-test, asterisks denote statistically significant differences (* p <0,05, ** p <0,01).

5. Dysfunctional mitochondria are present in PD astrocytes

We further investigate the functionality of the mitochondria by measuring the mitochondrial DNA copy number and mitochondrial membrane potential as they are two techniques which easily reports on mitochondrial function.

After harvesting control, PD and isogenic astrocytes, a DNA extraction was performed and the mitochondrial DNA quantified normalized by total DNA. The result suggested a decreased functionality in PD astrocytes compared to control astrocytes. Surprisingly, no changes in mitochondrial DNA copy number were found between PD and isogenic lines (see Fig. 23a).

The mitochondrial activity was also evaluated by testing the mitochondrial membrane potential, as it is known to be a sign of active mitochondria, using tetramethylrhodamine, methyl ester (TMRM). TMRM is a cell-permeant dye that accumulates in mitochondria with intact membrane potential. Cells were incubated for 30 minutes with TMRM dye and the fluorescence was measured using a cell sorter at 561 nm. PD astrocytes presented significant lower TMRM intensity indicating a decreased mitochondrial activity compared to control and isogenic astrocytes (see Fig. 23b).

In order to go deeply in the understanding of mitochondrial functionality of PD astrocytes, we performed a Seahorse assay. The Seahorse assay measures the oxygen consumption rate (OCR) being it proportional to mitochondrial respiration. During the assay, different compounds are added sequentially to the medium to measure different parameters related to mitochondrial function (see Materials and Methods).

The results of the Seahorse assay unveil a dysfunction of the mitochondria from the PD astrocytes compared to the isogenic astrocytes as they presented less oxygen consumption rates (see Fig. 23c). Differences were observed both

at basal and maximal respiration plus a lower ATP production (see Fig. 23d). All together, these results indicated a mitochondrial dysfunction specifically in PD astrocytes.

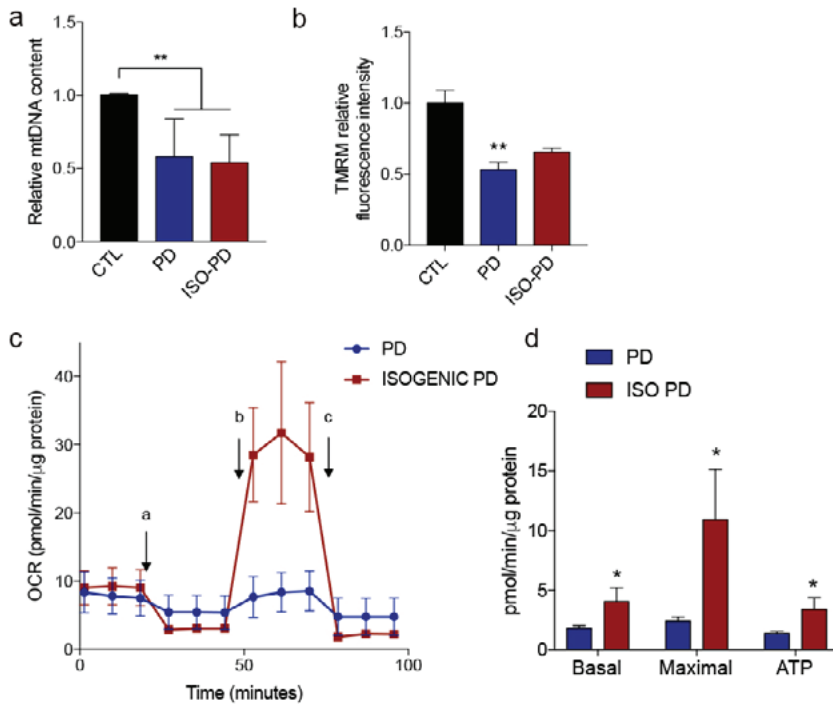


Figure 23. PD astrocytes present dysfunctional mitochondrial.

a. mtDNA copy number from control, PD and isogenic astrocytes. Results are shown as relative fold change to control cells. Data are averages \pm s.e.m. of at least three independent experiments. Unpaired t-test, asterisks denote statistically significant differences (** $p < 0,01$). **b.** Quantification of TMRM fluorescence showing a decreased mitochondrial membrane potential in PD astrocytes relative to levels of potential in control line. Data are averages \pm s.e.m. of at least three independent experiments. Unpaired t-test, asterisks denote statistically significant differences (** $p < 0,01$). **c.** Representative OCR measurement of PD and isogenic astrocytes. OCR is normalized by protein. OCR measured in basal conditions and after (a) oligomycin, (b) FCCP and (c) rotenone and antimycin addition. **d.** Quantification of basal and maximal respiration and mitochondrial ATP production of PD astrocytes compared to isogenic astrocytes. Data are averages \pm s.e.m. of two independent experiments. Unpaired t-test, asterisks denote statistically significant differences (* $p < 0,05$).

6. PD astrocytes exhibit increased sensitivity to oxidative stress

Being the mitochondria a basic actor for the maintenance of the balance between free radical generation, their detoxification and elimination, we decided to measure the reactive oxygen species (ROS) levels in the astrocytes. We used 2',7'-dichlorofluorescein diacetate (DCF-DA), a widely used probe to detect cellular ROS production. DCF-DA turns into highly fluorescent 2',7'-dichlorofluorescein (DCF) upon oxidation. After treatment with H₂O₂ mutant astrocytes presented an increased sensitivity to oxidative stress compared to control and isogenic astrocytes (see Fig. 24a).

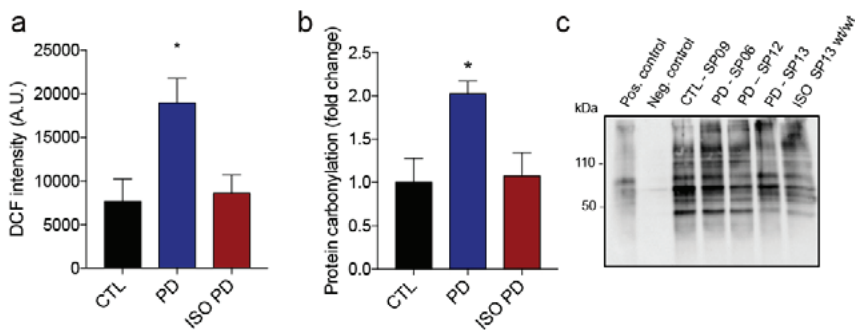


Figure 24. PD astrocytes exhibit increased oxidative stress compared to control and isogenic astrocytes.

a. Quantification of DCF fluorescence reveals the heightened ROS production in PD astrocytes compared to control and isogenic astrocytes. Data are averages \pm s.e.m. of at least three independent experiments. Unpaired t-test, asterisks denote statistically significant differences (* p <0,05, ** p <0,01). **b.** Oxyblot assay quantification of carbonylated protein levels showing altered oxidative condition of PD astrocytes in comparison to control and isogenic astrocytes. Data are averages \pm s.e.m. of at least three independent experiments. Unpaired t-test, asterisks denote statistically significant differences (* p <0,05, ** p <0,01). **c.** Representative image of an oxyblot assay blot.

To further confirm this phenotype, an Oxyblot assay was performed to detect the carbonyl groups introduced into proteins by oxidative reactions. In the Oxyblot assay, the carbonyl groups in the protein are derivatized to 2,4-dinitrophenylhydrazone (DNP-hydrazone) by reaction with 2,4-dinitrophenylhydrazine (DNPH). After that, a western blot is done in which

a primary antibody anti-DNP is used. A higher oxidation of the proteins was detected in the mutant astrocytes compared to control and isogenic astrocytes (see Fig. 24b-c). Thus, confirming the increased in oxidative stress in the PD astrocytes.

7. Urolithin A rescues mitochondrial alterations promoting mitophagy

As we have already shown, PD astrocytes present an impairment in the mitophagy machinery that leads to an accumulation of fragmented and dysfunctional mitochondria inside the cell with a consequent increase in ROS production. Moreover, mitochondrial biogenesis was found diminished and mitophagy was blocked suggesting an impaired turnover of mitochondria in PD astrocytes.

We next investigated whether enhancing mitochondrial clearance activity would ameliorate mitochondrial dysfunction in PD astrocytes. PD astrocytes were treated with 50uM Urolithin A (UA), which promotes mitophagy, for 24 hours and levels of TOM20 were analyzed by immunofluorescence. Mitochondrial fragmentation in PD astrocytes, treated with UA, diminished and recovered the typical organization and distribution observed in control and isogenic astrocytes. (see Fig. 25).

Mitochondrial clearance was also measured using mt-keima plasmid in live astrocytes treated with 50uM of UA for 24h. The mitophagy impairment was rescued since mitolysosomes area was double in size after adding UA together with CCCP in mutant astrocytes (see Fig. 26). Mitochondrial clearance was also measured using mt-keima plasmid in live astrocytes treated with 50uM of UA for 24h. The mitophagy impairment was rescued since mitolysosomes area was double in size after adding UA together with CCCP in mutant astrocytes (see Fig. 26).

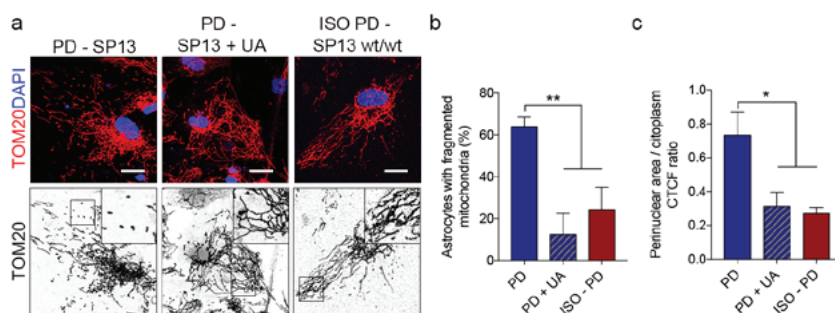


Figure 25. Urolithin A rescues mitochondrial fragmentation in PD astrocytes.
a. Representative ICC images of mitochondrial marker TOM20 in PD astrocytes in basal conditions and after treatment with Urolithin A and isogenic astrocytes as a control. Scale bar, 50 μ m. **b.** PD astrocyte cultures after treatment with Urolithin A display similar number of cells with fragmented mitochondria compared to isogenic astrocyte culture in basal conditions. Data are averages \pm s.e.m. of at least three independent experiments. Unpaired t-test, asterisks denote statistically significant differences (** $p < 0,01$). **c.** The treatment with Urolithin A corrects the perinuclear localization of mitochondria in PD astrocytes. Data are averages \pm s.e.m. of at least three independent experiments. Unpaired t-test, asterisks denote statistically significant differences (* $p < 0,05$).

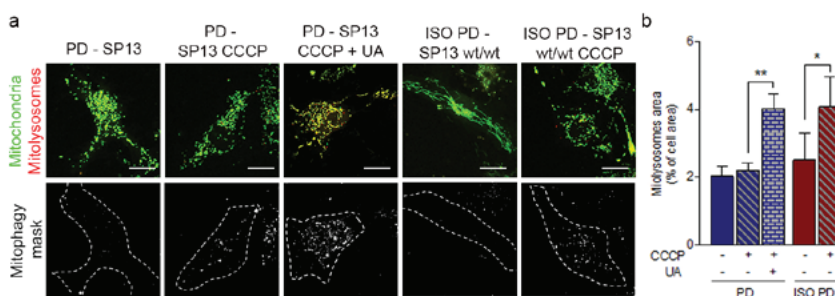


Figure 26. Urolithin A promotes mitophagy.
a. Representative live images of the mitophagy events measured using mt-Keima plasmid in PD and isogenic astrocytes in basal conditions and after the addition of CCCP and after UA treatment. Scale bar, 25 μ m. **b.** Quantification of the percentage of the cell occupied by mitolysosomes demonstrating that UA promotes mitophagy in PD astrocytes. Data are averages \pm s.e.m. of at least three independent experiments. Unpaired t-test, asterisks denote statistically significant differences (* $p < 0,05$, ** $p < 0,01$).

Next, the effect of UA treatment in mitochondrial biogenesis PD astrocytes was also tested. In UA treated PD astrocytes the expression of PGC1 α , TFAM and NFR1 was increased and normalized to levels of the isogenic astrocytes (see Fig. 27a).

Finally, we determined the levels of ROS production in PD astrocytes treated with UA. Results revealed that activation of mitophagy using UA not only

restored mitochondrial network and turnover but also recover their function, as ROS levels in treated PD astrocytes were similar to the levels of the isogenic astrocytes (see Fig. 27b).

Taken together these results indicates that promotion of mitophagy in PD astrocytes with urolithin A recover mitochondrial health and functionality.

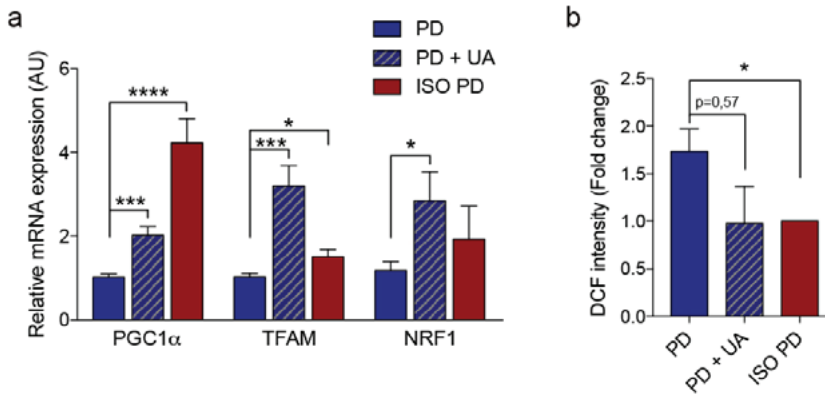


Figure 27. Urolithin A treatment promotes mitochondrial biogenesis and prevents oxidative stress.

a. Expression of genes related with mitochondrial biogenesis is increased after UA treatment in PD astrocytes. Unpaired t-test, asterisks denote statistically significant differences (* $p < 0,05$, ** $p < 0,01$, *** $p < 0,001$, **** $p < 0,0001$). **b.** Treatment with Urolithin A normalizes the levels of ROS production in PD astrocytes when compared to isogenic astrocytes. Unpaired t-test, asterisks denote statistically significant differences (* $p < 0,05$).

8. Contribution of astrocytic mitochondrial dysfunction to dopaminergic degeneration

8.1. PD astrocytes promotes neurodegeneration in control dopaminergic neurons

We have previously described the contribution of PD astrocytes to the neurodegeneration of dopaminergic neurons that was prevented by promoting the chaperone mediated autophagy in astrocytes (di Domenico et al., 2019). To determine whether the mitochondrial dysfunction in PD astrocytes can also contribute on DAn neurodegeneration, we established a co-culture system by culturing DAn derived from CTL iPSC together with PD astrocytes. Dopaminergic neurons were generated from healthy individuals using a previous published protocol (Kriks et al., 2011; Fedele et al., 2017) optimized in the lab. Once dopaminergic neurons were mature, the culture was dissociated and plated on top of a confluent layer of isogenic and PD astrocytes. After 4 weeks of co-culture, the cells were fixed and immunostained for GFAP and the dopaminergic neuron marker tyrosine hydroxylase (TH) to determine the morphology of the dopaminergic neurons (see Fig. 28a).

We found that both neurite length and number of terminals of the dopaminergic neurons were decreased in the co-culture with the PD astrocytes in comparison to the co-culture with the isogenic astrocytes (see Fig. 28b-d). These results confirmed the previous data obtained in the laboratory and shows that the mutation in LRRK2 in astrocytes drives neurodegeneration.

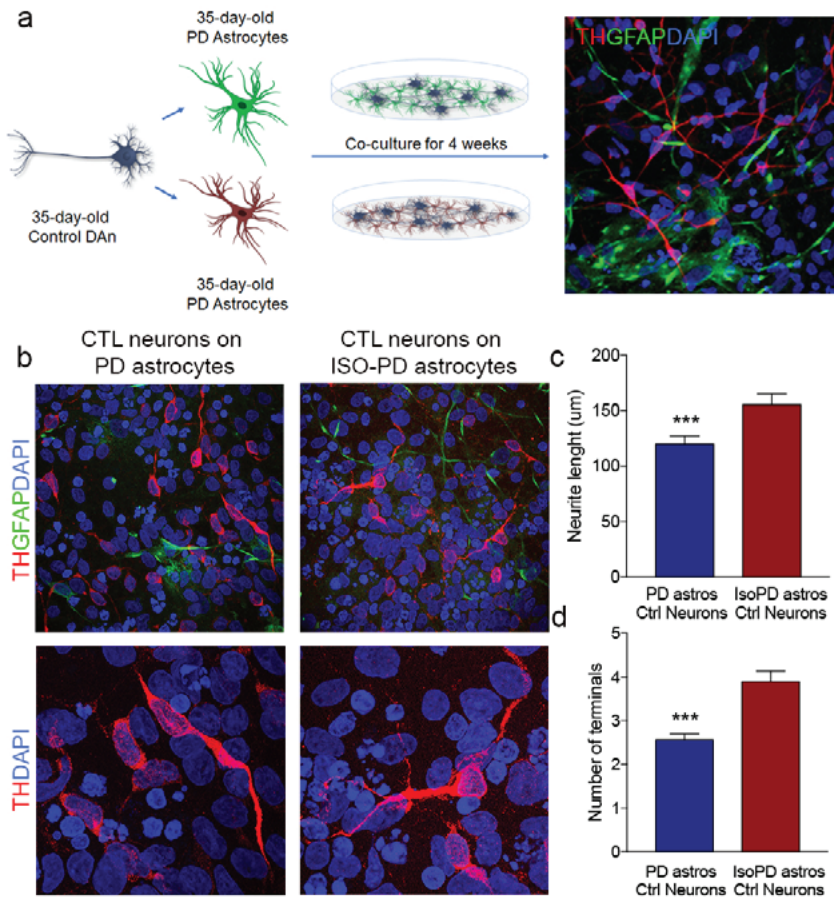


Figure 28. PD astrocytes promotes neurodegeneration when co-cultured with control DAN.

a. Diagram of co-culture system and a representative ICC image of Control DAN (TH) cultured on top of isogenic astrocytes (GFAP). **b.** Representative ICC images of control DAN (TH+) cultured on top of PD astrocytes and Isogenic astrocytes. **c and d.** Quantification of the neurite length (**c**) and number of terminals (**d**) of TH positive cells co-cultured on astrocytes showing increased number in co-culture with isogenic astrocytes.

8.2. Rescue of mitochondrial alterations in astrocytes prevents degeneration of DA neurons in co-culture

Then, to evaluate whether the treatment with Urolithin A would prevent the neurodegeneration observed in DAN when co-cultured with PD astrocytes, isogenic and PD astrocytes were co-cultured with control DAN and treated with

urolithin A for 4 weeks. After the treatment, we observed an increase in the neurite length and the number of terminals in the neurons co-cultured with PD astrocytes treated with Urolithin A (see Fig. 29). No significant changes were found in DAn cultures not co-cultured with astrocytes before and after UA treatment (see Fig. 29b-c).

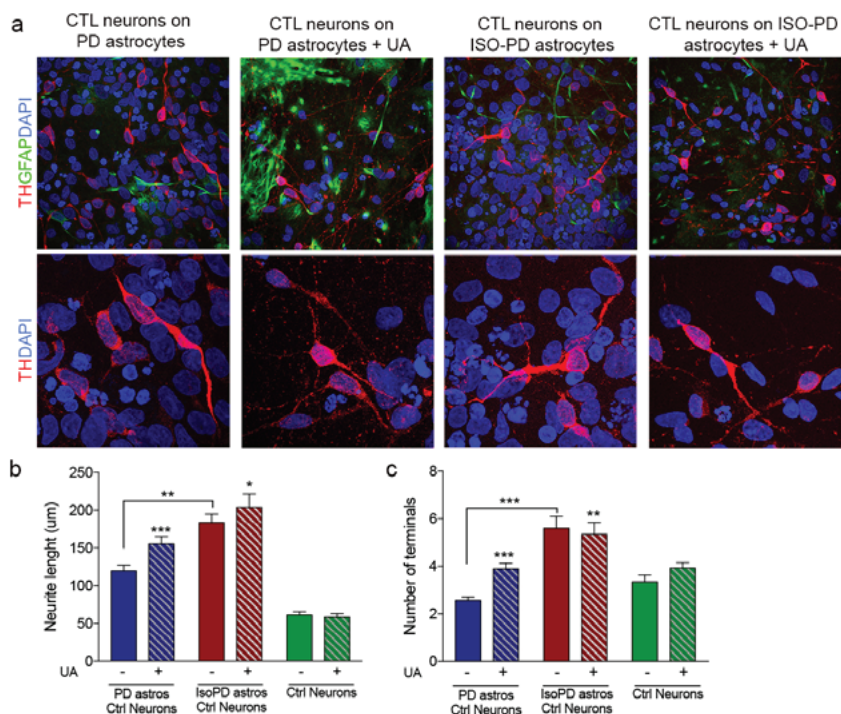


Figure 29. Mitophagy inducer Urolithin A rescues mitochondrial alterations in astrocytes preventing neurodegeneration in co-culture.

a. Representative ICC images of control DAn (TH+) cultured on top of PD astrocytes and Isogenic astrocytes in basal conditions and after the addition of Urolithin A. **b** and **c.** Quantification of the neurite length (**b**) and number of terminals (**c**) of TH positive cells co-cultured on astrocytes showing an improvement after the treatment with Urolithin A. These results suggested that the improvement of the mitochondrial alterations via promotion of mitophagy in astrocytes prevents degeneration of dopaminergic neurons.

DISCUSSION

Parkinson's disease (PD) is the second most common neurodegenerative disease. Around 80 years of age, 5% of the general population manifest symptoms of this disease. Current symptomatic therapies compensate the movement deficit efficiently over a period of 5 years, but are ineffective to alleviate the loss of autonomic, olfactory, sleep, affective and cognitive abilities. The locomotor impairment of PD patients is mainly caused by the degeneration of dopaminergic neurons projecting from the midbrain substantia nigra (SN) to the basal ganglia striatum, a pathological process which is accompanied microscopically by the formation of protein aggregates named Lewy bodies. Current therapies for PD are symptomatic and do not limit the progression of disability with time. The pathogenesis of PD is complicated and remains unclear, but growing evidence suggests the involvement of mitochondrial and lysosomal dysfunction. Mitophagy, the process of removing damaged mitochondria, is compromised in PD patients and models, and was found to be associated with accelerated neurodegeneration.

Moreover, several PD-associated genes have functions directly or indirectly related to mitochondrial pathways. Besides the importance of mitochondrial dysfunction in dopaminergic neurons, astrocytic mitochondrial dysfunction has lately gain interest in the Parkinson's disease research. As mitochondria function is link to key astrocytic functions there is the hypothesis that astrocytic mitochondrial dysfunction might have a detrimental effect on DAn survival.

The effect may come from a loss physiological functions of support or a gain of a toxic phenotype due to reactivity.

So far, there are only few studies that have analyzed in deep the mitochondrial dysfunction in human PD astrocytes and in particular astrocytes carrying the LRRK2^{G2019S} mutation. More importantly, no previous research has demonstrated that restoring the mitochondrial dysfunction in astrocytes could have a beneficial effect in dopaminergic neurons.

1. Characterization of iPSC-derived astrocytes

In this study, we have successfully generated five iPSC-derived astrocytes lines from healthy individuals and Parkinson's disease patients carrying the LRRK2^{G2019S} mutation. We found a purity of over a 90% GFAP positive cells and morphological and functional differences were not found between control and mutant lines (see Fig. 13), confirming the results from our previous study (di Domenico, 2019) and in line with the results from Sonninen et al., 2020. However, Ramos-Gonzalez and colleagues in their study claim that LRRK2^{G2019S} astrocytes are smaller and less complex compared to control astrocytes (Ramos-Gonzalez et al., 2021). The different platform used to generate the astrocytes may contribute to the contradictory results obtained in the different reports.

2. Mitochondrial dynamics in Parkinson's disease astrocytes

Several studies had linked G2019S mutation in LRRK2 to increased mitochondrial fragmentation in neurons (Niu et al., 2012; Wang et al., 2012). However, contradictory results were found in PD patient fibroblasts carrying the same mutation, both elongated and interconnected mitochondria (Mortiboys et al., 2010), and increased mitochondrial fragmentation (Su and Qi, 2013;

Grunewald et al., 2014; Smith et al., 2016) were found using this system. In our study using human astrocytes we have confirmed the results found in neural cultures. LRRK2-PD astrocytes presented heightened mitochondrial fission (see Fig.14). A number of proteins are responsible for the balance between fission and fusion events, namely DRP1 for fission events and OPA1, MFN1 and MFN1 for fusion events. Higher levels of phosphorylated DRP1, the active form of the protein, were found in LRRK2-PD astrocytes whereas no differences were found in fusion-related proteins (see Fig. 15 and Fig. 16). These results indicate that increased mitochondrial fragmentation can be explained by increased fission events. LRRK2 has been reported to directly interact with DRP1 and that the increase kinase activity of LRRK2^{G2019S} protein increases mitochondrial fragmentation via DRP1 activation (Wang et al., 2012; Ho et al., 2018).

3. Dysfunctional mitophagy as a pathogenic mechanism in Parkinson's disease

It was not until 2016 that Hsieh et al. reported an impairment in mitophagy events due to G2019S mutation in LRRK2 in iPSC-derived neurons. Before, other studies stated that the mutation increases mitophagy events in PD patient fibroblasts and non-human PD models. After that, other researchers have confirmed the results from Hsieh and described how increased kinase activity in LRRK2 impairs PINK1/Parkin dependent mitophagy (Bonello et al. 2019; Korecka 2019) and that it occurs via phosphorylation of Rab10 (Wauters et al., 2020). With our study, we show that mitophagy is impaired in LRRK2-PD astrocytes compared to healthy control astrocytes confirming the previous results. We found accumulation of mitochondrial proteins (see Fig. 17) and a blockage of mitochondrial clearance upon CCCP addition. Both Tim44 protein and mitochondrial nucleoids were quantified before and after the addition of CCCP and none or minimal differences were found in LRRK2-PD lines (see

Fig. 18 and 19). On the other hand, formation of mitolysosomes were analyzed by measuring the colocalization of TOM20 and LAMP1 markers and using the mtKeima plasmid, a method for the direct visualization of mitolysosomes formation in live cells, and results indicated that LRRK2-PD astrocytes failed to generate mitolysosomes (see Fig. 20 and 21). These results are the first demonstration that mitophagy is also impaired in astrocytes carrying the G2019S mutation in LRRK2. Several PD-related genes have been recognized to play a role in mitophagy as described above. This fact indicates that mitophagy may be relevant in PD pathology even though it has not been directly proven that plays an active role in it.

There is evidence that mitophagy and mitochondrial biogenesis are two processes closely connected and essential for the maintenance of healthy mitochondria (Palikaras et al., 2015; Sin et al., 2016; Ploumi et al., 2017). We have found that expression of key genes related to mitochondrial biogenesis was lower in LRRK2-PD astrocytes compared to control astrocytes (see Fig. 22). Since mitochondria are the major intracellular organelles that regulate both cell survival and death, clarifying the involvement of mitochondrial dysfunction and biogenesis in PD astrocytes could provide treatment strategies that might slow the progression of the disease.

4. Mitochondrial dysfunction in Parkinson's disease astrocytes

Mutant astrocytes exhibit a decrease mitochondrial membrane potential (see Fig. 23b) that is indicative of mitochondrial dysfunction and should promote the clearance of mitochondria. However, the blockage of mitophagy in the mutant astrocytes led to a defective system in which the oxygen consumption rate and ATP production were diminished (see Fig. 23). As a consequence of the accumulation of dysfunctional mitochondria, LRRK2-PD astrocytes present

higher ROS production and oxidation of proteins (see Fig. 24). Increased ROS production, higher sensitivity to oxidative stress and increased vulnerability to rotenone and valinomycin, associated to increased kinase activity in LRRK2 has been proven in many different PD models such as yeast, *C.elegans*, *Drosophila* and murine and human models like patients fibroblasts and iPSC-derived neurons from PD patients (Singh et al., 2018). Our findings confirm the preceding studies in which the G2019S mutation has already been associated to dysfunctional mitochondria in iPSC-derived LRRK2 astrocytes (Sonninen et al., 2020; Ramos-Gonzalez et al., 2021). It is well known that A9 dopaminergic neurons are especially susceptible to the heightened ROS production (Schapira et al., 1990; Parker et al., 2008). In fact, most mice PD models are based on the addition of neurotoxins which promote oxidative stress and subsequently dopaminergic neural loss (Tieu, 2011). Astrocytes increased ROS production may also contribute to dopaminergic cell loss as it has been proven how induced expression of antioxidant genes in astrocytes prevent neurotoxic effect of MPTP and 6-hydroxydopamine (Liddell et al., 2017).

5. Mitophagy as a potential therapeutic target for Parkinson's disease

Upon a more in-depth investigation on mitochondria clearance, we found that the mitophagy was blocked in LRRK2-PD astrocytes which contribute to the increase in oxidative stress and changes in metabolism. Taking into consideration that this important mechanism which involves selective sequestration and subsequent degradation of the dysfunctional mitochondrion seems to occur early during the development of the disease, we attempted to restore mitochondrial degradation by using a mitophagy inducer.

In recent years, Urolithin A has appeared as a novel and potent mitophagy inducer (Ryu et al., 2016). Urolithin A (UA) is a gut microbiota metabolite

from polyphenols that can cross the blood brain barrier. It promotes mitophagy subsequently to a reduction in the membrane potential, but it is not an uncoupler thus, not affecting respiration (Ryu et al., 2016). In a more recent study Andreux and colleagues demonstrated that Urolithin A promotes the expression of mitophagy- and biogenesis- related genes, leading to an overall improvement of cellular and mitochondrial health in humans (Andreux et al., 2019). These studies were focused on the muscle function however, the very interesting study in Alzheimer's disease from Fang et al. focuses on restoration of mitophagy in iPSC-derived human AD neurons and animal AD models (Fang et al., 2019). They demonstrated that the treatment with UA promotes mitophagy in SH-SY5Y neuroblastoma cells carrying Tau mutations and in both AD models, *C. elegans* and mouse. Consequently, cognitive decline link to AD was recovered in both systems. On the other hand, in iPSC-derived AD neurons OCR improved after the UA treatment.

Given these characteristics, it is a candidate to rescue the mitochondrial alterations in LRRK2-PD astrocytes that appear subsequently to the mitophagy blockage.

Our experiments confirmed the previous results as we found that after Urolithin A addition, LRRK2-PD astrocytes presented overall healthier mitochondria. Upon activation of mitophagy (see Fig. 26), mitochondrial fragmentation was restored (see Fig. 25) and ROS production normalized (see Fig. 27a). Moreover, the expression of the biogenesis-related genes PGC1 α , TFAM and NRF1, increased (see Fig. 27b). These results indicate that Urolithin A rescues the mitophagy impairment caused by the LRRK2^{G2019S} mutation in iPSC-derived astrocytes and improves mitochondrial functionality.

6. Restoration of mitostasis in PD astrocytes during co-culture of control neurons with PD astrocytes

Despite the considerable potential of Urolithin A in the treatment of Parkinson's disease pathology, few studies have focused on the effects of this polyphenol metabolite on prevention of DAN loss. Kujawska et al. demonstrated the neuroprotective effects of pomegranate (rich in polyphenols) juice, and specifically of Urolithin A, on a mouse PD model based on the administration of rotenone (Kujawska et al., 2020).

We have previously demonstrated that LRRK2-PD astrocytes co-cultured with dopaminergic neurons contribute to the neurodegeneration (di Domenico et al., 2019). Now we established a similar co-culture system and found that astrocytic mitochondrial dysfunction may also contribute to dopaminergic neuronal degeneration. Indeed, we found that in non-treated conditions control neurons show signs of neurodegeneration. Thus, we treated LRRK2-PD astrocytes with Urolithin A in co-culture with healthy neurons. Interestingly, we found that the treatment restored TH number, and decreased the number of TH positive cells with a degenerative morphology (see Fig. 29). Our findings reveal for the first time the beneficial effect of Urolithin A on the prevention of DAN degeneration in a human PD model. More importantly, we have demonstrated that astrocytes may be important actors in mediating beneficial effects impacting on the survival of DAN.

CONCLUSIONS

This study has revealed that LRRK2 mutant astrocytes present altered mitochondrial dynamics, altered mitophagy, increased oxidative stress, metabolic defects, that are most likely contributing to PD progression.

Specifically:

- Patient-specific astrocytes, three from LRRK2-PD iPSC, one from healthy individual and one from an isogenic corrected LRRK2-PD-iPSC, were successfully generated and fully characterized. In addition, human iPSC-derived dopaminergic neurons from a healthy individual, were also generated in order to devise a co-culture system and study the interaction between LRRK2^{G2019S}-bearing astrocytes and control neurons.
- iPSC-derived astrocytes of LRRK2-PD patients (LRRK2^{G2019S} PD) exhibited extensive perinuclear accumulation of fragmented mitochondria and a significant increase in DRP1 phosphorylation compared to control astrocytes.
- Fragmented mitochondria accumulated in LRRK2^{G2019S} PD astrocytes due to a defective mitophagy leading to an increase in oxidative stress.
- Oxygen consumption rate, ATP production and mitochondrial membrane potential were significantly decreased in LRRK2^{G2019S} PD astrocytes indicating altered mitochondrial function in PD astrocytes.

- LRRK2^{G2019S} PD astrocytes exhibited lower expression levels of mitochondrial biogenesis-related genes compared to control astrocytes.
- Correction of G2019S mutation in the LRRK2 gene by CRISPR-Cas9 gene editing normalized mitochondria morphology, clearance and function (reverting mitochondrial fragmentation, respiration impairment, ATP deficits, and increased oxidative stress) to those of control astrocytes.
- A mitophagy activator drug, Urolithin A, was able to rescue mitochondrial fragmentation and accumulation in LRRK2^{G2019S} PD astrocytes by inducing mitophagy, promoting expression of mitochondrial biogenesis-related genes and reducing ROS production in those astrocytes.
- In a co-culture system established between LRRK2^{G2019S} PD astrocytes and healthy DA neurons, the treatment with Urolithin A, prevented neuronal cell death, suggesting a potential astrocyte-targeted therapeutic.

In conclusion, this study provides the advantage for using iPSC-based modeling for assessing the consequences of mitochondrial dysfunctions in astrocytes and dissecting the initial mechanisms that lead to neuronal cell loss in PD. This modeling has uncovered mitophagy dysfunction as a relevant altered mechanism in PD astrocytes whose activation might represent an interesting therapeutic option for counteracting PD-related neurodegeneration.

REFERENCES

- Allen NJ. Astrocyte regulation of synaptic behavior. *Annu Rev Cell Dev Biol.* 2014;30:439-63. doi: 10.1146/annurev-cellbio-100913-013053. PMID: 25288116.
- Andreux PA, Blanco-Bose W, Ryu D, Burdet F, Ibberson M, Aebischer P, Auwerx J, Singh A, Rinsch C. The mitophagy activator urolithin A is safe and induces a molecular signature of improved mitochondrial and cellular health in humans. *Nat Metab.* 2019 Jun;1(6):595-603. doi: 10.1038/s42255-019-0073-4. Epub 2019 Jun 14. PMID: 32694802.
- Andriezen WL. The Neuroglia Elements in the Human Brain. *Br Med J.* 1893 Jul 29;2(1700):227-30. doi: 10.1136/bmj.2.1700.227. PMID: 20754383; PMCID: PMC2422013.
- Araki M, Ito G, Tomita T. Physiological and pathological functions of LRRK2: implications from substrate proteins. *Neuronal Signal.* 2018 Oct 10;2(4):NS20180005. doi: 10.1042/NS20180005. PMID: 32714591; PMCID: PMC7373236.
- Ascherio A, Schwarzschild MA. The epidemiology of Parkinson's disease: risk factors and prevention. *Lancet Neurol.* 2016 Nov;15(12):1257-1272. doi: 10.1016/S1474-4422(16)30230-7. Epub 2016 Oct 11. PMID: 27751556.
- Bantle CM, Hirst WD, Weihofen A, Shlevkov E. Mitochondrial Dysfunction in Astrocytes: A Role in Parkinson's Disease? *Front Cell Dev Biol.* 2021 Jan 7;8:608026. doi: 10.3389/fcell.2020.608026. PMID: 33537300; PMCID: PMC7849831.
- Barodia SK, McMeekin LJ, Creed RB, Quinones EK, Cowell RM, Goldberg MS. PINK1 phosphorylates ubiquitin predominantly in astrocytes. *NPJ Parkinsons Dis.* 2019 Dec 11;5:29. doi: 10.1038/s41531-019-0101-9. PMID: 31840043; PMCID: PMC6906478.
- Barres BA. The mystery and magic of glia: a perspective on their roles in health and disease. *Neuron.* 2008 Nov 6;60(3):430-40. doi: 10.1016/j.neuron.2008.10.013. PMID: 18995817.
- Billingsley KJ, Bandres-Ciga S, Saez-Atienzar S, Singleton AB. Genetic risk factors in Parkinson's disease. *Cell Tissue Res.* 2018 Jul;373(1):9-20. doi: 10.1007/s00441-018-2817-y. Epub 2018 Mar 13. PMID: 29536161; PMCID: PMC6201690.
- Biskup S, Moore DJ, Celsi F, Higashi S, West AB, Andrabi SA, Kurkinen K, Yu SW, Savitt JM, Waldvogel HJ, Faull RL, Emson PC, Torp R, Ottersen OP, Dawson TM, Dawson VL. Localization of LRRK2 to membranous and vesicular structures in mammalian brain. *Ann Neurol.* 2006 Nov;60(5):557-69. doi: 10.1002/ana.21019. PMID: 17120249.
- Blauwendraat C, Nalls MA, Singleton AB. The genetic architecture of Parkinson's disease.

Lancet Neurol. 2020 Feb;19(2):170-178. doi: 10.1016/S1474-4422(19)30287-X. Epub 2019 Sep 11. PMID: 31521533.

Bonello F, Hassoun SM, Mouton-Liger F, Shin YS, Muscat A, Tesson C, Lesage S, Beart PM, Brice A, Krupp J, Corvol JC, Corti O. LRRK2 impairs PINK1/Parkin-dependent mitophagy via its kinase activity: pathologic insights into Parkinson's disease. *Hum Mol Genet.* 2019 May 15;28(10):1645-1660. doi: 10.1093/hmg/ddz004. PMID: 30629163.

Bonifati V, Rizzu P, van Baren MJ, Schaap O, Breedveld GJ, Krieger E, Dekker MC, Squitieri F, Ibanez P, Joosse M, van Dongen JW, Vanacore N, van Swieten JC, Brice A, Meo G, van Duijn CM, Oostra BA, Heutink P. Mutations in the DJ-1 gene associated with autosomal recessive early-onset parkinsonism. *Science.* 2003 Jan 10;299(5604):256-9. doi: 10.1126/science.1077209. Epub 2002 Nov 21. PMID: 12446870.

Booth HDE, Hirst WD, Wade-Martins R. The Role of Astrocyte Dysfunction in Parkinson's Disease Pathogenesis. *Trends Neurosci.* 2017 Jun;40(6):358-370. doi: 10.1016/j.tins.2017.04.001. Epub 2017 May 17. PMID: 28527591; PMCID: PMC5462417.

Bosco DA, Fowler DM, Zhang Q, Nieva J, Powers ET, Wentworth P Jr, Lerner RA, Kelly JW. Elevated levels of oxidized cholesterol metabolites in Lewy body disease brains accelerate alpha-synuclein fibrilization. *Nat Chem Biol.* 2006 May;2(5):249-53. doi: 10.1038/nchembio782. Epub 2006 Mar 26. Erratum in: *Nat Chem Biol.* 2006 Jun;2(6):346. PMID: 16565714.

Bose A, Beal MF. Mitochondrial dysfunction in Parkinson's disease. *J Neurochem.* 2016 Oct;139 Suppl 1:216-231. doi: 10.1111/jnc.13731. Epub 2016 Aug 21. PMID: 27546335.

Bouzier-Sore AK, Pellerin L. Unraveling the complex metabolic nature of astrocytes. *Front Cell Neurosci.* 2013 Oct 11;7:179. doi: 10.3389/fncel.2013.00179. PMID: 24130515; PMCID: PMC3795301.

Braak H, Ghebremedhin E, Rüb U, Bratzke H, Del Tredici K. Stages in the development of Parkinson's disease-related pathology. *Cell Tissue Res.* 2004 Oct;318(1):121-34. doi: 10.1007/s00441-004-0956-9. Epub 2004 Aug 24. PMID: 15338272.

Braak H, Sastre M, Del Tredici K. Development of alpha-synuclein immunoreactive astrocytes in the forebrain parallels stages of intraneuronal pathology in sporadic Parkinson's disease. *Acta Neuropathol.* 2007 Sep;114(3):231-41. doi: 10.1007/s00401-007-0244-3. Epub 2007 Jun 19. PMID: 17576580.

Cai Q, Jeong YY. Mitophagy in Alzheimer's Disease and Other Age-Related Neurodegenerative Diseases. *Cells.* 2020 Jan 8;9(1):150. doi: 10.3390/cells9010150. PMID: 31936292; PMCID: PMC7017092.

Cerri S, Mus L, Blandini F. Parkinson's Disease in Women and Men: What's the Difference?

- J Parkinsons Dis.* 2019;9(3):501-515. doi: 10.3233/JPD-191683. PMID: 31282427; PMCID: PMC6700650.
- Cheng XY, Biswas S, Li J, Mao CJ, Chechneva O, Chen J, Li K, Li J, Zhang JR, Liu CF, Deng WB. Human iPSCs derived astrocytes rescue rotenone-induced mitochondrial dysfunction and dopaminergic neurodegeneration in vitro by donating functional mitochondria. *Transl Neurodegener.* 2020 Apr 24;9(1):13. doi: 10.1186/s40035-020-00190-6. PMID: 32345341; PMCID: PMC7325238.
- Chia SJ, Tan EK, Chao YX. Historical Perspective: Models of Parkinson's Disease. *Int J Mol Sci.* 2020 Apr 2;21(7):2464. doi: 10.3390/ijms21072464. PMID: 32252301; PMCID: PMC7177377.
- Clarke LE, Liddelow SA, Chakraborty C, Münch AE, Heiman M, Barres BA. Normal aging induces A1-like astrocyte reactivity. *Proc Natl Acad Sci U S A.* 2018 Feb 20;115(8):E1896-E1905. doi: 10.1073/pnas.1800165115. Epub 2018 Feb 7. PMID: 29437957; PMCID: PMC5828643.
- Connolly BS, Lang AE. Pharmacological treatment of Parkinson disease: a review. *JAMA.* 2014 Apr 23-30;311(16):1670-83. doi: 10.1001/jama.2014.3654. PMID: 24756517.
- Corti O, Lesage S, Brice A. What genetics tells us about the causes and mechanisms of Parkinson's disease. *Physiol Rev.* 2011 Oct;91(4):1161-218. doi: 10.1152/physrev.00022.2010. PMID: 22013209.
- Damier P, Hirsch EC, Agid Y, Graybiel AM. The substantia nigra of the human brain. II. Patterns of loss of dopamine-containing neurons in Parkinson's disease. *Brain.* 1999 Aug;122 (Pt 8):1437-48. doi: 10.1093/brain/122.8.1437. PMID: 10430830.
- Davis CH, Kim KY, Bushong EA, Mills EA, Boassa D, Shih T, Kinebuchi M, Phan S, Zhou Y, Bihlmeyer NA, Nguyen JV, Jin Y, Ellisman MH, Marsh-Armstrong N. Transcellular degradation of axonal mitochondria. *Proc Natl Acad Sci U S A.* 2014 Jul 1;111(26):9633-8. doi: 10.1073/pnas.1404651111. Epub 2014 Jun 16. PMID: 24979790; PMCID: PMC4084443.
- Dawson TM, Ko HS, Dawson VL. Genetic animal models of Parkinson's disease. *Neuron.* 2010 Jun 10;66(5):646-61. doi: 10.1016/j.neuron.2010.04.034. PMID: 20547124; PMCID: PMC2917798.
- Delamarre A, Meissner WG. Epidemiology, environmental risk factors and genetics of Parkinson's disease. *Presse Med.* 2017 Mar;46(2 Pt 1):175-181. doi: 10.1016/j.lpm.2017.01.001. Epub 2017 Feb 8. PMID: 28189372.
- Dickson DW, Braak H, Duda JE, Duyckaerts C, Gasser T, Halliday GM, Hardy J, Leverenz JB, Del Tredici K, Wszolek ZK, Litvan I. Neuropathological assessment of Parkinson's

disease: refining the diagnostic criteria. *Lancet Neurol.* 2009 Dec;8(12):1150-7. doi: 10.1016/S1474-4422(09)70238-8. Erratum in: *Lancet Neurol.* 2010 Feb;9(2):140. Erratum in: *Lancet Neurol.* 2010 Jan;9(1):29. PMID: 19909913.

Dickson DW. Neuropathology of Parkinson disease. *Parkinsonism Relat Disord.* 2018 Jan;46 Suppl 1(Suppl 1):S30-S33. doi: 10.1016/j.parkreldis.2017.07.033. Epub 2017 Aug 1. PMID: 28780180; PMCID: PMC5718208.

di Domenico A, Carola G, Calatayud C, Pons-Espinal M, Muñoz JP, Richaud-Patin Y, Fernandez-Carasa I, Gut M, Faella A, Parameswaran J, Soriano J, Ferrer I, Tolosa E, Zorzano A, Cuervo AM, Raya A, Consiglio A. Patient-Specific iPSC-Derived Astrocytes Contribute to Non-Cell-Autonomous Neurodegeneration in Parkinson's Disease. *Stem Cell Reports.* 2019 Feb 12;12(2):213-229. doi: 10.1016/j.stemcr.2018.12.011. Epub 2019 Jan 10. PMID: 30639209; PMCID: PMC6372974.

Dijkstra AA, Voorn P, Berendse HW, Groenewegen HJ; Netherlands Brain Bank, Rozemuller AJ, van de Berg WD. Stage-dependent nigral neuronal loss in incidental Lewy body and Parkinson's disease. *Mov Disord.* 2014 Sep;29(10):1244-51. doi: 10.1002/mds.25952. Epub 2014 Jul 3. PMID: 24996051.

Dunn KW, Kamocka MM, McDonald JH. A practical guide to evaluating colocalization in biological microscopy. *Am J Physiol Cell Physiol.* 2011 Apr;300(4):C723-42. doi: 10.1152/ajpcell.00462.2010. Epub 2011 Jan 5. PMID: 21209361; PMCID: PMC3074624.

Escartin C, Galea E, Lakatos A, O'Callaghan JP, Petzold GC, Serrano-Pozo A, Steinhäuser C, Volterra A, Carmignoto G, Agarwal A, Allen NJ, Araque A, Barbeito L, Barzilai A, Bergles DE, Bonvento G, Butt AM, Chen WT, Cohen-Salmon M, Cunningham C, Deneen B, De Strooper B, Díaz-Castro B, Farina C, Freeman M, Gallo V, Goldman JE, Goldman SA, Götz M, Gutiérrez A, Haydon PG, Heiland DH, Hol EM, Holt MG, Iino M, Kastanenka KV, Kettenmann H, Khakh BS, Koizumi S, Lee CJ, Liddelow SA, MacVicar BA, Magistretti P, Messing A, Mishra A, Molofsky AV, Murai KK, Norris CM, Okada S, Oliet SHR, Oliveira JF, Panatier A, Parpura V, Pekna M, Pekny M, Pellerin L, Perea G, Pérez-Nievas BG, Pfrieder FW, Poskanzer KE, Quintana FJ, Ransohoff RM, Riquelme-Perez M, Robel S, Rose CR, Rothstein JD, Rouach N, Rowitch DH, Semyanov A, Sirko S, Sontheimer H, Swanson RA, Vitorica J, Wanner IB, Wood LB, Wu J, Zheng B, Zimmer ER, Zorec R, Sofroniew MV, Verkhratsky A. Reactive astrocyte nomenclature, definitions, and future directions. *Nat Neurosci.* 2021 Mar;24(3):312-325. doi: 10.1038/s41593-020-00783-4. Epub 2021 Feb 15. PMID: 33589835; PMCID: PMC8007081.

Fang EF, Hou Y, Palikaras K, Adriaanse BA, Kerr JS, Yang B, Lautrup S, Hasan-Olive MM, Caponio D, Dan X, Rocktäschel P, Croteau DL, Akbari M, Greig NH, Fladby T, Nilsen H, Cader MZ, Mattson MP, Tavernarakis N, Bohr VA. Mitophagy inhibits amyloid- β and tau pathology and reverses cognitive deficits in models of Alzheimer's disease. *Nat Neurosci.* 2019 Mar;22(3):401-412. doi: 10.1038/s41593-018-0332-9. Epub 2019 Feb

11. PMID: 30742114; PMCID: PMC6693625.

- Fedele S, Collo G, Behr K, Bischofberger J, Müller S, Kunath T, Christensen K, Gündner AL, Graf M, Jagasia R, Taylor V. Expansion of human midbrain floor plate progenitors from induced pluripotent stem cells increases dopaminergic neuron differentiation potential. *Sci Rep*. 2017 Jul 20;7(1):6036. doi: 10.1038/s41598-017-05633-1. PMID: 28729666; PMCID: PMC5519680.
- Fellner L, Irschick R, Schanda K, Reindl M, Klimaschewski L, Poewe W, Wenning GK, Stefanova N. Toll-like receptor 4 is required for α -synuclein dependent activation of microglia and astroglia. *Glia*. 2013 Mar;61(3):349-60. doi: 10.1002/glia.22437. Epub 2012 Oct 25. PMID: 23108585; PMCID: PMC3568908.
- Fernandez-Fernandez S, Almeida A, Bolaños JP. Antioxidant and bioenergetic coupling between neurons and astrocytes. *Biochem J*. 2012 Apr 1;443(1):3-11. doi: 10.1042/BJ20111943. PMID: 22417747.
- Ferree A, Shirihai O. Mitochondrial dynamics: the intersection of form and function. *Adv Exp Med Biol*. 2012;748:13-40. doi: 10.1007/978-1-4614-3573-0_2. PMID: 22729853; PMCID: PMC5967395.
- Ferreira M, Massano J. An updated review of Parkinson's disease genetics and clinicopathological correlations. *Acta Neurol Scand*. 2017 Mar;135(3):273-284. doi: 10.1111/ane.12616. Epub 2016 Jun 8. PMID: 27273099.
- Fox SH, Katzenschlager R, Lim SY, Ravina B, Seppi K, Coelho M, Poewe W, Rascol O, Goetz CG, Sampaio C. The Movement Disorder Society Evidence-Based Medicine Review Update: Treatments for the motor symptoms of Parkinson's disease. *Mov Disord*. 2011 Oct;26 Suppl 3:S2-41. doi: 10.1002/mds.23829. PMID: 22021173.
- Francardo V. Modeling Parkinson's disease and treatment complications in rodents: Potentials and pitfalls of the current options. *Behav Brain Res*. 2018 Oct 15;352:142-150. doi: 10.1016/j.bbr.2017.12.014. Epub 2017 Dec 10. PMID: 29237549.
- Franco-Iborra S, Vila M, Perier C. The Parkinson Disease Mitochondrial Hypothesis: Where Are We at? *Neuroscientist*. 2016 Jun;22(3):266-77. doi: 10.1177/1073858415574600. Epub 2015 Mar 11. PMID: 25761946.
- Giasson BI, Covy JP, Bonini NM, Hurtig HI, Farrer MJ, Trojanowski JQ, Van Deerlin VM. Biochemical and pathological characterization of Lrrk2. *Ann Neurol*. 2006 Feb;59(2):315-22. doi: 10.1002/ana.20791. PMID: 16437584.
- Goedert M, Spillantini MG, Del Tredici K, Braak H. 100 years of Lewy pathology. *Nat Rev Neurol*. 2013 Jan;9(1):13-24. doi: 10.1038/nrneurol.2012.242. Epub 2012 Nov 27. PMID: 23183883.

- Grünewald A, Arns B, Meier B, Brockmann K, Tadic V, Klein C. Does uncoupling protein 2 expression qualify as marker of disease status in LRRK2-associated Parkinson's disease? *Antioxid Redox Signal*. 2014 May 1;20(13):1955-60. doi: 10.1089/ars.2013.5737. Epub 2014 Mar 7. PMID: 24251413; PMCID: PMC3993019.
- Grünewald A, Kumar KR, Sue CM. New insights into the complex role of mitochondria in Parkinson's disease. *Prog Neurobiol*. 2019 Jun;177:73-93. doi: 10.1016/j.pneurobio.2018.09.003. Epub 2018 Sep 13. PMID: 30219247.
- Gu XL, Long CX, Sun L, Xie C, Lin X, Cai H. Astrocytic expression of Parkinson's disease-related A53T alpha-synuclein causes neurodegeneration in mice. *Mol Brain*. 2010 Apr 21;3:12. doi: 10.1186/1756-6606-3-12. PMID: 20409326; PMCID: PMC2873589.
- Han BS, Iacovitti L, Katano T, Hattori N, Seol W, Kim KS. Expression of the LRRK2 gene in the midbrain dopaminergic neurons of the substantia nigra. *Neurosci Lett*. 2008 Sep 19;442(3):190-4. doi: 10.1016/j.neulet.2008.06.086. Epub 2008 Jul 10. PMID: 18634852; PMCID: PMC2737127.
- Henry AG, Aghamohammadzadeh S, Samaroo H, Chen Y, Mou K, Needle E, Hirst WD. Pathogenic LRRK2 mutations, through increased kinase activity, produce enlarged lysosomes with reduced degradative capacity and increase ATP13A2 expression. *Hum Mol Genet*. 2015 Nov 1;24(21):6013-28. doi: 10.1093/hmg/ddv314. Epub 2015 Aug 6. PMID: 26251043.
- Higashi S, Moore DJ, Colebrooke RE, Biskup S, Dawson VL, Arai H, Dawson TM, Emson PC. Expression and localization of Parkinson's disease-associated leucine-rich repeat kinase 2 in the mouse brain. *J Neurochem*. 2007 Jan;100(2):368-81. doi: 10.1111/j.1471-4159.2006.04246.x. Epub 2006 Nov 13. PMID: 17101029.
- Ho DH, Je AR, Lee H, Son I, Kweon HS, Kim HG, Seol W. LRRK2 Kinase Activity Induces Mitochondrial Fission in Microglia via Drp1 and Modulates Neuroinflammation. *Exp Neurobiol*. 2018 Jun;27(3):171-180. doi: 10.5607/en.2018.27.3.171. Epub 2018 Jun 30. PMID: 30022868; PMCID: PMC6050415.
- Hsieh CH, Shaltouki A, Gonzalez AE, Bettencourt da Cruz A, Burbulla LF, St Lawrence E, Schüle B, Krainc D, Palmer TD, Wang X. Functional Impairment in Miro Degradation and Mitophagy Is a Shared Feature in Familial and Sporadic Parkinson's Disease. *Cell Stem Cell*. 2016 Dec 1;19(6):709-724. doi: 10.1016/j.stem.2016.08.002. Epub 2016 Sep 8. PMID: 27618216; PMCID: PMC5135570.
- Indo HP, Yen HC, Nakanishi I, Matsumoto K, Tamura M, Nagano Y, Matsui H, Gusev O, Cornette R, Okuda T, Minamiyama Y, Ichikawa H, Suenaga S, Oki M, Sato T, Ozawa T, Clair DK, Majima HJ. A mitochondrial superoxide theory for oxidative stress diseases and aging. *J Clin Biochem Nutr*. 2015 Jan;56(1):1-7. doi: 10.3164/jcbn.14-42. Epub 2014 Dec 23. PMID: 25834301; PMCID: PMC4306659.

- Jackson-Lewis V, Blesa J, Przedborski S. Animal models of Parkinson's disease. *Parkinsonism Relat Disord.* 2012 Jan;18 Suppl 1:S183-5. doi: 10.1016/S1353-8020(11)70057-8. PMID: 22166429.
- Jeong GR, Lee BD. Pathological Functions of LRRK2 in Parkinson's Disease. *Cells.* 2020 Nov 30;9(12):2565. doi: 10.3390/cells9122565. PMID: 33266247; PMCID: PMC7759975.
- Kalia LV, Lang AE. Parkinson's disease. *Lancet.* 2015 Aug 29;386(9996):896-912. doi: 10.1016/S0140-6736(14)61393-3. Epub 2015 Apr 19. PMID: 25904081.
- Katayama H, Kogure T, Mizushima N, Yoshimori T, Miyawaki A. A sensitive and quantitative technique for detecting autophagic events based on lysosomal delivery. *Chem Biol.* 2011 Aug 26;18(8):1042-52. doi: 10.1016/j.chembiol.2011.05.013. PMID: 21867919.
- Kim JM, Cha SH, Choi YR, Jou I, Joe EH, Park SM. DJ-1 deficiency impairs glutamate uptake into astrocytes via the regulation of flotillin-1 and caveolin-1 expression. *Sci Rep.* 2016 Jun 27;6:28823. doi: 10.1038/srep28823. PMID: 27346864; PMCID: PMC4922019.
- Koehler RC, Roman RJ, Harder DR. Astrocytes and the regulation of cerebral blood flow. *Trends Neurosci.* 2009 Mar;32(3):160-9. doi: 10.1016/j.tins.2008.11.005. Epub 2009 Jan 21. PMID: 19162338.
- Korecka JA, Thomas R, Christensen DP, Hinrich AJ, Ferrari EJ, Levy SA, Hastings ML, Hallett PJ, Isacson O. Mitochondrial clearance and maturation of autophagosomes are compromised in LRRK2 G2019S familial Parkinson's disease patient fibroblasts. *Hum Mol Genet.* 2019 Oct 1;28(19):3232-3243. doi: 10.1093/hmg/ddz126. PMID: 31261377; PMCID: PMC6859523.
- Kriks S, Shim JW, Piao J, Ganat YM, Wakeman DR, Xie Z, Carrillo-Reid L, Auyeung G, Antonacci C, Buch A, Yang L, Beal MF, Surmeier DJ, Kordower JH, Tabar V, Studer L. Dopamine neurons derived from human ES cells efficiently engraft in animal models of Parkinson's disease. *Nature.* 2011 Nov 6;480(7378):547-51. doi: 10.1038/nature10648. PMID: 22056989; PMCID: PMC3245796.
- Kujawska M, Jourdes M, Kurpik M, Szulc M, Szaefer H, Chmielarz P, Kreiner G, Krajka-Kuźniak V, Mikołajczak PŁ, Teissedre PL, Jodynis-Liebert J. Neuroprotective Effects of Pomegranate Juice against Parkinson's Disease and Presence of Ellagitannins-Derived Metabolite-Urolithin A-In the Brain. *Int J Mol Sci.* 2019 Dec 27;21(1):202. doi: 10.3390/ijms21010202. PMID: 31892167; PMCID: PMC6981883.
- Langston JW, Ballard P, Tetrud JW, Irwin I. Chronic Parkinsonism in humans due to a product of meperidine-analog synthesis. *Science.* 1983 Feb 25;219(4587):979-80. doi: 10.1126/science.6823561. PMID: 6823561.
- Lázaro DF, Rodrigues EF, Langohr R, Shahpasandzadeh H, Ribeiro T, Guerreiro P, Gerhardt

- E, Kröhnert K, Klucken J, Pereira MD, Popova B, Kruse N, Mollenhauer B, Rizzoli SO, Braus GH, Danzer KM, Outeiro TF. Systematic comparison of the effects of alpha-synuclein mutations on its oligomerization and aggregation. *PLoS Genet.* 2014 Nov 13;10(11):e1004741. doi: 10.1371/journal.pgen.1004741. PMID: 25393002; PMCID: PMC4230739.
- Lázaro DE, Pavlou MAS, Outeiro TF. Cellular models as tools for the study of the role of alpha-synuclein in Parkinson's disease. *Exp Neurol.* 2017 Dec;298(Pt B):162-171. doi: 10.1016/j.expneurol.2017.05.007. Epub 2017 May 16. PMID: 28526239.
- Lee HJ, Suk JE, Patrick C, Bae EJ, Cho JH, Rho S, Hwang D, Masliah E, Lee SJ. Direct transfer of alpha-synuclein from neuron to astroglia causes inflammatory responses in synucleinopathies. *J Biol Chem.* 2010 Mar 19;285(12):9262-72. doi: 10.1074/jbc.M109.081125. Epub 2010 Jan 13. PMID: 20071342; PMCID: PMC2838344.
- Lees AJ, Hardy J, Revesz T. Parkinson's disease. *Lancet.* 2009 Jun 13;373(9680):2055-66. doi: 10.1016/S0140-6736(09)60492-X. Erratum in: *Lancet.* 2009 Aug 29;374(9691):684. PMID: 19524782.
- LeWitt PA, Fahn S. Levodopa therapy for Parkinson disease: A look backward and forward. *Neurology.* 2016 Apr 5;86(14 Suppl 1):S3-12. doi: 10.1212/WNL.0000000000002509. Epub 2016 Apr 4. PMID: 27044648.
- Liddell JR. Are Astrocytes the Predominant Cell Type for Activation of Nrf2 in Aging and Neurodegeneration? *Antioxidants (Basel).* 2017 Aug 18;6(3):65. doi: 10.3390/antiox6030065. PMID: 28820437; PMCID: PMC5618093.
- Liddel SA, Guttenplan KA, Clarke LE, Bennett FC, Bohlen CJ, Schirmer L, Bennett ML, Münch AE, Chung WS, Peterson TC, Wilton DK, Frouin A, Napier BA, Panicker N, Kumar M, Buckwalter MS, Rowitch DH, Dawson VL, Dawson TM, Stevens B, Barres BA. Neurotoxic reactive astrocytes are induced by activated microglia. *Nature.* 2017 Jan 26;541(7638):481-487. doi: 10.1038/nature21029. Epub 2017 Jan 18. PMID: 28099414; PMCID: PMC5404890.
- Lin MK, Farrer MJ. Genetics and genomics of Parkinson's disease. *Genome Med.* 2014 Jun 30;6(6):48. doi: 10.1186/gm566. PMID: 25061481; PMCID: PMC4085542.
- Mahlknecht P, Seppi K, Poewe W. The Concept of Prodromal Parkinson's Disease. *J Parkinsons Dis.* 2015;5(4):681-97. doi: 10.3233/JPD-150685. PMID: 26485429; PMCID: PMC4927924.
- Mahmoud S, Gharagozloo M, Simard C, Gris D. Astrocytes Maintain Glutamate Homeostasis in the CNS by Controlling the Balance between Glutamate Uptake and Release. *Cells.* 2019 Feb 20;8(2):184. doi: 10.3390/cells8020184. PMID: 30791579; PMCID: PMC6406900.

- Maiti P, Manna J, Dunbar GL. Current understanding of the molecular mechanisms in Parkinson's disease: Targets for potential treatments. *Transl Neurodegener.* 2017 Oct 25;6:28. doi: 10.1186/s40035-017-0099-z. PMID: 29090092; PMCID: PMC5655877.
- Manzoni C, Mamais A, Dihanich S, Abeti R, Soutar MPM, Plun-Favreau H, Giunti P, Tooze SA, Bandopadhyay R, Lewis PA. Inhibition of LRRK2 kinase activity stimulates macroautophagy. *Biochim Biophys Acta.* 2013 Dec;1833(12):2900-2910. doi: 10.1016/j.bbamcr.2013.07.020. Epub 2013 Aug 1. PMID: 23916833; PMCID: PMC3898616.
- Marras C, Hincapié CA, Kristman VL, Cancelliere C, Soklaridis S, Li A, Borg J, af Geijerstam JL, Cassidy JD. Systematic review of the risk of Parkinson's disease after mild traumatic brain injury: results of the International Collaboration on Mild Traumatic Brain Injury Prognosis. *Arch Phys Med Rehabil.* 2014 Mar;95(3 Suppl):S238-44. doi: 10.1016/j.apmr.2013.08.298. PMID: 24581909.
- Melrose HL, Lincoln SJ, Tyndall GM, Farrer MJ. Parkinson's disease: a rethink of rodent models. *Exp Brain Res.* 2006 Aug;173(2):196-204. doi: 10.1007/s00221-006-0461-3. Epub 2006 Apr 26. PMID: 16639500.
- Morales I, Sanchez A, Puertas-Avenidaño R, Rodriguez-Sabate C, Perez-Barreto A, Rodriguez M. Neuroglial transmyelinopathy and Parkinson's disease. *Glia.* 2020 Nov;68(11):2277-2299. doi: 10.1002/glia.23839. Epub 2020 May 16. PMID: 32415886.
- Mortiboys H, Johansen KK, Aasly JO, Bandmann O. Mitochondrial impairment in patients with Parkinson disease with the G2019S mutation in LRRK2. *Neurology.* 2010 Nov 30;75(22):2017-20. doi: 10.1212/WNL.0b013e3181ff9685. PMID: 21115957.
- Nakabeppu Y, Tsuchimoto D, Yamaguchi H, Sakumi K. Oxidative damage in nucleic acids and Parkinson's disease. *J Neurosci Res.* 2007 Apr;85(5):919-34. doi: 10.1002/jnr.21191. PMID: 17279544.
- Niu J, Yu M, Wang C, Xu Z. Leucine-rich repeat kinase 2 disturbs mitochondrial dynamics via Dynamin-like protein. *J Neurochem.* 2012 Aug;122(3):650-8. doi: 10.1111/j.1471-4159.2012.07809.x. Epub 2012 Jun 22. PMID: 22639965.
- Orenstein SJ, Kuo SH, Tasset I, Arias E, Koga H, Fernandez-Carasa I, Cortes E, Honig LS, Dauer W, Consiglio A, Raya A, Sulzer D, Cuervo AM. Interplay of LRRK2 with chaperone-mediated autophagy. *Nat Neurosci.* 2013 Apr;16(4):394-406. doi: 10.1038/nn.3350. Epub 2013 Mar 3. PMID: 23455607; PMCID: PMC3609872.
- Pajares M, I Rojo A, Manda G, Boscá L, Cuadrado A. Inflammation in Parkinson's Disease: Mechanisms and Therapeutic Implications. *Cells.* 2020 Jul 14;9(7):1687. doi: 10.3390/cells9071687. PMID: 32674367; PMCID: PMC7408280.
- Palikaras K, Lionaki E, Tavernarakis N. Coordination of mitophagy and mitochondrial

- biogenesis during ageing in *C. elegans*. *Nature*. 2015 May 28;521(7553):525-8. doi: 10.1038/nature14300. Epub 2015 Apr 20. PMID: 25896323.
- Parker WD Jr, Parks JK, Swerdlow RH. Complex I deficiency in Parkinson's disease frontal cortex. *Brain Res*. 2008 Jan 16;1189:215-8. doi: 10.1016/j.brainres.2007.10.061. Epub 2007 Nov 1. PMID: 18061150; PMCID: PMC2295283.
- PD Med Collaborative Group, Gray R, Ives N, Rick C, Patel S, Gray A, Jenkinson C, McIntosh E, Wheatley K, Williams A, Clarke CE. Long-term effectiveness of dopamine agonists and monoamine oxidase B inhibitors compared with levodopa as initial treatment for Parkinson's disease (PD MED): a large, open-label, pragmatic randomised trial. *Lancet*. 2014 Sep 27;384(9949):1196-205. doi: 10.1016/S0140-6736(14)60683-8. Epub 2014 Jun 11. Erratum in: *Lancet*. 2014 Sep 27;384(9949):1186. PMID: 24928805.
- Perestelo-Pérez L, Rivero-Santana A, Pérez-Ramos J, Serrano-Pérez P, Panetta J, Hilarion P. Deep brain stimulation in Parkinson's disease: meta-analysis of randomized controlled trials. *J Neurol*. 2014 Nov;261(11):2051-60. doi: 10.1007/s00415-014-7254-6. Epub 2014 Feb 2. PMID: 24487826.
- Perier C, Bové J, Dehay B, Jackson-Lewis V, Rabinovitch PS, Przedborski S, Vila M. Apoptosis-inducing factor deficiency sensitizes dopaminergic neurons to parkinsonian neurotoxins. *Ann Neurol*. 2010 Aug;68(2):184-92. doi: 10.1002/ana.22034. PMID: 20695011.
- Ploumi C, Daskalaki I, Tavernarakis N. Mitochondrial biogenesis and clearance: a balancing act. *FEBS J*. 2017 Jan;284(2):183-195. doi: 10.1111/febs.13820. Epub 2016 Aug 11. PMID: 27462821.
- Poewe W, Seppi K, Tanner CM, Halliday GM, Brundin P, Volkmann J, Schrag AE, Lang AE. Parkinson disease. *Nat Rev Dis Primers*. 2017 Mar 23;3:17013. doi: 10.1038/nrdp.2017.13. PMID: 28332488.
- Polymeropoulos MH, Lavedan C, Leroy E, Ide SE, Dehejia A, Dutra A, Pike B, Root H, Rubenstein J, Boyer R, Stenroos ES, Chandrasekharappa S, Athanassiadou A, Papapetropoulos T, Johnson WG, Lazzarini AM, Duvoisin RC, Di Iorio G, Golbe LI, Nussbaum RL. Mutation in the alpha-synuclein gene identified in families with Parkinson's disease. *Science*. 1997 Jun 27;276(5321):2045-7. doi: 10.1126/science.276.5321.2045. PMID: 9197268.
- Pons-Espinal M, Blasco-Agell L, Consiglio A. Dissecting the non-neuronal cell contribution to Parkinson's disease pathogenesis using induced pluripotent stem cells. *Cell Mol Life Sci*. 2021 Mar;78(5):2081-2094. doi: 10.1007/s00018-020-03700-x. Epub 2020 Nov 18. PMID: 33210214; PMCID: PMC7966189.
- Puspita L, Chung SY, Shim JW. Oxidative stress and cellular pathologies in Parkinson's disease. *Mol Brain*. 2017 Nov 28;10(1):53. doi: 10.1186/s13041-017-0340-9. PMID: 29183391;

PMCID: PMC5706368.

- Ramos-Gonzalez P, Mato S, Chara JC, Verkhatsky A, Matute C, Cavaliere F. Astrocytic atrophy as a pathological feature of Parkinson's disease with LRRK2 mutation. *NPJ Parkinsons Dis.* 2021 Mar 30;7(1):31. doi: 10.1038/s41531-021-00175-w. PMID: 33785762.
- Rannikko EH, Weber SS, Kahle PJ. Exogenous α -synuclein induces toll-like receptor 4 dependent inflammatory responses in astrocytes. *BMC Neurosci.* 2015 Sep 7;16:57. doi: 10.1186/s12868-015-0192-0. PMID: 26346361; PMCID: PMC4562100.
- Raza C, Anjum R, Shakeel NUA. Parkinson's disease: Mechanisms, translational models and management strategies. *Life Sci.* 2019 Jun 1;226:77-90. doi: 10.1016/j.lfs.2019.03.057. Epub 2019 Apr 10. PMID: 30980848.
- Reich SG, Savitt JM. Parkinson's Disease. *Med Clin North Am.* 2019 Mar;103(2):337-350. doi: 10.1016/j.mcna.2018.10.014. Epub 2018 Dec 3. PMID: 30704685.
- Ryu D, Mouchiroud L, Andreux PA, Katsyuba E, Moullan N, Nicolet-Dit-Félix AA, Williams EG, Jha P, Lo Sasso G, Huzard D, Aebischer P, Sandi C, Rinsch C, Auwerx J. Urolithin A induces mitophagy and prolongs lifespan in *C. elegans* and increases muscle function in rodents. *Nat Med.* 2016 Aug;22(8):879-88. doi: 10.1038/nm.4132. Epub 2016 Jul 11. PMID: 27400265.
- Sanchez G, Varaschin RK, Büeler H, Marcogliese PC, Park DS, Trudeau LE. Unaltered striatal dopamine release levels in young Parkin knockout, Pink1 knockout, DJ-1 knockout and LRRK2 R1441G transgenic mice. *PLoS One.* 2014 Apr 14;9(4):e94826. doi: 10.1371/journal.pone.0094826. PMID: 24733019; PMCID: PMC3986353.
- Sánchez-Danés A, Richaud-Patin Y, Carballo-Carbajal I, Jiménez-Delgado S, Caig C, Mora S, Di Guglielmo C, Ezquerra M, Patel B, Giralt A, Canals JM, Memo M, Alberch J, López-Barneo J, Vila M, Cuervo AM, Tolosa E, Consiglio A, Raya A. Disease-specific phenotypes in dopamine neurons from human iPS-based models of genetic and sporadic Parkinson's disease. *EMBO Mol Med.* 2012 May;4(5):380-95. doi: 10.1002/emmm.201200215. Epub 2012 Mar 8. PMID: 22407749; PMCID: PMC3403296.
- Schapira AH, Cooper JM, Dexter D, Clark JB, Jenner P, Marsden CD. Mitochondrial complex I deficiency in Parkinson's disease. *J Neurochem.* 1990 Mar;54(3):823-7. doi: 10.1111/j.1471-4159.1990.tb02325.x. PMID: 2154550.
- Schindelin J, Arganda-Carreras I, Frise E, Kaynig V, Longair M, Pietzsch T, Preibisch S, Rueden C, Saalfeld S, Schmid B, Tinevez JY, White DJ, Hartenstein V, Eliceiri K, Tomancak P, Cardona A. Fiji: an open-source platform for biological-image analysis. *Nat Methods.* 2012 Jun 28;9(7):676-82. doi: 10.1038/nmeth.2019. PMID: 22743772; PMCID: PMC3855844.

- Schousboe A, Bak LK, Waagepetersen HS. Astrocytic Control of Biosynthesis and Turnover of the Neurotransmitters Glutamate and GABA. *Front Endocrinol (Lausanne)*. 2013 Aug 15;4:102. doi: 10.3389/fendo.2013.00102. PMID: 23966981; PMCID: PMC3744088.
- Schwarz ST, Xing Y, Tomar P, Bajaj N, Auer DP. In Vivo Assessment of Brainstem Depigmentation in Parkinson Disease: Potential as a Severity Marker for Multicenter Studies. *Radiology*. 2017 Jun;283(3):789-798. doi: 10.1148/radiol.2016160662. Epub 2016 Nov 7. PMID: 27820685.
- Sebastián D, Zorzano A. Mitochondrial dynamics and metabolic homeostasis. *Current Opinion in Physiology*. 2018 Jun; 3:34-40. doi: <https://doi.org/10.1016/j.cophys.2018.02.006>
- Serio A, Bilican B, Barmada SJ, Ando DM, Zhao C, Siller R, Burr K, Haghi G, Story D, Nishimura AL, Carrasco MA, Phatnani HP, Shum C, Wilmut I, Maniatis T, Shaw CE, Finkbeiner S, Chandran S. Astrocyte pathology and the absence of non-cell autonomy in an induced pluripotent stem cell model of TDP-43 proteinopathy. *Proc Natl Acad Sci U S A*. 2013 Mar 19;110(12):4697-702. doi: 10.1073/pnas.1300398110. Epub 2013 Feb 11. PMID: 23401527; PMCID: PMC3607024.
- Sin J, Andres AM, Taylor DJ, Weston T, Hiraumi Y, Stotland A, Kim BJ, Huang C, Doran KS, Gottlieb RA. Mitophagy is required for mitochondrial biogenesis and myogenic differentiation of C2C12 myoblasts. *Autophagy*. 2016;12(2):369-80. doi: 10.1080/15548627.2015.1115172. PMID: 26566717; PMCID: PMC4836019.
- Singh A, Zhi L, Zhang H. LRRK2 and mitochondria: Recent advances and current views. *Brain Res*. 2019 Jan 1;1702:96-104. doi: 10.1016/j.brainres.2018.06.010. Epub 2018 Jun 9. PMID: 29894679; PMCID: PMC6281802.
- Singh F, Ganley IG. Parkinson's disease and mitophagy: an emerging role for LRRK2. *Biochem Soc Trans*. 2021 Mar 26;BST20190236. doi: 10.1042/BST20190236. Epub ahead of print. PMID: 33769432.
- Smirnova E, Griparic L, Shurland DL, van der Bliek AM. Dynamin-related protein Drp1 is required for mitochondrial division in mammalian cells. *Mol Biol Cell*. 2001 Aug;12(8):2245-56. doi: 10.1091/mbc.12.8.2245. PMID: 11514614; PMCID: PMC58592.
- Smith GA, Jansson J, Rocha EM, Osborn T, Hallett PJ, Isacson O. Fibroblast Biomarkers of Sporadic Parkinson's Disease and LRRK2 Kinase Inhibition. *Mol Neurobiol*. 2016 Oct;53(8):5161-77. doi: 10.1007/s12035-015-9435-4. Epub 2015 Sep 23. PMID: 26399642; PMCID: PMC5012155.
- Sofroniew MV. Molecular dissection of reactive astrogliosis and glial scar formation. *Trends Neurosci*. 2009 Dec;32(12):638-47. doi: 10.1016/j.tins.2009.08.002. Epub 2009 Sep 24. PMID: 19782411; PMCID: PMC2787735.

- Sofroniew MV, Vinters HV. Astrocytes: biology and pathology. *Acta Neuropathol.* 2010 Jan;119(1):7-35. doi: 10.1007/s00401-009-0619-8. Epub 2009 Dec 10. PMID: 20012068; PMCID: PMC2799634.
- Sonninen TM, Hämäläinen RH, Koskivi M, Oksanen M, Shakirzyanova A, Wojciechowski S, Puttonen K, Naumenko N, Goldsteins G, Laham-Karam N, Lehtonen M, Tavi P, Koistinaho J, Lehtonen Š. Metabolic alterations in Parkinson's disease astrocytes. *Sci Rep.* 2020 Sep 2;10(1):14474. doi: 10.1038/s41598-020-71329-8. PMID: 32879386; PMCID: PMC7468111.
- Spillantini MG, Schmidt ML, Lee VM, Trojanowski JQ, Jakes R, Goedert M. Alpha-synuclein in Lewy bodies. *Nature.* 1997 Aug 28;388(6645):839-40. doi: 10.1038/42166. PMID: 9278044.
- Stadtfeld M, Hochedlinger K. Induced pluripotency: history, mechanisms, and applications. *Genes Dev.* 2010 Oct 15;24(20):2239-63. doi: 10.1101/gad.1963910. PMID: 20952534; PMCID: PMC2956203.
- Su YC, Qi X. Inhibition of excessive mitochondrial fission reduced aberrant autophagy and neuronal damage caused by LRRK2 G2019S mutation. *Hum Mol Genet.* 2013 Nov 15;22(22):4545-61. doi: 10.1093/hmg/ddt301. Epub 2013 Jun 27. PMID: 23813973.
- Sun N, Yun J, Liu J, Malide D, Liu C, Rovira II, Holmström KM, Fergusson MM, Yoo YH, Combs CA, Finkel T. Measuring In Vivo Mitophagy. *Mol Cell.* 2015 Nov 19;60(4):685-96. doi: 10.1016/j.molcel.2015.10.009. Epub 2015 Nov 5. PMID: 26549682; PMCID: PMC4656081.
- Surmeier DJ, Obeso JA, Halliday GM. Selective neuronal vulnerability in Parkinson disease. *Nat Rev Neurosci.* 2017 Jan 20;18(2):101-113. doi: 10.1038/nrn.2016.178. PMID: 28104909; PMCID: PMC5564322
- Takahashi K, Tanabe K, Ohnuki M, Narita M, Ichisaka T, Tomoda K, Yamanaka S. Induction of pluripotent stem cells from adult human fibroblasts by defined factors. *Cell.* 2007 Nov 30;131(5):861-72. doi: 10.1016/j.cell.2007.11.019. PMID: 18035408.
- Taymans JM, Van den Haute C, Baekelandt V. Distribution of PINK1 and LRRK2 in rat and mouse brain. *J Neurochem.* 2006 Aug;98(3):951-61. doi: 10.1111/j.1471-4159.2006.03919.x. Epub 2006 Jun 12. PMID: 16771836.
- Tieu K. A guide to neurotoxic animal models of Parkinson's disease. *Cold Spring Harb Perspect Med.* 2011 Sep;1(1):a009316. doi: 10.1101/cshperspect.a009316. PMID: 22229125; PMCID: PMC3234449.
- Torrent R, De Angelis Rigotti F, Dell'Era P, Memo M, Raya A, Consiglio A. Using iPS Cells toward the Understanding of Parkinson's Disease. *J Clin Med.* 2015 Mar 30;4(4):548-66.

doi: 10.3390/jcm4040548. PMID: 26239346; PMCID: PMC4470155.

- Tysnes OB, Storstein A. Epidemiology of Parkinson's disease. *J Neural Transm (Vienna)*. 2017 Aug;124(8):901-905. doi: 10.1007/s00702-017-1686-y. Epub 2017 Feb 1. PMID: 28150045.
- Vasile F, Dossi E, Rouach N. Human astrocytes: structure and functions in the healthy brain. *Brain Struct Funct*. 2017 Jul;222(5):2017-2029. doi: 10.1007/s00429-017-1383-5. Epub 2017 Mar 9. PMID: 28280934; PMCID: PMC5504258.
- Wakabayashi K, Hayashi S, Yoshimoto M, Kudo H, Takahashi H. NACP/alpha-synuclein-positive filamentous inclusions in astrocytes and oligodendrocytes of Parkinson's disease brains. *Acta Neuropathol*. 2000 Jan;99(1):14-20. doi: 10.1007/pl00007400. PMID: 10651022.
- Wang X, Yan MH, Fujioka H, Liu J, Wilson-Delfosse A, Chen SG, Perry G, Casadesus G, Zhu X. LRRK2 regulates mitochondrial dynamics and function through direct interaction with DLP1. *Hum Mol Genet*. 2012 May 1;21(9):1931-44. doi: 10.1093/hmg/dds003. Epub 2012 Jan 6. PMID: 22228096; PMCID: PMC3315202.
- Wauters F, Cornelissen T, Imberechts D, Martin S, Koentjoro B, Sue C, Vangheluwe P, Vandenberghe W. LRRK2 mutations impair depolarization-induced mitophagy through inhibition of mitochondrial accumulation of RAB10. *Autophagy*. 2020 Feb;16(2):203-222. doi: 10.1080/15548627.2019.1603548. Epub 2019 Apr 19. PMID: 30945962; PMCID: PMC6984591.
- Williams JA, Zhao K, Jin S, Ding WX. New methods for monitoring mitochondrial biogenesis and mitophagy in vitro and in vivo. *Exp Biol Med (Maywood)*. 2017 Apr;242(8):781-787. doi: 10.1177/1535370216688802. Epub 2017 Jan 1. PMID: 28093935; PMCID: PMC5407538.
- Xie LL, Shi F, Tan Z, Li Y, Bode AM, Cao Y. Mitochondrial network structure homeostasis and cell death. *Cancer Sci*. 2018 Dec;109(12):3686-3694. doi: 10.1111/cas.13830. Epub 2018 Nov 16. PMID: 30312515; PMCID: PMC6272111.
- Xu X, Fu Z, Le W. Exercise and Parkinson's disease. *Int Rev Neurobiol*. 2019;147:45-74. doi: 10.1016/bs.irm.2019.06.003. Epub 2019 Jun 20. PMID: 31607362.

Publications in indexed journals in which I have collaborated during my doctoral programme:

Kim H, Calatayud C, Guha S, **Fernández-Carasa I**, Berkowitz L, Carballo-Carbajal I, Ezquerra M, Fernández-Santiago R, Kapahi P, Raya Á, Miranda-Vizueté A, Lizcano JM, Vila M, Caldwell KA, Caldwell GA, Consiglio A, Dalfo E. The Small GTPase RAC1/CED-10 Is Essential in Maintaining Dopaminergic Neuron Function and Survival Against α -Synuclein-Induced Toxicity. *Mol Neurobiol.* 2018 Sep;55(9):7533-7552. **Impact factor: 4.586**

Suh H, Zhou Q-G, **Fernández-Carasa I**, Clemenson GD Jr, Pons-Espinal M, Ro EJ, Marti M, Raya A, Gage FH and Consiglio A (2018) Long-Term Labeling of Hippocampal Neural Stem Cells by a Lentiviral Vector. *Front. Mol. Neurosci.* 11:415. **Impact factor: 3.82**

di Domenico A, Carola G, Calatayud C, Pons-Espinal M, Muñoz JP, Richaud-Patin Y, **Fernández-Carasa I**, Gut M, Faella A, Parameswaran J, Soriano J, Ferrer I, Tolosa E, Zorzano A, Cuervo AM, Raya A, Consiglio A. Patient-Specific iPSC-Derived Astrocytes Contribute to Non-Cell-Autonomous Neurodegeneration in Parkinson's Disease. *Stem Cell Reports.* 2019 Jan 6. pii: S2213-6711(18)30530-7. **Impact factor: 6.032**


Calatayud C, Carola G, **Fernández-Carasa I**, Valtorta M, Jiménez-Delgado S, Díaz M, Soriano-Fradera J, Cappelletti G, García-Sancho J, Raya Á, Consiglio A. CRISPR/Cas9-mediated generation of a tyrosine hydroxylase reporter iPSC

line for live imaging and isolation of dopaminergic neurons. *Scientific Reports*. 2019 May 2;9(1):6811. doi: 10.1038/s41598-019-43080-2. **Impact factor: 3.998**

Cai R, Zhang Y, Simmering JE, Schultz JL, Li Y, **Fernández-Carasa I**, Consiglio A, Raya A, Polgreen PM, Narayanan NS, Yuan Y, Chen Z, Su W, Han Y, Zhao C, Gao L, Ji X, Welsh MJ, Liu L. Enhancing glycolysis attenuates Parkinson's disease progression in models and clinical databases. *J Clin Invest*. 2019 Sep 16. pii: 129987. doi: 10.1172/JCI129987. **Impact factor: 11.864**



The Small GTPase RAC1/CED-10 Is Essential in Maintaining Dopaminergic Neuron Function and Survival Against α -Synuclein-Induced Toxicity

Hanna Kim¹ · Carles Calatayud^{2,3,4} · Sanjib Guha⁵ · Irene Fernández-Carasa^{2,3} · Laura Berkowitz¹ · Iria Carballo-Carbajal⁶ · Mario Ezquerro⁷ · Rubén Fernández-Santiago⁷ · Pankaj Kapahi⁵ · Ángel Raya^{4,8} · Antonio Miranda-Vizuete⁹ · Jose Miguel Lizzano¹⁰ · Miquel Vila^{6,8,10} · Kim A. Caldwell¹ · Guy A. Caldwell¹ · Antonella Consiglio^{2,3,11} · Esther Dalfo^{10,12} 

Received: 14 August 2017 / Accepted: 7 January 2018 / Published online: 10 February 2018
© The Author(s) 2018

Abstract

Parkinson's disease is associated with intracellular α -synuclein accumulation and ventral midbrain dopaminergic neuronal death in the *Substantia Nigra* of brain patients. The Rho GTPase pathway, mainly linking surface receptors to the organization of the actin and microtubule cytoskeletons, has been suggested to participate to Parkinson's disease pathogenesis. Nevertheless, its exact contribution remains obscure. To unveil the participation of the Rho GTPase family to the molecular pathogenesis of Parkinson's disease, we first used *C. elegans* to demonstrate the role of the small GTPase *RAC1* (*ced-10* in the worm) in maintaining dopaminergic function and survival in the presence of alpha-synuclein. In addition, *ced-10* mutant worms determined an increase of alpha-synuclein inclusions in comparison to control worms as well as an increase in autophagic vesicles. We then used a human neuroblastoma cells (M17) stably over-expressing alpha-synuclein and found that *RAC1* function decreased the amount of amyloidogenic alpha-synuclein. Further, by using dopaminergic neurons derived from patients of familial LRRK2-Parkinson's disease we report that human RAC1 activity is essential in the regulation of dopaminergic cell death, alpha-synuclein

Hanna Kim, Carles Calatayud and Sanjib Guha contributed equally to this work.

Electronic supplementary material The online version of this article (<https://doi.org/10.1007/s12035-018-0881-7>) contains supplementary material, which is available to authorized users.

✉ Antonella Consiglio
consiglio@ub.edu

✉ Esther Dalfo
esther.dalfo@uab.cat

¹ Department of Biological Sciences, The University of Alabama, Tuscaloosa, AL 35487, USA

² Department of Pathology and Experimental Therapeutics, Bellvitge University Hospital-IDIBELL, 08028 L'Hospitalet de Llobregat, Spain

³ Institute of Biomedicine of the University of Barcelona (IBUB), Barcelona 08908, Spain

⁴ Center of Regenerative Medicine in Barcelona (CMRB), Center for Networked Biomedical Research on Bioengineering, Biomaterials and Nanomedicine (CIBER-BBN), Hospital Duran i Reynals, 08908 L'Hospitalet de Llobregat, Spain

⁵ Buck Institute for Research on Aging, 8001 Redwood Boulevard, Novato, CA 94945, USA

⁶ Neurodegenerative Diseases Research Group, Vall d'Hebron Research Institute-Center for Networked Biomedical Research on Neurodegenerative Diseases (CIBERNED), 08035 Barcelona, Spain

⁷ Laboratory of Parkinson Disease and Other Neurodegenerative Movement Disorders, Department of Neurology: Clinical and Experimental Research, IDIBAPS – Hospital Clínic de Barcelona, 08036 Barcelona, Spain

⁸ Catalan Institution for Research and Advanced Studies (ICREA), 08010 Barcelona, Spain

⁹ Instituto de Biomedicina de Sevilla, Hospital Universitario Virgen del Rocío/CSIC/ Universidad de Sevilla, 41013 Sevilla, Spain

¹⁰ Department of Biochemistry and Molecular Biology, Institut de Neurociències, Faculty of Medicine, M2, Universitat Autònoma de Barcelona (UAB), Bellaterra Campus, Cerdanyola del Vallès, Barcelona, Spain

¹¹ Department of Molecular and Translational Medicine, University of Brescia, Brescia, Spain

¹² Faculty of Medicine, University of Vic-Central University of Catalonia (UVic-UCC), Can Baumann, 08500 Vic, Spain

accumulation, participates in neurite arborization and modulates autophagy. Thus, we determined for the first time that *RAC1/ced-10* participates in Parkinson's disease associated pathogenesis and established *RAC1/ced-10* as a new candidate for further investigation of Parkinson's disease associated mechanisms, mainly focused on dopaminergic function and survival against α -synuclein-induced toxicity.

Keywords Parkinson's disease · Dopaminergic neurons · Alpha-synuclein accumulation · Autophagy impairment · *RAC1/ced-10*

Introduction

Parkinson's disease (PD) is the second most frequent neurodegenerative disorder in the elderly. While most of cases are sporadic, monogenic PD caused by pathogenic point mutations in PD-associated genes occurs in less than 10% of cases (reviewed in [1]). The common neuropathological hallmarks of PD include a selective loss of the dopaminergic neurons (DAn) in the *Substantia Nigra pars compacta* and aggregation of the protein alpha-synuclein (α -SYN) in the surviving DAn and in the so called Lewy bodies (LB) and Lewy neurites (LN) which are found in the few surviving DAn (reviewed in [2]). α -SYN is intrinsically misfolded in pathological conditions such as PD [3] and forms multiple conformations, including amyloidogenic oligomers [4, 5] implicated in α -SYN toxicity [6].

There exist evidences of an essential role of actin cytoskeleton disruptions in both DAn cell death [7, 8] and α -SYN accumulation [9]. In fact, the cytoskeleton is an important target of α -SYN [10] and neuronal microtubule-kinesin function could be impaired by α -SYN oligomers [11]. Actin cytoskeletal organization is regulated by small GTPases of the Rho family encompassing Rho, Cdc42 and Rac subfamily members [7]. These proteins act as molecular switches as they alternate between the active GTP-bound and the inactive GDP-bound forms [8, 16]. GTP binding increases the activity, and the hydrolysis of GTP to GDP renders the protein inactive. More specifically, RAC1 activity is mainly associated with cellular processes involving the regulation of actin polymerization such as cell migration, lamellipodia extension or the phagocytosis of dead cells or engulfment [12]. In addition, RAC1 participates in the extension and retraction of neurites [13] and, together with other members of the Rho family, govern changes in neuronal morphology and the dynamics of neuronal processes (reviewed in [8]).

RAC1 function has been associated with two PD-related genes. We have previously shown in *C elegans* that RAC1 is ubiquitinated by PARKIN [14], mutated in the juvenile variant of PD. Likewise, Leucine-rich repeat kinase 2 (LRRK2), in which mutations cause the most common form of familial PD [15], strongly and selectively binds to RAC1 [16]. Furthermore, neuronal apoptosis induced in DAn in vitro is correlated with decreased RAC1 activity [17]. In contrast, in a monkey model of PD, it was suggested that aberrant activation of RAC1 in microglia may contribute to enhanced production

of ROS underlying the death of neighboring DAn [18]. Therefore understanding the cytoskeletal mechanisms associated with DA cell death and α -SYN degradation is important to elucidate other causative agents of the PD pathophysiology.

Autophagic flux is profoundly disrupted in PD patients (reviewed in [1]) and α -SYN is normally degraded by autophagy [19]. Indeed, autophagy has been associated with PD pathogenesis through several genes, such as *LRRK2* [20], *ATG9A* [21] or *ATG8/LC3* [22], and cellular processes such as lysosomal disruption [23, 24]. In addition, autophagy-related gene products are required for apoptotic clearance, either in dying cells or through a role in engulfment, in where *RAC1* has a pivotal role [25–27].

In the present study we have systematically investigated *RAC1* function in three disease models of PD including the following: (a) *C elegans* models of PD; (b) human-derived neuroblastoma BE(2) (M17) cells stably over-expressing α -SYN, wherein amyloidogenic accumulation of α -SYN is induced by sodium butyrate; and (c) iPSC-derived DAn generated by cell reprogramming of somatic skin cells from patients with monogenic LRRK2-associated PD [20]. Using these models, we determine for the first time that *RAC1/ced-10* participates specifically in PD-associated pathogenesis and establish *RAC1/ced-10* as a new candidate to be considered for the investigation of PD-associated mechanisms, mainly focused on DA function and survival against α -SYN-induced toxicity.

Results

RAC1/ced-10* Cell-Autonomous Depletion in DAn Hampers Dopamine- Associated Behavior in the Presence of α -SYN and Accelerates α -SYN Induced DAn Death in *C elegans

We first investigated the role of *RAC1/ced-10* in DAn function, by performing behavioral assays through analyzing the DA behavior in *ced-10(n3246)* mutant animals. The mutation *ced-10(n3246)* is a G-to-A transition resulting in a change of glycine 60 of CED-10 to arginine (G60R) which results in non-null altered function [28, 29]. The severity of this allele is stronger in contrast to other *ced-10* alleles (11). To explore the role of *ced-10* in PD pathogenesis, all the experiments included in this study involving the *ced-10* gene were performed in a *ced-*

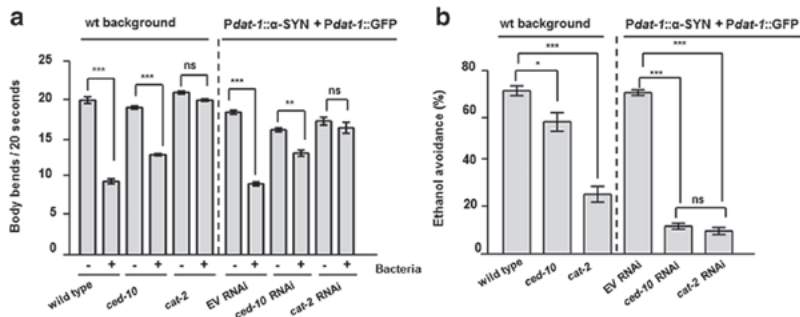


Fig. 1 DAN function is hampered by specific depletion of *RAC1/ced-10* in DAN expressing α -SYN in *C. elegans*. **a** Modulation of the locomotor rate. Well-fed animals were transferred to assay plates without or with a bacterial lawn (–/+) and 5 min later, the locomotor rate (body bends every 20 s) of each animal was analyzed. Statistical significance shows comparison of the bending within same genotype animals (wild type, *ced-10*(n3246) and *cat-2* (e1112)) without (–) or with (+) bacteria. RNAi experiments indicate *Pdat-1::α-SYN + Pdat-1::GFP* worms fed with EV (empty vector) or with the indicated RNAi clones. **b** Test of ethanol avoidance. The percentage (%) of ethanol avoidance was

analyzed at the indicated genotypes. Statistical analysis shows comparisons between wild type animals and mutants, and *Pdat-1::α-SYN + Pdat-1::GFP* worms fed either with EV (empty vector) or with the indicated RNAi clones. *cat-2* (e1112) mutant worms were included as positive controls for both assays. Slow response assay and ethanol avoidance behaviors were hampered in *ced-10* depleted animals and not in *ced-10*(n3246) mutants. Data are mean \pm SEM. * $P < 0.05$, ** $P < 0.01$, *** $P < 0.001$, ns non-significant. Statistics: one-way ANOVA, Tukey post hoc test for multiple comparisons. Between 20 and 30 worms were used in three independent replicates

10(n3246) mutant background. To simplify, *ced-10*(n3246) is named *ced-10* from here on.

The basal slowing response is a DA dependent behavior widely used in *C. elegans* for analyzing the functionality of the DA system [30–32]. Briefly, worms decrease locomotion speed when in physical contact with a food source whereas the turn frequency increases when worms leave the food source [31, 33]. The *cat-2* gene encodes the enzyme tyrosine hydroxylase required for the synthesis of dopamine. Accordingly, *cat-2*(e1112) mutant worms have decreased levels of dopamine and altered DA behavior [30, 33] and were used as positive control.

The locomotion speed of the nematodes, represented by the body bends every 20 s, was measured in the absence/presence of bacteria (+/–) (Fig. 1a). In a wild type background (wt background), both wild type and *ced-10* animals decreased the locomotion speed in the presence of food, thus showing unaltered basal slowing response. In contrast, in *cat-2*(e1112) mutants the locomotion speed was not significantly decreased by the presence of food (Fig. 1a wt background, and Table 1). Similarly to

the slow basal response, avoidance against ethanol is a sensory behavior associated with DA signaling [34]. A slight decrease was observed in the ethanol avoidance test performed in *ced-10* mutant animals in a wt background (Fig. 1b wt background and Table 2).

The absence of significant dopaminergic behavioral alterations observed in *ced-10* mutants might be the consequence of compensating mechanisms existing in the worm that mask the effect of *ced-10* function specifically in DAN. To discard any effect of *ced-10* function onto DA responses, *ced-10* was depleted conditionally in DAN by RNAi, in a *C. elegans* PD model in which DAN undergo age-dependent neurodegeneration following human α -SYN overexpression [35]. In this model, animals express both α -SYN and GFP in DAN. Importantly, this is a neuronal-sensitive RNAi strain whereby the impact of RNAi knockdown targeting gene candidates can be selectively examined exclusively in the DAN [36]. To simplify, this strain is called *Pdat-1::α-SYN + Pdat-1::GFP* herein. Animals exposed to *ced-10* RNAi showed a mild but significant altered slow

Table 1 Slow dose response quantifications

Genotype	W/o food (body bends/20 s)	With food (body bends/20 s)	Significance (P value)
Wild type	20.00 \pm 0.423	9.55 \pm 0.328	$P < 0.001$
<i>ced-10</i> (n3246)	19.05 \pm 0.211	13.00 \pm 0.145	$P < 0.001$
<i>cat-2</i> (e1112)	21.00 \pm 0.191	20.00 \pm 0.162	ns
UA196 on EV	18.40 \pm 0.255	9.20 \pm 0.257	$P < 0.001$
UA196 on <i>ced-10</i> RNAi	16.00 \pm 0.254	13.15 \pm 0.392	$P < 0.001$
UA196 on <i>cat-2</i> RNAi	17.25 \pm 0.502	16.40 \pm 0.689	ns

Mean and SEM reported, $n = 20$. One-way ANOVA

Table 2 Ethanol avoidance quantifications

Genotype	Avoidance (% of worms)	N	Significance (P value)
Wild type	71.21 ± 2.120	155	–
<i>ced-10(m3246)</i>	57.80 ± 3.957	94	<i>P</i> < 0.05
<i>cat-2 (e1112)</i>	26.67 ± 3.335	80	<i>P</i> < 0.001
UA196 on EV	70.35 ± 1.213	122	–
UA196 on <i>ced-10</i> RNAi	12.95 ± 1.328	95	<i>P</i> < 0.001
UA196 on <i>cat-2</i> RNAi	10.902 ± 1.524	175	<i>P</i> < 0.001

Mean and SEM reported. One-way ANOVA

response assay (Fig. 1a and Table 1). In addition, selective depletion of *ced-10* in DAN resulted in similar avoidance against ethanol as *cat-2* depleted animals in the ethanol avoidance test (Fig. 1b and Table 2). Therefore, in the presence of α -SYN, *ced-10* function is specifically necessary in *C. elegans* DAN to execute a correct DA behavioral response.

This negative impact of *ced-10* depletion on DAN behavior brought us to explore the relevance of *ced-10* deficiency in DAN cell death in the above mentioned strain *Pdat-1:: α -SYN + Pdat-1::GFP*. There exist four pairs of DAN in *C. elegans* hermaphrodites, three of them (CEPD, CEPV and ADE) located in the anterior part, and one pair, the PDE, located in the posterior part of the nematode [37]. In this nematode, when human α -SYN is expressed in DAN, the six DAN within the anterior region of the worm display progressive degenerative characteristics [38]. To draw parallels between human PD evidenced in aged populations and this worm model, we sought to determine the relevance of *ced-10* depletion at 9 days (L4 + 7) post hatching. Cell bodies and neuronal processes were assessed to determine whether these structures were normal or displayed degenerative changes, and consequently considered wild type neurons (Fig. 2). After feeding worms with EV RNAi, 24.93 ± 2.54% of animals showed the six anterior wild type DAN. In contrast, *ced-10* RNAi knockdown significantly enhanced DA neurodegeneration, 8.33 ± 1.67% of animals showed the intact set of DAN (***P* < 0.001) in comparison with EV control (Fig. 2a, b). Animals expressing the fusion protein, CFP::*CED-10*, under *ced-10* promoter, rescued α -SYN induced-neurodegeneration (***P* < 0.001) (Fig. 2a, b). We found that neurodegeneration was accelerated already at day 3 and 5 (L4 + 1 and L4 + 3, respectively) post hatching (Online Resource 1) thus corroborating the impact of *ced-10* in α -SYN-induced DA cell death at younger ages.

CED-10 Expression Decreases α -SYN Inclusions Formation in *C. elegans*

The term phagocytosis refers also to the mechanism by which certain cells engulf and digest other cells and also larger particles or even anomalous inclusions or aggregates [39, 40].

RAC1/ced-10 is the converging gene of the engulfment machinery mobilizing actin pseudopodia in phagocytic cells [12]. Therefore, we considered the possibility of *ced-10* playing a role in the clearance/phagocytosis of α -SYN inclusions. We used a nematode model of PD, in which human α -SYN is fused to the yellow fluorescent protein (YFP) under control of the body wall muscle *unc-54* promoter, transgene *pkIs2386* [*Punc-54:: α -SYN::YFP*] [41]. With this approach we examined changes in apparent aggregate density or aggregate count of pathogenic α -SYN conjugated to fluorescent YFP in muscle cells [42], without considering neuronal side effects. Accordingly, *ced-10* animals were crossed with *pkIs2386* worms and the number of α -SYN aggregates was evaluated in aged worms at 7 days post hatching. This *ced-10* mutation increased to 1.5 units the apparent density of α -SYN inclusions in comparison to control worms (0.9 ± 0.06 vs. 1.49 ± 0.06 , respectively; ***P* < 0.001) (Fig. 3a, b) thus suggesting a deleterious effect of the *ced-10* mutation in the generation of α -SYN aggregates. Importantly, the increase in α -SYN apparent aggregates was abolished in transgenic *ced-10* mutants expressing the CFP::*CED-10* fusion protein (array *baEx167[Pced-10::CFP::ced-10]*) (0.42 ± 0.03 in worms expressing *CED-10* wild type vs. 1.49 ± 0.06 in *ced-10* mutant worms respectively and Fig. 3a, b, ***P* < 0.001), showing that the lack of *ced-10* is contributing to α -SYN accumulation.

The number of body thrashes or thrashing have been used extensively to identify modifiers of protein aggregation [41, 43]. Thrashing in *C. elegans* can be measured in liquid media by counting the number of body bends per unit of time [44]. Using this method, we confirmed the observed damaged motility (Fig. 3c and Online Resources 2–4) of the PD worms in a *ced-10* background. Whereas a decrease of 27% in the bending are observed in animals expressing YFP:: α -SYN in comparison to the wild type N2 wild type strain (55.01 ± 7.5 vs. 75.96 ± 2.8 bends/min, respectively), the number of bends decreases almost 90% in animals harboring the *ced-10* mutation in a YFP::*SYN* background in comparison with N2 wild type animals (7.93 ± 4.4 vs. 75.96 ± 2.8 bends/min, respectively) and 70% in comparison with worms expressing YFP::*SYN*, without the *ced-10* mutation (7.93 ± 4.4 vs. 55.01 ± 7.5 bends/min, respectively). Thus, increased α -SYN in muscle with its concomitant locomotion decrease in *ced-10* mutants, indicate the involvement of *RAC1/ced-10* in the process of α -SYN accumulation in *C. elegans*.

α -SYN variants that form oligomers and protofibrils are associated to the most severe DAN nigral loss in PD models [1, 6]. To identify the biochemical nature of the apparent α -SYN aggregates increased by this *ced-10* mutation, worm lysates from *pkIs2386* worms without and with the *ced-10* mutation at L4+ 5 days of development, were sequentially extracted by detergent-containing buffers [45] and the amount of α -SYN extracted in each fraction was assessed by immunoblotting (Fig. 3d). A faint band of 19 kDa was detected in

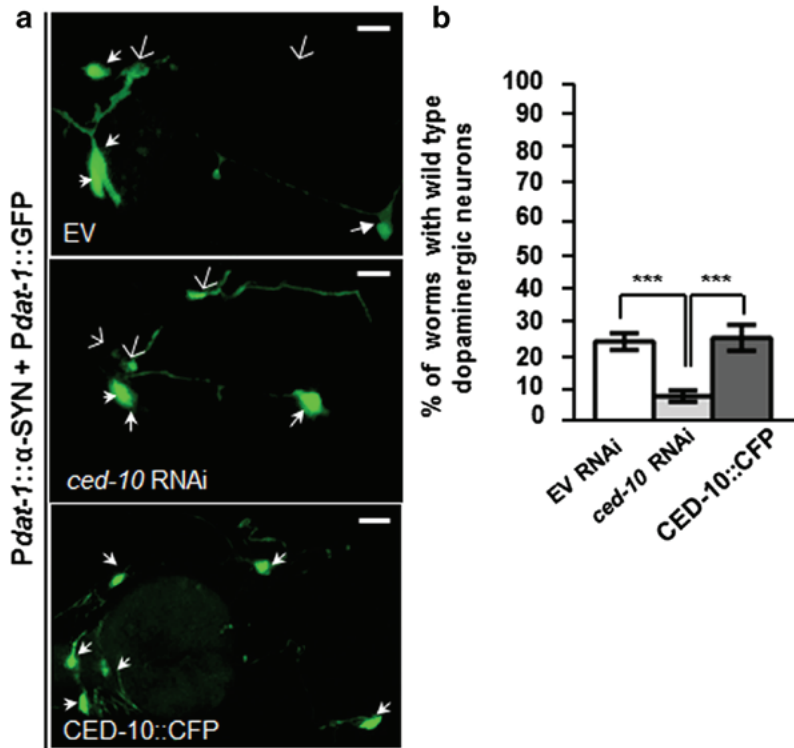


Fig. 2 CED-10 protects DAN from α -SYN-induced DA cell death in *C. elegans*. Representative RNAi empty vector (EV) fed worms expressing GFP and α -SYN specifically in DAN (*Pdat-1::\alpha*-SYN + *Pdat-1::GFP*) at L4 + 7 days (9 days post hatching) and fed with empty vector (EV) or *ced-10* RNAi clones. Filled white arrowhead labels healthy neurons whereas degenerated or missing neurons are labeled with an open arrow. **a** *ced-10* depletion reduces the amount of DAN per worm and the expression of the CED-10::CFP transgene {*baEx167* [*Pced-10::CFP::ced-10*]} delays the DA cell death at the same age. Magnification bar is 30 μ m. **b** Percentage of *Pdat-1::\alpha*-SYN + *Pdat-1::GFP* worms non-depleted and *ced-10*

depleted by RNAi, that had the full complement of six anterior DAN at day 7 post L4. The transgenic derivative strain UA281 expressing CFP::CED-10 (CED-10 wild type), carrying the array *baEx167* [*Pced-10::CFP::ced-10*] ameliorates the DA cell death. Data are mean \pm SEM. Statistics were obtained by comparing *ced-10* RNAi depleted worms or worms containing the CFP::CED-10 array with the corresponding EV fed animals. Statistics: *** P < 0.001, one-way ANOVA, Tukey's post hoc test. Number of animals is 30–35 per condition, and the experiment was repeated three times independently

the Tris-HCl fraction, most probably corresponding to the α -SYN monomer staining. The number of oligomeric species is increased in *ced-10* mutant animals within all analyzed fractions.

Autophagy Is Impaired in *ced-10(n3246)* Mutant Animals

Autophagy is considered one of the main pathways involved in α -SYN clearance [19, 46]. Given the role of *RAC1/ced-10* detected in α -SYN levels and in α -SYN-induced DAN cell death, we further sought to determine the participation of *ced-10* in the modulation of autophagy in *C. elegans*. To this end, we first crossed *ced-10* mutant animals with those carrying the array *adls2122*

[*P**lgg-1::gfp::lgg-1*]. The gene *lgg-1* encodes a ubiquitin-like protein belonging to the Atg8/LC3 protein family, and the respective GFP::LGG-1 translational fusion thus allows to monitor autophagosome formation via fluorescence microscopy [47]. To explore the role of *ced-10* in autophagy, we manually counted the number of GFP::LGG-1 puncta present in the seam cells [48]. At the L3 stage, the number of puncta present in the seam cells were increased in animals harboring the *ced-10* mutation, in comparison to animals without the mutation, in where the GFP::LGG-1 pattern is mainly diffuse (Fig. 4a, b). An increase in the number of GFP::LGG-1 puncta may result from either elevated or impaired autophagic flux [48, 49]. Therefore, we investigated the involvement of *RAC1/ced-10* in autophagic pathways

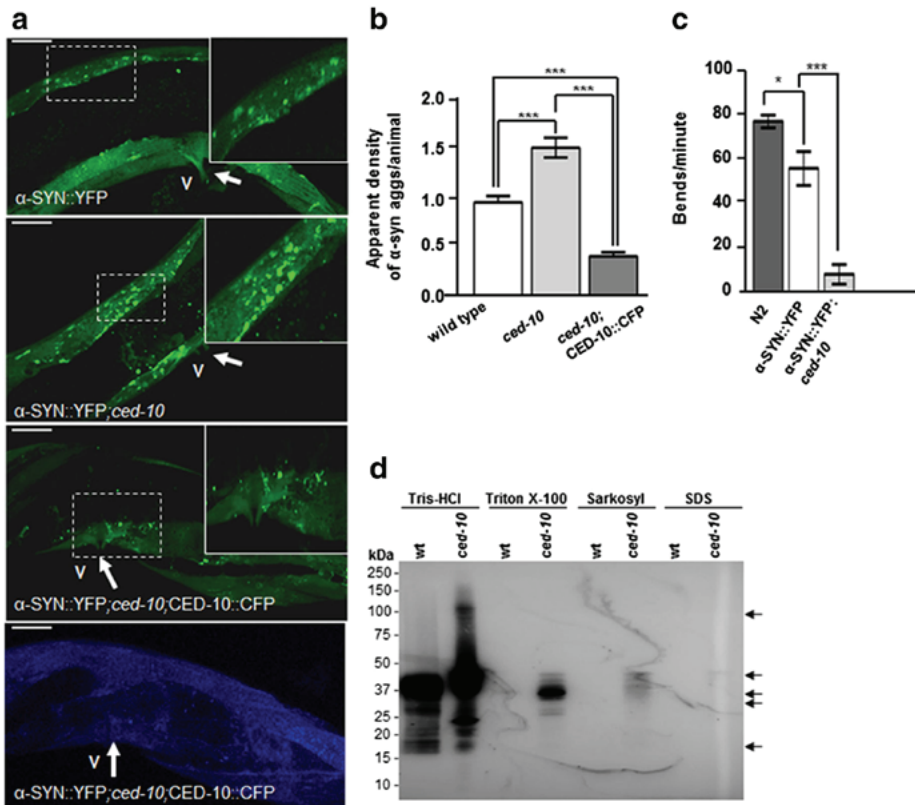


Fig. 3 *ced-10* decreases α -SYN inclusions in *C. elegans*. **a** Representative confocal pictures obtained from animals containing the genomic array *pkIs2386* [*Punc-54:: α -SYN::YFP*] expressing α -SYN in body wall muscle cells at L4 + 5 days of development (7 days post hatching). Green staining in all figures represents α -SYN::YFP inclusions in muscle cells. The vulva (V, thick arrow) was used as a reference to analyze the same central section in all worms. A representative area was highlighted and expanded in each panel, to better visualize the α -SYN::YFP accumulation. **a** (first panel) α -SYN inclusions were detected in a *C. elegans* model of α -SYN miss folding in which α -SYN is expressed under the control of the *unc-54* promoter. **a** (second panel) α -SYN apparent aggregates are increased in *ced-10*(*n3246*) mutant nematodes. **a** (third panel) CFP::CED-10 expression (array *baEx167* [*Pced-10::CFP::CED-10*]) decreased the number of α -SYN inclusions in a *ced-10*(*n3246*) background. **a** (fourth panel) The blue fluorescence marker (CFP) represented the endogenous expression

of CED-10 in a *ced-10*(*n3246*) background for rescuing α -SYN accumulation. Magnification bar is 10 μ m. **b** Quantification of the number of α -SYN inclusions per area. Data are mean \pm SEM. Between 30 and 35 animals were analyzed per genotype. Three different transgenic lines expressing CFP::CED-10 were generated and analyzed independently. Statistics: one-way ANOVA with a Tukey post hoc test. $***P < 0.005$. **c** The movement of YFP:: α -SYN animals is hampered by the mutation *ced-10*(*n3246*). Thrashing behavior (bends/min) was video recorded and the resulting images were analyzed by the ImageJ software. Data are mean \pm SEM. Between 20 and 30 animals were recorded per experiment and the same experiment was repeated 3 independent times. **d** Immunoblotting analysis of protein extracts from 5 days post L4 old YFP:: α -SYN synchronized animals, using anti- α -SYN antibody without and with the *ced-10*(*n3246*) mutation (wild type and *ced-10* respectively). The amount of α -SYN insoluble species was increased by the *ced-10*(*n3246*) mutation.

by analyzing the impact of the *ced-10* mutation in the autophagy-associated reporter strain *bpIs51* [*Psqst-1::sqst-1::gfp* + *unc-76*(+)]. The *C. elegans* SeQueSTosome-related protein, SQST-1, exhibits sequence similarity to mammalian SQSTM1/p62 and is degraded by autophagy [48, 50]. As such, autophagy impairment is often associated with SQST-1::GFP accumulation [48–50]. Similarly to the results obtained with

the GFP::LGG-1 reporter, *ced-10* mutant animals displayed increased SQST-1::GFP internal density (Fig. 4c–e). Whereas SQST-1::GFP staining was barely detected in wild type animals (Fig. 4c, d upper panels, and e), *ced-10* worms displayed SQST-1::GFP accumulation (Fig. 4c, d bottom panels, and e). Cumulatively, these results suggest a role of *RAC1/ced-10* in the regulation of autophagy.

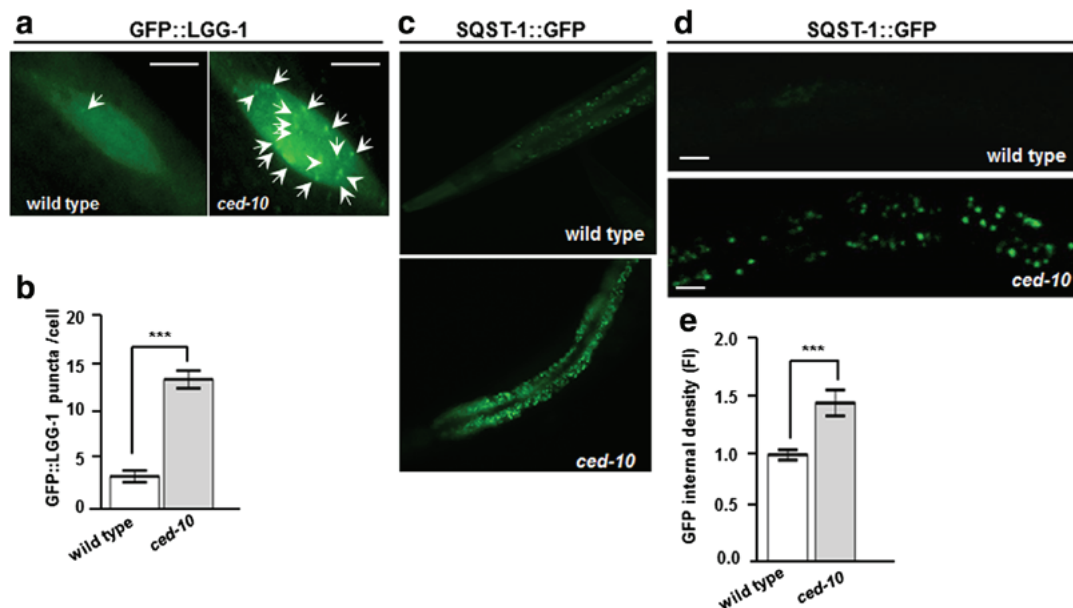


Fig. 4 Autophagic markers accumulate in *ced-10* mutant worms. **a** L4 worms expressing the reporter GFP::LGG-1 (*adIs2122 [P_{lgg-1}::GFP::lgg-1; rol-6(su1006)]*) in hypodermal seam cells, without (left panel, wild type) and with (right panel) the *ced-10(n3246)* mutation. GFP::LGG-1 puncta are labeled with an filled arrow. Magnification bar is 5 μ m. **b** The bar graph indicates the number of GFP::LGG-1 foci per cell at the indicated genotypes. These results are mean \pm SEM of three independent experiments performed in triplicate. Statistics is Student's *t* test. ****P* \leq 0.001. **c, d** Worms expressing the autophagy reporter SQST-1::GFP (*bpls151[P_{sqst-1}::sqst-1::GFP]*) were crossed with *ced-10(3246)* animals and the GFP fluorescence intensity (FI) was analyzed under a

fluorescence (**c**) or a confocal (**d**) microscope. **d** (upper panel) L4 animals expressing the array SQST-1::GFP without induction of the GFP reporter in normal conditions. **d** (bottom panel) The *ced-10(n3246)* mutation increased GFP intensity and aggregation. Magnification bar is 20 μ m. **e** Normalized fluorescence intensity (FI) observed in SQST-1::GFP animals without and with the *ced-10(n3246)* mutation. Thirty animals were analyzed per genotype. Data are represented as the mean \pm SEM and were obtained by comparing wild type animals (without the *ced-10(n3246)* mutation) with *ced-10* mutated animals. Statistics, ****P* $<$ 0.001, Student's *t* test

Human RAC1 Expression Reduces α -SYN Accumulation and Amyloidogenic Aggregation in a Neuroblastoma Cell Line

We further explored the effect of *RAC1* on α -SYN accumulation using a stable BE(2)-M17 neuroblastoma cell line over-expressing wild type α -SYN. As previously reported [51], differentiation with retinoic acid (RA) and treatment with the histone deacetylases inhibitor sodium butyrate (SB) increased α -SYN expression by twofold and induced the accumulation of small α -SYN cytoplasmic aggregates (Online Resource 5a–b). Differentiated cells treated with SB were transduced with a lentiviral vector (LV) expressing either RAC1 wild type (WT)-GFP (in which RAC1-GTP and RAC1-GDP coexist) or RAC1 constitutively active (CA)-GFP (only expressing RAC1-GTP) and analyzed 4 days post-transduction, using the empty vector (Control-GFP) as a control. Infection with both, RAC1 (WT) and RAC1 (CA) decreased α -SYN expression level (Online Resource 5b) and

aggregation, as shown by Thioflavin S (ThyoS) dye (Fig. 5), which specifically stains cross-beta sheet fibrils, such those forming amyloid aggregates [52]. The area covered by ThyoS -positive α -SYN aggregates per cell was decreased by 90% in RAC1(WT) and RAC1(CA) infected cultures (Fig. 5) thus suggesting a role of RAC1 in either the formation or clearance of toxic α -SYN species and corroborating the data obtained by western blot in the nematode.

High RAC1 Activity Reduces α -SYN Levels and Increases Neurite Arborization in PD Patient-Specific Midbrain iPSC-Derived DAN

Lastly, to connect the nematode data with the human PD, we differentiated DAN upon cell reprogramming of skin fibroblasts into induced pluripotent stem cells (iPSC) from PD patients carrying the G2019S (G/S) mutation in the *LRRK2* gene. While preserving the patient genetic background, this model exhibits some characteristic

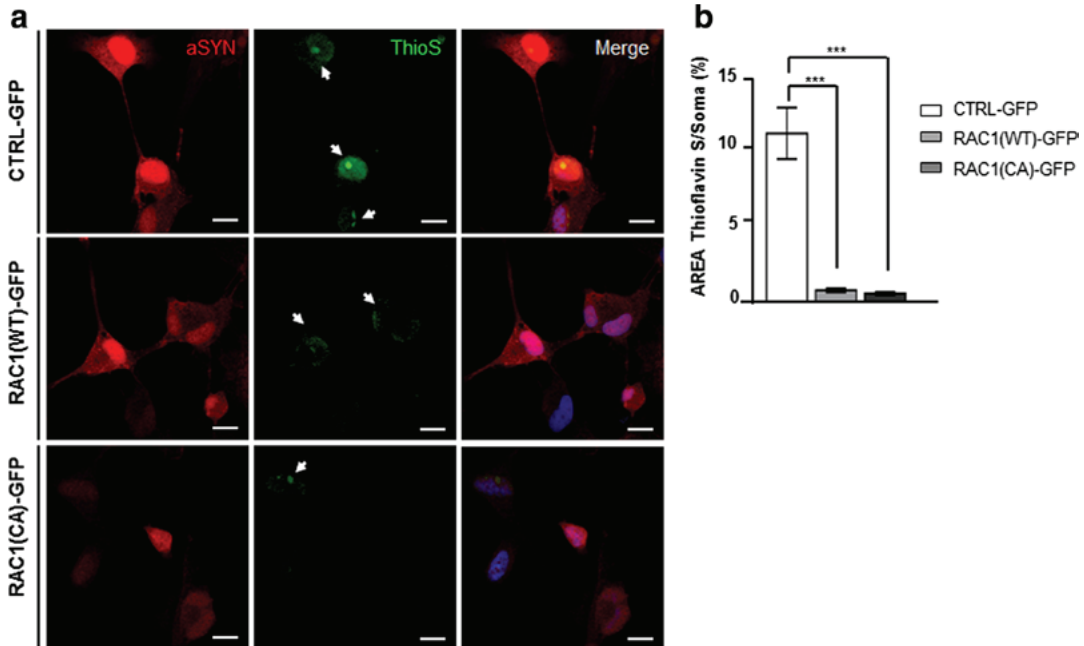


Fig. 5 Rac1 activity decreases α -SYN accumulation and aggregation in the neuroblastoma cell line BE(2)-M17. **a** Representative confocal images of α -SYN over-expressing cells induced with 10 μ M retinoic acid (RA) and treated with 10 mM sodium butyrate (SB) for 36 h. Cells were transduced with Control-GFP (upper row), RAC1 (WT)-GFP (middle row) and RAC1 (CA)-GFP (bottom row), and co-stained for Thioflavin S (green) and α -SYN (red). Arrows indicate Thioflavin S positive aggregates with

amyloid structure. **b** Bar graph showing the quantitative analyses of the neuronal soma area (in percentage %) covered by Thioflavin S positive stain in individual cells transduced with (WT)- or (CA) RAC1 or with the corresponding control. $N = 14$ (EV), $N = 25$ (WT), and $N = 24$ (CA), from at least three independent experiments. Data are presented as mean \pm SEM. Statistics, $***P < 0.001$, one-way ANOVA with Bartlett's test correction followed by post hoc Tukey test. Scale bars represent 10 μ m

features and cellular phenotypes of PD including reduced axonal outgrowth, α -SYN accumulation, α -SYN-induced DAN cell death, and impaired autophagy [20]. Therefore, it represents a suitable tool to contextualize and compare the nematode encountered data.

At 30 days of differentiation, patient iPSC-derived DAN do not show overt morphological signs of neurodegeneration [20]. However, almost 40% of DAN positive for the DA marker tyrosine hydroxylase (TH) showed detectable amounts of α -SYN [20]. For this reason, and to explore early events affecting PD, we next investigated the contribution of RAC1 in PD by rescuing α -SYN accumulation in DAN. For this purpose, PD-iPSC-derived midbrain DAN (at 30 days of differentiation when α -SYN accumulation is already evident), were transduced with lentivirus (LV) expressing either RAC1 wild type (RAC1 (WT)-GFP) or a highly active form of RAC1 (RAC1 (CA)-GFP), and LV-GFP as control (Control-GFP) (Online Resource 6a, c and d), and analyzed 7 days after transduction. We found that LRRK2-PD-derived DAN, transduced with Control-GFP showed significant

increase in α -SYN content in comparison with non-PD-derived DAN (Fig. 6a, first and second panels, and scatter dot plot) confirming previous results [20]. A 18% decrease in α -SYN accumulation was observed in PD-derived cells infected with RAC1 (WT)-GFP, and it was even stronger (48.15%) in PD-derived cells infected with RAC1 (CA)-GFP (Fig. 6a, third and fourth panels, and scatter dot plot, $***P < 0.001$). By analyzing the number and length of neurites, to explore the capacity of Rac1 in rescuing neuronal degeneration (Online Resource 7), we found a decrease in neurite arborization in PD-derived DAN (Fig. 6b), confirming previous reports showing reduction in neurite length/branching and defects of Rac signaling in LRRK2-associated parkinsonism [53]. Importantly, overexpression of RAC1 (CA)-GFP, but not RAC1 (WT)-GFP, was associated with significant increase of neurite arborization (Fig. 6b, fourth panel and left graph), consistent with a role for RAC1 in organizing the actin cytoskeleton [58]. The neurite length was not rescued in any of the conditions tested (Fig. 6b, right graph).

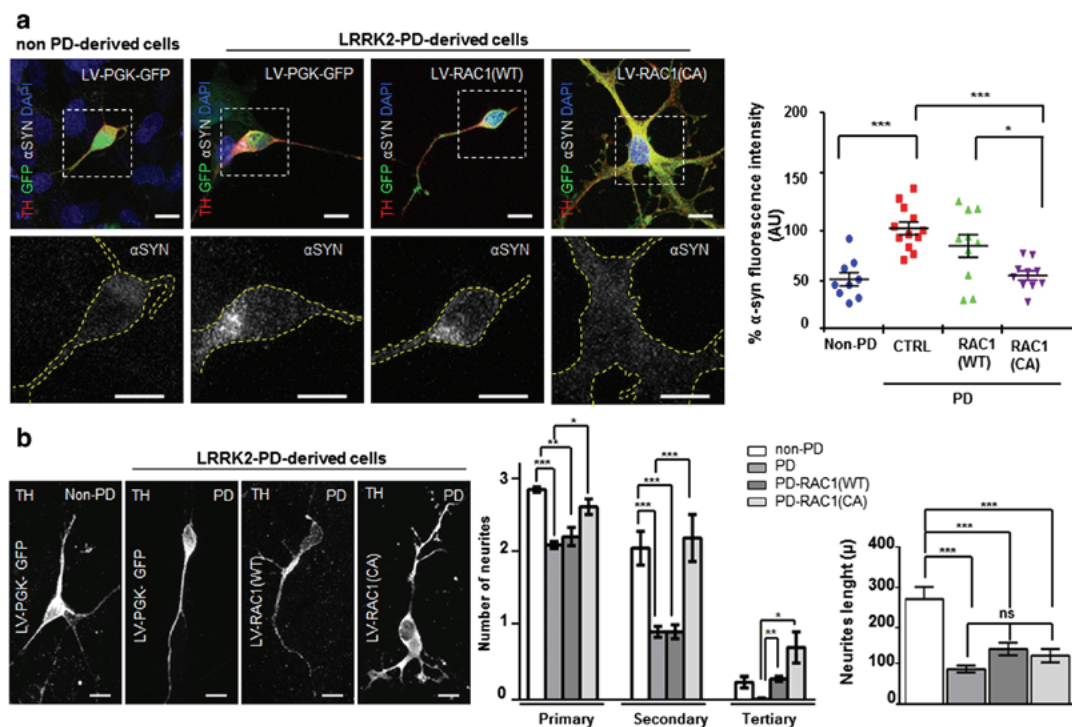


Fig. 6 Rac1 activity rescues α -SYN accumulation and neurite degeneration in early LRRK2-PD-derived DA cells. **a** First row shows confocal images of non-PD (first panel) and LRRK2-PD-iPSC-derived DAN (second, third, and fourth panels) at 30 days of differentiation transduced with Control-GFP (first and second panels), RAC1 (WT)-GFP (third panel) and RAC1 (CA)-GFP (fourth panel), and co-stained for GFP (green), Tyrosine hydroxylase (TH) (red) and α -SYN (gray). Nuclei are counterstained with DAPI, shown in blue. Second row shows confocal images representing the expanded pictures of the corresponding above neurons highlighted within the white dashed square, evidencing α -SYN staining. Dot plot shows the quantification of the average (in %) of α -SYN fluorescent intensity in every analyzed neuron positive for TH and GFP. Statistical analysis is the result of comparing α -SYN staining intensity of non-PD with LV-transduced DAN. Data is the average of at least two-independent experiments and are presented as mean \pm SEM. Statistics is one-way ANOVA with a Tukey's post hoc analysis $**P < 0.01$. **b** Representative confocal

micrographs of single DAN derived from non-PD (first panel) and LRRK2-2PD patients, transfected with Control-GFP (second panel), RAC1 (WT)-GFP (third panel) or RAC1 (CA)-GFP (fourth panel). Extension bars are 10 μ m. (Left graph) This bar graph represents the number of neurites per neuron (primary, secondary and tertiary), according to the indicated transduction, in non-PD and in PD-derived cells. Statistical analysis is the result of comparing neurite number non-PD with LRRK2-PD-derived DA cells transduced with RAC1 (WT)-GFP or RAC1 (CA)-GFP. Data is the average of at least two-independent experiments and are presented as mean \pm SEM. Statistics is One-way ANOVA, $*P < 0.05$ and $**P < 0.01$. (Right graph) Quantitative analyses of the neurite length (in μ m) in DAN derived from non-PD and LRRK2-PD-derived patients. Statistical analysis is the result of comparing neurite number non-PD with LRRK2-PD-derived DA cells transduced with RAC1 (WT)-GFP or RAC1 (CA)-GFP. Data are presented as mean \pm SEM. Statistics is one-way ANOVA. $***P < 0.001$

By transcriptome analysis we have previously reported that iPSC-derived DAN from PD patients exhibited a large number of gene expression changes. More specifically, we identified 437 differentially expressed genes (DEGs) in PD vs. controls of which 254 were up-regulated in PD patients and 183 were down-regulated [54]. Here, to gain further insight into the canonical pathways affected by differential gene expression detected at early PD, we performed a biological enrichment analysis at 30 days of differentiation, by using the software and databases of Ingenuity Pathway Analysis (IPA). We found that the signaling by Rho family GTPases pathway was the

top-1 statistically most significant canonical pathway in PD patients compared to controls ($P = 2.56 \times 10^{-4}$) (Online Resource 8). From the total of 245 members comprised in this pathway, 16 DEGs of which 9 genes were up-regulated and 7 down-regulated in PD DAN (Online Resource 9). Interestingly, the top 2 statistically most significant canonical pathway was the related Rho GDI pathway ($P = 7.91 \times 10^{-4}$). Overall, the results from this unbiased biological enrichment analysis identifies Rho family GTPases as top deregulated canonical pathway in iPSC-derived DAN from PD patients.

RAC1 Activity Increases the Long-Term Survival of PD-Patient-Derived DAN and Alleviates the Impairment of Autophagy

To assess whether the protective effect of RAC1 in reducing α -SYN levels correlated with increased survival rates over time, neurons were further cultured for 75 days (Online Resource 6b) by co-culturing them over a monolayer of mouse post-natal cortical astrocytes [55], which supported viable cultures of DAN for up to 75 days [20].

After this time span, differentiated cultures from genetic LRRK2-PD-patient derived DAN showed higher numbers of apoptotic DAN when compared to those derived from healthy subjects [20] and Fig. 7(a, b, and e). Overexpression of both RAC1 (CA)-GFP and RAC1 (WT)-GFP prevented cell death by reducing the amount of DAN positively stained for cleaved caspase-3 to the levels of the non-PD-patient-derived DA cells (Fig. 7(c–d and e)). We and others have described that LRRK2 G2019S mutation has negative effects in the autophagic flux by seemingly impairing autophagosome-lysosome fusion [20]. In this specific case, RAC1 CA (RAC1-(CA) but not RAC1 wild type (RAC1-(WT) displayed autophagosome vesicle numbers similar to those of the non-PD-patient-derived neurons (Fig. 7). Therefore, these results suggest a mechanism by which a better performance of the autophagic clearance promoted by RAC1 alleviates the accumulation of aggregation-prone proteins, such as α -SYN, thus contributing to increase the survival of DAN.

In conclusion, these results obtained in DAN derived from LRRK2-associated PD patients are in line with findings in the nematode models of PD, where RAC1 activity is directly involved with DAN survival in the presence of α -SYN, α -SYN inclusions formation and autophagic mechanisms.

Discussion

Here, we demonstrate in *C. elegans* and in human-derived PD cells that *RAC1/ced-10* participates in the main pathogenic manifestations of PD such as DAN death, α -SYN accumulation and impaired autophagy. Besides, the results obtained in the nematode, suggest a role of *ced-10* modulating DA behavior in the presence of α -SYN. Furthermore, *RAC1* function is associated with the considered toxic α -SYN species. Overall, in this manuscript we propose *RAC1/ced-10* as a potential therapeutic target for the treatment of PD-related disorders.

RAC1/ced-10 and DAN Death

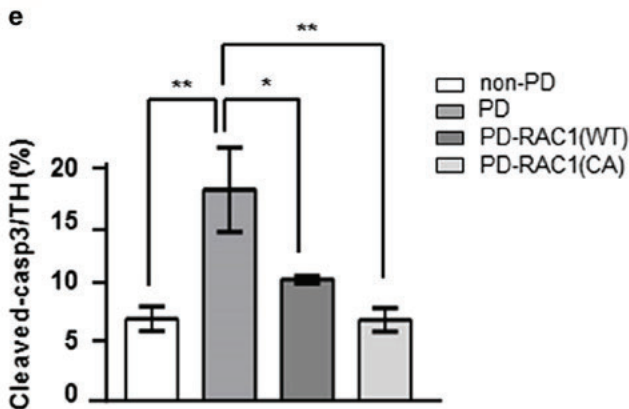
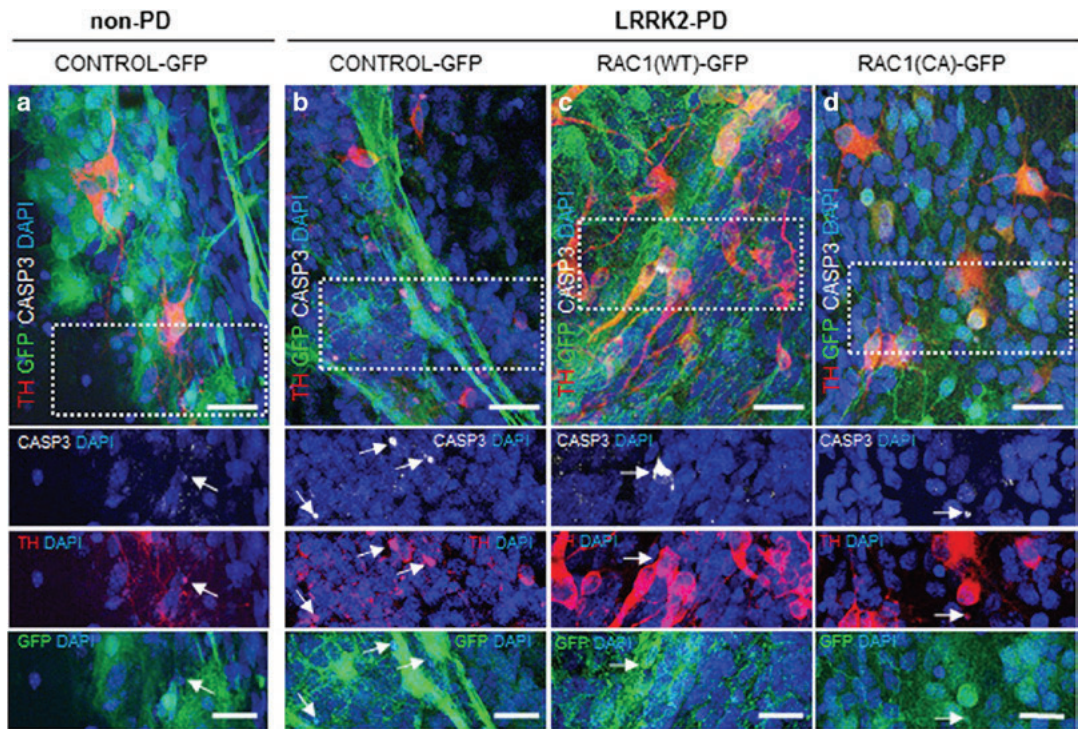
Previous research has shown that Rac GTPases play an essential neuroprotective and pro-survival role in neuronal models and diseases [17, 56–58]. Indeed, our in depth analysis of the RAC1 signaling pathway arose from the transcriptomic data in human

Fig. 7 RAC1 activity increases the long-term survival of PD-derived DAN and alleviates autophagy impairment. (A–D) Confocal images of non-PD (A) and PD-iPSC-derived DA cultures transduced with Control-GFP (B), RAC1 (WT)-GFP (C), and RAC1 (CA)-GFP (D), stained for GFP (green), TH (red) and cleaved Caspase-3 (white). A representative area was highlighted in dashed lines and expanded in below panels. The corresponding lower insets show higher magnification images of each separate channel, cleaved caspase-3, TH and RAC1-GFP respectively. TH+ neurons, stained with Caspase-3 and transduced with RAC1-GFP constructs are labeled with white arrow tips. Caspase-3 positive nuclei are counterstained with DAPI, shown in blue. PD-derived cells transduced with Control-GFP (second panel) showed increased numbers of triple positive TH/GFP/Caspase 3 staining in TH+ neurons in comparison to the other conditions tested, where cells were non-PD (first panel left) or transduced with RAC1 (WT)-GFP and RAC1 (CA)-GFP (third and fourth panels respectively). Extension bar from A–D is 20 and 10 μ m for top and bottom panels respectively. **e** Bar graph showing the quantification of the number of TH/GFP double-positive neurons presenting cleaved Caspase-3 staining. Data is the average of at least two independent experiments and are presented as mean \pm SEM. Statistics, * P < 0.05, ** P < 0.01, and *** P < 0.001, Two-way ANOVA, Tukey post hoc test. **f** Confocal images of non-PD (left panel) and PD-iPSC-derived DA cultures transduced with Control-GFP (second row), RAC1 (WT)-GFP (third row), and RAC1 (CA)-GFP (fourth row), stained for GFP (green), TH (red) and LC3 (gray). Non-PD cells (first row) and PD cells transduced with RAC1 (CA)-GFP (fourth row) showed similar amount of LC3-II positive vesicles in TH+/GFP+ neurons. Nuclei are counterstained with DAPI, shown in blue. Extension bar is 5 μ m. **g** Bar graph showing the quantification of the neuronal soma area (in percentage %) covered by LC3-II positive vesicles in at least 15 DA neurons. Data is the average of at least two independent experiments and are presented as mean \pm SEM. Statistics, * P < 0.05, Two-way ANOVA, post hoc Tukey test

iPSC-derived DAN from PD patients, showing altered Rho signaling as top deregulated pathway, points to this same direction (Online Resources 8–9). However, Rac GTPases modulation in different cell types is much more complex. Loss of Rac GTPase activity may contribute to the death of DAN while increased Rac-GTP activity in microglia may contribute to the formation of toxic ROS [59]. Hence, this complicated RAC1 modulation depending upon the tissue and the ROS state, might explain the behavioral differences observed between whole *ced-10* mutant animals and *RAC1/ced-10* specifically depleted in DAN in the presence of α -SYN (Fig. 1). Interestingly, a cell non-autonomous function for hypodermal *RAC1/ced-10* in the maintenance of axonal survival has been recently proposed in *C. elegans* [60]. Consequently, the influence of RAC1 activity in the neighboring tissues cannot be obviated.

There exist positive correlation between neuronal apoptosis and decreased RAC1 GTPase activity [17]. Very different cellular models, such as human lymphoma cells or primary cerebellar granule neurons, suggest the inhibition of caspase-induced apoptosis by RAC1, whereby AKT-dependent pro-survival pathways and the consequent Bcl-2-associated death protein (BAD) phosphorylation were downstream and activated by RAC1 [59, 61].

The activation of the AKT by RAC1, also participates in the cytoskeleton reorganization and cellular growth [62, 63]



and a failure to maintain the integrity of DAN after they are formed could cause DAN death [64]. Accordingly, RAC1-modulated processes involved in the maintenance of cell integrity, might be crucial for cell survival.

LRRK2-PD-patient-derived DAN show increased neurite numbers after being transduced with RAC1 (Fig. 6), thus expanding the role of this GTPase in the maintenance and in the generation of new neurites [13], and thus contributing accordingly to DAN survival (Fig. 7). Therefore, our results

are in accordance with LRRK2 inducing neurite retraction through diminished RAC1 GTPase activity [16]. Surprisingly, neurite length was not rescued with any of the infected RAC1 constructs in the present manuscript. Differences between results can be explained based on the different cellular models used in both laboratories, since our results are provided directly from PD-derived cells, whereas the neuroblastoma cell line SHSY5Y is the model used by Chan et al. [16]. In addition, the existing actin-microtubule

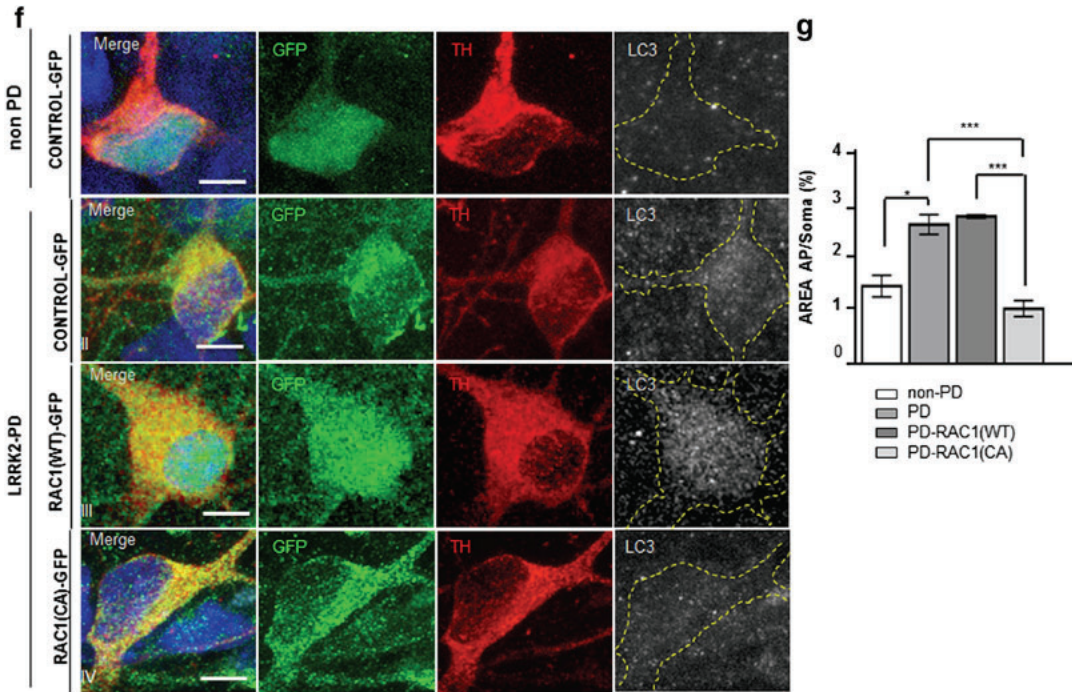


Fig. 7 (continued)

cross talk in the process of neurite outgrowth and elongation has to be considered [65, 66]. Microtubules are the main cytoskeletal components of neurites [66] and decreased stability of microtubules is a common feature of neurodegenerative diseases [67]. Interestingly, LRRK2-PD variants are characterized by defects in microtubule associated processes [68] and LRRK2 regulates microtubule stability [69]. However, extension and navigation of neurites are normally driven by actin-rich growth cones and inhibition of microtubules dynamics does not stop neurite outgrowth [66]. Thus, our results are consistent with cellular dysfunction in PD, with RAC1 modulating actin-associated mechanisms better than in microtubule linked processes.

RAC1/*ced-10* and α -SYN Accumulation

One of the main factors linked with DAN death in PD progression is α -SYN accumulation. α -SYN overexpression in model systems, and its concomitant aggregation and deposition precede neuronal cell death. In the case of DAN, its degeneration is influenced by intracellular and extracellular α -SYN accumulation, mainly in its oligomeric form [70]. Interestingly, extracellular oligomeric α -SYN impairs RAC1 activity in neuroblastoma cells [70]. Considering the increased intracellular α -SYN

aggregates together with increased oligomeric α -SYN species observed in *ced-10* mutant animals, we hypothesize that altered RAC1/*ced-10* function might accelerate α -SYN accumulation and the formation of α -SYN oligomers which might bind concurrently RAC1/*ced-10* [70] thus increasing the severity of RAC1/*ced-10* altered function. Moreover, and considering the modulation of the actin cytoskeletal dynamics by α -SYN [71], a synergistic regulation between RAC1 and α -SYN cannot be excluded.

Additional experiments, where the amount of α -SYN could be tightly controlled, will provide some clues about the relevance of RAC1/ α -SYN interaction in the progress of PD.

α -SYN accumulation in PD patients is associated with failure of the two major protein breakdown pathways, the ubiquitin proteasome system (UPS) and autophagy [72–74], which, in cooperation, reduce the misfolded protein burden [75]. Stably increased levels of α -SYN can lead to impaired proteasome function [76] and *ced-10* is proteasome regulated in the phagocytosis of dead cells [14]. Hence, we hypothesize that increased α -SYN in a *ced-10* mutant background might reinforce the severity of the *ced-10* mutation in the degradation of α -SYN, due to the interaction of α -SYN with the proteasomal machinery.

Overexpression of α -SYN results in the inhibition of autophagy [77]. Here we suggest *RAC1/ced-10* being necessary for autophagy to occur (Figs. 3 and 7). Accordingly, α -SYN accumulation, due to *ced-10* impairment, might increase the severity of *ced-10* mutation. Therefore we add RAC1 to the already proposed feedback loop between proteasome activity and autophagy [1] and we propose that a tight regulation of RAC1 function is required to avoid excess of α -SYN accumulation and the concomitant cell death.

Impaired autophagy associated with LRRK2 mutations are already reported [78, 79], with the G2019S mutation showing less autophagic activity [80]. In the context of LRRK-2 induced phenotypes, we propose RAC1-LRRK2 interaction as relevant factor favoring autophagy to occur, and helping in the clearance of α -SYN aggregates, thus warranting the proper neurite growth and maintenance.

Future scientific research is needed to unravel the mechanisms associated with PD-related disorders for finding efficient therapies. In light of our results the pharmacological modulation of RAC1 and RAC1-derived signaling pathways could be of therapeutic value.

Experimental Procedures

Worm Experiments

C. elegans Strains

Nematodes were maintained using standard procedures [81]. We obtained the strains CB1112 *cat-2(e1112)*, NL5901, *unc-119(ed3) III*; [*pkIs2386 (Punc-54:: α -SYN::YFP; unc-119(+))*]; DA2123 *adIs2122* [*Plgg-1::lgg-1::GFP; rol-6(su1006)*] and HZ589, *bpIs151* [*Psqst-1::sqst-1::GFP; unc-76(+)*] *IV*; *him-5(e1490) V* from the *Caenorhabditis elegans* Genetic Center (CGC). The strain BR3579, *ced-10(n3246)* was a generous gift from Dr. Ralf Baumeister (Albert-Ludwing University, Freiburg/Breisgau, Germany).

The strain BR3579 was crossed with NL5901 animals to generate the strain EDC101, *unc-119(ed3) III*; [*pkIs2386 (Punc-54:: α -SYN::YFP; unc-119(+))*]; *ced-10(n3246)*.

The following strains is used to analyze the DAN degeneration as reported in Harrington et al., 2010 [36]: *Pdat-1:: α -SYN +Pdat-1::GFP* from the main text is named UA196, with the genotype: *sid-1(pk3321); baln33 [Pdat-1::sid-1; Pmyo-2::mCherry]; baln11 [Pdat-1:: α -SYN; Pdat-1::GFP]*.

For autophagy experiments, males from the DA2123 strain [*Plgg-1::lgg-1::GFP; rol-6(su1006)*] were crossed with *ced-10(n3246)* hermaphrodites. Males from the HZ589 *bpIs151* [*Psqst-1::sqst-1::GFP; unc-76(+)*] *IV*; *him-5(e1490) V*] strain, expressing SQST-1::GFP crossed with *ced-10(n3246)* hermaphrodites.

N2 (Bristol) was used as the *C. elegans* wild-type (wt) strain. Hermaphrodites were used throughout of the study.

RNAi Feeding

For feeding RNAi bacteria, egg lay from gravid adults were directly transferred to NGM plates containing 1 mM of isopropyl β -D-1-thiogalactopyranoside/ IPTG (referred to as RNAi plates) seeded with 20X concentrated bacteria containing 50 μ g/ml ampicillin, carrying desired plasmid for RNAi of a specific gene (*ced-10* or *cat-1*, depending upon the experiment) or bacteria carrying empty (EV) pL4440 as control and allowed to grow on plates for approximately 50 h to reach the L4 stage and then another 16 h for the conduction of actual experiment.

Note: Bacterial clones for RNAi feeding protocol were obtained from the Ahringer library (Source Bioscience, Nottingham, UK) [82] and were then streaked on LB-Tetracycline-Ampicillin plate which was then incubated at 37 °C. Individual colonies from this freshly streaked plate were grown for 10–12 h constantly shaking at 37 °C in LB medium containing 50 μ g/ml ampicillin.

Blinding of Experiments and Replicates

All behavioral studies were completed such that the experimenter was blind to the genotype of the worms. Strains were given letter codes by another member of the laboratory and the code was not broken until all of the replicates for a particular assay were completed. For all assays, we completed a minimum of three biological replicates per strain.

Behavioral Experiments

Locomotor Rate Assay Locomotor rate assay was performed as described in [33]. Briefly, assay plates were prepared by spreading the *E. coli* strain OP50-1 in a ring on NGM agar [81] in 5-cm petri plates. Assay plates were always freshly spread with bacteria, incubated overnight at 37 °C, and allowed to cool to room temperature before use. Plates for measuring locomotor rate in the absence of bacteria were also incubated at 37 °C. Only synchronized young adult hermaphrodites (16 h after the late L4 larval stage) were tested. For well-fed animals, locomotor rate was measured by removing 5 animals from plates with ample bacteria, washing the animals twice in S basal buffer [81], and transferring them to an assay plate in a drop of buffer using a capillary pipette. The drop of buffer used to transfer the animals was absorbed with a Kimwipe. Five minutes after transfer, the number of body bends in 20 s intervals was sequentially counted for each of

the five animals on the assay plate and then repeated the same thing for next set of animals in a different assay plate.

Ethanol Avoidance Assay Ethanol avoidance assay was performed as described [34] (Cooper et al. 2015). Synchronized young adult hermaphrodites (16 h after the late L4 larval stage) were transferred to assay plates, which are divided into four quadrants: two quadrants seeded with 50 μ l of 100% ethanol and the others without. Worms are placed in the center of the assay plate and allowed to move for 30 min at which point the entire plate is imaged and the worms are scored for their quadrant of preference. Ethanol avoidance is calculated as [(number of worms in control quadrants) – (number of worms in ethanol quadrants)]/total number of worms.

Generation of the Rescue Construct *Pced-10::CFP::ced-10* *Pced-10::CFP::ced-10* plasmids were co-injected into worm strain EDC101 and UA196 to generate UA281, *baEx167* [*Pced-10::CFP::ced-10, rol-6(su1006)*]; [*Punc-54:: α -SYN::YFP;ced-10(n3246)*] and UA282, *baEx167* [*Pced-10::CFP::ced-10; rol-6(su1006)*]; *sid-1(pk3321)*; *baln33* [*Pdat-1::sid-1, Pmyo-2::mCherry*]; *baln11* [*Pdat-1:: α -SYN; Pdat-1::GFP*]). Hermaphrodites were used throughout of the study.

Site-Directed Mutagenesis The construct *Pced-10::GFP::ced-10* was provided by Erik Lundquist (University of Kansas, Lawrence, KS, USA) as a gift. TagMaster Site-directed mutagenesis (GM Biosciences, Rockville, USA) was used to create mutations (Y66W, Y145F, and M153T) in GFP sequence for changing fluorescence marker as CFP. The product plasmid *Pced-10::CFP::ced-10* was sequenced (Eurofins Genomics, Huntsville, AL, USA) to confirm the presence of the desired mutations.

***C. elegans* Neurodegeneration Assays** Worms were analyzed for DA neurodegeneration as described previously [38]. Briefly, 10 L1-stage worms (neuron-specific RNAi worm strain with α -Syn UA196 were transferred to the plates (empty vector (EV) and *ced-10* RNAi) and grown at 20 °C until adulthood. Adult worms were then transferred to corresponding freshly made RNAi plates and allowed to lay eggs for 6 h to synchronize. α -SYN-induced DA neurodegeneration was scored at the indicated days after hatching (L4 + 7; L4 + 3; L4 + 1). To investigate the effect of CED-10 overexpression on α -SYN-induced DA degeneration, the strain UA282 was analyzed at L4 + 7 days of aging. Worms were considered normal when all six anterior DA neurons (four CEP (cephalic) and two ADE (anterior deirid)) were present without any visible signs of degeneration. If a worm displayed degeneration in at least one of the six neurons, it was scored as exhibiting degeneration. In total, at least 50 adult worms

were analyzed for each independent transgenic line or RNAi treatment.

Aggregate Quantification The quantification of aggregates was performed as previously described [83]. Briefly, NL5901 animals without and with *ced-10(n3246)* mutation, together with the EDC101, were age-synchronized by bleaching with NaOCl and left overnight to hatch. L1 animals were transferred onto individual NGM plates seeded with *Escherichia coli*. Aggregates were counted for each animal staged at L4 + 5 days. Images were captured using a Leica SP5 confocal microscope with a \times 40 oil immersion lens (HCX PL APO CS). The number of α -syn aggregates was determined in the mid body of each animal, taking the vulva position (V) as a reference. Aggregates were defined as discrete, bright structures, with boundaries distinguishable from surrounding fluorescence. Measurements on inclusions were performed using ImageJ software taking into consideration the area dimensions.

Thrashing Assays At L4 + 5 days, animals from the strains N2 wild type, NL5901 [*unc-119(ed3) III; pklIs2386*] [*Punc-54:: α -SYN::YFP; unc-119(+)*] and EDC01 *unc-119(ed3) III; pklIs2386* [*Punc-54:: α -SYN::YFP; unc-119(+)*]; *ced-10(n3246)* were placed in a drop of M9 buffer and allowed to recover for 120 s (to avoid observing behavior associated with stress) after which the number of body bends was counted for 1 min. Movies of swimming worms were recorded using a Leica MZFFLIII stereomicroscope at nominal magnification of 30X and the Hamamatsu ORCA-Flash 4.0LT camera at 17 frames per second (17 fps) for 1 min. Bends per minute were obtained with the Worm Tracker plugin (wrMTrack), from the ImageJ software [84]. Thirty animals were counted in each experiment unless stated otherwise. Experiments were carried out in triplicate. Statistical analysis was performed using Graphpad Prism version 6.00 for Windows, GraphPad Software, La Jolla, CA, USA).

Detergent Fractionation α -SYN oligomeric species were isolated by detergent fractionation as described (Kuwahara et al. 2012) with slight modifications. Briefly, worms were washed three times with M9 buffer, collected as a 100 μ l pellet, and the pellet was snap-frozen in liquid nitrogen. The pellets were homogenized in 1 mL of 50 mM Tris-HCl buffer at pH 7.5 with complete protease inhibitor mixture (Roche Applied Science) by brief sonication. Sonicates were centrifuged two times at 1000 \times g for 5 min to remove debris of worm tissue. The supernatant was then ultracentrifuged at 350,000 \times g for 15 min, and the supernatant was collected as a Tris-HCl soluble fraction. The resulting pellet was subsequently extracted by sonication in 500 μ l of Triton X-100 (Tris-HCl buffer with 1% TritonX-100), 200 μ l of Sarkosyl (Tris-HCl with 1% Sarkosyl), and 100 μ l of SDS (TrisHCl with SDS sample

buffer containing 2% SDS) followed by centrifugation at $350,000\times g$ for 15 min. The Tris-HCl fraction containing 20 μg of total proteins, along with equal volumes of Triton X-100, Sarkosyl, and SDS fractions to the Tris-HCl fraction, were loaded onto the acrylamide gel and separated by SDS-PAGE.

Immunoblotting Twenty microliters of protein per strain were loaded from each sample and fraction on Novex NuPAGE 4–12% Bis-Tris Gels (Thermo Fisher) and run in MES SDS buffer at 200 V for 40 min. Resolved proteins were transferred onto 0.45 μm nitrocellulose membranes (Amersham) at 200 mA for 1 h. Blocking was done in 5% milk powder in PBS for 1 h, followed by overnight incubation at 4 °C with a mouse monoclonal antibody against α -synuclein (1:1000, BD Biosciences, #610787) diluted in 2% bovine serum albumin (BSA)/PBS. Incubation with a donkey anti-mouse (1:5000, Amersham) secondary antibody diluted in 1% milk powder/PBS was performed for 1 h at room temperature.

Membranes were developed using Supersignal West Femto (Thermo Scientific) in a ImageQuant RT ECL Imager (GE Healthcare).

Autophagy Measurements For measuring the involvement of *ced-10(n3246)* mutation in autophagy, we followed specific *C. elegans* protocols [48, 85]. LGG-1::GFP foci were analyzed in the hypodermal seam cells at L3 stage of development. Images were not considered for quantification where the hypodermis was not clear. In total, at least 40 total regions were quantified from 30 different worm samples per genotype.

To confirm the involvement of *ced-10* in impairing autophagy, we followed the protocol described in [86]. Pictures of L1 animals (whole animal) and L4 animals (whole intestine), were analyzed by using a 63 \times objective. The GFP internal intensity (FI), corresponding to SQST-GFP foci, was quantified at L4 stage of development. The presence of the *ced-10* mutation was checked by PCR as described [14]. The presence of the GFP reporter was double checked by PCR using the *gfp* primers, and under the fluorescence microscope.

Microscopy and Imaging For neurodegeneration assays and aggregates quantification animals were mounted with a coverslip on a 4% agarose pad in M9, containing 10 mM of sodium azide. Confocal microscopy was performed using a Leica TCS-SP5 confocal spectral microscope (Leica, Barcelona, Spain) and analyzed using ImageJ software (NIH, ver. 1.43, Schindelin, 2015). Animals were examined at 100 \times magnification to examine α -SYN induced DA cell death and at 40X to examine α -SYN apparent aggregates.

For autophagy measurements, animals were placed in a 5 μL drop of 10 mM solution of levamisole (Sigma-Aldrich, Madrid, Spain). For each independent experiment, between

20 and 30 7-day-old worms of each treatment were examined under a Nikon EclipseTE2000-E epifluorescence microscope equipped with a monochrome camera (Hamamatsu ORCA-ER) coupled to the Metamorph software (Molecular Devices Corp., Sunnyvale, CA). The system acquires a series of frames at specific Z-axis position (focal plane) using a Z-axis motor device.

Cell Culture Experiments in BE(2)-M17 Neuroblastoma Cell Line

Cell Culture

Human neuroblastoma cell line BE(2)-M17 over-expressing wild type α -SYN were maintained at 37 °C and 5% CO₂ in OptiMem medium (Gibco) (Thermo-Fisher Scientific, Madrid, Spain) supplemented with 10% fetal bovine serum (Gibco) (Thermo-Fisher Scientific, Madrid, Spain), 500 $\mu\text{g}/\text{ml}$ G418 (Geneticin) (Sigma-Aldrich, Madrid, Spain) and Penicillin/Streptomycin (Sigma-Aldrich, Madrid, Spain). For immunofluorescence, 2×10^4 cells/well were seeded in 24-well plates on coverslips coated with poly-D-lysine. α -SYN aggregation was induced as previously reported ([51] by differentiation with 10 μM retinoic acid (Sigma-Aldrich, Madrid, Spain) for 10 days, followed by treatment with the histone deacetylases inhibitor sodium butyrate (SB) (Sigma-Aldrich, Madrid, Spain) at a concentration of 10 mM for 36 h. To analyze the effect of RAC1 on α -SYN aggregation, cells were transduced 24 h before SB treatment with either the lentiviral empty vector or with the wild type or the constitutively active isoforms of RAC1 at an estimated multiplicity of infection (MOI) of 5.

Immunofluorescence

BE(2)-M17 cells were fixed in 4% paraformaldehyde (PFA) (Sigma-Aldrich, Madrid, Spain) in phosphate saline buffer (PBS) for 30 min at 4 °C and permeabilized with Tris-buffered saline (TBS) containing 0.5% Triton X-100 (Sigma-Aldrich, Madrid, Spain) for 5 min. Cells were then blocked with 3% normal goat serum (NGS) (Vector Laboratories, Palex Medical, Sant Cugat del Vallès, Spain) in TBS for 1 h and subsequently incubated with the corresponding primary antibody in 1%NGS/TBS overnight at 4 °C. The following primary antibodies were used: mouse anti- α -SYN (610,787; 1:500) (BD Biosciences, Madrid, Spain), rabbit anti- α -SYN (2642; 1:500) (Cell Signaling, Leiden, The Netherlands). Incubation with goat secondary antibodies conjugated with Alexa488 (anti-mouse, A11001; or Alexa594 (anti-mouse, A11005; anti-rabbit, A11012) (Thermo-Fisher Scientific, Madrid, Spain) was done in 1% NGS/TBS for 1 h at RT. Between each incubation period cells were rinsed three times in TBS.

Thioflavin S Staining

After incubation with the antibodies, coverslips were immersed in 0.005% thioflavin S (Sigma-Aldrich, Madrid, Spain) in PBS for 8 min and then rinsed twice in ethanol 70% and once in PBS. Only after thioflavin S staining, nuclei were counterstained with Hoechst 33342 (Thermo Fisher Scientific, Madrid, Spain, 1:10,000 in PBS) for 10 min.

Microscopy and IF Quantification

Cells were cover slipped using Dako Cytomation Fluorescent Mounting Medium (Dako, Sant Just Desvern, Spain). Immunofluorescence images were acquired using standard filter sets using an Olympus FluoView TM FV1000 confocal microscope and the FV10_ASW 4.2 visualization software.

α -SYN fluorescence intensity for each condition was analyzed in an average of 150 cells from 6 different random fields at an objective magnification of 40 \times . Quantification of Thioflavin S positive aggregates in each condition was analyzed in an average of 20 cells from 3 different random fields by measuring the fluorescent area per cell. All quantification analyses were done using ImageJ software (NIH, USA).

Cell Culture Experiments with iPSC Cell Lines Derived from Human Patients

Previously generated iPSC lines SP-11.1 (from control) and SP-12.3 (from patients with familial PD with the LRRK2 G2019S mutation) were used and culture and differentiation were carried out as described, (34), following a protocol approved by the Spanish competent authorities (Commission on Guarantees concerning the Donation and Use of Human Tissues and Cells of the Carlos III Health Institute). Briefly, hiPSC were cultured on matrigel (Corning Limited, Life Sciences, UK) and maintained in hESC medium, consisting on KO-DMEM (Invitrogen, Thermo Fisher Scientific, Madrid, Spain) supplemented with 20% KO-Serum Replacement (Invitrogen, Thermo Fisher Scientific, Madrid, Spain), 2 mM Glutamax (Invitrogen, Thermo Fisher Scientific, Madrid, Spain), 50 μ M 2-mercaptoethanol (Invitrogen, Thermo Fisher Scientific, Madrid, Spain), non-essential aminoacids (Cambrex, Nottingham, UK) and 10 ng/ml bFGF (Peprotech, London, UK). Medium was preconditioned overnight by irradiated mouse embryonic fibroblast and hiPSC were maintained on Matrigel (Corning Limited, Life Sciences, UK) at 37 $^{\circ}$ C, 5% CO₂.

For DAN differentiation, iPSC were transduced with LV.NES.LMX1A.GFP and processed as previously described (79). Briefly, confluent iPSC 10 cm dishes were disaggregated with accutase and embryoid bodies (EB) were generated using forced aggregation method in V-shaped 96 well plates. Two days later, EBs were patterned as ventral midbrain by

culturing them in suspension for 10 days in N2B27 supplemented with 100 ng/ml SHH (Peprotech, London, UK), 100 ng/ml FGF8 (Peprotech, London, UK) and 10 ng/ml FGF2 (Peprotech, London, UK). Then, for α -SYN and neurite analysis, differentiation to midbrain DAN was performed on the top of PA6 murine stromal cells for 3 weeks (79). To analyze α -SYN levels, neuronal cultures were gently trypsinized and re-plated in matrigel-coated slides for 3 days, then transduced with the two different RAC1 isoforms or the control LV, at an estimated MOI of 10. Cells were fixed and analyzed 7 days after transduction. For long-term culture studies, EBs were mechanically dissociated by repeated pipetting after the induction step. Salient EB fragments were transduced with the two different RAC1 isoforms or the control LV at an estimated MOI of 3. Three days post-transduction, the aggregates were seeded on primary murine astrocytes and cultured for 9 weeks.

Lentiviral Vectors

RAC1 wild type (WT) and constitutively active (V12) (CA) forms were amplified by means of PCR from expression plasmids kindly provided by (Dr Francisco Sánchez-Madrid; Spanish National Center for Cardiovascular Research (CNIC), Madrid, Spain). Subsequently, RAC1-(WT) and RAC1-(CA) cDNA were cloned under the human phosphoglycerate kinase (PGK) promoter of pCCL.cPPT-hPGK-IRES.eGFP-WPRE lentiviral transfer vector. High-titer vesicular stomatitis virus (VSV)-pseudotyped LV stocks were produced in 293T cells by calcium phosphate-mediated transient transfection of the transfer vector, the late generation packaging construct pMDL, and the VSV envelope-expressing construct pMD2.G, and purified by ultracentrifugation as previously described [87]. Expression titers, determined on HeLa cells by fluorescence-activated cell sorter (FACS) analysis (FACSCalibur, Becton Dickinson), were as follows: LV-RAC1 (WT): $2.60 \cdot 10^8$ TU/mL; LV-RAC1 (CA): $2.24 \cdot 10^8$ TU/mL; LV-PGK-GFP: $5.08 \cdot 10^9$ TU/mL.

Immunofluorescence for iPSC-Derived Cells

iPSC-derived cells were fixed with 4% paraformaldehyde (PFA) in Tris-buffered saline (TBS) buffer for 20 min and blocked in 0.3% Triton X-100 (Sigma-Aldrich, Madrid, Spain) with 3% donkey serum for 2 h. In the case of α -SYN and LC3 staining, Triton X-100 was kept at 0.01% for the blocking and antibody incubation steps. The following primary antibodies were used: mouse anti- α -SYN (610787; 1:500) (BD Biosciences, Madrid, Spain), rabbit anti-TH (sc-14007; 1:500) (Santa Cruz Biotechnology, Madrid, Spain), chicken anti-GFP (1020; 1:250) from Aves Labs (Cosmo Bio, AbBcn S.L., Bellaterra, Spain), rabbit anti-cleaved Caspase3 (9664; 1:400) (Cell Signaling) and LC3B (2775; 1:100) (Cell

Signaling). Images were acquired using a Leica SP5 confocal microscope.

α -SYN and Neurite Analysis

α -SYN and neurite analysis were performed after a total of 4 weeks of differentiation plus 1 week after LV transduction on iPSC-derived DA neurons. DA neurons were randomly selected, using a Leica SP5 confocal microscope, and analyzed with ImageJ for α -SYN intensity levels and with the ImageJ plugin NeuronJ to determine the number of neurites per cell, number of terminals and branch points.

Cleaved Caspase-3, Apoptotic Cell Number and Autophagosome Accumulation and Analysis

Cleaved caspase-3, apoptotic cell number and autophagosome accumulation analysis were performed after a total of 9 weeks of differentiation on iPSC-derived DAn grown on murine astrocytes. DA neurons were randomly selected, using a Leica SP5 confocal microscope, and analyzed with ImageJ to determine the fraction of the neuronal soma area stained by cleaved caspase-3 or covered by LC3-positive particles.

Statistical Analysis

All experiments were performed at least three independent times. All data are presented as mean \pm SEM. Group means were compared with either the Student's *t* test or ANOVA. All *P* values were two tailed, and a *P* value of less than 0.05 was considered statistically significant. All statistical analyses were analyzed using GraphPad Prism (San Diego, CA, USA) software.

Outlier values were identified with the Grubbs' tests and excluded from the analysis.

Differences among means were analyzed either by 1- or 2-way analysis of variance (ANOVA), as appropriate, using the post hoc Tukey's multiple comparison test. In all cases, the null hypothesis was rejected at the 0.05 level.

Biological Enrichment Analysis

Transcriptomic analysis of iPSC-derived DAn from PD patients ($n = 10$) and healthy controls ($n = 4$) was done as previously described [54]. Identified differentially expressed genes (DEGs) after multiple testing adjustment of *P* values ($n = 437$) were subjected to biological enrichment analysis. To this end, we used the Core Analysis module of the Ingenuity® Pathway Analysis (IPA) software (Qiagen, Redwood City, www.qiagen.com/ingenuity) to identify biological enrichment of canonical pathways deregulated in iPSC-derived DAn from PD patients. More specifically, we used the Ingenuity Knowledge Base of Genes, and considered only direct

molecules and/or relationships for humans. Statistical significance of canonical pathways was computed by using the Fischer's exact test and significance levels were set at *P* below 0.05. Using IPA we also calculated Z-score values which consider the directional effect of one molecule on another molecule or on a process, and also the direction of change of molecules in the dataset and provide predictions about whether the pathway is predicted to be activated or inhibited, or if the pathway is ineligible for such an assessment.

Acknowledgements The genetic strain BR3579 was kindly provided by Dr. Ralf Baumeister (Albert-Ludwing University, Freiburg/Brigsgau, Germany). Plasmids Rac1-GFP WT and Rac1-GFP (CA) HYM772 were kindly provided by Dr. Francisco Sánchez-Madrid (Spanish National Center for Cardiovascular Research (CNIC), Madrid, Spain). The construct *Pced-10::CFP::CED-10* was a generous gift provided by Erik Lundquist (University of Kansas, Lawrence, KS, USA). Human neuroblastoma cell line BE(2)-M17 over-expressing wild type α -SYN was provided by Dr. B. Wolozin (Boston University School of Medicine).

Funding This work was supported by the following grants: Instituto de Salud Carlos III (PI15/01255), co-funded by European Union (ERDF/ESF, "investing in your future"; Spanish Ministry of Economy and Competitiveness (MINECO) (BFU2015-64408-P) and the Instituto de Salud Carlos III (PI11/00072, co-financed by the Fondo Social Europeo) to AMV; Spanish Ministry of Economy and Competitiveness (MINECO) (SAF2016-77541-R) to MV; (SAF2015-69706-R) and Instituto de Salud Carlos III (ISCIII)/FEDER (Red de Terapia Celular-TerCel RD16/0011/0024) to AR; and (BFU2016-80870-P) to AC. This work was also supported by the European Research Council (ERC) 2012-StG (311736-PD-HUMMODEL) to AC. The authors also thank the CERCA Program from the Generalitat de Catalunya and AGAUR (2014-SGR-1460). ED and AV are members of the GENIE and EU-ROS Cost Action of the European Union. CC was partially supported by pre-doctoral fellowships from the Spanish Ministry of Education-MEC (FPU12/03332).

ED and AV are members of the GENIE and EU-ROS Cost Action of the European Union.

Compliance with Ethical Standards All experiments were performed under the guidelines and protocols of the Ethical Committee for Animal Experimentation (CEEA) of the University of Barcelona. All procedures adhered to internal and EU guidelines for research involving derivation of pluripotent cell lines. All subjects gave informed consent for the study using forms approved by the Ethical Committee on the Use of Human Subjects in Research at Hospital Clinic in Barcelona, Spain. Generation of iPSC lines was approved by the Advisory Committee for Human Tissue and Cell Donation and Use, by the Commission on Guarantees concerning the Donation and Use of Human Tissues and Cells of the Carlos III Health Institute, Madrid, Spain. All procedures were done in accordance with institutional guidelines following the Spanish legislation.

Conflict of Interest The authors declare that they have no conflict of interest.

Open Access This article is distributed under the terms of the Creative Commons Attribution 4.0 International License (<http://creativecommons.org/licenses/by/4.0/>), which permits use, duplication, adaptation, distribution and reproduction in any medium or format, as long as you give appropriate credit to the original author(s) and the source, provide a link to the Creative Commons license, and indicate if changes were made.

References

- Michel PP, Hirsch EC, Hunot S (2016) Understanding dopaminergic cell death pathways in Parkinson disease. *Neuron* 90(4):675–691. <https://doi.org/10.1016/j.neuron.2016.03.038>
- Dehay B, Bourdenx M, Gorry P, Przedborski S, Vila M, Hunot S, Singleton A, Olanow CW et al (2015) Targeting α -synuclein for treatment of Parkinson's disease: mechanistic and therapeutic considerations. *Lancet Neurol* 14(8):855–866. [https://doi.org/10.1016/S1474-4422\(15\)00006-X](https://doi.org/10.1016/S1474-4422(15)00006-X)
- Weinreb PH, Zhen W, Poon AW, Conway KA, Lansbury PT (1996) NACP, a protein implicated in Alzheimer's disease and learning, is natively unfolded. *Biochemistry* 35(43):13709–13715. <https://doi.org/10.1021/bi961799n>
- Iwai A, Masliah E, Yoshimoto M, Ge N, Flanagan L, Rohan de Silva HA, Kittel A, Saitoh T (1995) The precursor protein of non-A beta component of Alzheimer's disease amyloid is a presynaptic protein of the central nervous system. *Neuron* 14(2):467–475. [https://doi.org/10.1016/0896-6273\(95\)90302-X](https://doi.org/10.1016/0896-6273(95)90302-X)
- Wong YC, Krainc D (2017) α -synuclein toxicity in neurodegeneration: mechanism and therapeutic strategies. *Nat Med* 23(2):1–13. <https://doi.org/10.1038/nm.4269>
- Winner B, Jappelli R, Maji SK, Desplats PA, Boyer L, Aigner S, Hetzer C, Lohr T et al (2011) In vivo demonstration that alpha-synuclein oligomers are toxic. *Proc Natl Acad Sci U S A* 108(10):4194–4199. <https://doi.org/10.1073/pnas.1100976108>
- Hall A, Lalli G (2010) Rho and Ras GTPases in axon growth, guidance, and branching. *Cold Spring Harb Perspect Biol* 2(2):a001818. <https://doi.org/10.1101/cshperspect.a001818>
- Musilli M, Ciotti MT, Pieri M, Martino A, Borrelli S, Dinallo V, Diana G (2016) Therapeutic effects of the Rho GTPase modulator CNF1 in a model of Parkinson's disease. *Neuropharmacology* 109:357–365. <https://doi.org/10.1016/j.neuropharm.2016.06.016>
- Schnack C, Danzer KM, Hengerer B, Gillardon F (2008) Protein array analysis of oligomerization-induced changes in alpha-synuclein protein-protein interactions points to an interference with Cdc42 effector proteins. *Neuroscience* 154(4):1450–1457. <https://doi.org/10.1016/j.neuroscience.2008.02.049>
- Koch JC, Bitow F, Haack J, d'Hedouville Z, Zhang JN, Tönges L, Michel U, Oliveira LMA et al (2015) Alpha-Synuclein affects neurite morphology, autophagy, vesicle transport and axonal degeneration in CNS neurons. *Cell Death Dis* 6(7):e1811. <https://doi.org/10.1038/ctd.2015.169>
- Prots I, Veber V, Brey S, Campioni S, Buder K, Riek R, Böhm KJ, Winner B (2013) α -Synuclein oligomers impair neuronal microtubule-kinesin interplay. *J Biol Chem* 288(30):21742–21754. <https://doi.org/10.1074/jbc.M113.451815>
- Kinchen JM, Cabello J, Klingele D, Wong K, Feichtinger R, Schnabel H, Schnabel R, Hengartner MO (2005) Two pathways converge at CED-10 to mediate actin rearrangement and corpse removal in *C. elegans*. *Nature* 434(7029):93–99. <https://doi.org/10.1038/nature03263>
- Hou ST, Jiang SX, Smith RA (2008) Permissive and repulsive cues and signalling pathways of axonal outgrowth and regeneration. *Int Rev Cell Mol Biol* 267:125–181. [https://doi.org/10.1016/S1937-6448\(08\)00603-5](https://doi.org/10.1016/S1937-6448(08)00603-5)
- Cabello J et al (2014) PDR-1/hParkin negatively regulates the phagocytosis of apoptotic cell corpses in *Caenorhabditis elegans*. *Cell Death Dis* 5
- Paisán-Ruiz C et al (2004) Cloning of the gene containing mutations that cause PARK8-linked Parkinson's disease. *Neuron* 44(4):595–600. <https://doi.org/10.1016/j.neuron.2004.10.023>
- Chan D, Citro A, Cordy JM, Shen GC, Wolozin B (2011) Rac1 protein rescues neurite retraction caused by G2019S leucine-rich repeat kinase 2 (LRRK2). *J Biol Chem* 286(18):16140–16149. <https://doi.org/10.1074/jbc.M111.234005>
- Pesaresi MG, Amori I, Giorgi C, Ferri A, Fiorenza P, Gabanella F, Salvatore AM, Giorgio M et al (2011) Mitochondrial redox signaling by p66Shc mediates ALS-like disease through Rac1 inactivation. *Hum Mol Genet* 20(21):4196–4208. <https://doi.org/10.1093/hmg/ddr347>
- Philippens IH et al (2013) Oral treatment with the NADPH oxidase antagonist apocynin mitigates clinical and pathological features of parkinsonism in the MPTP marmoset model. *J NeuroImmune Pharmacol* 8(3):715–726. <https://doi.org/10.1007/s11481-013-9450-z>
- Vogiatzi T, Xilouri M, Vekrellis K, Stefanis L (2008) Wild type alpha-synuclein is degraded by chaperone-mediated autophagy and macroautophagy in neuronal cells. *J Biol Chem* 283(35):23542–23556. <https://doi.org/10.1074/jbc.M801992200>
- Sánchez-Dañés A, Richaud-Patin Y, Carballo-Carbajal I, Jiménez-Delgado S, Caig C, Mora S, di Guglielmo C, Ezquerro M et al (2012) Disease-specific phenotypes in dopamine neurons from human iPSC-based models of genetic and sporadic Parkinson's disease. *EMBO Mol Med* 4(5):380–395. <https://doi.org/10.1002/emmm.201200215>
- Zavodszky E et al (2014) Mutation in VPS35 associated with Parkinson's disease impairs WASH complex association and inhibits autophagy. *Nat Commun* 5:3828
- Huang Y, Chegini F, Chua G, Murphy K, Gai W, Halliday GM (2012) Macroautophagy in sporadic and the genetic form of Parkinson's disease with the A53T α -synuclein mutation. *Transl Neurodegener* 1(1):2. <https://doi.org/10.1186/2047-9158-1-2>
- Ramirez A, Heimbach A, Gründemann J, Stiller B, Hampshire D, Cid LP, Goebel I, Mubaidin AF et al (2006) Hereditary parkinsonism with dementia is caused by mutations in ATP13A2, encoding a lysosomal type 5 P-type ATPase. *Nat Genet* 38(10):1184–1191. <https://doi.org/10.1038/ng1884>
- Schapira AH (2015) *Glucocerebrosidase and Parkinson disease: recent advances*. *Mol Cell Neurosci* 66(Pt A):37–42
- Qu X, Zou Z, Sun Q, Luby-Phelps K, Cheng P, Hogan RN, Gilpin C, Levine B (2007) Autophagy gene-dependent clearance of apoptotic cells during embryonic development. *Cell* 128(5):931–946. <https://doi.org/10.1016/j.cell.2006.12.044>
- Li W, Zou W, Yang Y, Chai Y, Chen B, Cheng S, Tian D, Wang X et al (2012) Autophagy genes function sequentially to promote apoptotic cell corpse degradation in the engulfing cell. *J Cell Biol* 197(1):27–35. <https://doi.org/10.1083/jcb.201111053>
- Cheng S, Wu Y, Lu Q, Yan J, Zhang H, Wang X (2013) Autophagy genes coordinate with the class II PI3K/Akt/mTOR pathway to regulate apoptotic cell clearance in *C. elegans*. *Autophagy* 9(12):2022–2032. <https://doi.org/10.4161/auto.26323>
- Reddien PW, Horvitz HR (2000) CED-2/CrkII and CED-10/Rac control phagocytosis and cell migration in *Caenorhabditis elegans*. *Nat Cell Biol* 2(3):131–136. <https://doi.org/10.1038/35004000>
- Shakir MA, Gill JS, Lundquist EA (2006) Interactions of UNC-34 enabled with Rac GTPases and the NIK kinase MIG-15 in *Caenorhabditis elegans* axon pathfinding and neuronal migration. *Genetics* 172(2):893–913. <https://doi.org/10.1534/genetics.105.046359>
- Ezcurra M, Tanizawa Y, Swoboda P, Schafer WR (2011) Food sensitizes *C. elegans* avoidance behaviours through acute dopamine signalling. *EMBO J* 30(6):1110–1122. <https://doi.org/10.1038/emboj.2011.22>
- Hills T, Brockie PJ, Maricq AV (2004) Dopamine and glutamate control area-restricted search behavior in *Caenorhabditis elegans*. *J Neurosci* 24(5):1217–1225. <https://doi.org/10.1523/JNEUROSCI.1569-03.2004>
- Sanyal S, Wintle RF, Kindt KS, Nuttley WM, Arvan R, Fitzmaurice P, Bigras E, Merz DC et al (2004) Dopamine modulates the

- plasticity of mechanosensory responses in *Caenorhabditis elegans*. *EMBO J* 23(2):473–482. <https://doi.org/10.1038/sj.emboj.7600057>
33. Sawin ER, Ranganathan R, Horvitz HR (2000) *C. elegans* locomotory rate is modulated by the environment through a dopaminergic pathway and by experience through a serotonergic pathway. *Neuron* 26(3):619–631. [https://doi.org/10.1016/S0896-6273\(00\)81199-X](https://doi.org/10.1016/S0896-6273(00)81199-X)
 34. Lee J, Jee C, McIntire SL (2009) Ethanol preference in *C. elegans*. *Genes Brain Behav* 8(6):578–585. <https://doi.org/10.1111/j.1601-183X.2009.00513.x>
 35. Hamamichi S, Rivas RN, Knight AL, Cao S, Caldwell KA, Caldwell GA (2008) Hypothesis-based RNAi screening identifies neuroprotective genes in a Parkinson's disease model. *Proc Natl Acad Sci U S A* 105(2):728–733. <https://doi.org/10.1073/pnas.0711018105>
 36. Harrington AJ, Hamamichi S, Caldwell GA, Caldwell KA (2010) *C. elegans* as a model organism to investigate molecular pathways involved with Parkinson's disease. *Dev Dyn* 239(5):1282–1295. <https://doi.org/10.1002/dvdy.22231>
 37. Sulston J, Dew M, Brenner S (1975) Dopaminergic neurons in the nematode *Caenorhabditis elegans*. *J Comp Neurol* 163(2):215–226. <https://doi.org/10.1002/cne.901630207>
 38. Cao S, Gelwix CC, Caldwell KA, Caldwell GA (2005) Torsin-mediated protection from cellular stress in the dopaminergic neurons of *Caenorhabditis elegans*. *J Neurosci* 25(15):3801–3812. <https://doi.org/10.1523/JNEUROSCI.5157-04.2005>
 39. Hochreiter-Hufford A, Ravichandran KS (2013) Clearing the dead: apoptotic cell sensing, recognition, engulfment, and digestion. *Cold Spring Harb Perspect Biol* 5(1):a008748. <https://doi.org/10.1101/cshperspect.a008748>
 40. Oczypok EA, Oury TD, Chu CT (2013) It's a cell-eat-cell world: *autophagy and phagocytosis*. *Am J Pathol* 182(3):612–622. <https://doi.org/10.1016/j.ajpath.2012.12.017>
 41. van Ham TJ, Thijssen KL, Breiting R, Hofstra RM, Plasterk RH, Nollen EA (2008) *C. elegans* model identifies genetic modifiers of alpha-synuclein inclusion formation during aging. *PLoS Genet* 4(3):e1000027. <https://doi.org/10.1371/journal.pgen.1000027>
 42. Martinez BA, Kim H, Ray A, Caldwell GA, Caldwell KA (2015) A bacterial metabolite induces glutathione-tractable proteostatic damage, proteasomal disturbances, and PINK1-dependent autophagy in *C. elegans*. *Cell Death Dis* 6(10):e1908. <https://doi.org/10.1038/cddis.2015.270>
 43. van der Goot AT, Zhu W, Vazquez-Manrique RP, Seinstra RI, Dettmer K, Michels H, Farina F, Krijnen J et al (2012) Delaying aging and the aging-associated decline in protein homeostasis by inhibition of tryptophan degradation. *Proc Natl Acad Sci U S A* 109(37):14912–14917. <https://doi.org/10.1073/pnas.1203083109>
 44. Gidalevitz T, Krupinski T, Garcia S, Morimoto RI (2009) Destabilizing protein polymorphisms in the genetic background direct phenotypic expression of mutant SOD1 toxicity. *PLoS Genet* 5(3):e1000399. <https://doi.org/10.1371/journal.pgen.1000399>
 45. Kuwahara T, Tonegawa R, Ito G, Mitani S, Iwatsubo T (2012) Phosphorylation of alpha-synuclein protein at Ser-129 reduces neuronal dysfunction by lowering its membrane binding property in *Caenorhabditis elegans*. *J Biol Chem* 287(10):7098–7109. <https://doi.org/10.1074/jbc.M111.237131>
 46. Cuervo AM, Stefanis L, Fredenburg R, Lansbury PT, Sulzer D (2004) Impaired degradation of mutant alpha-synuclein by chaperone-mediated autophagy. *Science* 305(5688):1292–1295. <https://doi.org/10.1126/science.1101738>
 47. Büttner S, Broeskamp F, Sommer C, Markaki M, Habernig L, Alavian-Ghavanini A, Carmona-Gutierrez D, Eisenberg T et al (2014) Spermidine protects against alpha-synuclein neurotoxicity. *Cell Cycle* 13(24):3903–3908. <https://doi.org/10.4161/15384101.2014.973309>
 48. Zhang H, Chang JT, Guo B, Hansen M, Jia K, Kovács AL, Kumsta C, Lapiere LR et al (2015) Guidelines for monitoring autophagy in *Caenorhabditis elegans*. *Autophagy* 11(1):9–27. <https://doi.org/10.1080/15548627.2014.1003478>
 49. Guo B, Huang X, Zhang P, Qi L, Liang Q, Zhang X, Huang J, Fang B et al (2014) Genome-wide screen identifies signaling pathways that regulate autophagy during *Caenorhabditis elegans* development. *EMBO Rep* 15(6):705–713. <https://doi.org/10.1002/embr.201338310>
 50. Tian Y, Li Z, Hu W, Ren H, Tian E, Zhao Y, Lu Q, Huang X et al (2010) *C. elegans* screen identifies autophagy genes specific to multicellular organisms. *Cell* 141(6):1042–1055. <https://doi.org/10.1016/j.cell.2010.04.034>
 51. Jiang P, Gan M, Ebrahim A, Lin WL, Melrose HL, Yen SHC (2010) ER stress response plays an important role in aggregation of alpha-synuclein. *Mol Neurodegener* 5(1):56. <https://doi.org/10.1186/1750-1326-5-56>
 52. Raiss CC, Braun TS, Konings IBM, Grabmayr H, Hassink GC, Sidhu A, le Feber J, Bausch AR et al (2016) Functionally different alpha-synuclein inclusions yield insight into Parkinson's disease pathology. *Sci Rep* 6(1):23116. <https://doi.org/10.1038/srep23116>
 53. MacLeod D, Dowman J, Hammond R, Leete T, Inoue K, Abeliovich A (2006) The familial parkinsonism gene LRRK2 regulates neurite process morphology. *Neuron* 52(4):587–593. <https://doi.org/10.1016/j.neuron.2006.10.008>
 54. Fernández-Santiago R et al (2015) Aberrant epigenome in iPSC-derived dopaminergic neurons from Parkinson's disease patients. *EMBO Mol Med* 7(12):1529–1546. <https://doi.org/10.15252/emmm.201505439>
 55. Johnson MA, Weick JP, Pearce RA, Zhang SC (2007) Functional neural development from human embryonic stem cells: accelerated synaptic activity via astrocyte coculture. *J Neurosci* 27(12):3069–3077. <https://doi.org/10.1523/JNEUROSCI.4562-06.2007>
 56. Tahirovic S, Hellal F, Neukirchen D, Hindges R, Garvalov BK, Flynn KC, Stradal TE, Chrostek-Grashoff A et al (2010) Rac1 regulates neuronal polarization through the WAVE complex. *J Neurosci* 30(20):6930–6943. <https://doi.org/10.1523/JNEUROSCI.5395-09.2010>
 57. Lorenzetto E, Ettore M, Pontelli V, Bolomini-Vittori M, Bolognini S, Zorzan S, Laudanna C, Buffelli M (2013) Rac1 selective activation improves retina ganglion cell survival and regeneration. *PLoS One* 8(5):e64350. <https://doi.org/10.1371/journal.pone.0064350>
 58. Kanekura K, Hashimoto Y, Kita Y, Sasabe J, Aiso S, Nishimoto I, Matsuoka M (2005) A Rac1/phosphatidylinositol 3-kinase/Akt3 anti-apoptotic pathway, triggered by Alsin/LF, the product of the ALS2 gene, antagonizes Cu/Zn-superoxide dismutase (SOD1) mutant-induced motoneuronal cell death. *J Biol Chem* 280(6):4532–4543. <https://doi.org/10.1074/jbc.M410508200>
 59. Stankiewicz TR, Linsman DA (2014) Rho family GTPases: key players in neuronal development, neuronal survival, and neurodegeneration. *Front Cell Neurosci* 8:314
 60. Nichols AL et al (2016) The apoptotic engulfment machinery regulates axonal degeneration in *C. elegans* neurons. *Cell Rep* 14(7):1673–1683. <https://doi.org/10.1016/j.celrep.2016.01.050>
 61. Zhang B, Zhang Y, Shacter E (2004) Rac1 inhibits apoptosis in human lymphoma cells by stimulating bad phosphorylation on Ser-75. *Mol Cell Biol* 24(14):6205–6214. <https://doi.org/10.1128/MCB.24.14.6205-6214.2004>
 62. Cheng C, Kong X, Wang H, Gan H, Hao Y, Zou W, Wu J, Chi Y et al (2009) Trihydrophobin I interacts with PAK1 and regulates ERK/MAPK activation and cell migration. *J Biol Chem* 284(13):8786–8796. <https://doi.org/10.1074/jbc.M806144200>
 63. Cicenas J (2008) The potential role of Akt phosphorylation in human cancers. *Int J Biol Markers* 23(1):1–9. <https://doi.org/10.5301/IJBM.2008.618>

64. Nagarajan A, Ning Y, Reisner K, Buraci Z, Larsen JP, Hobert O, Doitsidou M (2014) Progressive degeneration of dopaminergic neurons through TRP channel-induced cell death. *J Neurosci* 34(17):5738–5746. <https://doi.org/10.1523/JNEUROSCI.4540-13.2014>
65. Coles CH, Bradke F (2015) Coordinating neuronal actin-microtubule dynamics. *Curr Biol* 25(15):R677–R691. <https://doi.org/10.1016/j.cub.2015.06.020>
66. Chia JX, Efimova N, Svitkina TM (2016) Neurite outgrowth is driven by actin polymerization even in the presence of actin polymerization inhibitors. *Mol Biol Cell* 27(23):3695–3704. <https://doi.org/10.1091/mbc.E16-04-0253>
67. Dubey J, Ratnakaran N, Koushika SP (2015) Neurodegeneration and microtubule dynamics: death by a thousand cuts. *Front Cell Neurosci* 9:343
68. Godena VK, Brookes-Hocking N, Moller A, Shaw G, Oswald M, Sancho RM, Miller C CJ, Whitworth AJ et al (2014) Increasing microtubule acetylation rescues axonal transport and locomotor deficits caused by LRRK2 Roc-COR domain mutations. *Nat Commun* 5:5245. <https://doi.org/10.1038/ncomms6245>
69. Gandhi PN, Wang X, Zhu X, Chen SG, Wilson-Delfosse AL (2008) The Roc domain of leucine-rich repeat kinase 2 is sufficient for interaction with microtubules. *J Neurosci Res* 86(8):1711–1720. <https://doi.org/10.1002/jnr.21622>
70. Okada T, Hirai C, Badawy SMM, Zhang L, Kajimoto T, Nakamura Si (2016) Impairment of PDGF-induced chemotaxis by extracellular α -synuclein through selective inhibition of Rac1 activation. *Sci Rep* 6(1):37810. <https://doi.org/10.1038/srep37810>
71. Sousa VL, Bellani S, Giannandrea M, Yousuf M, Valtorta F, Meldolesi J, Chieriegatti E (2009) α -synuclein and its A30P mutant affect actin cytoskeletal structure and dynamics. *Mol Biol Cell* 20(16):3725–3739. <https://doi.org/10.1091/mbc.E08-03-0302>
72. Crews L, Spencer B, Desplats P, Patrick C, Paulino A, Rockenstein E, Hansen L, Adame A et al (2010) Selective molecular alterations in the autophagy pathway in patients with Lewy body disease and in models of alpha-synucleinopathy. *PLoS One* 5(2):e9313. <https://doi.org/10.1371/journal.pone.0009313>
73. Mak SK, McCormack AL, Manning-Boğ AB, Cuervo AM, di Monte DA (2010) Lysosomal degradation of alpha-synuclein in vivo. *J Biol Chem* 285(18):13621–13629. <https://doi.org/10.1074/jbc.M109.074617>
74. Vijayakumaran S, Wong M, Antony H, Pountney D (2015) Direct and/or indirect roles for SUMO in modulating alpha-synuclein toxicity. *Biomol Ther* 5(3):1697–1716. <https://doi.org/10.3390/biom5031697>
75. Ahmed I, Liang Y, Schools S, Dawson VL, Dawson TM, Savitt JM (2012) Development and characterization of a new Parkinson's disease model resulting from impaired autophagy. *J Neurosci* 32(46):16503–16509. <https://doi.org/10.1523/JNEUROSCI.0209-12.2012>
76. Ebrahimi-Fakhari D, Cantuti-Castelvetri I, Fan Z, Rockenstein E, Masliah E, Hyman BT, McLean PJ, Unni VK (2011) Distinct roles in vivo for the ubiquitin-proteasome system and the autophagy-lysosomal pathway in the degradation of α -synuclein. *J Neurosci* 31(41):14508–14520. <https://doi.org/10.1523/JNEUROSCI.1560-11.2011>
77. Winslow AR, Chen CW, Corrochano S, Acevedo-Arozena A, Gordon DE, Peden AA, Lichtenberg M, Menzies FM et al (2010) α -Synuclein impairs macroautophagy: implications for Parkinson's disease. *J Cell Biol* 190(6):1023–1037. <https://doi.org/10.1083/jcb.201003122>
78. Orenstein SJ, Kuo SH, Tasset I, Arias E, Koga H, Fernandez-Carasa I, Cortes E, Honig LS et al (2013) Interplay of LRRK2 with chaperone-mediated autophagy. *Nat Neurosci* 16(4):394–406. <https://doi.org/10.1038/nn.3350>
79. Alegre-Abarrategui J, Christian H, Lufino MMP, Mutihac R, Venda LL, Ansong O, Wade-Martins R (2009) LRRK2 regulates autophagic activity and localizes to specific membrane microdomains in a novel human genomic reporter cellular model. *Hum Mol Genet* 18(21):4022–4034. <https://doi.org/10.1093/hmg/ddp346>
80. Saha S, Liu-Yesucevitz L, Wolozin B (2014) Regulation of autophagy by LRRK2 in *Caenorhabditis elegans*. *Neurodegener Dis* 13(2–3):110–113. <https://doi.org/10.1159/000355654>
81. Brenner S (1974) The genetics of *Caenorhabditis elegans*. *Genetics* 77(1):71–94
82. Kamath RS, Ahringer J (2003) Genome-wide RNAi screening in *Caenorhabditis elegans*. *Methods* 30(4):313–321. [https://doi.org/10.1016/S1046-2023\(03\)00050-1](https://doi.org/10.1016/S1046-2023(03)00050-1)
83. Nollen EA et al (2004) Genome-wide RNA interference screen identifies previously undescribed regulators of polyglutamine aggregation. *Proc Natl Acad Sci U S A* 101(17):6403–6408. <https://doi.org/10.1073/pnas.0307697101>
84. Schindelin J, Rueden CT, Hiner MC, Eliceiri KW (2015) The ImageJ ecosystem: an open platform for biomedical image analysis. *Mol Reprod Dev* 82(7–8):518–529. <https://doi.org/10.1002/mrd.22489>
85. Palmisano NJ, Meléndez A (2016) Detection of autophagy in *Caenorhabditis elegans*. *Cold Spring Harb Protoc* 2016(2):pdb.top070466. <https://doi.org/10.1101/pdb.top070466>
86. Lapierre LR et al (2013) The TFEB orthologue HLH-30 regulates autophagy and modulates longevity in *Caenorhabditis elegans*. *Nat Commun* 4:2267
87. Consiglio A, Gritti A, Dolcetta D, Follenzi A, Bordignon C, Gage FH, Vescovi AL, Naldini L (2004) Robust in vivo gene transfer into adult mammalian neural stem cells by lentiviral vectors. *Proc Natl Acad Sci U S A* 101(41):14835–14840. <https://doi.org/10.1073/pnas.0404180101>



Long-Term Labeling of Hippocampal Neural Stem Cells by a Lentiviral Vector

Hoonkyo Suh^{1*}, Qi-Gang Zhou^{1†}, Irene Fernandez-Carasa^{2,3}, Gregory Dane Clemenson Jr.⁴, Meritxell Pons-Espinal^{2,3}, Eun Jeoung Ro¹, Mercè Martí^{5,6}, Angel Raya^{5,6,7}, Fred H. Gage⁴ and Antonella Consiglio^{2,3,8*}

¹ Department of Neurosciences, Cleveland Clinic, Lerner Research Institute, Cleveland, OH, United States, ² Department of Pathology and Experimental Therapeutics, Institut d'Investigació Biomèdica de Bellvitge, Bellvitge University Hospital, Barcelona, Spain, ³ Institute of Biomedicine of the University of Barcelona, Barcelona, Spain, ⁴ Gene Expression Laboratory, The Salk Institute for Biological Studies, La Jolla, CA, United States, ⁵ Center of Regenerative Medicine in Barcelona, Hospital Duran i Reynals, Barcelona, Spain, ⁶ Biomedical Research Networking Center in Bioengineering, Biomaterials and Nanomedicine, Madrid, Spain, ⁷ Institutació Catalana de Recerca i Estudis Avançats (ICREA), Barcelona, Spain, ⁸ Department of Molecular and Translational Medicine, University of Brescia, Brescia, Italy

OPEN ACCESS

Edited by:

Annalisa Buffo,
Università degli Studi di Torino, Italy

Reviewed by:

Mariagrazia Grilli,
Università degli Studi del Piemonte
Orientale "Amedeo Avogadro", Italy
Chiara Rolando,
Universität Basel, Switzerland

*Correspondence:

Hoonkyo Suh
suhh2@ccl.org
Antonella Consiglio
consiglio@ub.edu;
aconsiglio@libub.pcb.ub.es

†Present address:

Qi-Gang Zhou,
Department of Clinical Pharmacology,
School of Pharmacy, Nanjing Medical
University, Nanjing, China

Received: 01 June 2018

Accepted: 25 October 2018

Published: 15 November 2018

Citation:

Suh H, Zhou Q-G, Fernandez-Carasa I, Clemenson GD Jr, Pons-Espinal M, Ro EJ, Martí M, Raya A, Gage FH and Consiglio A (2018) Long-Term Labeling of Hippocampal Neural Stem Cells by a Lentiviral Vector. *Front. Mol. Neurosci.* 11:415. doi: 10.3389/fnmol.2018.00415

Using a lentivirus-mediated labeling method, we investigated whether the adult hippocampus retains long-lasting, self-renewing neural stem cells (NSCs). We first showed that a single injection of a lentiviral vector expressing a green fluorescent protein (LV PGK-GFP) into the subgranular zone (SGZ) of the adult hippocampus enabled an efficient, robust, and long-term marking of self-renewing NSCs and their progeny. Interestingly, a subset of labeled cells showed the ability to proliferate multiple times and give rise to Sox2⁺ cells, clearly suggesting the ability of NSCs to self-renew for an extensive period of time (up to 6 months). In addition, using GFP⁺ cells isolated from the SGZ of mice that received a LV PGK-GFP injection 3 months earlier, we demonstrated that some GFP⁺ cells displayed the essential properties of NSCs, such as self-renewal and multipotency. Furthermore, we investigated the plasticity of NSCs in a perforant path transection, which has been shown to induce astrocyte formation in the molecular layer of the hippocampus. Our lentivirus (LV)-mediated labeling study revealed that hippocampal NSCs are not responsible for the burst of astrocyte formation, suggesting that signals released from the injured perforant path did not influence NSC fate determination. Therefore, our studies showed that a gene delivery system using LVs is a unique method to be used for understanding the complex nature of NSCs and may have translational impact in gene therapy by efficiently targeting NSCs.

Keywords: lentiviral vectors, hippocampal neurogenesis, targeting, neural stem cells, lesion

INTRODUCTION

Evidence from several studies has shown that self-renewing and multipotent neural stem cells (NSCs) are responsible for hippocampal neurogenesis, a process that maintains a NSC pool and generates newborn neurons (Gage, 2000; Suh et al., 2007; Eisch et al., 2008; Bonaguidi et al., 2011). This life-long production and integration of newborn neurons into the hippocampal neural

circuits plays a crucial role in learning and memory as well as emotional and stress response (Deng et al., 2010). The regenerative capacity of NSCs has raised hopes that NSCs could be used to replace degenerating cells as a part of therapy for various neurodegenerative and neuropsychiatric disorders. This therapeutic potential of NSCs underscores the importance of understanding the properties of hippocampal NSCs.

The idea that hippocampal NSCs are multipotent and have a self-renewal capacity has been widely accepted. However, the details of these critical features of NSCs are still unclear. For example, although hippocampal NSCs can differentiate into both neurons and astrocytes, a series of fate-mapping studies and lineage analyses revealed that hippocampal NSCs produce predominantly neurons, whereas the generation of astrocytes and oligodendrocytes is minimal to non-existent (Seri et al., 2001; Kronenberg et al., 2003; Suh et al., 2007; Lugert et al., 2010; Bonaguidi et al., 2011; Encinas et al., 2011; Beckervordersandforth et al., 2014; Rolando et al., 2016; Pons-Espinal et al., 2017). However, it remains to be determined whether NSCs are continuously self-renewing over the long term or whether they are short-lived cells (Bonaguidi et al., 2011; Encinas et al., 2011; Beckervordersandforth et al., 2014). Both models can explain the presence of self-renewing NSCs, but they do not indicate whether NSCs are continuously self-renewing or live only for a short time. These inconclusive observations regarding key features of NSCs are partially due to the technical challenges involved in labeling and tracing complex NSC populations over time.

To address this issue directly, we used a lentivirus (LV)-mediated gene delivery system that has shown to transduce both dividing and non-dividing cells, including NSCs as well as their progeny over a long-term marking period (Consiglio et al., 2004; Suh et al., 2007). By taking advantage of LV's ability to efficiently transduce a GFP reporter gene in adult NSCs *in vivo*, we clearly demonstrated the presence of long-lasting NSCs that can proliferate multiple times when spaced by month intervals and produce cells expressing a NSC marker, Sox2. Importantly, when we isolated, cultured, and examined the properties of GFP-labeled cells 3 months after we injected LV PGK-GFP into the dentate gyrus (DG), we observed that the same population labeled by LV PGK-GFP *in vivo* could expand and produce neurons as well as astrocytes *in vitro*. Using a LV PGK-GFP, we subsequently tested whether hippocampal NSCs underlies the burst of astrocyte formation that occurs during periformant path (PP) injury. In the PP injury model that induces astrocyte production in the hippocampus (Gage et al., 1988; Fagan and Gage, 1994), we found that NSCs did not contribute to the burst of astrocytes. Our studies demonstrate that a LV is a robust and efficient gene delivery system that allows us to dissect the detailed characteristics of hippocampal NSCs.

MATERIALS AND METHODS

LV Production and Stereotactic Surgery

The production and determination of LV PGK-GFP expression were previously described in detail (Consiglio et al., 2004). We

used LV PGK-GFP that has 5×10^9 to 1×10^{10} transducing units per ml with an HIV-1 p24 concentration of 100 $\mu\text{g/ml}$. All procedures using animals were done in accordance with protocols approved by the Animal Care and Use Committee of the Salk Institute for Biological Studies and the Parc Científic of Barcelona. Six- to eight-week old female C57BL/6 (Harlan) mice were used for all experiments. Mice were anesthetized with a mixture of ketamine (100 mg/kg) and xylazine (10 mg/kg), and 1 μl of vector was injected into the right hippocampal dentate gyrus at a rate of 0.2 $\mu\text{l/min}$ using a Hamilton (Reno, NV, United States) syringe. Stereotactic coordinates were as follows: AP = -2, ML = +1.5, DV = -2 in mm from bregma. Mice were analyzed 15 days and 3 and 6 months after injection.

BrdU Administration

To understand the long-term proliferation of GFP-transduced cells in the adult hippocampus, 100 mg/kg of Bromodeoxyuridine (BrdU) was administered daily by intraperitoneal (IP) injection for 7 days [83 and 173 days post injection (dpi)]. Animals were sacrificed 24 h after the last BrdU injection (90 and 180 dpi). To examine the differentiation potential of GFP-labeled cells, a group of mice received the same amount of BrdU at 30 dpi for 7 days and were analyzed 4 weeks later.

Tissue Processing and Immunohistochemistry

Detailed procedures regarding tissue processing and antibody staining, including BrdU detection, were previously described (Suh et al., 2007). Primary antibodies used were mouse anti-Neuronal Nuclei (NeuN 1:10; kindly provided by Dr. R. Mullen, University of Utah); mouse anti-Nestin (1:500; Pharmingen); goat anti-Doublecortin (DCX 1:200; Santa Cruz Biotechnologies); rabbit anti-Glial Fibrillary Acidic Protein (GFAP 1:1000; Dako); rabbit anti-S-100 β (1:5000; Swant); rat anti-BrdU (1:200; Accurate Chemicals); rabbit anti-Ki67 (1:200; Novocastra); rabbit anti-Sox2 (1:200, Chemicon); rabbit anti-brain lipid binding protein (BLBP 1:1000; kindly provided by N. Heintz, Rockefeller); rat anti-MUSASHI-1 (1:1000; a kind gift from O. Hideyuki, Keiyo University, Japan); rabbit anti-GFP (1:100, Molecular Probes); and guinea pig anti-GFAP (1:1,000). Fluorescence immunohistochemistry (IHC) was performed using corresponding FITC, Cy3, or Cy5 secondary antibodies (1:200, all raised in donkey, Jackson ImmunoResearch, West Grove, PA, United States). DAPI (10 mg/ml, Sigma) was used as a fluorescent counterstain.

Confocal stack images of brain slices (40 μm) were obtained with the Confocal A1 Nikon Inverted SFC with 40 \times objective and the Zeiss Spinning Disk with a 20 \times objective. Cell quantification and analysis was performed using NIS-Elements software (Nikon) and Zen Blue (Zeiss).

Cell Counting

To quantify the percentage of labeled cells in coronal sections stained for GFP and BrdU, the number of BrdU-positive nuclei was identified in a selected optical field and counted. The fraction

of labeled nuclei showing GFP-positive cytoplasm in the same field was then assessed. The analysis was performed on three randomly chosen fields taken from two or three independent non-sequential sections from three mice per experimental group.

Perforant Path (PP) Lesion

Lentiviral vector expressing a green fluorescent protein was injected into the right side of the dentate gyrus of six- to eight-week old C57BL/6 female mice ($n = 5$). One month later, these mice received ipsilateral aspirative lesions that resulted in the ablation of the PP as previously described (Fagan and Gage, 1994). Brains were harvested and analyzed 7 days post-surgery.

Preparation of Hippocampal Progenitors

Six- to eight-week old C57BL/6 female mice were injected with LV PGK-GFP in the DG. Three months later, hippocampi were isolated from these mice and used to prepare hippocampal progenitor cells as previously described (Ray and Gage, 2006; Suh et al., 2007). Briefly, 3–5 LV PGK-GFP injected hippocampi were isolated from these mice and digested in PPD solution [papain (2.5 U/ml, Worthington), pronase (1 U/ml, Roche), and DNase (250 U/ml, Worthington)] and sucrose gradient was applied to remove cell debris and myelin. Then cells were plated in the presence of FGF2 (Fibroblast Growth Factor, 20 ng/ml; PeproTech), EGF (Epidermal Growth Factor, 20 ng/ml; PeproTech), and heparin (5 μ g/ml; Sigma) in DMEM/F12 (Life Technology) basal media supplemented with N2 (Life Technology). Once NSCs were established and expanded in the presence of FGF2 and EGF, we sorted out GFP-expressing cells via FACS and established three clonally expanded NSCs lines. The number of total GFP-expressing cells isolated by FACS was around 2×10^4 cells per preparation. To differentiate GFP-expressing NSCs, 10^5 cells/cm² were plated on the laminin-coated glass chamber slides (Nalge Nunc International) and cultured in differentiation medium consisting of DMEM/F12, N2 supplement, and 5 μ M forskolin (Sigma), for 7 more days.

Immunofluorescence

The immunofluorescence staining on cell cultures was performed after fixing NSCs for 30 min with 4% paraformaldehyde (PFA) followed by extensive washings with PBS for 30 min. Cells were washed three times with PBS 0.1% Triton X-100 (PBS-T) and blocked for 2 h with PBS-T containing 5% normal goat serum (Vector laboratories), followed by overnight incubation with primary antibodies: rabbit anti-GFAP (1:1000; Dako); mouse anti-Nestin (1:500; Pharmingen); rabbit anti-Sox2 (1:200; Chemicon); anti-TUJ-1 (1:1,000; Chemicon). The next day, after washing extensively with PBS-T, cells were incubated with secondary antibodies. Cells were mounted in mounting medium and counterstained with fluorescent nuclear dye DAPI (Invitrogen). Images were obtained using the microscope Nikon Eclipse at 20 or 40 \times magnification and quantification was performed using a Cell-counter plugin in FIJI (Fiji is Just ImageJ).

RESULTS

LV-Mediated Long-Term Labeling of NSCs in the Hippocampus

To test the ability of LV to transduce hippocampal NSCs *in vivo*, we injected a vesicular stomatitis virus-pseudotyped, late-generation LV expressing the GFP into the right DG of the mouse hippocampus (Consiglio et al., 2004). GFP expression in the LVs was driven by the ubiquitously expressed phosphoglycerate kinase promoter and by the posttranscriptional regulatory element of the woodchuck hepadnavirus. Mice were sacrificed after 2 weeks to assess cell phenotype shortly after transduction or after 3 and 6 months as the longest time point. Robust GFP-expressing cells were identified in both DG and the hilus after 2 weeks of injection and during a six-month period (Figures 1A,B). Because neither the VSV-G envelope nor the PGK promoter provided neural precursor cell (NPCs) specificity, the majority of GFP-labeled cells expressed post-mitotic immature and mature neuronal markers (data not shown).

Next, we tested whether the LV successfully labeled hippocampal NSCs. Interestingly, IHC with NSCs markers showed that a population of GFP⁺ cells located along the subgranular zone (SGZ) co-localized with BLBP, NESTIN, SOX2, GFAP, and MUSASH-1 2 weeks and 6 months after LV PGK-GFP injection (Suh et al., 2007; Figures 1C–J).

Three-dimensional confocal images revealed that $38 \pm 5.3\%$ ($n = 3$) of the GFP-positive cells in the SGZ expressed BLBP marker, known to label a subset of neurogenic radial glia (Filippov et al., 2003; Fukuda et al., 2003; Mignone et al., 2004; Gebara et al., 2016), and $7 \pm 2.2\%$ ($n = 3$) was expressed in non-radial cells (SOX2⁺ cells), suggesting the ability of LV PGK-GFP to target NSCs that have the potential to self-renew and differentiate into neurons in the adult hippocampus (Suh et al., 2007; Bonaguidi et al., 2011; Gebara et al., 2016).

LV Marks a Cell Population That Retains Multiple Proliferation Capacity

To test whether LV PGK-GFP is successfully transduced in NSCs that have proliferation capacity over a long period of time, we introduced BrdU 6 months post LV PGK-GFP injection. The hippocampus was then examined to identify proliferating cells 24 h after the final BrdU injection. We found that $6.25 \pm 1.8\%$ of GFP⁺ cells were positive for BrdU in the SGZ of the DG. This observation indicates that initially targeted cells or their progeny retain proliferation capacity over 6 months (Figure 2A). We identified that $10 \pm 1.4\%$ of these GFP/BrdU double-labeled cells expressed SOX2 marker ($n = 3$; Figure 2B), known to represent the self-renewing and multipotent NSCs (Suh et al., 2007). Doublecortin (DCX), a transient marker that labels both neuroblasts and immature neurons, was used to measure a continuous neurogenesis from GFP⁺ cells (Steiner et al., 2006). Indeed, we observed both GFP/DCX double-labeled cells ($26.8 \pm 2\%$ of GFP⁺ cells; $n = 3$ Figure 2C) and GFP/BrdU/DCX cells triple-labeled cells ($60 \pm 2.3\%$ $n = 3$; Figure 2D). Interestingly, these results collectively suggest that

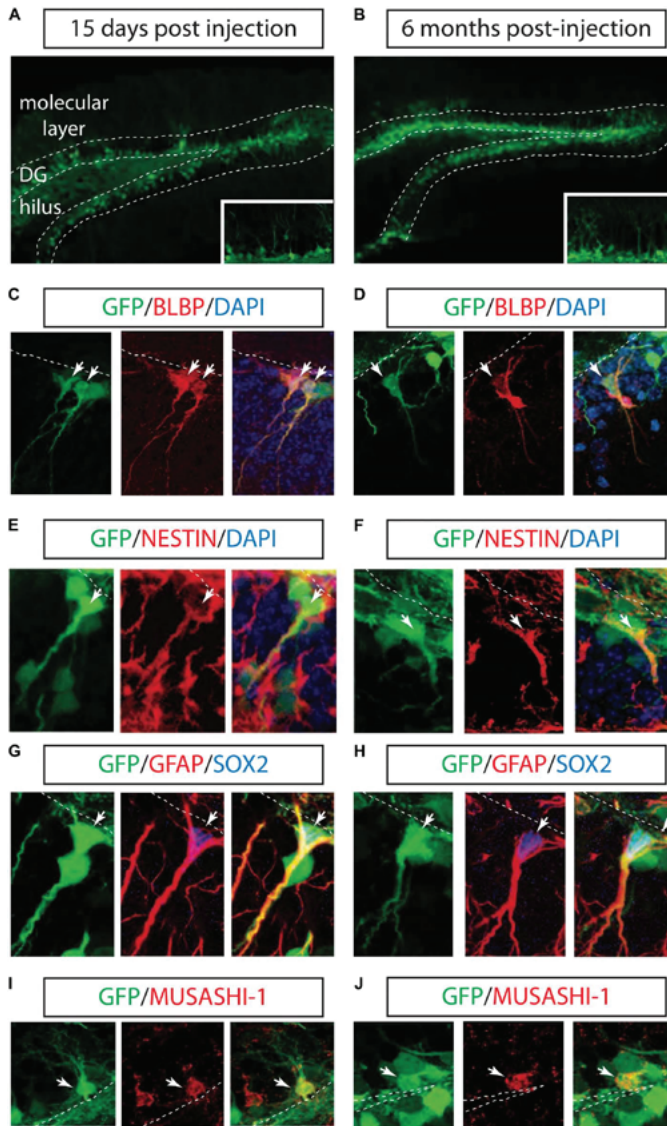
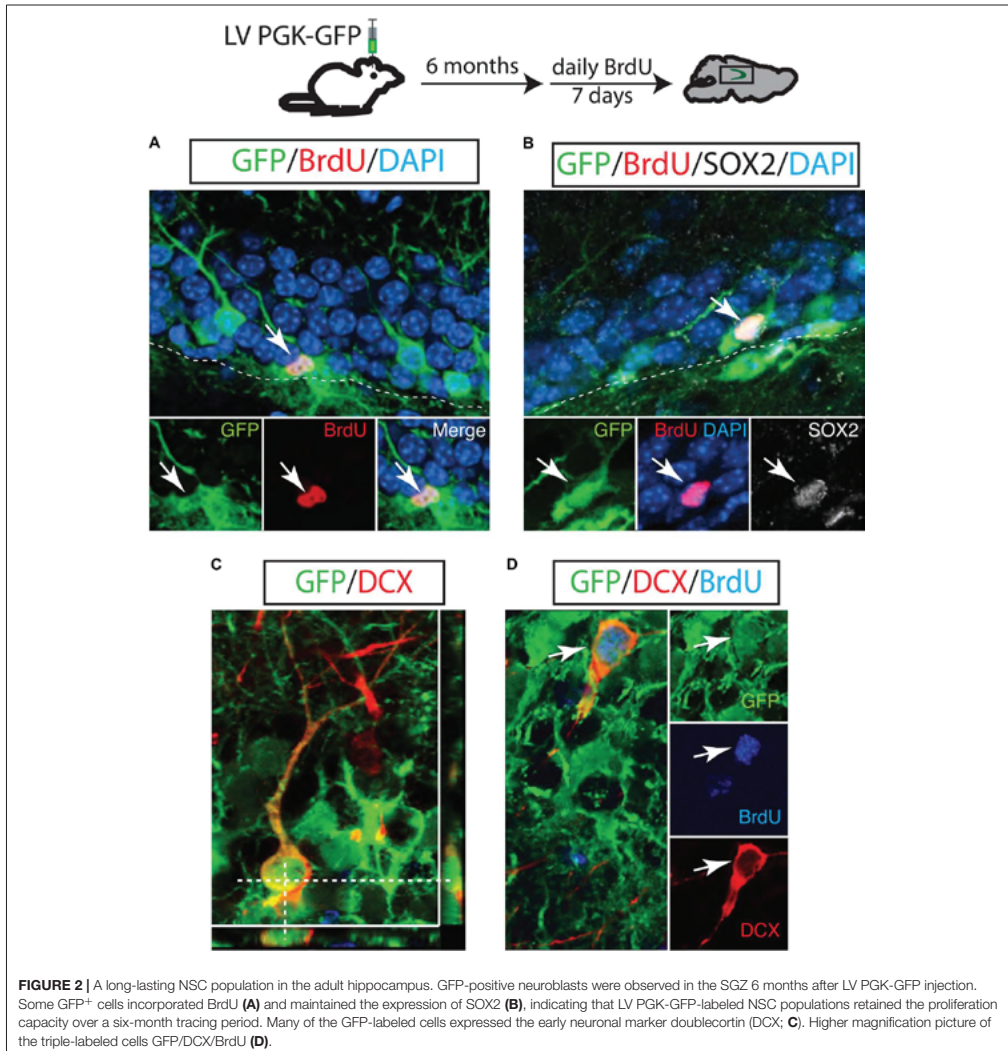


FIGURE 1 | Long-term marking of hippocampal NSCs by LV PGK-GFP. LV PGK-GFP was unilaterally injected into the hippocampal DG; brain sections were analyzed 15 days (A) and 6 months (B) later. GFP expression was evident in the DG at both time points. A higher magnification view is displayed in insets (A,B). GFP-expressing cells co-labeled with NSCs markers such as BLBP (C,D), NESTIN (E,F), SOX2, GFAP (G,H), and MUSASHI-1 (I,J) (arrows). Note that some GFP-positive cells stained for SOX2 showed co-localization with radial glial cell markers such as GFAP in their processes (G,H). DG, dentate gyrus; SGZ is marked with dotted lines.



NSCs are continuously generated from targeted GFP⁺ cells and actively produce neuroblasts even 6 months after LV injection.

Long-Term Maintenance of NSCs in the Hippocampus

Next, we investigated the cell fate of the proliferating GFP⁺ cells and their extensive proliferation ability. One month after the LV PGK-GFP injection, mice were injected with BrdU daily

for 7 days and sacrificed 4 weeks after the last BrdU injection. The majority of progeny of proliferating GFP⁺ cells (GFP/BrdU double-labeled cells) gave rise to $87.5 \pm 2.5\%$ neurons which account for 40% DCX⁺ and 60% NeuN⁺ (**Figure 3A**). Specifically, neurons positive for NeuN expressed a granular neuron-specific marker, Prox1 (data not shown) and displayed distinctive morphological features of mature granular neurons in the DG. In contrast to a dominant neuronal differentiation of GFP-labeled cells, proliferating GFP⁺ (GFP/BrdU⁺) cells

produced a significantly lower number of mature astrocytes that co-labeled with S-100 β ($3.9 \pm 0.49\%$ GFP/BrdU/S-100 β + cells) (Figure 3B); the generation of new oligodendrocytes was not detected in our experimental paradigm. These results are in line with those obtained by using other labeling methods (Song et al., 2002; Maslov et al., 2004; Steiner et al., 2004; Suh et al., 2007, 2009; Zhao et al., 2008; Venere et al., 2012). We also performed IHC with BrdU and MCM2 to test the proliferation capacity of GFP⁺ cells (Maslov et al., 2004). A triple staining revealed a subset of GFP/BrdU double positive cells expressing MCM2 ($2.3 \pm 1.2\%$), indicating that GFP⁺ cells had proliferated 1 month after LV injection and were in continuous cell cycle for an additional month (Figure 3C).

Our assessment of the differentiation capacity of GFP⁺ cells *in vivo* was in sharp contrast to the multipotency capacity of the hippocampal NSCs *in vitro* that has been reported in many studies: while GFP⁺ cells *in vivo* differentiated predominantly to neurons, cultured NSCs produced more astrocytes than neurons. This finding raised the possibility that neurogenic cells labeled by LV PGK-GFP might differ from the cell population that gives rise to hippocampal NSCs *in vitro*. To test this hypothesis, we isolated the hippocampal NSCs 3 months after we injected LV PGK-GFP into the DG and established NSCs with clonally derived GFP⁺ cells. Clonally expanded GFP⁺ NSCs showed their ability to propagate at least 20 times, maintaining the expression of NSC markers of NESTIN and SOX2 (Figure 3D). When the NSCs were induced to differentiate in the presence of forskolin, the majority of GFP⁺ NSCs differentiated into astrocytes positive for GFAP, although a moderate amount of GFP⁺ NSCs gave rise to neurons positive for Tuj1 (Figures 3E,F). These results showed that LV PGK-GFP clearly targeted the same cell populations that serve as a source of both *in vitro* and *in vivo* NSCs, though the *in vitro* conditions favored astroglial differentiation.

Differentiation Potential of NSCs in the Perforant Path Injury

It has been shown that unilateral injury of the perforant path (PP) induces degeneration of axon terminals of the entorhinal neurons and a burst of astrocyte formation in the molecular layer of the ipsilateral hippocampus (Gage et al., 1988; Fagan and Gage, 1994). It has been a long lasting question whether NSCs in the dentate gyrus could contribute to the PP injury-induced astrocytes. To directly answer to this question, 1 month after LV PGK-GFP was injected to label NSCs in the DG, a unilateral transection of the PP was performed. BrdU was injected for 3 days and the brain was analyzed 4 days later.

Consistent with previous reports, the generation of astrocytes expressing GFAP increased on the ipsilateral side of the molecular layer (Figure 4A). Thus, by immunofluorescence analyses, we confirmed that the ablation of inputs from entorhinal cortex to the granular neurons causes degeneration of axons and results in increased astrocyte proliferation (GFAP/BrdU double positive cells), specifically in the DG-molecular layer of the lesioned side (Figure 4A). However, the contribution of GFP⁺ cells to newly generated astrocytes was not detected, suggesting that

GFP⁺ NSCs were not responsible for the burst of astrocytes (Figure 4B).

DISCUSSION

Self-renewing and multipotent NSCs are responsible for continuous neurogenesis in the adult hippocampus. These two properties of NSCs are critical for the production of newborn neurons and maintenance of a stem cell pool throughout life. As neurogenesis occurs, adult NSCs undergo changes in their intrinsic properties such as morphology, gene expression, proliferation kinetics, and self-renewal capacity and ultimately produce differentiated neural cells (Zhao et al., 2008; Suh et al., 2009). In the normal brain, the production, and integration of newborn neurons into the preexisting neural circuits play a key role in hippocampus-dependent learning and memory (Aimone et al., 2011). In pathological conditions, however, injury-associated signals appear to affect many aspects of neurogenesis, leading to changes in the proliferation of NSCs, survival and fate determination of newborn cells (Lindvall and Kokaia, 2006; Llorens-Bobadilla et al., 2015). Dysregulated neurogenesis has been implicated in functional deficits. In this report, we investigated the precise characteristics of LV-targeted NSCs to understand how NSCs contribute to neurogenesis in normal and injured brains.

Two different models have been proposed to address the nature of the longevity of NSCs in the adult hippocampus: long-lasting and continuously self-renewing NSCs vs. one-time activated and short-living NSCs. In the former model, NSCs continuously proliferate to maintain a NSC pool and produce newborn neurons and astrocytes (Suh et al., 2007; Bonaguidi et al., 2011). In the latter model, however, NSCs are proposed to be activated only once throughout life, to proliferate a limited number of times and sequentially generate neurons and astrocytes within a period of a month (Encinas et al., 2011). This latter model of short-lived NSCs is in line with previous *in vitro* studies, suggesting that the adult hippocampus does not contain NSCs but only lineage-committed and transiently proliferating cells (Seaberg and van der Kooy, 2002; Bull and Bartlett, 2005). The key difference between these models is whether NSCs have a long-term or short-term self-renewal ability. Here, using an advanced-generation LV (Consiglio et al., 2004), we showed that a subpopulation of GFP⁺ cells (indicating lentivirus-mediated labeling), retained the proliferative capacity over a six-month labeling period analyzed. Moreover, some GFP⁺ cells divided multiple times (GFP/BrdU/MCM2) within a one-month interval, producing progeny expressing a NSC marker (GFP/BrdU/SOX2) over the two-month period analyzed. That NSCs were targeted *in vivo* by LVs was further validated by culturing experiments demonstrating that some of the transduced SGZ cells behaved as long-term self-renewing progenitors *in vitro* and they could propagate for up to 5 months (the latest time tested). Interestingly, when we analyzed the differentiation ability of the labeled cells *in vitro*, our results showed that while GFP⁺ cells *in vivo* differentiated predominantly to neurons, cultured NSCs produced more astrocytes than neurons, indicating that *in vitro*

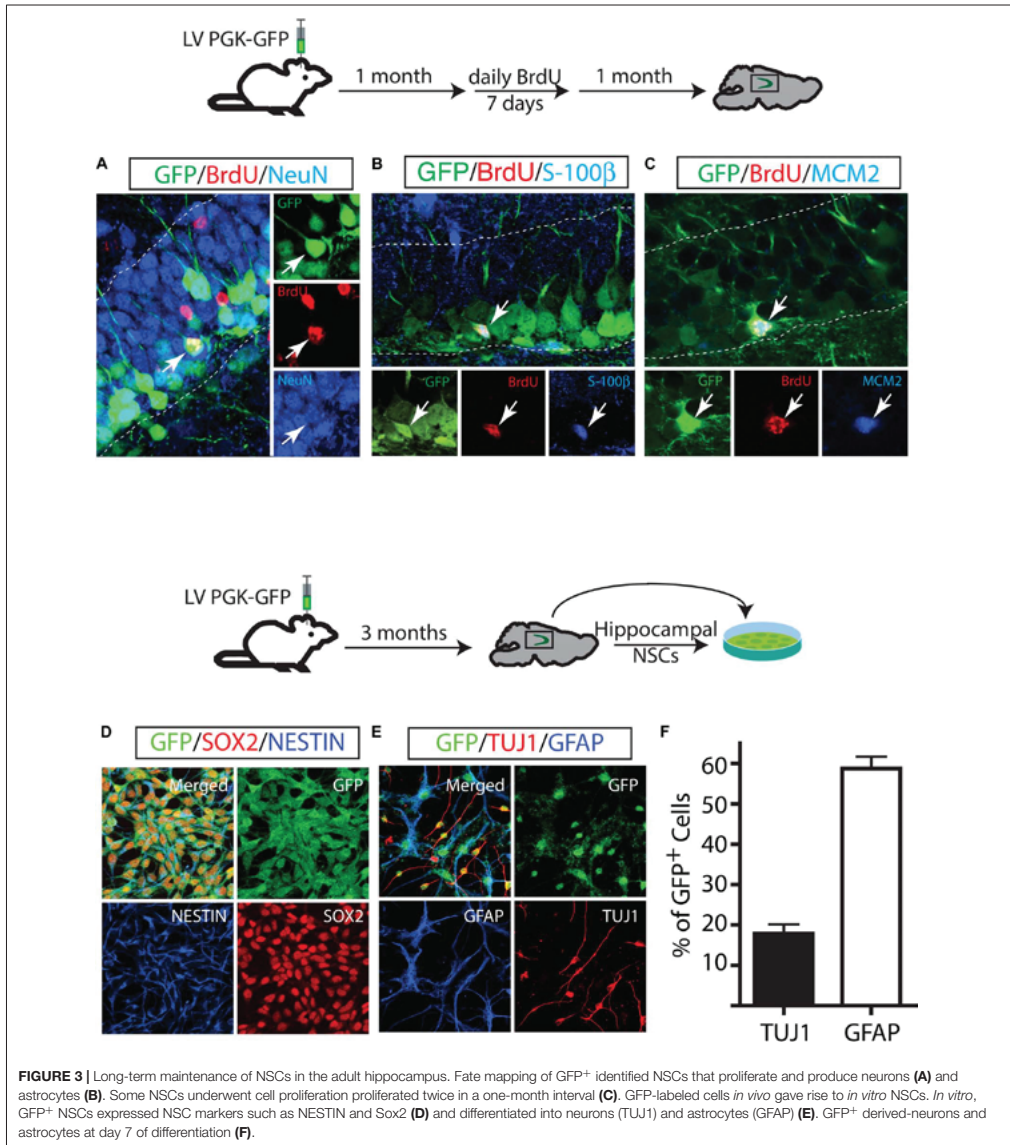
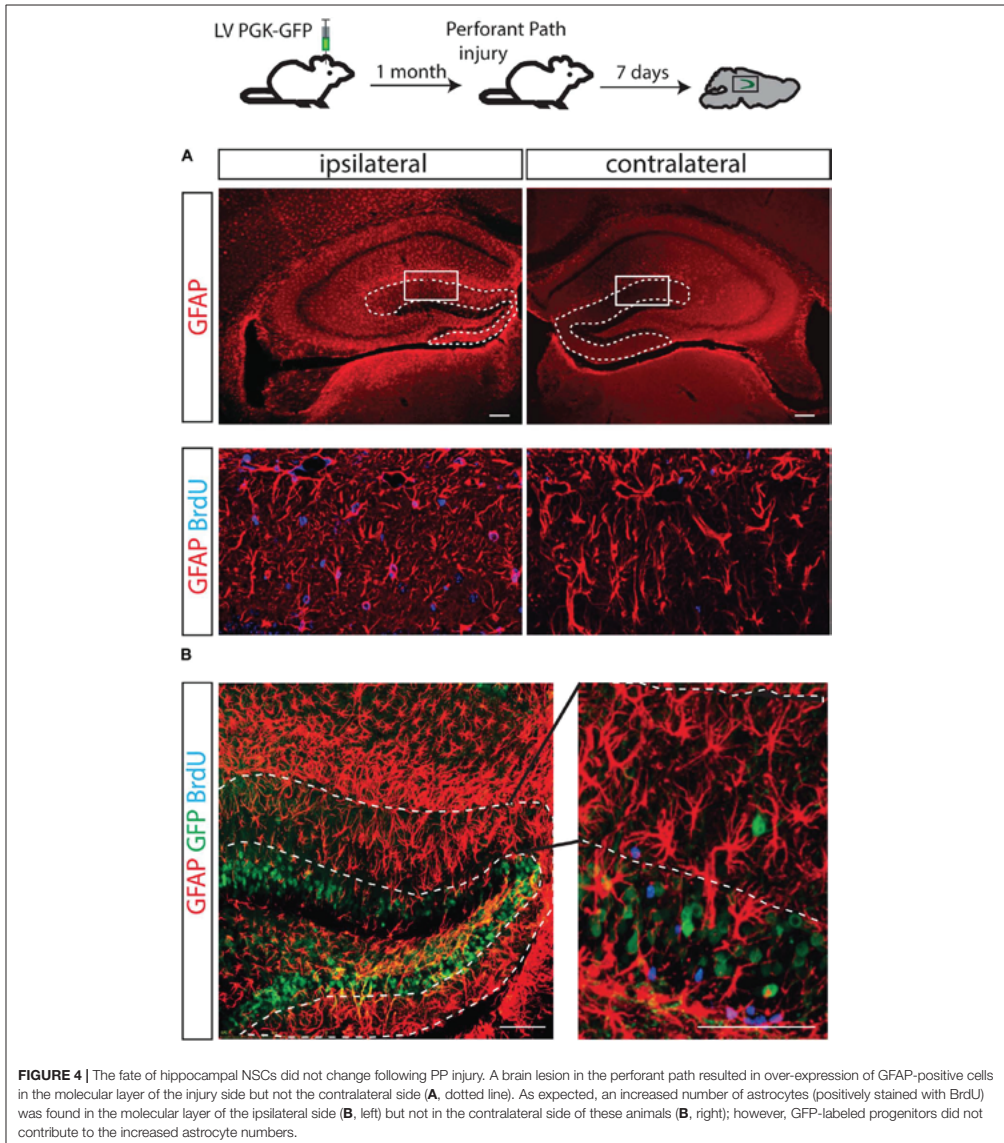


FIGURE 3 | Long-term maintenance of NSCs in the adult hippocampus. Fate mapping of GFP⁺ identified NSCs that proliferate and produce neurons (A) and astrocytes (B). Some NSCs underwent cell proliferation proliferated twice in a one-month interval (C). GFP-labeled cells *in vivo* gave rise to *in vitro* NSCs. *In vitro*, GFP⁺ NSCs expressed NSC markers such as NESTIN and Sox2 (D) and differentiated into neurons (TUJ1) and astrocytes (GFAP) (E). GFP⁺ derived-neurons and astrocytes at day 7 of differentiation (F).

conditions favored astroglial differentiation. When we clonally expanded GFP⁺ NSCs that had already been established *in vitro*, they all showed the similar differentiation ratio of neuron and astrocytes, suggesting this preferred astrocyte differentiation is likely to reflect the general NSC properties *in vitro*.

Using our LV system, we directly asked whether NSCs in the DG directly contributed to astrocytes formation by performing a unilateral transection of the PP, which induces astrocyte production specifically in the molecular layer of the ipsilateral DG (Gage et al., 1988; Fagan and Gage, 1994). Since the site of



astrocyte induction is geographically separated from the injury site, our experimental paradigm has the advantage of ruling out the possibility that the cellular phenotypes we observed were caused by the direct physical damage to the brain. In such an experimental condition that facilitates astrocyte induction,

we predicted we would observe increased astrocyte formation derived from NSCs labeled by a lentiviral vector. Contrary to what was expected, our fate mapping showed that NSCs did not contribute to the formation of astrocytes. LV-mediated fate mapping revealed that the fate determination of NSCs might be

less influenced by environmental cues in the injured brains, and astrocyte progenitors located in the molecular layer might be responsible for astrocyte induction in the case of the PP injury model (Buffo et al., 2008; Zhang and Barres, 2010).

Although these findings support the conclusion that our lentiviral system is able to induce transgene expression in a long-lasting, self-renewing NSCs within the hippocampus of the adult mouse brain that continually give rise to proliferating neuronal progenitors that contribute to maintain neurogenesis in the hippocampus, the fraction of NSC that were actually transduced *in vivo* remains to be determined. An unequivocal characterization of the cell type originally transduced by the LV may require the use of cell type specific promoters restricted to NPCs. However, in spite of its uncertain identity, our findings indicate that LV, in combination with BrdU-labeling and morphological analysis, allows long-term studies of adult NSCs properties *in vivo*. In future experiments, we will test whether the combination of the usage of cell type specific promoters and different glycoprotein will improve targeting specificity, which is a critical factor also for successful gene therapy.

AUTHOR CONTRIBUTIONS

HS, FG, and AC conceived the study. HS, Q-GZ, GC, IF-C, and MP-E contributed to methodology. HS and AC performed the formal analysis. HS, Q-GZ, GC, IF-C, MP-E, ER, AR, MM, and AC investigated the analysis. HS, FG, and AC validated

the results. HS, FG, and AC wrote, reviewed, and edited the manuscript. HS, FG, and AC acquired funding. HS, FG, and AC supervised the study. All authors edited and approved the final manuscript.

FUNDING

This work was supported by grants from the European Research Council-ERC (2012-STG-311736-PD-HUMMODEL) and the Spanish Ministry of Economy and Competitiveness-MINECO (BFU2013-49157-P and BFU2016-80870-P) to AC and by the Whitehall Foundation Research Grant and NIH grant (R01AA022377) to HS. Additional funding came from MINECO (SAF2015-69706-R), Instituto de Salud Carlos III-ISCIII/FEDER (Red de Terapia Celular – TerCel RD16/0011/0024 and PIE14/00061), ACCIÓ/FEDER (AdvanceCat), Generalitat de Catalunya-AGAUR (2017-SGR-899), and CERCA Programme/Generalitat de Catalunya.

ACKNOWLEDGMENTS

We thank Lola Mulero Pérez and Haleigh Golub for bioimaging and technical assistance, and Carles Terol for help with experiments. We also thank Carles Calatayud for helpful discussion and Mary Lynn Gage for editorial comments.

REFERENCES

- Aimone, J. B., Deng, W., and Gage, F. H. (2011). Resolving new memories: a critical look at the dentate gyrus, adult neurogenesis, and pattern separation. *Neuron* 70, 589–596. doi: 10.1016/j.neuron.2011.05.010
- Beckervordersandforth, R., Deshpande, A., Schaffner, I., Huttner, H. B., Lepier, A., Lie, D. C., et al. (2014). In vivo targeting of adult neural stem cells in the dentate gyrus by a split-cre approach. *Stem Cell Rep.* 2, 153–162. doi: 10.1016/j.stemcr.2014.01.004
- Bonaguidi, M. A., Wheeler, M. A., Shapiro, J. S., Stadel, R. P., Sun, G. J., Ming, G. L., et al. (2011). In vivo clonal analysis reveals self-renewing and multipotent adult neural stem cell characteristics. *Cell* 145, 1142–1155. doi: 10.1016/j.cell.2011.05.024
- Buffo, A., Rite, I., Tripathi, P., Lepier, A., Colak, D., Horn, A. P., et al. (2008). Origin and progeny of reactive gliosis: a source of multipotent cells in the injured brain. *Proc. Natl. Acad. Sci. U.S.A.* 105, 3581–3586. doi: 10.1073/pnas.0709002105
- Bull, N. D., and Bartlett, P. F. (2005). The adult mouse hippocampal progenitor is neurogenic but not a stem cell. *J. Neurosci.* 25, 10815–10821. doi: 10.1523/JNEUROSCI.3249-05.2005
- Consiglio, A., Gritti, A., Dolcetta, D., Follenzi, A., Bordignon, C., Gage, F. H., et al. (2004). Robust in vivo gene transfer into adult mammalian neural stem cells by lentiviral vectors. *Proc. Natl. Acad. Sci. U.S.A.* 101, 14835–14840. doi: 10.1073/pnas.0404180101
- Deng, W., Aimone, J. B., and Gage, F. H. (2010). New neurons and new memories: how does adult hippocampal neurogenesis affect learning and memory? *Nat. Rev. Neurosci.* 11, 339–350. doi: 10.1038/nrn2822
- Eisch, A. J., Cameron, H. A., Encinas, J. M., Meltzer, L. A., Ming, G. L., and Overstreet-Wadiche, L. S. (2008). Adult neurogenesis, mental health, and mental illness: hope or hype? *J. Neurosci.* 28, 11785–11791. doi: 10.1523/JNEUROSCI.3798-08.2008
- Encinas, J. M., Michurina, T. V., Peunova, N., Park, J. H., Tordo, J., Peterson, D. A., et al. (2011). Division-coupled astrocytic differentiation and age-related depletion of neural stem cells in the adult hippocampus. *Cell Stem Cell* 8, 566–579. doi: 10.1016/j.stem.2011.03.010
- Fagan, A. M., and Gage, F. H. (1994). Mechanisms of sprouting in the adult central nervous system: cellular responses in areas of terminal degeneration and reinnervation in the rat hippocampus. *Neuroscience* 58, 705–725. doi: 10.1016/0306-4522(94)90449-9
- Filippov, V., Kronenberg, G., Pivneva, T., Reuter, K., Steiner, B., Wang, L. P., et al. (2003). Subpopulation of nestin-expressing progenitor cells in the adult murine hippocampus shows electrophysiological and morphological characteristics of astrocytes. *Mol. Cell. Neurosci.* 23, 373–382. doi: 10.1016/S1044-7431(03)00060-5
- Fukuda, S., Kato, F., Tozuka, Y., Yamaguchi, M., Miyamoto, Y., and Hisatsune, T. (2003). Two distinct subpopulations of nestin-positive cells in adult mouse dentate gyrus. *J. Neurosci.* 23, 9357–9366. doi: 10.1523/JNEUROSCI.23-09357.2003
- Gage, F. H. (2000). Mammalian neural stem cells. *Science* 287, 1433–1438. doi: 10.1126/science.287.5457.1433
- Gage, F. H., Olejniczak, P., and Armstrong, D. M. (1988). Astrocytes are important for sprouting in the septohippocampal circuit. *Exp. Neurol.* 102, 2–13. doi: 10.1016/0014-4886(88)90073-8
- Gebara, E., Bonaguidi, M. A., Beckervordersandforth, R., Sultan, S., Udry, F., Gijss, P. J., et al. (2016). Heterogeneity of radial glia-like cells in the adult hippocampus. *Stem Cells* 34, 997–1010. doi: 10.1002/stem.2266
- Kronenberg, G., Reuter, K., Steiner, B., Brandt, M. D., Jessberger, S., Yamaguchi, M., et al. (2003). Subpopulations of proliferating cells of the adult hippocampus respond differently to physiologic neurogenic stimuli. *J. Comp. Neurol.* 467, 455–463. doi: 10.1002/cne.10945
- Lindvall, O., and Kokaia, Z. (2006). Stem cells for the treatment of neurological disorders. *Nature* 441, 1094–1096. doi: 10.1038/nature04960
- Llorens-Bobadilla, E., Zhao, S., Baser, A., Saiz-Castro, G., Zwaldlo, K., and Martin-Villalba, A. (2015). Single-cell transcriptomics reveals a population of dormant neural stem cells that become activated upon brain injury. *Cell Stem Cell* 3, 329–340. doi: 10.1016/j.stem.2015.07.002

- Lugert, S., Basak, O., Knuckles, P., Haussler, U., Fabel, K., Gotz, M., et al. (2010). Quiescent and active hippocampal neural stem cells with distinct morphologies respond selectively to physiological and pathological stimuli and aging. *Cell Stem Cell* 6, 445–456. doi: 10.1016/j.stem.2010.03.017
- Maslov, A. Y., Barone, T. A., Plunkett, R. J., and Pruitt, S. C. (2004). Neural stem cell detection, characterization, and age-related changes in the subventricular zone of mice. *J. Neurosci.* 24, 1726–1733. doi: 10.1523/JNEUROSCI.4608-03.2004
- Mignone, J. L., Kukekov, V., Chiang, A. S., Steindler, D., and Enikolopov, G. (2004). Neural stem and progenitor cells in nestin-GFP transgenic mice. *J. Comp. Neurol.* 469, 311–324. doi: 10.1002/cne.10964
- Pons-Espinal, M., de Luca, E., Marzi, M. J., Beckervordersandforth, R., Armirotti, A., Nicassio, F., et al. (2017). Synergic functions of miRNAs determine neuronal fate of adult neural stem cells. *Stem Cell Rep.* 11, 1046–1061. doi: 10.1016/j.stemcr.2017.02.012
- Ray, J., and Gage, F. H. (2006). Differential properties of adult rat and mouse brain-derived neural stem/progenitor cells. *Mol. Cell. Neurosci.* 31, 560–573. doi: 10.1016/j.mcn.2005.11.010
- Rolando, C., Ermi, A., Grison, A., Beattie, R., Engler, A., Gokhale, P. J., et al. (2016). Multipotency of adult hippocampal NSCs in vivo is restricted by Drosha/NFIB. *Cell Stem Cell* 19, 653–662. doi: 10.1016/j.stem.2016.07.003
- Seaberg, R. M., and van der Kooy, D. (2002). Adult rodent neurogenic regions: the ventricular subependyma contains neural stem cells, but the dentate gyrus contains restricted progenitors. *J. Neurosci.* 22, 1784–1793. doi: 10.1523/JNEUROSCI.22-05-01784.2002
- Seri, B., Garcia-Verdugo, J. M., McEwen, B. S., and Alvarez-Buylla, A. (2001). Astrocytes give rise to new neurons in the adult mammalian hippocampus. *J. Neurosci.* 21, 7153–7160. doi: 10.1523/JNEUROSCI.21-18-07153.2001
- Song, H. J., Stevens, C. F., and Gage, F. H. (2002). Neural stem cells from adult hippocampus develop essential properties of functional CNS neurons. *Nat. Neurosci.* 5, 438–445. doi: 10.1038/nn844
- Steiner, B., Klempin, F., Wang, L., Kott, M., Kettenmann, H., and Kempermann, G. (2006). Type-2 cells as link between glial and neuronal lineage in adult hippocampal neurogenesis. *Glia* 54, 805–814. doi: 10.1002/glia.20407
- Steiner, B., Kronenberg, G., Jessberger, S., Brandt, M. D., Reuter, K., and Kempermann, G. (2004). Differential regulation of gliogenesis in the context of adult hippocampal neurogenesis in mice. *Glia* 46, 41–52. doi: 10.1002/glia.10337
- Suh, H., Consiglio, A., Ray, J., Sawai, T., D'Amour, K. A., and Gage, F. H. (2007). In vivo fate analysis reveals the multipotent and self-renewal capacities of Sox2(+) neural stem cells in the adult hippocampus. *Cell Stem Cell* 1, 515–528. doi: 10.1016/j.stem.2007.09.002
- Suh, H., Deng, W., and Gage, F. H. (2009). Signaling in adult neurogenesis. *Annu. Rev. Cell Dev. Biol.* 25, 253–275. doi: 10.1146/annurev.cellbio.042308.113256
- Venere, M., Han, Y. G., Bell, R., Song, J. S., Alvarez-Buylla, A., and Bbleloch, R. (2012). Sox1 marks an activated neural stem/progenitor cell in the hippocampus. *Development* 139, 3938–3949. doi: 10.1242/dev.081133
- Zhang, Y., and Barres, B. A. (2010). Astrocyte heterogeneity: an underappreciated topic in neurobiology. *Curr. Opin. Neurobiol.* 20, 588–594. doi: 10.1016/j.conb.2010.06.005
- Zhao, C., Deng, W., and Gage, F. H. (2008). Mechanisms and functional implications of adult neurogenesis. *Cell* 132, 645–660. doi: 10.1016/j.cell.2008.01.033

Conflict of Interest Statement: The authors declare that the research was conducted in the absence of any commercial or financial relationships that could be construed as a potential conflict of interest.

Copyright © 2018 Suh, Zhou, Fernandez-Carasa, Clemenson, Pons-Espinal, Ro, Marti, Rayu, Gage and Consiglio. This is an open-access article distributed under the terms of the Creative Commons Attribution License (CC BY). The use, distribution or reproduction in other forums is permitted, provided the original author(s) and the copyright owner(s) are credited and that the original publication in this journal is cited, in accordance with accepted academic practice. No use, distribution or reproduction is permitted which does not comply with these terms.

Patient-Specific iPSC-Derived Astrocytes Contribute to Non-Cell-Autonomous Neurodegeneration in Parkinson's Disease

Angelique di Domenico,^{1,2,14} Giulia Carola,^{1,2,14} Carles Calatayud,^{1,2,3} Meritxell Pons-Espinal,^{1,2} Juan Pablo Muñoz,⁴ Yvonne Richaud-Patin,^{3,5} Irene Fernandez-Carasa,^{1,2} Marta Gut,⁶ Armida Faella,^{1,2} Janani Parameswaran,^{1,2} Jordi Soriano,^{7,8} Isidro Ferrer,^{2,9} Eduardo Tolosa,^{9,10} Antonio Zorzano,⁴ Ana Maria Cuervo,¹¹ Angel Raya,^{3,5,12,15,*} and Antonella Consiglio^{1,2,13,15,*}

¹Department of Pathology and Experimental Therapeutics, Bellvitge University Hospital-IDIBELL, Hospitalet de Llobregat, Barcelona 08908, Spain

²Institute of Biomedicine of the University of Barcelona (IBUB), Barcelona 08028, Spain

³Center of Regenerative Medicine in Barcelona (CMRB), Hospital Duran i Reynals, Hospitalet de Llobregat, Barcelona 08908, Spain

⁴Institute for Research in Biomedicine (IRB), Carrer Baldori Reixac 10, Barcelona 08028, Spain

⁵Centre for Networked Biomedical Research on Bioengineering, Biomaterials, and Nanomedicine (CIBER-BBN), Madrid 28029, Spain

⁶Centre Nacional d'Anàlisi Genòmica (CNAG-CRG), Parc Científic de Barcelona, Barcelona 08028, Spain

⁷Departament de Física de la Matèria Condensada, Universitat de Barcelona, Barcelona 08028, Spain

⁸Universitat de Barcelona Institute of Complex Systems (UBICS), Barcelona 08028, Spain

⁹Centre for Networked Biomedical Research on Neurodegenerative Diseases (CIBERNED), Madrid 28049, Spain

¹⁰Department of Neurology, Hospital Clinic de Barcelona, Institut d'Investigacions Biomèdiques August Pi i Sunyer (IDIBAPS), University of Barcelona (UB), Barcelona 08036, Spain

¹¹Albert Einstein College of Medicine, Bronx, NY 10461, USA

¹²Institució Catalana de Recerca i Estudis Avançats (ICREA), Barcelona 08010, Spain

¹³Department of Molecular and Translational Medicine, University of Brescia, Brescia 25121, Italy

¹⁴Co-first author

¹⁵Co-senior author

*Correspondence: araya@cmrb.eu (A.R.), consiglio@ub.edu (A.C.)

<https://doi.org/10.1016/j.stemcr.2018.12.011>

SUMMARY

Parkinson's disease (PD) is associated with the degeneration of ventral midbrain dopaminergic neurons (vmDAn) and the accumulation of toxic α -synuclein. A non-cell-autonomous contribution, in particular of astrocytes, during PD pathogenesis has been suggested by observational studies, but remains to be experimentally tested. Here, we generated induced pluripotent stem cell-derived astrocytes and neurons from familial mutant *LRRK2* G2019S PD patients and healthy individuals. Upon co-culture on top of PD astrocytes, control vmDAn displayed morphological signs of neurodegeneration and abnormal, astrocyte-derived α -synuclein accumulation. Conversely, control astrocytes partially prevented the appearance of disease-related phenotypes in PD vmDAn. We additionally identified dysfunctional chaperone-mediated autophagy (CMA), impaired macroautophagy, and progressive α -synuclein accumulation in PD astrocytes. Finally, chemical enhancement of CMA protected PD astrocytes and vmDAn via the clearance of α -synuclein accumulation. Our findings unveil a crucial non-cell-autonomous contribution of astrocytes during PD pathogenesis, and open the path to exploring novel therapeutic strategies aimed at blocking the pathogenic cross talk between neurons and glial cells.

INTRODUCTION

Parkinson's disease (PD) is the second most prevalent neurodegenerative disease after Alzheimer's disease, affecting 7 to 10 million people worldwide (Global Burden of Disease Study Collaborators, 2015). PD is characterized by a significant loss of ventral midbrain dopaminergic neurons (vmDAn) in the substantia nigra pars compacta. The presence of intracellular protein aggregates of α -synuclein (α -syn) in the surviving vmDAn has been reported in post-mortem PD tissue (Greenamyre and Hastings, 2004). Most PD cases are sporadic (85%), but familial mutations are accountable for 15% of patients (Lill, 2016). Mutations in the gene encoding leucine-rich repeat kinase 2 (*LRRK2*), causing an autosomal dominant form of PD, account for 5% of familial cases and 2% of sporadic cases (Gilks et al., 2005; Nichols et al., 2005). *LRRK2* is a highly complex protein with both GTPase and protein kinase domains

involved in several cellular functions, including autophagy (Cookson, 2016; Orenstein et al., 2013; Su et al., 2015).

Correlations between mutant *LRRK2* and several pathogenic mechanisms linked to PD progression have been previously reported, including alterations in autophagy and consequent accumulation of α -syn (Cookson, 2017). Neuronal mutant *LRRK2* toxicity was found to depend on *LRRK2* levels and α -syn accumulation as opposed to kinase activity or inclusion bodies in induced pluripotent stem cell (iPSC)-derived neurons (Skibinski et al., 2014). During PD pathogenesis, mutant *LRRK2* was found to directly bind LAMP2A, the receptor responsible for chaperone-mediated autophagy (CMA) normally used by both *LRRK2* and α -syn for degradation (Orenstein et al., 2013). This binding blocks the proper functioning of the CMA translocation complex, resulting in defective CMA, leading to the accumulation of α -syn and cell death.





iPSCs derived from healthy individuals and patients have accelerated advances in developing genuinely human experimental models of diseases (Zeltner and Studer, 2015). In the case of PD, previous studies by our groups and others have generated iPSCs from patients with PD associated with *LRRK2* mutations, and described the appearance of disease-specific phenotypes in iPSC-derived neurons, including impaired axonal outgrowth and deficient autophagic vacuole clearance (Heman-Ackah et al., 2017; Nguyen et al., 2011; Sanchez-Danes et al., 2012; Skibinski et al., 2014). Moreover, dopaminergic (DA) neurons from *LRRK2*-mutant iPSCs displayed alterations in CMA that were, at least in part, responsible for the abnormal accumulation of α -syn observed in these cells, which predated any morphological signs of neurodegeneration (Orenstein et al., 2013).

Studies investigating PD pathogenesis have been mostly focused on the mechanisms underlying vmdAn degeneration and death. However, there is evidence of astrocytes accumulating α -syn during PD through postmortem analysis (Braak et al., 2007; Wakabayashi et al., 2000). Altered α -syn released by axon terminals in the surrounding synapses is taken up by astrocytes, supporting the hypothesis of the spread of α -syn through neuron-astrocyte interactions (Braak et al., 2007; Lee et al., 2010). Overexpression of mutant *SNCA* in primary astrocytes altered their normal functioning and impaired proper blood-brain barrier control and glutamate homeostasis, and eventually resulted in a significant loss of vmdAns (Gu et al., 2010). In a study using human brain homogenates from PD patients with Lewy bodies, α -syn was found to be taken up and spread from astrocytes to neurons, leading to neuronal death (Cavaliere et al., 2017). As a result, a role of astrocyte dysfunction in PD pathogenesis is emerging (Booth et al., 2017).

In the present study, we generated patient-specific iPSC-derived astrocytes and vmdAns from PD patients with the *LRRK2* G2019S mutation and healthy individuals. We consistently generated a population of human vmdAns *in vitro* that expressed postmitotic dopaminergic markers and fired action potentials. Subsequently, we co-cultured healthy iPSC-derived vmdAns with iPSC-derived astrocytes expressing the mutated form of *LRRK2* associated with PD. In co-culture experiments, we detected a significant decrease in the number of vmdAns in the presence of *LRRK2*-PD astrocytes, which correlated with the abnormal accumulation of astrocyte-derived α -syn. Conversely, control astrocytes were able to partially rescue disease-related phenotypes in *LRRK2*-PD vmdAns during co-culture. A more in-depth investigation revealed impaired autophagic machinery, as well as progressive accumulation of endogenous α -syn in PD astrocytes, compared with control astrocytes. By treating the cells with an activator

Table 1. Summary of the Healthy Controls and Patients Used in This Study

Code	Status	Sex	Age at Biopsy	Mutation	Isogenic Control
SP09	control	M	66	no	
SP11	control	M	52	no	
SP17	control	F	48	no	
SP06	Parkinson's disease	M	44	<i>LRRK2</i> G2019S	
SP12	Parkinson's disease	F	63	<i>LRRK2</i> G2019S	
SP13	Parkinson's disease	F	68	<i>LRRK2</i> G2019S	<i>LRRK2</i> G2019S corrected

of CMA, we were able to prevent the appearance of PD-related phenotypes in patients' astrocytes. Overall, our findings represent a direct indication that dysfunctional astrocytes play a crucial role during PD pathogenesis and may have broad implications for future intervention in early stages of PD.

RESULTS

Generation and Characterization of iPSC-Derived Patient-Specific Astrocytes

To establish an *in vitro* human cellular model for dissecting the interplay between neurons and astrocytes in PD, we first derived astrocyte-like cells from iPSCs, using a previously published protocol (Serio et al., 2013). Specifically, astrocyte cultures were successfully established from iPSC lines from three PD patients carrying the G2019S mutation in the *LRRK2* gene (PD SP06, PD SP12, and PD SP13) and two healthy age-matched controls (Ctrl SP09 and Ctrl SP17) (see Table 1 and Tables S1 and S2 for a summary of the iPSC lines used, and Experimental Procedures for details on their origin). Immunocytochemistry (ICC) detection of key astrocyte markers showed robust expression of CD44, glial fibrillary acidic protein (GFAP), and S100 calcium-binding protein β (S100 β), as well as of the excitatory amino acid transporter 2 (EAAT2, also known as GLT1), in all human iPSC-derived astrocytes (Figure 1A). No evident contamination by other cell types, such as neurons or oligodendroglial progenitors, was found as assessed by immunostaining with anti-MAP2 or NG2 antibody, respectively (Figures 1A and 1B). The astrocytic identity was further confirmed by quantitative RT-PCR of *GFAP* and additional astrocyte-specific genes, including *MLC1*, *SOX9*, *ALDH1L1*, *AQP4*, *DIO2*, and *SLC4A4*, which were expressed in Ctrl and PD astrocytes, and in human primary astrocytes, but not in iPSCs (Figures S1A–S1C).

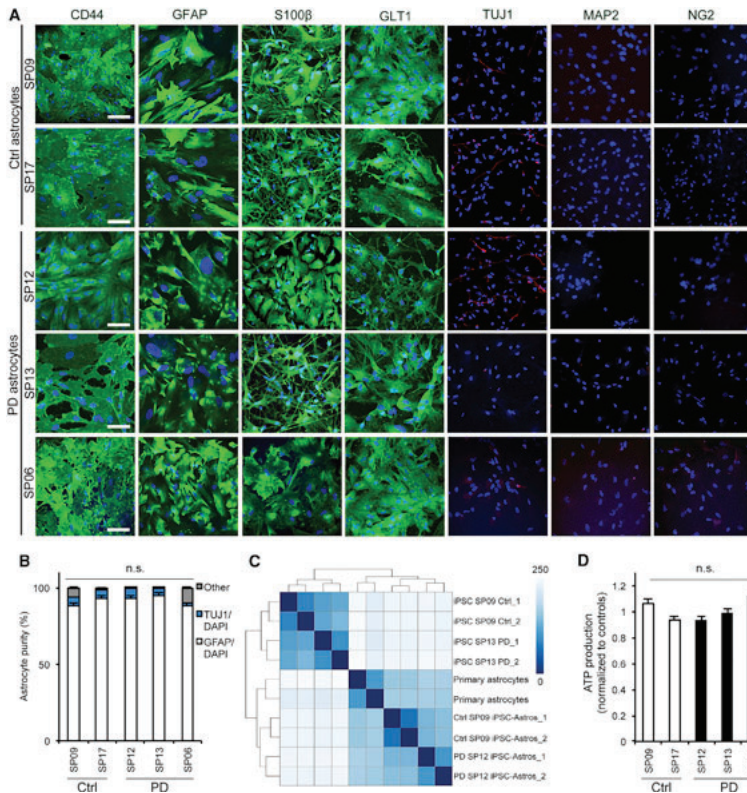


Figure 1. iPSC-Derived Patient-Specific Astrocyte Generation and Characterization

(A) Representative ICC images of astrocytes from two Ctrl iPSC lines (Ctrl SP09 and Ctrl SP17) and three PD iPSC lines (PD SP12, PD SP13, and PD SP06) staining positive for CD44 (astrocytic precursor marker), GFAP (general astrocytes), S100β (mature astrocytes), and GLT1 (excitatory amino acid transporter 2), and negative for TUJ1 (immature neurons), MAP2 (mature neurons), and NG2 (oligodendrocytes) expression. Number of independent astrocyte lines generated from iPSC per patient = 3. Number of independent experiments per astrocyte line generated = 3. Scale bar, 100 μm.

(B) Astrocyte cultures are composed of approximately 95% astrocytes, 4% neurons, and 1% other (n = 3).

(C) Heatmap showing sample similarities taking the \log_2 transformed data and Euclidean distances between samples. iPSC-derived astrocyte (Ctrl SP09 and PD SP12) samples cluster closer to the human primary astrocytes than the corresponding iPSC group (n = 2).

(D) Functional ATP production luminescence (counts normalized to controls) in both Ctrl (SP09 and SP17) and PD (SP13, SP12, and SP06) astrocytes (n = 3). Data are expressed as mean ± SEM, unpaired two-tailed Student's t test.

To validate astrocyte cell type identity, we also tested the expression of astrocyte-specific genes revealed by the Human Astrocyte RNA-Seq database (www.brainrnaseq.org/) in our iPSC-derived astrocytes, through RNA sequencing. We found that the transcriptomic profile of

both Ctrl and PD iPSC-derived astrocytes was closer to that of human primary astrocytes than to that of their corresponding iPSC line, thus confirming their identity (Figure 1C). We next determined the functional maturation of iPSC-derived astrocytes by confirming their capacity

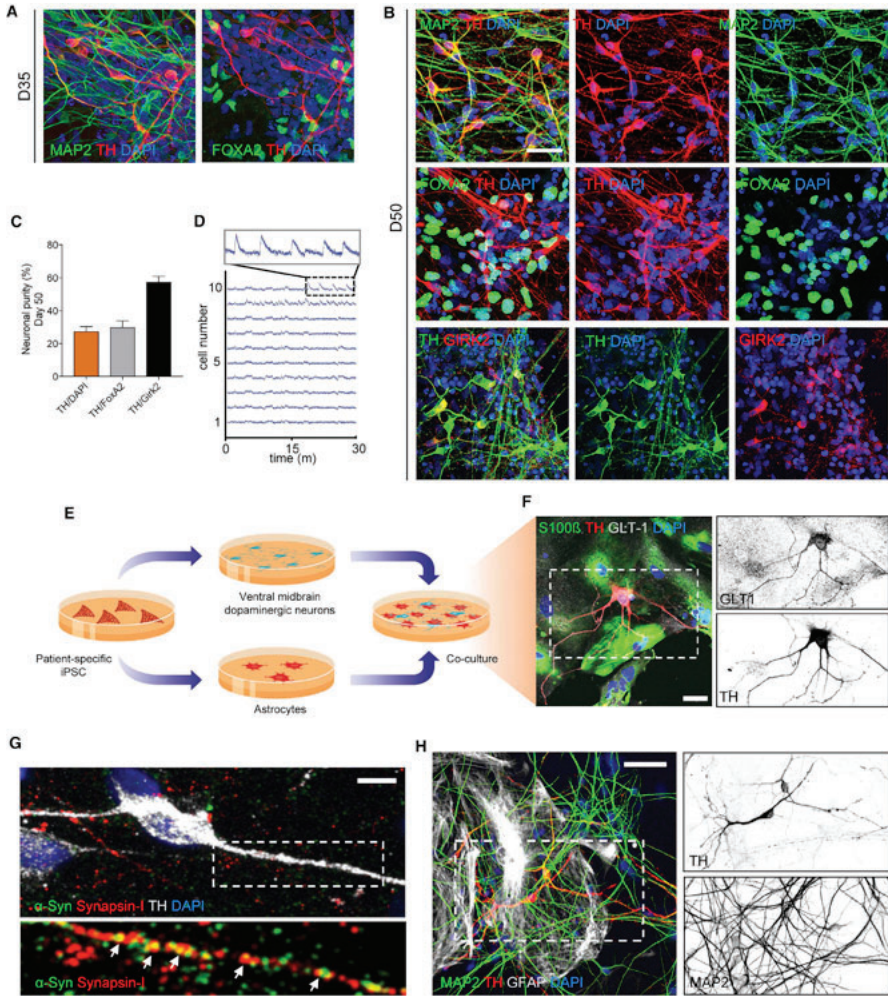


Figure 2. vmDAN Generation, Characterization, and Co-culture Setup

(A and B) Representative immunofluorescence images of Ctrl SP11 vmDAN after (A) 35 or (B) 50 days of neuronal differentiation. iPSC-derived neural cultures express markers specific for neurons (MAP2), DANs (TH), and midbrain-type DANs (FOXA2 and GIRK2). Scale bar, 20 μ m.

(C) Percentage of differentiated cells that stained positive for TH and double positive for TH and FOXA2 and TH and GIRK2 after 50 days of differentiation (n = 4).

(legend continued on next page)



to produce ATP (Figure 1D) and propagate intercellular Ca^{2+} waves (Figures S1D–S1H). Indeed, by using the Fluo-4 AM Ca^{2+} indicator, recordings from Ctrl and PD astrocytes showed a heterogeneous pattern of Ca^{2+} fluctuations under basal conditions, revealing their functionality. All together, these data support the successful generation of highly pure populations of functionally equivalent astrocyte-like cells, which represent a continuous source of human Ctrl and PD astrocytes for subsequent analyses.

Generation of vMDAns and Setup of Neuron-Astrocyte Co-culture System

To investigate whether astrocytes contribute to PD pathogenesis, we established a co-culture system of iPSC-derived astrocytes and iPSC-derived vMDAns. PD vMDAns were generated from iPSC lines from two PD patients carrying the G2019S mutation in the *LRRK2* gene (iPSC lines PD SP12 and PD SP13), whereas Ctrl vMDAns were obtained from two independent iPSC clones (Ctrl SP11 and Ctrl SP11#4) from a healthy age-matched control (see Tables 1, S1, and S2 for a summary of the iPSC lines used). To differentiate iPSCs toward vMDAns, we used a combination of two previously published (Chambers et al., 2009; Kriks et al., 2011) midbrain floor-plate differentiation protocols that was comparably effective in all iPSC lines analyzed. Under these conditions, ~20% of cells in the cultures were committed to DA neuron fate by day 35 of differentiation, as judged by the expression of tyrosine hydroxylase (TH) and forkhead box protein A2 (FOXA2) (Figure 2A). By day 50 of differentiation, the percentage of TH⁺ neurons reached ~30%, most of which also expressed the A9-domain-specific marker G-protein-activated inward rectifier potassium channel 2 (GIRK2), and displayed spontaneous action potential firing (Figures S2B–S2D). For co-culture experiments with control astrocytes, we dissociated vMDAn cultures after 35 days of differentiation and plated them onto a confluent layer of Ctrl iPSC-derived astrocytes (Figure 2E). After 4 weeks of co-culture, we found that astrocyte-neuron glutamate exchange was present through glutamate transporter 1 (GLT1) expression (Figure 2F) and neuronal synapse formation (Figure 2G). Accordingly, an overall healthy

neuronal network comprising MAP2-positive cells was formed upon co-culture (Figure 2H).

Control vMDAns Show Morphological Signs of Neurodegeneration when Co-cultured with PD Astrocytes

We then examined the effects of astrocytes expressing mutated *LRRK2* on the survival of Ctrl iPSC-derived vMDAns upon co-culture (Figure 3A). After 2 weeks of co-culture with PD astrocytes, Ctrl vMDAns displayed morphological alterations, including shortened neurites, and significantly decreased cell survival compared with co-cultures with Ctrl astrocytes (Figures S2A–S2C). These alterations were much more evident after 4 weeks of co-culture, when Ctrl vMDAns cultured on top of PD astrocytes showed extensive signs of neurodegenerative phenotypes (fewer and shorter neurites, and abundance of beaded-necklace neurites) and severely compromised cell survival (less than ~25% of control), compared with co-cultures with control astrocytes (Figures 3B–3F). The fact that the numbers of vMDAns did not change significantly during the co-culture with control astrocytes, but progressively declined when co-cultured with PD astrocytes, strongly suggests that vMDAns were lost under the latter conditions as a result of neurodegeneration, rather than a blockade in vMDAn differentiation or maturation.

Viability tests of both Ctrl and PD astrocytes at 2 and 4 weeks of co-culture revealed highly similar values, indicating that neurodegenerative signs displayed by Ctrl vMDAns were not caused by a dying PD astrocyte (Figure S2D). Interestingly, vMDAn neurodegeneration upon co-culture with PD astrocytes was specific to this type of neuron, because non-dopaminergic neurons (TH⁻/MAP2⁺) did not significantly change in numbers or morphology after co-culture with Ctrl or PD astrocytes (Figures S2E–S1J). All together, these results indicate a neurotoxic capacity of PD astrocytes toward vMDAns, with no effects on other neuronal types concomitantly present in cultures.

Control vMDAns Accumulate α -syn when Co-cultured with PD Astrocytes

Given the relevance of α -syn in the context of PD pathogenesis (Braak et al., 2007), we sought to examine whether

(D) Calcium wave flux recording over 30 min with calcium tracer Fluo-8 AM of vMDAns at day 50 (n = 3).

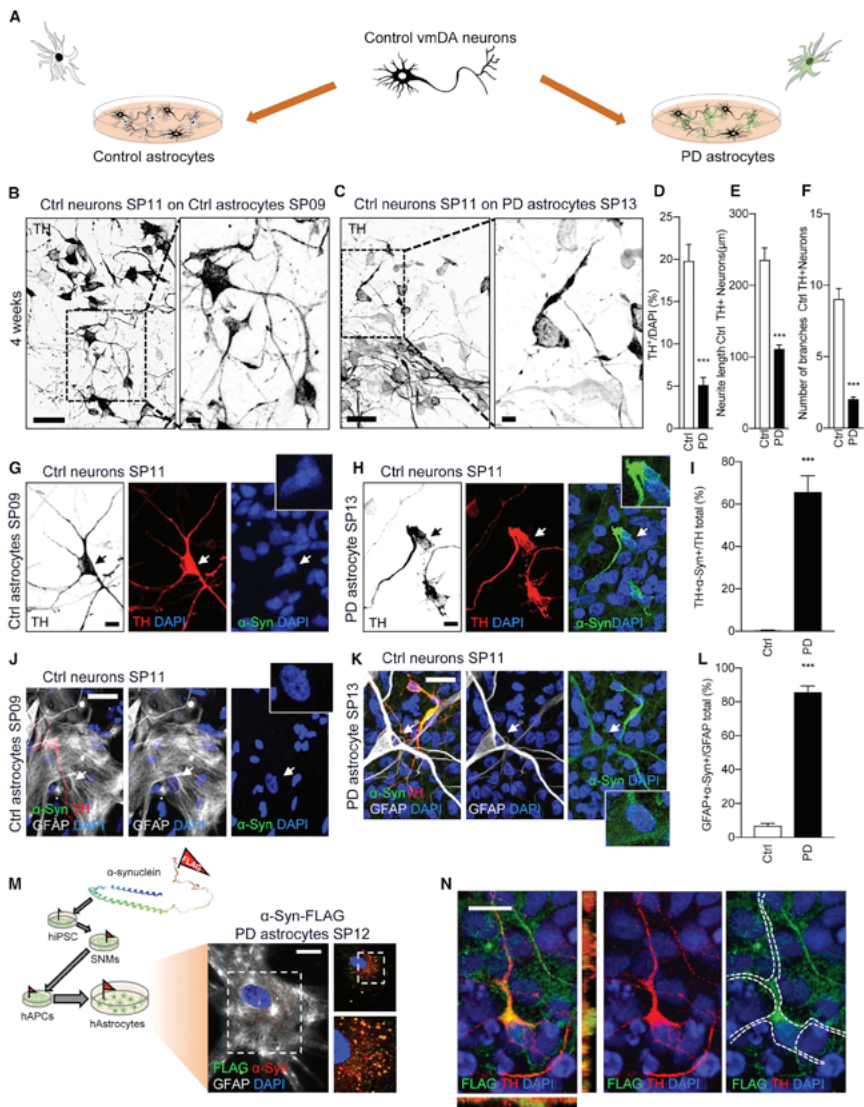
(E) Diagram of co-culture system.

(F) Representative ICC images of 4-week co-culture staining positive for Ctrl SP11 vMDAns (TH), Ctrl SP17 astrocytes (S100 β), excitatory amino acid transporter 2 (GLT1), and nuclear DAPI. Scale bar, 20 μ m.

(G) Representative ICC images of presynaptic markers α -syn and synapsin-1 of a Ctrl SP11 vMDAn (TH) on the top of Ctrl SP11 astrocytes after 4 weeks in co-culture. Scale bar, 10 μ m.

(H) Representative ICC images of Ctrl SP11 vMDAns (TH) and mature neurons (MAP2) on the top of Ctrl SP09 astrocytes (GFAP) during a 4-week co-culture period. Scale bar, 20 μ m.

Boxed area on the left in (F), (G), and (H) is shown on the right.



(legend on next page)



vmDAns co-cultured with PD astrocytes abnormally accumulated α -syn. α -syn was barely detectable in the cytoplasm of Ctrl vmDAns cultured alone (data not shown) or when co-cultured with Ctrl astrocytes (Figure 3G). In contrast, Ctrl vmDAns accumulated high levels of α -syn throughout the neurites and cell body after 4 weeks of co-culture with PD astrocytes (Figures 3H and 3I). Notably, while Ctrl astrocytes had undetectable levels of α -syn (Figure 3J), PD astrocytes displayed high levels of α -syn (Figures 3K and 3L), raising the intriguing possibility that α -syn from PD astrocytes might be transferred to Ctrl vmDAns. To directly address if this was the case, we genetically engineered two iPSC lines (representing one PD patient and one healthy control) using CRISPR/Cas9 technology so that the endogenous α -syn would be tagged with a FLAG peptide (α -syn-FLAG iPSC lines; Figures S2K and S2L and Tables S2 and S3). α -syn-FLAG-tagged astrocytes were generated and fully characterized (Figure S2M). As expected, PD α -syn-FLAG tagged astrocytes accumulated abnormally high levels of α -syn, which co-localized with anti-FLAG staining (Figure 3M). More importantly, the co-culture of Ctrl vmDAns on top of α -syn-FLAG-tagged PD astrocytes for 4 weeks resulted in FLAG-tagged α -syn accumulation in neurons, demonstrating the direct transfer of astrocytic α -syn to neurons (Figure 3N).

In addition to co-culturing cells with direct glia-neuron contact, we tested the effect of culturing Ctrl vmDAns with medium conditioned by Ctrl or PD astrocytes at

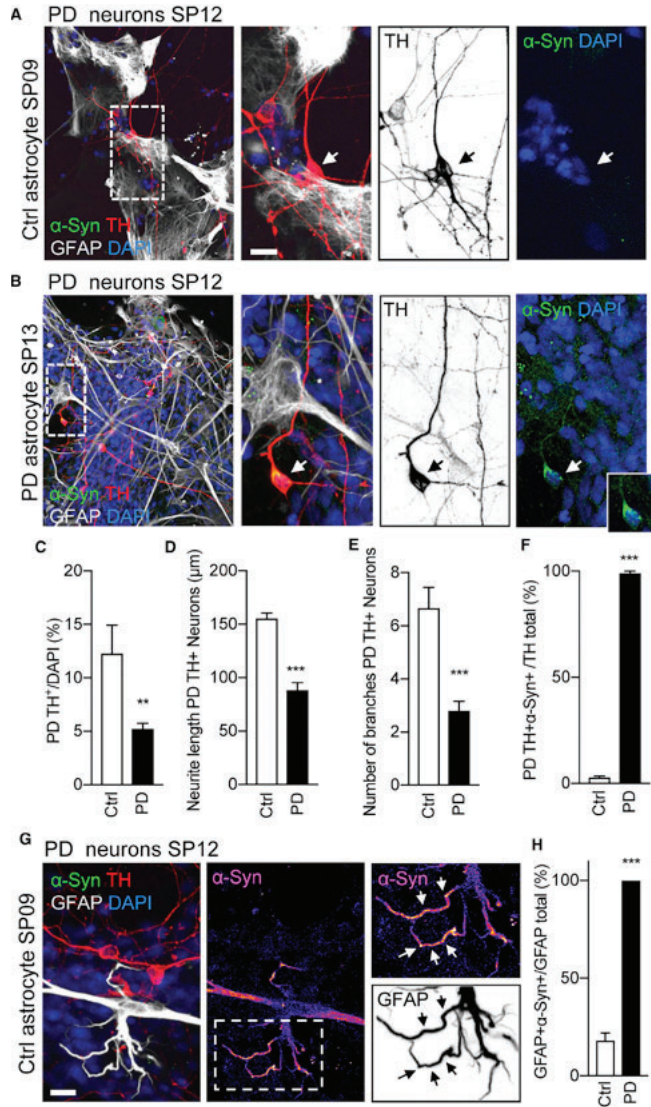
different concentrations (Figure S3A). Exposure of Ctrl vmDAns to PD astrocyte-conditioned medium for 1 week, even at low concentrations, resulted in α -syn accumulation, morphological alterations suggestive of neurodegeneration, and decreased cell survival (Figures S3B–S3H), indicating that PD astrocytes secrete a molecule(s) that is toxic to vmDAns. Direct uptake by vmDAns of α -syn from conditioned medium was tested by exposing Ctrl vmDAns to medium collected from PD α -syn-FLAG-tagged astrocytes (Figures S3I–S3J), suggesting that the neurotoxic effect of PD astrocytes on vmDAns is, at least in part, mediated by secretion of α -syn.

Control Astrocytes Partially Rescue Neurodegeneration of PD vmDAns

We have previously shown that vmDAns derived from PD-iPSCs show signs of neurodegeneration (including reduced numbers of neurites and neurite arborization, as well as accumulation of abnormal α -syn in the soma) after 50 days of culture, which are not evident in Ctrl vmDAns (Sanchez-Danes et al., 2012). To test whether the neurodegeneration could be rescued or prevented by healthy astrocytes, we co-cultured PD vmDAns with Ctrl or PD astrocytes. After a 4-week co-culture, PD vmDAns showed a partially recovered neurite number and complex neurite arborization when co-cultured on control astrocytes, compared with co-cultures with PD astrocytes (Figures 4A–4E). This rescue was partial, since PD vmDAns

Figure 3. Ctrl Neurons Show Signs of Neurodegeneration and Accumulate α -syn when Co-cultured with PD Astrocytes

- (A) Scheme representing co-culture system of Ctrl neurons on the top of Ctrl or PD astrocytes for 4 weeks.
- (B and C) Representative ICC images of tyrosine hydroxylase (TH, black) from co-cultures of Ctrl SP11 neurons with (B) Ctrl SP09 astrocytes and (C) PD SP13 astrocytes for 4 weeks. Images on the right show a magnification of the area boxed in the left images; scale bars, (left) 20 μ m and (right) 0.2 μ m.
- (D) Percentage of TH⁺/DAPI of Ctrl SP11 and Ctrl SP11#4 neurons when co-cultured with Ctrl SP09, Ctrl SP17, or PD SP12, PD SP13, and PD SP06 astrocytes for 4 weeks (n = 3 per combination).
- (E and F) (E) Neurite length quantification and (F) number of branches of Ctrl SP11 TH-positive neurons and Ctrl SP11#4 TH-positive neurons when co-cultured on Ctrl SP09, Ctrl SP17, and Ctrl SP11 astrocytes or PD SP12, PD SP13, and PD SP06 astrocytes for 4 weeks (n = 3); 30 neurons counted per experiment.
- (G and H) Representative ICC images of Ctrl SP11 vmDAns co-cultured with (G) Ctrl SP09 and (H) PD SP13 astrocytes after 4 weeks and stained for TH (vmDan), α -syn, and DAPI. Arrows indicate the selected cell for which an insert is shown at higher magnification. Scale bar, 0.2 μ m.
- (I) Quantitative analysis of the percentage of vmDAns stained positive for α -syn when Ctrl SP11 and Ctrl SP11#4 neurons were co-cultured with Ctrl SP09, Ctrl SP17, or PD SP12, PD SP13, and PD SP06 astrocytes for 4 weeks (n = 3).
- (J and K) Representative ICC images of (J) Ctrl SP09 or (K) PD SP13 astrocytes co-cultured with Ctrl SP11 vmDAns for 4 weeks, stained for TH (vmDan), GFAP (astrocytes), α -syn, and DAPI. Arrows indicate the selected cell for which an insert is shown at higher magnification. Scale bar, 20 μ m.
- (L) Quantitative analysis of the percentage of astrocytes stained positive for α -syn when Ctrl SP11 and Ctrl SP11#4 neurons were co-cultured with Ctrl SP09, Ctrl SP17, or PD SP12, PD SP13, and PD SP06 astrocytes for 4 weeks (n = 3).
- (M) Scheme representing the generation of CRISPR/Cas9 edited α -syn-FLAG astrocyte line. Representative image of α -syn-FLAG PD SP12 astrocyte (GFAP) showing perfect α -syn (red) and FLAG (green) co-localization. Scale bar, 20 μ m.
- (N) Representative ICC image depicting astrocyte-derived FLAG (green) inside of a TH-positive Ctrl SP11 neuron (red) during a 4-week co-culture period with PD SP12 α -syn-FLAG astrocytes (n = 3). Dashed line shows the outline of the cell. Scale bar, 10 μ m.
- Data are expressed as mean \pm SEM, unpaired two-tailed Student's t test, ***p < 0.001.



(legend on next page)



co-cultured with control astrocytes did not reach the levels of cell survival and complex neurite arborization seen in co-cultures of Ctrl vmdAns and Ctrl astrocytes (compare Figures 4A and 4C–4E with 3B and 4D–4F). Moreover, co-culture with Ctrl astrocytes also prevented the accumulation of α -syn in PD vmdAns that was evident in co-cultures with PD astrocytes (Figures 4A, 4B, and 4F). Notably, most Ctrl astrocytes when co-cultured with PD vmdAns adopted a flat morphology with moderate levels of α -syn; however, some harbored a hypertrophic morphology with retracted processes that accumulated very high levels of α -syn (Figures 4G and 4H), suggesting that reactive astrocytes may contribute to the clearance of vmdAn α -syn accumulation. Culture of PD vmdAns with medium conditioned by Ctrl astrocytes also rescued cell survival, morphological alterations, and α -syn accumulation (Figures S3K–S3S), indicating that direct neuronal-glia contact was not necessary for the neuroprotective effect.

We next investigated the causative role of the genetic background of patient-specific astrocyte cells by ectopically expressing mutated *LRRK2* G2019S in Ctrl astrocytes. In these experiments, Ctrl astrocytes were transfected with a plasmid expressing V5-tagged *LRRK2* G2019S, or with a Ctrl plasmid expressing GFP, and analyzed 7 days after transfection for the presence of α -syn. Astrocytes transfected with *LRRK2* G2019S exhibited diffuse cytoplasmic accumulations of α -syn (Figure S4A), which were not present in GFP-transfected cells (Figure S4B). The transfection efficiencies (30%–40%, as evaluated by co-staining for V5/GFAP or GFP/GFAP) were comparable under both conditions (Figure S4C). Next, we co-cultured Ctrl vmdAns for 4 weeks with *LRRK2* G2019S-transfected Ctrl astrocytes, or with GFP-transfected astrocytes as a control, and we found α -syn accumulation in 50% of the TH⁺ neurons only in co-cultures with *LRRK2* G2019S-transfected astrocytes (Figures S4D–S4G). Overall in these cultures we found

decreased survival of vmdAns and evident morphological alterations (Figures S4H–S4I), including fewer and shorter neurites compared with vmdAns cultured on top of GFP-transfected astrocytes, indicating that the expression of pathogenic *LRRK2* in Ctrl astrocytes is deleterious for the survival of dopaminergic neurons.

For the converse experiment, we generated isogenic PD astrocytes lacking the *LRRK2* G2019S mutation by CRISPR/Cas9-mediated gene editing of PD iPSCs (iPSC line PD SP13, from here on referred to as PD iso), and fully characterized these cells (Figures S5A–S5E). Abnormal α -syn accumulation did not occur in gene-corrected astrocytes, in contrast with their isogenic mutant counterparts (Figures S5F and S5G). Moreover, co-culturing gene-corrected astrocytes with Ctrl vmdAns for 4 weeks prevented the accumulation of α -syn and decrease in neuron survival observed when Ctrl vmdAns were co-cultured with PD astrocytes (Figures S5H–S5J), further supporting that the expression of mutant *LRRK2* in astrocytes is pathogenic to Ctrl vmdAns.

Dysfunctional Chaperone-Mediated Autophagy and Progressive α -syn Accumulation in PD Astrocytes

Since PD astrocytes displayed higher levels of α -syn compared with controls, we next investigated possible differences in α -syn turnover in these cells. Degradation of α -syn in lysosomes occurs in large extent through CMA (Cuervo et al., 2004; Martinez-Vicente et al., 2008). To investigate possible changes in CMA in PD astrocytes, we first stained at 6 and 14 days for both α -syn and LAMP2A, the receptor for CMA (Figures 5A and S6A). Ctrl astrocytes showed LAMP2A in the perinuclear area (perinuclear lysosomal positioning occurs during CMA activation; Kiffin et al., 2004) and barely detectable levels of α -syn at both 6 and 14 days (Figures 5A, 5B, and S6A). In contrast, PD astrocytes displayed LAMP2A-positive vesicles all around

Figure 4. PD Neurons Restore Arborized Morphology and Accumulate Less α -syn when Co-cultured with Ctrl Astrocytes

(A and B) Representative ICC images of PD SP12 vmdAns during 4-week co-cultures with (A) Ctrl SP09 or (B) PD SP13 astrocytes stained for TH (vmdAns), α -syn, GFAP (astrocytes), and DAPI. Images on the right show a magnification of the area boxed in the left images. Arrows indicate the selected cell for which an insert is shown at higher magnification with α -syn accumulation. Scale bar, 20 μ m.

(C) Quantitative analysis of the percentage of PD SP12 vmdAns remaining after 4-week co-culture with Ctrl SP09, PD SP13, and PD SP12 astrocytes (n = 3).

(D and E) (D) Neurite length quantification and (E) number of branches of PD SP12 TH-positive neurons when co-cultured on PD SP12 or PD SP13 astrocytes for 4 weeks compared with the wild-type condition Ctrl SP11 neurons on Ctrl SP09, Ctrl SP17, and Ctrl SP11 astrocytes for 4 weeks (n = 3); 40 neurons counted per experiment.

(F) Quantitative analysis of the percentage of PD SP12 vmdAns that stained positive for α -syn when co-cultured on the top of Ctrl SP09, Ctrl SP17, Ctrl SP11, PD SP13, and PD SP12 astrocytes for 4 weeks (n = 3).

(G) Immunofluorescence analysis of PD SP12 neurons on the top of Ctrl SP09 astrocytes stained for TH, GFAP, α -syn, and DAPI. Images on the right show a magnification of the area boxed in the left image. Arrows in the inset shows α -syn accumulation inside Ctrl SP09 astrocyte processes. Inset scale bar, 20 μ m.

(H) Quantitative analysis of the percentage of astrocytes that stained positive for α -syn after being cultured with PD SP12 neurons for 4 weeks. Ctrl astrocytes were derived from SP09, SP11, and SP17 iPSCs, while PD astrocytes were derived from SP12 and SP13 iPSCs (n = 3). Data are expressed as mean \pm SEM, unpaired two-tailed Student's t test, **p < 0.01, ***p < 0.001).

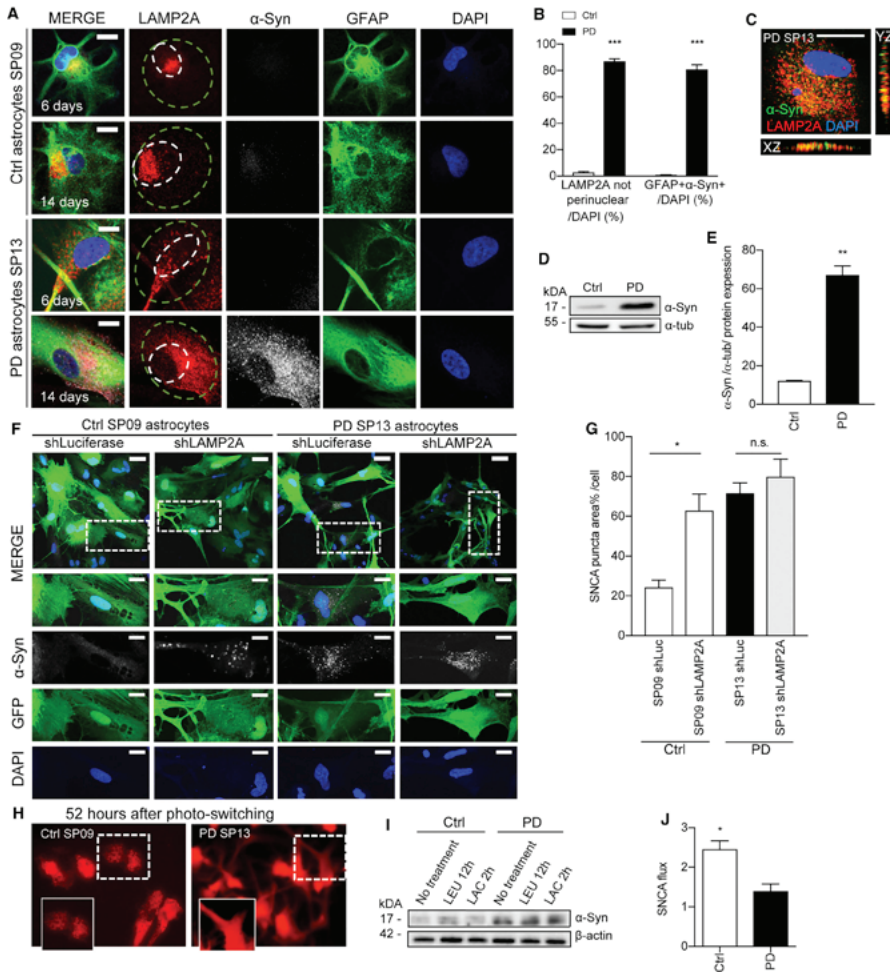


Figure 5. Altered CMA and α -syn Accumulation in LRRK2-PD Astrocytes

(A) Representative ICC images of CMA receptor (LAMP2A), astrocyte marker GFAP, α -syn, and nuclear marker DAPI in Ctrl SP09 and PD SP13 astrocytes at 6 and 14 days. Scale bar, 20 μ m. Smaller white circles represent perinuclear area, whereas larger green circle represents non-perinuclear area.

(B) Percentage of astrocytes with LAMP2A-positive puncta positioning outside of perinuclear area and percentage of astrocytes that stained positive for α -syn. Astrocyte lines used in the experiment were Ctrl SP09, Ctrl SP17, PD SP12, and SP13 (n = 3).

(C) Representative ICC image of positive co-localization of LAMP2A and α -syn in PD SP13 astrocytes. Scale bar, 10 μ m.

(legend continued on next page)



the cell body as early as 6 days, which continued to be present after 14 days (Figures 5A, 5B, and 56A). Moreover, abnormal accumulation of α -syn was confirmed in PD astrocytes after 14 days of culture, compared with Ctrl astrocytes (Figures 5A–5E). Interestingly, this accumulation was not present after 6 days of culture, suggesting progressive α -syn accumulation over the 14-day time period. Co-localization analyses of α -syn with the LAMP2A receptor revealed a positive co-localization that was more evident in PD astrocytes (Figures 5C and 56B). CMA substrates are usually rapidly internalized and degraded inside lysosomes, but we have previously described a similar persistent association of α -syn with LAMP2A-positive lysosomes in PD models due to blockage in α -syn translocation inside lysosomes (Orenstein et al., 2013). These findings suggest, thus, a similar CMA blockage in the PD astrocytes at the receptor level. Also supportive of reduced α -syn degradation, western blot analysis confirmed a higher monomeric protein level of α -syn in PD astrocytes compared with controls (Figures 5D, 5E, and 57A). By using an antibody that detects specifically oligomeric α -syn, we were able to detect other pathogenic forms of α -syn in PD astrocytes, which were similar to those of PD postmortem brain tissue (Figure 57B).

To investigate the contribution of the defect in CMA to the progressive accumulation of α -syn in PD astrocytes, we next performed a knockdown of LAMP2A using lentiviral-mediated short hairpin RNA (shRNA) targeting and silencing the LAMP2A spliced transcript (shLAMP2A), or an shRNA targeting the Luciferase gene (shLuc) as a control (Figure 5F). The shLuc control astrocytes displayed an expected low level of α -syn, whereas after shLAMP2A transduction, there was a statistically significant ($p < 0.001$) 2.5-fold increase in α -syn puncta, comparable to the levels observed in PD astrocytes (Figure 5G). Knockdown of LAMP2A did not change α -syn puncta levels in PD astrocytes, further suggesting defective CMA for α -syn in these cells. CMA activity was monitored using a photoactivatable CMA reporter, KFERQ-Dendra (Koga et al., 2011), in all astrocyte lines at 52 hr after photoactivation (Figures 5H

and 56C). KFERQ-Dendra is present in the cytosol (diffuse fluorescent pattern) but as it is delivered to lysosomes via CMA it changes to a fluorescent punctate pattern. Ctrl astrocytes displayed these puncta, indicative of functional CMA, whereas the signal in PD astrocytes remained diffused in the cytosol, suggestive of an inactive CMA.

Since PD astrocytes displayed higher levels of α -syn compared with Ctrl astrocytes, we next investigated possible differences in α -syn turnover in these cells. α -syn has previously been shown to undergo degradation both by the ubiquitin/proteasome system and by autophagy (Cuervo et al., 2004; Webb et al., 2003); therefore α -syn flux in the presence of lysosomal and proteasome inhibitors (leupeptin and lactacystin, respectively) was evaluated in Ctrl and PD astrocytes at 14 days (Figures 5I, 5J, and 57D). An increase of ~40% in α -syn levels was found in Ctrl astrocytes after leupeptin treatment, while this increase was not found in PD astrocytes analyzed under the same conditions, indicating an impaired flux. No changes were found in either Ctrl or PD astrocytes after lactacystin treatment (Figures 5I, 5J, and 57D). These findings suggest major alterations in α -syn proteostasis due to poor degradation by lysosomal systems in PD astrocytes.

Impaired Macroautophagy in PD Astrocytes

Cells often respond to blockage in CMA by upregulating other autophagic pathways such as macroautophagy (Massey et al., 2006; Schneider et al., 2015). However, altered macroautophagy has also been reported in the context of PD (Sanchez-Danes et al., 2012; Winslow et al., 2010). To investigate the status of macroautophagy, the endo/lysosomal marker LAMP1, autophagosome marker LC3, astrocyte marker GFAP, and nuclear DAPI were used during ICC on all astrocyte lines at both 6 and 14 days. In Ctrl astrocytes, there was lysosomal LAMP1 staining in the perinuclear area and very few visible autophagic vacuoles (LC3-positive vesicles) at both 6 and 14 days (Figures 6A, 6B, and 56D). In PD astrocytes, as for LAMP2A, LAMP1-positive vesicles lost the preferable perinuclear distribution and were found throughout the entire cell (Figures 6A, 6B,

(D and E) (D) Western blot of α -syn and α -tubulin as a loading control and (E) quantification in Ctrl SP09 and PD SP13 astrocytes after 14 days in culture ($n = 4$).

(F) Representative ICC images of Ctrl SP09 and PD SP13 astrocytes after 14 days of transduction with either LV-shLAMP2A or LV-shLuciferase (as a control) stained for α -syn, GFP, and DAPI. Boxed areas highlight the region for which high magnification images are shown. Scale bars, 20 and 10 μ m, respectively.

(G) Percentage of α -syn puncta area per cell in Ctrl SP09 and PD SP13 astrocytes transduced with LV-shLuciferase or LV-shLAMP2A ($n = 3$).

(H) KFERQ-DENDRA (CMA reporter) in Ctrl SP09 and PD SP13 astrocytes 52 hr after photo-switching with UV light ($n = 3$). Images in the insets at the bottom are a magnification of the boxed area.

(I and J) (I) Western blot of α -syn and β -actin as a loading control and (J) quantification of α -syn flux ratio normalized to β -actin in Ctrl SP09 and PD SP13 after the addition of inhibitors of lysosomal proteolysis (leupeptin [LEU], 100 μ M) for 12 hr and proteasomal degradation (lactacystin [LAC], 5 μ M) for 2 hr ($n = 3$).

Data are expressed as mean \pm SEM, unpaired two-tailed Student's *t* test, * $p < 0.05$, ** $p < 0.01$, *** $p < 0.001$.

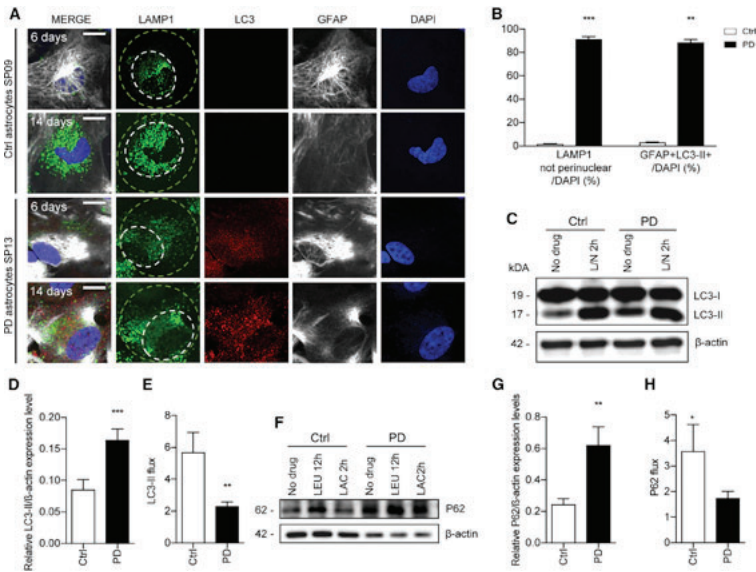


Figure 6. Dysfunctional Macroautophagy in LRRK2-PD Astrocytes

(A) Representative ICC images of lysosomal protein marker LAMP1 and autophagosome marker LC3 in Ctrl SP09 and PD SP13 astrocytes (GFAP) at 6 and 14 days. Smaller white circles represent perinuclear area, whereas larger green circle represents non-perinuclear area. Scale bar, 20 μ m.

(B) Percentage of astrocytes with LAMP1-positive puncta positioning outside of perinuclear area and percentage of astrocytes that stained positive for LC3-II. Astrocyte lines used in the experiment were Ctrl SP09 and SP13 ($n = 3$).

(C–E) (C) Western blot of LC3-II protein levels and β -actin as loading control with corresponding quantification of (D) the LC3-II basal expression and (E) LC3-II flux with or without lysosomal inhibitors NH_4Cl and leupeptin (L/N) for 2 hr in Ctrl SP09 and PD SP13 astrocytes ($n = 3$).

(F–H) (F) Western blot of p62 protein levels and β -actin as loading control with corresponding quantification of (G) the P62 basal expression and (H) P62 flux without inhibitors or with inhibitors leupeptin for 12 hr and lactacystin for 2 hr in Ctrl SP09 and PD SP13 astrocytes ($n = 3$).

Data are expressed as mean \pm SEM, unpaired two-tailed Student's t test, * $p < 0.05$, ** $p < 0.01$, *** $p < 0.001$.

and S6D). In addition, there was a marked increase in autophagic vacuoles starting as early as 6 days that continued increasing through the 14-day time point (Figures 6A, 6B, and S6D). Most of the accumulated LC3-positive vesicles in PD astrocytes did not co-localize with LAMP1 lysosomes (Figures S6E and S6F), suggesting that they were autophagosomes that persisted in these cells due to their poor clearance by lysosomes.

In agreement with the immunofluorescence studies, western blot analyses detected higher basal levels of LC3-II in PD astrocytes compared with Ctrl (Figures 6C, 6D, and S7C). To monitor the autophagy flux and to gain

insights into the mechanism behind the accumulated LC3-II levels in PD astrocytes, both Ctrl and PD astrocytes were treated with leupeptin and NH_4Cl , inhibitors of lysosomal proteolysis, to inhibit LC3-II degradation. Under these conditions, PD astrocytes exhibited lower increase in LC3-II levels compared with controls, suggesting an impairment of the autophagy flux in PD astrocytes (Figures 6E and S7C). Moreover, we found higher p62 levels in PD astrocytes at baseline compared with controls, and lower flux ratio in the presence of inhibitor (Figures 6F–6H and S7E). Overall these findings suggest that reduced function in both autophagic pathways, CMA and macroautophagy,

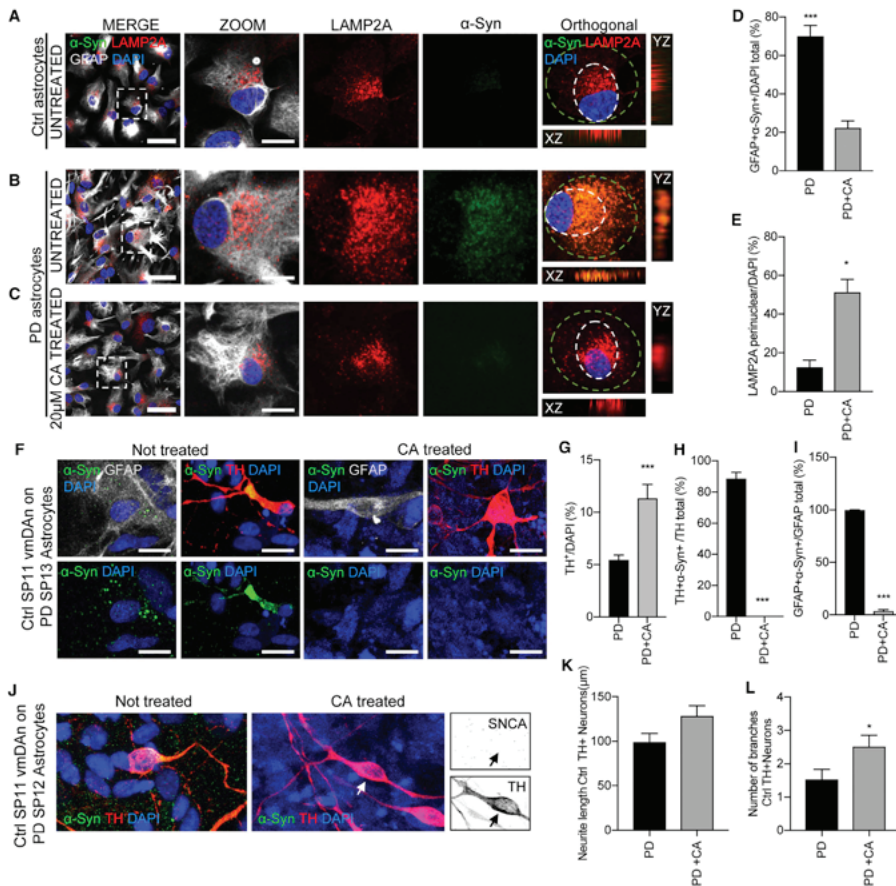


Figure 7. CMA Activator Drug Treatment Rescues α -syn Accumulation in Neurons Cultured with PD Astrocytes

(A and B) Representative ICC images of (A) Ctrl and (B) PD astrocytes after 2 weeks in culture without treatment stained for LAMP2A, α -syn, GFAP, and DAPI. Orthogonal views reveal positive co-localization of α -syn to LAMP2A in PD untreated sample. Images on the right show a magnification of the area boxed in the left images. Dashed circles outline the perinuclear area of the cell. Scale bars, 100 and 20 μ m in merge and zoom, respectively.

(C) Representative ICC images of PD astrocytes after 20 μ g of CA drug treatment stained for LAMP2A, α -syn, GFAP, and DAPI. Scale bars, 100 and 20 μ m in merge and zoom, respectively.

(D and E) (D) Quantitative analysis of PD astrocytes (SP13 and SP12) stained positive for α -syn either not treated or treated with CA; (E) quantitative analysis of the same astrocytes under the same conditions, showing LAMP2A puncta in the perinuclear area (n = 3).

(F) Representative ICC images of 4-week Ctrl.SP11 vmDAn co-cultured on PD SP13 astrocytes (left) or treated with CA for 2 weeks (right). Samples were stained for GFAP, TH, α -syn, and DAPI. Scale bars, 20 μ m.

(legend continued on next page)



contribute to the altered α -syn proteostasis observed in PD astrocytes.

Restoration of α -Syn Proteostasis in PD Astrocytes Alone and during Co-culture of Control Neurons with PD Astrocytes

Intracellular accumulation of α -syn has been shown to contribute to cellular toxicity in PD and to further disrupt functioning of cellular proteostasis systems (reviewed in [Abeliovich and Gitler, 2016](#)). We next investigated whether α -syn accumulation in PD astrocytes could be ameliorated by enhancing lysosomal activity. PD astrocytes were treated with a CMA activator (CA), which operates through the release of the endogenous inhibition of the retinoic receptor- α signaling pathway over CMA ([Anguiano et al., 2013](#)). Cells were treated with a concentration of 20 μ M for 5 days and levels of α -syn were analyzed by immunofluorescence ([Figure 7](#)). LAMP2A-positive lysosomes in PD astrocytes treated with the CA ([Figures 7C–7E](#)) recovered the perinuclear distribution observed in Ctrl cells ([Figure 7A](#)) compared with when not treated ([Figure 7B](#)), suggesting reactivation of CMA in these cells. Consistent with higher CMA activity, CA-treated cells had significantly lower α -syn content than untreated cells ([Figures 7C–7E](#)).

In addition, we treated PD astrocytes when in co-culture with Ctrl neurons ([Figure 7F](#)). Under untreated conditions, Ctrl neurons accumulate astrocytic α -syn and show signs of neurodegeneration. Interestingly, the treatment with CA cleared out α -syn not only in astrocytes, but also in vmdAns, partially restored neuron survival, and decreased the number of TH-positive cells with a degenerative morphology ([Figures 7G–7L](#)). These findings suggest that although multiple protein degradation pathways fail to efficiently degrade α -syn in PD cells, reactivation of one of these pathways, in our case CMA, is able to restore functional α -syn proteostasis.

DISCUSSION

Astrocytes from three PD patients carrying the G2019S mutation in the *LRRK2* gene and two healthy individuals were successfully generated using a previously published protocol and fully characterized. By implementing a patient

iPSC-based co-culture model, in this study we describe a role for PD astrocytes in midbrain neuronal cell death. Specifically, in a 4-week co-culture system, we found morphological alterations resembling those of neurodegeneration, such as short and few neurites as well as beaded necklace-like neurites, typically observed in neurons upon transport alterations ([Fu et al., 2005](#); [Garrido et al., 2011](#)), and increased neuronal loss in Ctrl neurons co-cultured with PD astrocytes. We interpret these altered phenotypes as representing PD astrocyte-induced vmdAn neurodegeneration. An alternative explanation could be that PD astrocytes impinged on the differentiation and/or maturation of DAn progenitors in our iPSC-derived co-culture system. However, while we cannot formally rule out this possibility, two lines of evidence strongly argue against it playing a significant role in the phenotypes described here. First, we used vmdA neural differentiation cultures at 35 days of differentiation for our co-culture experiments. At this time, most vmdAns are already committed in fate (TH⁺/FOXA2⁺, see [Figure 2A](#)), but are still at a stage of maturation that does not compromise their survival upon cell dissociation and plating on top of the astrocyte cultures. Second, the numbers of vmdAns at different time points along the co-culture experiments showed progressive decline in co-cultures with PD astrocytes, but no significant changes when co-cultured with Ctrl astrocytes ([Figure S2C](#)). These results indicate that few new TH⁺ neurons are generated during co-culture, and further support that the decreased numbers of vmdAns observed upon co-culture with PD astrocytes are a consequence of vmdAn degeneration. Importantly, the altered phenotypes were specifically observed in the subpopulation of midbrain dopaminergic neurons, as numbers of MAP2⁺/TH⁻ neurons did not change significantly upon co-culture with Ctrl or PD astrocytes. In accordance with this, it has been already shown that α -syn toxicity was responsible for nigrostriatal neuronal cell death in midbrain cultures ([Petrucci et al., 2002](#)), a relevant finding regarding the particular vulnerability of nigral neurons in PD. However, it remains to be tested whether, in prolonged culture, PD astrocytes also impair the survival of TH⁻ populations.

Postmortem brain tissue of PD patients revealed α -syn accumulation in astrocytes ([Wakabayashi et al., 2000](#)).

(G–I) (G) Quantitative analysis of the percentage of vmdAns remaining after being co-cultured with PD SP12 or PD SP13 (without treatment or treated with CA) for 4 weeks. Percentage of the (H) vmdAns or (I) astrocytes that stained positive for α -syn 4 weeks after the same co-culture conditions (n = 6).

(J) Representative ICC images of 4-week Ctrl SP11 vmdAns co-cultured on PD SP12 astrocytes with or without CA treatment for 2 weeks. Samples were stained for TH, α -syn, and DAPI. Arrows indicate the absence of α -syn accumulation in the selected TH-positive cell. Scale bars, 20 μ m.

(K and L) (K) Neurite length quantification and (L) number of branches of 4-week Ctrl SP11 vmdAns when co-cultured on PD SP12 or PD SP13 astrocytes with or without CA treatment for 2 weeks (n = 4); 20 neurons counted per experiment.

Data are expressed as mean \pm SEM, unpaired two-tailed Student's t test, *p < 0.05; ***p < 0.001.



It has been previously described that astrocytes accumulate neuronal-derived α -syn as a mechanism of neuroprotection (Booth et al., 2017). Indeed, in our study we found that Ctrl astrocytes accumulate α -syn when co-cultured with PD neurons and partially rescued the morphological phenotype of neurodegeneration and clearance of neuronal α -syn. This behavior suggests a neuroprotective effect via inflammatory-mediated activation of the Ctrl astrocytes. In addition, by using a CRISPR/Cas9 gene-edited cell line tagging the endogenous SNCA locus with an FLAG tag, our results reveal that PD astrocytes also accumulate and transfer α -syn to the surrounding neurons, suggesting that astrocytes actively contribute to the distribution of α -syn.

Taking into account that our PD astrocytes come from patients carrying the *LRRK2* G2019S mutation, we investigated whether disease-specific phenotypes related to the mutation were present. The α -syn accumulation in our co-culture system indicated a disruption in the way α -syn is usually degraded in PD astrocytes. Degradation of α -syn has been shown to occur by both proteasome and autophagic pathways, and conversely, high levels of α -syn have been demonstrated to be toxic for both systems (Tanaka et al., 2001; Webb et al., 2003; Winslow et al., 2010). Here we found that lysosomal degradation of α -syn was severely inhibited in PD astrocytes. We have previously described in PD neurons that one of the early events in the dysfunction of the proteostasis systems in these cells is the disruption of CMA by mutant *LRRK2* binding to the LAMP2A, thus causing the accumulation of α -syn (Orenstein et al., 2013). Here we demonstrate that CMA is also altered in PD astrocytes and confirm that α -syn degradation by CMA in these cells was almost completely abolished.

The increase in intracellular levels of α -syn, due to its poor degradation in PD astrocytes by CMA, may contribute to precipitating malfunctioning of other proteostasis mechanisms, such as the proteasome and macroautophagy. In fact, we demonstrated that macroautophagy was also markedly impaired in these cells, by showing higher basal levels of autophagic vacuoles (LC3-II) and the autophagic cargo p62, and reduced autophagic flux (for both LC3-II and p62). The lower co-localization between the autophagosomal and lysosomal markers observed in PD astrocytes suggests that the reduced autophagic flux is due to a defect in autophagosome/lysosome fusion, similar to that previously described in PD neurons.

Taking into account the coordinate functioning of the proteolytic systems, and the fact that CMA disruption seems to occur early during the development of PD pathology, we attempted to restore normal α -syn proteostasis by enhancing CMA activity. Our findings in cells treated with a chemical activator of CMA suggest that upregulation of CMA is still possible in these cells and that this intervention is sufficient to return levels of α -syn close to those in

Ctrl cells. Although α -syn was cleared, restoration during a co-culture with Ctrl neurons was only partial in terms of neurite length and number, suggesting that the neurodegeneration observed could also be due to other non- α -syn-related factors secreted by PD astrocytes.

Overall, our findings propose a specific role for astrocytes in mediating dopaminergic cell death during PD. PD-specific phenotypes specifically related to dysfunctions in the pathways of protein degradation have been observed in PD astrocytes and not in Ctrl astrocytes. Dysfunctional CMA, progressive α -syn accumulation, and glia-to-neuron transfer found in our PD astrocytes are all aspects that can compromise neuronal survival during PD pathogenesis. Future studies will identify whether additional factors other than α -syn are being secreted by (or lacking in) PD astrocytes, and thus contributing to triggering vmdA neuronal cell death. iPSC-based technology allows for the proper recapitulation of patient-specific disease-related phenotypes, which will aid in the discovery of new therapies.

EXPERIMENTAL PROCEDURES

Experimental procedures are also provided in [Supplemental Information](#).

iPSC-Derived Astrocyte Generation and Culture

The parental iPSC lines used in our studies were previously generated and fully characterized (Sanchez-Danes et al., 2012). The generation and use of human iPSCs in this work were approved by the Spanish competent authorities (Commission on Guarantees concerning the Donation and Use of Human Tissues and Cells of the Carlos III National Institute of Health). iPSCs were differentiated into astrocytes following a previously published protocol (Serio et al., 2013). See [Supplemental Information](#) for more details.

iPSC-Derived vmdAn Generation

Four different iPSCs, two PD (SP12 and SP13) and two Ctrl (SP11 and SP11#4), were differentiated into dopaminergic neurons using a combination of two previously published protocols for midbrain induction (Chambers et al., 2009; Kriks et al., 2011). Detailed methods are provided in [Supplemental Information](#).

ICC

ICC on cell cultures was performed as described in [Supplemental Information](#).

Statistical Analysis

Statistical analyses of the obtained data were performed using two-tailed unequal variance Student's *t* tests and ANOVA (**p* < 0.05, ***p* < 0.01, ****p* < 0.001), and the mean and standard error of the mean were plotted using Prism (Mac OS X). Number of independent experiments (*n*) is indicated in each figure legend.

SUPPLEMENTAL INFORMATION

Supplemental Information includes Supplemental Experimental Procedures, seven figures, and three tables and can be found



with this article online at <https://doi.org/10.1016/j.stemcr.2018.12.011>.

AUTHOR CONTRIBUTIONS

Conceptualization, A.C. and A.R.; Methodology, I.F., J.P.M., A.Z., A.M.C., and J.S.; Investigation, Y.R.P., A.D., G.C., C.C., M.P.-E., M.G., I.F.-C., J.P., and A.F.; Validation, A.C. and A.R.; Writing – Original Draft, A.D.; Writing – Review & Editing, A.C. and A.R.; Visualization, A.D.; Resources, A.Z., A.M.C., J.S., E.T., A.C., and A.R.; Funding Acquisition, A.C.; Supervision, A.C.

ACKNOWLEDGMENTS

The authors are indebted to the patients with PD who have participated in this study. The authors thank Chrysanthi Blithikioti for helping with some co-culture experiments and ICC, Neus Bayó-Puxan for her advice on western blotting, Jose Miquel Andres Vaquero (CMRB) for performing flow cytometry analysis, and David Maynar for excellent artwork. We are thankful to Mark Cookson for the LRRK2 G2019S plasmid (Addgene Plasmid No. 29401). We are grateful to the Advanced Fluorescence Microscopy Unit of the Institute of Biomedicine of the University of Barcelona (especially to Elena Rebollo Arredondo). Research from the authors' laboratories is supported by the European Research Council (ERC) (2012-STG-311736-PD-HUMMODEL), the Spanish Ministry of Economy and Competitiveness (MINECO) (FIS2016-78507-C2-2-P, SAF2015-69706-R, and BFU2016-80870-P), Instituto de Salud Carlos III (ISCIII/FEDER) (Red de Terapia Celular [TerCel] RD16/0011/0024), AGAUR (2014-SGR-878 and 2017-SGR-899), and CERCA Program/Generalitat de Catalunya. A.D. is supported by the PD-HUMMODEL ERC-Ideas PhD fellowship. C.C. and G.C. are partially supported by predoctoral fellowships from the Spanish Ministry of Education (MEC) (FPU12/03332) and MINECO (BES-2014-069603), respectively.

Received: April 7, 2018

Revised: December 11, 2018

Accepted: December 13, 2018

Published: January 10, 2019

SUPPORTING CITATIONS

The following references appear in the Supplemental Information: Alwin et al., 2005; Kita-Matsuo et al., 2009; Massey et al., 2008; Mussolino et al., 2011; Park et al., 2015.

REFERENCES

Abeliovich, A., and Gitler, A.D. (2016). Defects in trafficking bridge Parkinson's disease pathology and genetics. *Nature* **539**, 207–216.

Alwin, S., Gere, M.B., Guhl, E., Effertz, K., Barbas, C.F., 3rd, Segal, D.J., Weitzman, M.D., and Cathomen, T. (2005). Custom zinc-finger nucleases for use in human cells. *Mol. Ther.* **12**, 610–617.

Anguiano, J., Garner, T.P., Mahalingam, M., Das, B.C., Gavathiotis, E., and Cuervo, A.M. (2013). Chemical modulation of chaperone-mediated autophagy by retinoic acid derivatives. *Nat. Chem. Biol.* **9**, 374–382.

Booth, H.D.E., Hirst, W.D., and Wade-Martins, R. (2017). The role of astrocyte dysfunction in Parkinson's disease pathogenesis. *Trends Neurosci.* **40**, 358–370.

Braak, H., Sastre, M., and Del Tredici, K. (2007). Development of alpha-synuclein immunoreactive astrocytes in the forebrain parallels stages of intraneuronal pathology in sporadic Parkinson's disease. *Acta Neuropathol.* **114**, 231–241.

Cavaliere, F., Cerf, L., Dehay, B., Ramos-Gonzalez, P., De Giorgi, F., Bourdenx, M., Bessedé, A., Obeso, J.A., Matute, C., Ichas, F., et al. (2017). In vitro alpha-synuclein neurotoxicity and spreading among neurons and astrocytes using Lewy body extracts from Parkinson disease brains. *Neurobiol. Dis.* **103**, 101–112.

Chambers, S.M., Fasano, C.A., Papapetrou, E.P., Tomishima, M., Sadelain, M., and Studer, L. (2009). Highly efficient neural conversion of human ES and iPS cells by dual inhibition of SMAD signaling. *Nat. Biotechnol.* **27**, 275–280.

Cookson, M.R. (2016). Cellular functions of LRRK2 implicate vesicular trafficking pathways in Parkinson's disease. *Biochem. Soc. Trans.* **44**, 1603–1610.

Cookson, M.R. (2017). Mechanisms of mutant LRRK2 neurodegeneration. *Adv. Neurobiol.* **14**, 227–239.

Cuervo, A.M., Stefanis, L., Fredenburg, R., Lansbury, P.T., and Sulzer, D. (2004). Impaired degradation of mutant alpha-synuclein by chaperone-mediated autophagy. *Science* **305**, 1292–1295.

Fu, L., Gao, Y.S., Tousson, A., Shah, A., Chen, T.L., Vertel, B.M., and Sztul, E. (2005). Nuclear aggregates form by fusion of PML-associated aggregates. *Mol. Biol. Cell* **16**, 4905–4917.

Garrido, M., Tereshchenko, Y., Zhevtsova, Z., Taschenberger, G., Bahr, M., and Kugler, S. (2011). Glutathione depletion and overproduction both initiate degeneration of nigral dopaminergic neurons. *Acta Neuropathol.* **121**, 475–485.

Gilks, W.P., Abou-Sleiman, P.M., Gandhi, S., Jain, S., Singleton, A., Lees, A.J., Shaw, K., Bhatia, K.P., Bonifati, V., Quinn, N.P., et al. (2005). A common LRRK2 mutation in idiopathic Parkinson's disease. *Lancet* **365**, 415–416.

Global Burden of Disease Study Collaborators. (2015). Global, regional, and national incidence, prevalence, and years lived with disability for 301 acute and chronic diseases and injuries in 188 countries, 1990–2013: a systematic analysis for the Global Burden of Disease Study 2013. *Lancet* **386**, 743–800.

Greenamyre, J.T., and Hastings, T.G. (2004). Biomedicine. Parkinson's—divergent causes, convergent mechanisms. *Science* **304**, 1120–1122.

Gu, X.L., Long, C.X., Sun, L., Xie, C., Lin, X., and Cai, H. (2010). Astrocytic expression of Parkinson's disease-related A53T alpha-synuclein causes neurodegeneration in mice. *Mol. Brain* **3**, 12.

Heman-Ackah, S.M., Manzano, R., Hoozemans, J.J.M., Scheper, W., Flynn, R., Haerty, W., Cowley, S.A., Bassett, A.R., and Wood, M.J.A. (2017). Alpha-synuclein induces the unfolded protein response in Parkinson's disease SNCA triplication iPSC-derived neurons. *Hum. Mol. Genet.* **26**, 4441–4450.

Kiffin, R., Christian, C., Knecht, E., and Cuervo, A.M. (2004). Activation of chaperone-mediated autophagy during oxidative stress. *Mol. Biol. Cell* **15**, 4829–4840.



- Kita-Matsuo, H., Barcova, M., Prigozhina, N., Salomonis, N., Wei, K., Jacot, J.G., Nelson, B., Spiering, S., Haverslag, R., Kim, C., et al. (2009). Lentiviral vectors and protocols for creation of stable hESC lines for fluorescent tracking and drug resistance selection of cardiomyocytes. *PLoS One* *4*, e5046.
- Koga, H., Martinez-Vicente, M., Macian, F., Verkhusa, V.V., and Cuervo, A.M. (2011). A photoconvertible fluorescent reporter to track chaperone-mediated autophagy. *Nat. Commun.* *2*, 386.
- Kriks, S., Shim, J.W., Piao, J., Ganat, Y.M., Wakeman, D.R., Xie, Z., Carrillo-Reid, L., Auyeung, G., Antonacci, C., Buch, A., et al. (2011). Dopamine neurons derived from human ES cells efficiently engraft in animal models of Parkinson's disease. *Nature* *480*, 547–551.
- Lee, H.J., Suk, J.E., Patrick, C., Bae, E.J., Cho, J.H., Rho, S., Hwang, D., Masliah, E., and Lee, S.J. (2010). Direct transfer of alpha-synuclein from neuron to astroglia causes inflammatory responses in synucleinopathies. *J. Biol. Chem.* *285*, 9262–9272.
- Lill, C.M. (2016). Genetics of Parkinson's disease. *Mol. Cell Probes* *30*, 386–396.
- Martinez-Vicente, M., Talloczy, Z., Kaushik, S., Massey, A.C., Mazzulli, J., Mosharov, E.V., Hodara, R., Fredenburg, R., Wu, D.C., Follenzi, A., et al. (2008). Dopamine-modified alpha-synuclein blocks chaperone-mediated autophagy. *J. Clin. Invest.* *118*, 777–788.
- Massey, A.C., Follenzi, A., Kiffin, R., Zhang, C., and Cuervo, A.M. (2008). Early cellular changes after blockage of chaperone-mediated autophagy. *Autophagy* *4*, 442–456.
- Massey, A.C., Kaushik, S., Sovak, G., Kiffin, R., and Cuervo, A.M. (2006). Consequences of the selective blockage of chaperone-mediated autophagy. *Proc. Natl. Acad. Sci. U S A* *103*, 5805–5810.
- Mussolino, C., Morbitzer, R., Lutge, F., Dannemann, N., Lahaye, T., and Cathomen, T. (2011). A novel TALE nuclease scaffold enables high genome editing activity in combination with low toxicity. *Nucleic Acids Res.* *39*, 9283–9293.
- Nguyen, H.N., Byers, B., Cord, B., Shcheglovitov, A., Byrne, J., Gujar, P., Kee, K., Schule, B., Dolmetsch, R.E., Langston, W., et al. (2011). LRRK2 mutant iPSC-derived DA neurons demonstrate increased susceptibility to oxidative stress. *Cell Stem Cell* *8*, 267–280.
- Nichols, W.C., Pankratz, N., Hernandez, D., Paisan-Ruiz, C., Jain, S., Halter, C.A., Michaels, V.E., Reed, T., Rudolph, A., Shults, C.W., et al. (2005). Genetic screening for a single common LRRK2 mutation in familial Parkinson's disease. *Lancet* *365*, 410–412.
- Orenstein, S.J., Kuo, S.H., Tasset, I., Arias, E., Koga, H., Fernandez-Carasa, I., Cortes, E., Honig, L.S., Dauer, W., Consiglio, A., et al. (2013). Interplay of LRRK2 with chaperone-mediated autophagy. *Nat. Neurosci.* *16*, 394–406.
- Park, C., Suh, Y., and Cuervo, A.M. (2015). Regulated degradation of Chk1 by chaperone-mediated autophagy in response to DNA damage. *Nat. Commun.* *6*, 6823.
- Petrucelli, L., O'Farrell, C., Lockhart, P.J., Baptista, M., Kehoe, K., Vink, L., Choi, P., Wolozin, B., Farrer, M., Hardy, J., et al. (2002). Parkin protects against the toxicity associated with mutant alpha-synuclein: proteasome dysfunction selectively affects catecholaminergic neurons. *Neuron* *36*, 1007–1019.
- Sanchez-Danes, A., Richaud-Patin, Y., Carballo-Carbajal, I., Jimenez-Delgado, S., Caig, C., Mora, S., Di Guglielmo, C., Ezquerro, M., Patel, B., Giral, A., et al. (2012). Disease-specific phenotypes in dopamine neurons from human iPSC-based models of genetic and sporadic Parkinson's disease. *EMBO Mol. Med.* *4*, 380–395.
- Schneider, J.L., Villarroya, J., Diaz-Carretero, A., Patel, B., Urbanska, A.M., Thi, M.M., Villarroya, F., Santambrogio, L., and Cuervo, A.M. (2015). Loss of hepatic chaperone-mediated autophagy accelerates proteostasis failure in aging. *Aging Cell* *14*, 249–264.
- Serio, A., Bilican, B., Barmada, S.J., Ando, D.M., Zhao, C., Siller, R., Burr, K., Haghi, G., Story, D., Nishimura, A.L., et al. (2013). Astrocyte pathology and the absence of non-cell autonomy in an induced pluripotent stem cell model of TDP-43 proteinopathy. *Proc. Natl. Acad. Sci. U S A* *110*, 4697–4702.
- Skibinski, G., Nakamura, K., Cookson, M.R., and Finkbeiner, S. (2014). Mutant LRRK2 toxicity in neurons depends on LRRK2 levels and synuclein but not kinase activity or inclusion bodies. *J. Neurosci.* *34*, 418–433.
- Su, Y.C., Guo, X., and Qi, X. (2015). Threonine 56 phosphorylation of Bcl-2 is required for LRRK2 G2019S-induced mitochondrial depolarization and autophagy. *Biochim. Biophys. Acta* *1852*, 12–21.
- Tanaka, Y., Engelender, S., Igarashi, S., Rao, R.K., Wanner, T., Tanzi, R.E., Sawa, A., Dawson, V., Dawson, T.M., and Ross, C.A. (2001). Inducible expression of mutant alpha-synuclein decreases proteasome activity and increases sensitivity to mitochondria-dependent apoptosis. *Hum. Mol. Genet.* *10*, 919–926.
- Wakabayashi, K., Hayashi, S., Yoshimoto, M., Kudo, H., and Takahashi, H. (2000). NACP/alpha-synuclein-positive filamentous inclusions in astrocytes and oligodendrocytes of Parkinson's disease brains. *Acta Neuropathol.* *99*, 14–20.
- Webb, J.L., Ravikumar, B., Atkins, J., Skepper, J.N., and Rubinsztein, D.C. (2003). Alpha-Synuclein is degraded by both autophagy and the proteasome. *J. Biol. Chem.* *278*, 25009–25013.
- Winslow, A.R., Chen, C.W., Corrochano, S., Acevedo-Arozena, A., Gordon, D.E., Peden, A.A., Lichtenberg, M., Menzies, F.M., Ravikumar, B., Imapriso, S., et al. (2010). alpha-Synuclein impairs macroautophagy: implications for Parkinson's disease. *J. Cell Biol.* *190*, 1023–1037.
- Zeltner, N., and Studer, L. (2015). Pluripotent stem cell-based disease modeling: current hurdles and future promise. *Curr. Opin. Cell Biol.* *37*, 102–110.

SCIENTIFIC REPORTS

OPEN

CRISPR/Cas9-mediated generation of a tyrosine hydroxylase reporter iPSC line for live imaging and isolation of dopaminergic neurons

Received: 19 October 2018
Accepted: 10 April 2019
Published online: 02 May 2019

Carles Calatayud^{1,2,3}, Giulia Carola^{1,2}, Irene Fernández-Carasa^{1,2}, Marco Valtorta^{1,2,4}, Senda Jiménez-Delgado^{3,5}, Mònica Díaz^{3,5}, Jordi Soriano-Fradera⁶, Graziella Cappelletti⁶, Javier García-Sancho⁷, Ángel Raya^{3,5,8} & Antonella Consiglio^{1,2,9}

Patient-specific induced pluripotent stem cells (iPSCs) are a powerful tool to investigate the molecular mechanisms underlying Parkinson's disease (PD), and might provide novel platforms for systematic drug screening. Several strategies have been developed to generate iPSC-derived tyrosine hydroxylase (TH)-positive dopaminergic neurons (DAn), the clinically relevant cell type in PD; however, they often result in mixed neuronal cultures containing only a small proportion of TH-positive DAn. To overcome this limitation, we used CRISPR/Cas9-based editing to generate a human iPSC line expressing a fluorescent protein (mOrange) knocked-in at the last exon of the *TH* locus. After differentiation of the TH-mOrange reporter iPSC line, we confirmed that mOrange expression faithfully mimicked endogenous TH expression in iPSC-derived DAn. We also employed calcium imaging techniques to determine the intrinsic functional differences between dopaminergic and non-dopaminergic ventral midbrain neurons. Crucially, the brightness of mOrange allowed direct visualization of TH-expressing cells in heterogeneous cultures, and enabled us to isolate live mOrange-positive cells through fluorescence-activated cell sorting, for further differentiation. This technique, coupled to refined imaging and data processing tools, could advance the investigation of PD pathogenesis and might offer a platform to test potential new therapeutics for PD and other neurodegenerative diseases.

Parkinson's disease (PD) is an incurable neurodegenerative disorder in the elderly that is characterized by the progressive loss of dopaminergic neurons (DAn) in the substantia nigra pars compacta¹. Its incidence in Western countries is rising due to the progressive aging of the population, imposing a major burden on national healthcare systems. Despite decades of intense research, the pathogenic mechanisms of PD remain unclear owing to the lack of experimental models that recapitulate the main features of the disease. The development of induced pluripotent stem cell (iPSC) technology has opened new horizons for modeling PD, as iPSCs can be generated from patients' somatic cells and differentiated into disease-relevant cell types, which would capture the genetic complexity of PD. Furthermore, human iPSC-derived neuronal models offer unprecedented access to the early stages of the disease, allowing the investigation of the events that initiate the pathologic process in PD^{2,3}.

The development of hiPSC-based strategies to treat or model PD, however, is hampered by the lack of efficient protocols for the directed differentiation of stem cells into DAn with the appropriate characteristics of A9-subtype

¹Department of Pathology and Experimental Therapeutics, Bellvitge University Hospital-IDIBELL, 08908, Hospitalet de Llobregat, Spain. ²Institute of Biomedicine (IBUB) of the University of Barcelona (UB), 08028, Barcelona, Spain. ³Center of Regenerative Medicine in Barcelona (CMRB), Hospital Duran i Reynals, Hospitalet de Llobregat, 08908, Barcelona, Spain. ⁴Department of Bioscience, University of Milan, Via Festa del Perdono 7, Milan, 20122, Italy. ⁵Center for Networked Biomedical Research on Bioengineering, Biomaterials and Nanomedicine (CIBER-BBN), Hospitalet de Llobregat, 08098, Barcelona, Spain. ⁶Department of Condensed Matter Physics, University of Barcelona, Avinguda de la Diagonal 645, 08028, Barcelona, Spain. ⁷Instituto de Biología y Genética Molecular (IBGM), Universidad de Valladolid, Calle Sanz y Forés 3, 47003, Valladolid, Spain. ⁸Institució Catalana de Recerca i Estudis Avançats (ICREA), 08010, Barcelona, Spain. ⁹Department of Molecular and Translational Medicine, University of Brescia, Piazza del Mercato 15, 25121, Brescia, Italy. Correspondence and requests for materials should be addressed to A.R. (email: araya@cmrb.eu) or A.C. (email: consiglio@ub.edu)

ventral midbrain neurons – the neuronal cell type lost in PD (for review, see⁴). Indeed, although several protocols have been developed to differentiate stem cells into functional DAn^{5–8}, the differentiated progeny are a heterogeneous mix of DA and non-DA cells, which impedes identifying live DAn. Moreover, the wide variability in terms of differentiation ability among different iPSC lines represents a further limitation in the field, which hinders data interpretation^{9–11}.

Several strategies have evolved in recent years to overcome these issues, based mainly on the use of DAn lineage reporters and, in particular, the expression of tyrosine hydroxylase (TH) – the first and rate-limiting step in the synthesis of dopamine – as a marker for identifying DAn¹². However, classical approaches relying on the expression of a reporter construct controlled by the proximal promoter of the gene of interest have been unsatisfactory^{13,14}. New gene-editing strategies have been more successful, enabling the insertion of reporter genes under the control of endogenous regulatory sequences. In this regard, two recent studies showed that the insertion of reporter constructs into the *TH* gene locus faithfully mimics endogenous TH expression during *in vitro* and *in vivo* differentiation^{15,16}. But neither of these reporter lines allowed for the direct visualization of TH-positive (TH⁺) neurons in living cells, likely due to the low absolute expression of TH even in DAn.

In the present work, we used a CRISPR/Cas9-based editing strategy to generate a human iPSC line carrying the fluorescent protein mOrange knocked-in at the last exon of *TH*. We first confirmed the exact colocalization of mOrange expression from the reporter gene with endogenous *TH* expression in TH-mOrange hiPSC differentiated into DAn. We then used flow cytometry to evaluate mOrange reporter expression, which could be detected as early as 25 days *in vitro*. Calcium imaging experiments revealed electrophysiological differences between ventral midbrain dopaminergic neurons and non-dopaminergic neurons. This approach also enabled us to isolate pure and viable DAn cell populations from heterogeneous cultures. We thus provide a novel cellular model to study PD phenotypes *in vitro*, which may be useful for the implementation of high throughput biological discovery applications including drug target identification.

Results

CRISPR/Cas9-mediated knock-in of a P2A-mOrange cassette in-frame with *TH* gene. With the aim of identifying TH⁺ neurons among living cells, we generated a genetic reporter construct that could robustly and faithfully label DAn. We used CRISPR/Cas9 genome-editing to knock-in a P2A-mOrange fluorescent construct adjacent to the last exon of the *TH* gene. We chose mOrange because it is one of the brightest monomeric fluorescent proteins available¹⁷. The designed CRISPR/Cas9 guide RNA spacer sequence overlapped the *TH* stop codon, thereby preventing retargeting of properly edited alleles. The hiPSC line SP_11¹, generated from a healthy control, was co-transfected with the homology-directed repair (HDR) and CRISPR/Cas9 plasmids (Fig. 1A). The HDR plasmid contained a LoxP-flanked pRex1-Neo^R cassette, allowing selection of recombination events. Resistant clones were molecularly characterized and the selection cassette excised (Figs 1B,C and S1). This editing approach induced >50% of biallelic integration of the exogenous sequences (data not shown). The edited hiPSC line was then expanded and characterized for the expression of pluripotency markers including OCT4, SOX2, NANOG, SSEA4, SSEA3 and TRA-1-81, and also karyotype integrity (Fig. 1D,E).

mOrange expression faithfully recapitulates endogenous TH expression in ventral midbrain dopaminergic neurons.

To differentiate the edited iPSC line towards ventral midbrain DAn (vmDAn), we followed a previously published midbrain floor plate differentiation protocol⁶ (see Methods for details) (Fig. 2A,B). Under these conditions, some fluorescent mOrange-positive cells could be observed as early as 25 days of differentiation, and the number and the fluorescence intensity of the cells increased over time. At day 50 of differentiation, cells were live-imaged (Fig. 2C) and fixed to confirm the fidelity of the reporter. Immunofluorescence analysis of fluorescent neurons revealed an absolute correlation between the mOrange signal and TH- and mRFP1-immunoreactivity (mOrange is an mRFP1 derivative) (Fig. 2D). By contrast, MAP2-positive neurons that were negative for TH immunoreactivity were also negative for mOrange (Fig. 2D), confirming the specificity of the transgene in replicating the endogenous TH expression pattern.

Further analysis at day 50 of differentiation demonstrated that ~30% of TH/mOrange-positive cells expressed the ventral midbrain forkhead box protein A2 (FOXA2) and, more importantly, the same proportion of cells also expressed the A9 domain-specific marker G protein-activated inward rectifier potassium channel 2 (GIRK2) (Fig. 2E,G). No differences between TH-mOrange edited and non-edited parental SP_11 iPSC lines were observed regarding the expression of vmDAn markers upon differentiation (Fig. 2F,G), indicating that differentiation was not perturbed by the insertion of the transgene.

Overall, our results show that the generated TH-mOrange iPSC line faithfully reports endogenous TH expression and that the genetic modification does not impair mDA specification.

Ventral midbrain dopaminergic neurons have electrophysiological features distinct from non-dopaminergic neurons.

The most defining feature of a neuron is its ability to fire action potentials in response to neurotransmitters from other neurons. In this regard, we exploited the possibility of identifying live DAn to analyze their capability to fire action potentials through studying calcium fluxes. The TH-mOrange iPSC line was differentiated towards floor plate derivatives and the resulting neuronal cultures were incubated with the calcium sensor Fluo-4 AM and imaged for periods of 30 minutes. Single calcium traces were dichotomized depending on whether they were recorded from mOrange⁺ or mOrange⁻ cells (Fig. 3A,B). Both fluorescent and non-fluorescent neurons showed sharp spontaneous increases of Fluo-4 AM signal corresponding to the sudden influxes of calcium occurring during bursts (repeated action potentials) (blue arrowheads in Fig. 3B). While both groups of neurons showed similar firing patterns, we noted small but significant differences in the amplitude of the bursts. At day 35 of differentiation, the amplitude of the burst fired by mOrange⁻ neurons was approximately 12% larger than those fired by mOrange⁺ neurons (2.954 ± 0.127 vs 3.296 ± 0.050 ; $p = 0.030$). This difference

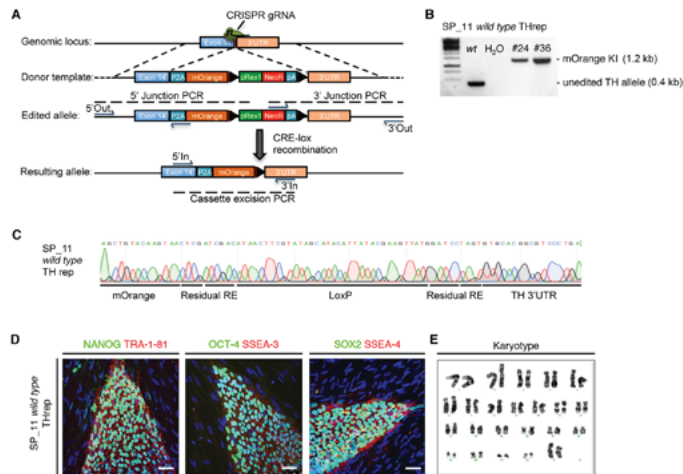


Figure 1. Generation of the TH-mOrange reporter iPSC line using CRISPR/Cas9-mediated gene editing. (A) Scheme describing the recombination steps during the edition process. Blue arrows represent the primers used for the PCR screening procedure. Black triangles represent LoxP sites surrounding the selection cassette. (B) Molecular analysis of the correctly targeted clones to confirm proper P2A-mOrange cassette integration and selection cassette excision in the control iPSC line. Full-length gels are included in Fig. S1C. (C) Sanger sequencing confirmed successful excision of the LoxP site-flanked cassette. (D) Immunofluorescence analysis of representative colonies of the TH reporter (SP_11) iPSC line staining positive for the pluripotency-associated markers NANOG, OCT4 and SOX2 (green) and TRA-1-81, SSEA3 and SSEA4 (red). Scale bar, 50 μm. (E) Normal karyotype of the TH reporter control iPSC line.

widened to 23% at day 50 of differentiation (2.494 ± 0.106 vs 3.082 ± 0.090 ; $p = 0.026$) (Fig. 3C). These results underscore the importance of sampling a homogeneous and defined neuronal population in order to gain resolution when investigating disease-related phenotypes.

Flow cytometry-based isolation of homogenous populations of mOrange-labeled iPSC dopaminergic neurons. To obtain a homogenous population of mOrange-labeled iPSC-derived DAN, edited-iPSC DAN were isolated using fluorescence-activated cell sorting (FACS) at 27 days of differentiation. For this specific analysis, we utilized an alternative DAN differentiation protocol using dual-SMAD inhibition to obtain neural progenitor cells (NPCs) (Fig. S2A, B). With this protocol, NPCs can be expanded in the presence of fibroblast growth factor 2 (FGF2) and epidermal growth factor (EGF), cryopreserved, and rapidly differentiated into DAN^{13,18,19}. Indeed, when we differentiated the TH-mOrange reporter line using this protocol, mOrange⁺ DAN could be visualized after only seven days of mitogen withdrawal. After 27 days of differentiation, cells were mechanically disaggregated, FACS-sorted and subsequently re-seeded on Matrigel-coated plates (Fig. 4A,B). Newly extended neurites were readily visible one day after sorting and the neuronal network continued gaining complexity over the following days (Fig. 4C,D), therefore that mOrange⁺ DAN are amenable to FACS-sorting procedures while remaining viable and maintaining their DA identity. Quantification analysis after immunostaining with an antibody to TH confirmed robust DAN purification from the mOrange⁺ sorted cells (>95% of cells were TH/mOrange-double positive). In addition, mOrange-negative sorted cells showed similar levels of mOrange⁺/TH⁺ neurons as the unsorted cells (60.8% vs. 67.5%), suggesting that the mOrange⁻ population contains mitotically active undifferentiated progenitors or neurons that have not yet switched on TH expression (Fig. 4E). These results were confirmed by FACS analysis of the sorted neurons seven days after the initial isolation (Fig. 4B).

Collectively, these results demonstrate that post-mitotic fluorescent DAN can be purified from heterogeneous cultures and maintained in culture after sorting.

Discussion

Genetic reporters are extremely useful tools to study signaling and regulatory networks, and offer a potentially powerful approach to identify and specifically isolate a cell type of interest from mixed cell populations. They also allow live real-time tracking, which provides a more in-depth approach to the study cellular dynamics and fate, for example, during the development of cell therapy applications.

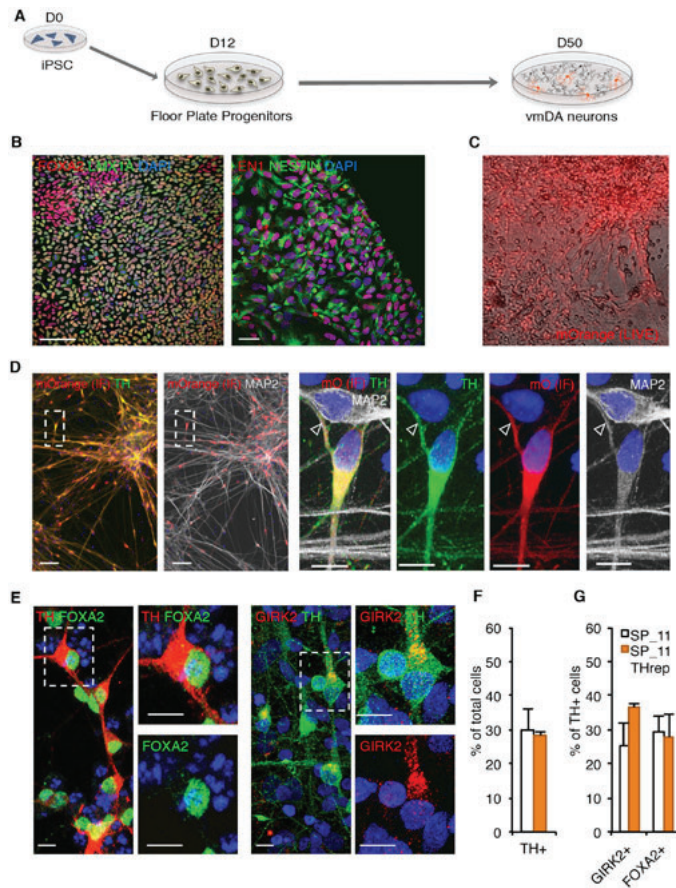


Figure 2. Characterization of ventral midbrain dopaminergic neurons differentiated from the TH-mOrange reporter iPSC line. (A) Scheme depicting iPSC differentiation towards floor plate specific ventral midbrain dopaminergic neurons (vmDAn). (B) Immunofluorescence analysis of representative floor plate progenitors from SP_11 TH reporter iPSCs after 13 days of ventral midbrain patterning staining positive for the floor plate markers FOXA2 and EN1 (red), LMX1A and NESTIN (green). Scale bar, 50 μ m. (C) Live imaging of differentiated TH-mOrange iPSC cell line towards floor plate vmDAn, showing fluorescent neuronal cells after 50 days of differentiation. (D) Immunofluorescence analysis of DAN differentiated for 50 days and stained positive for tyrosine hydroxylase (TH; green), mOrange (red) and MAP2 (grey). Inset show in detail double-labeled mOrange⁺/TH⁺ DAN as well as double negative mOrange⁻/TH⁻ MAP2⁺ non-DAN (empty arrowhead) confirming faithful reporter activity. Nuclei were counterstained with DAPI. Scale bars 50 μ m and 10 μ m for the large images and the insets respectively. (E) Immunofluorescence analysis of DAN differentiated for 50 days and stained for TH and FOXA2 (red and green respectively; left) or GIRK2 and TH (red and green respectively; right). Nuclei were counterstained with DAPI. Scale bar, 10 μ m both main image and insets. (F) Quantitative analysis of the percentage of cells differentiated from either original SP_11 or TH-mOrange iPSC lines stained positive for TH. (G) Percentage of TH⁺ cells stained positive for GIRK2 or FOXA2.

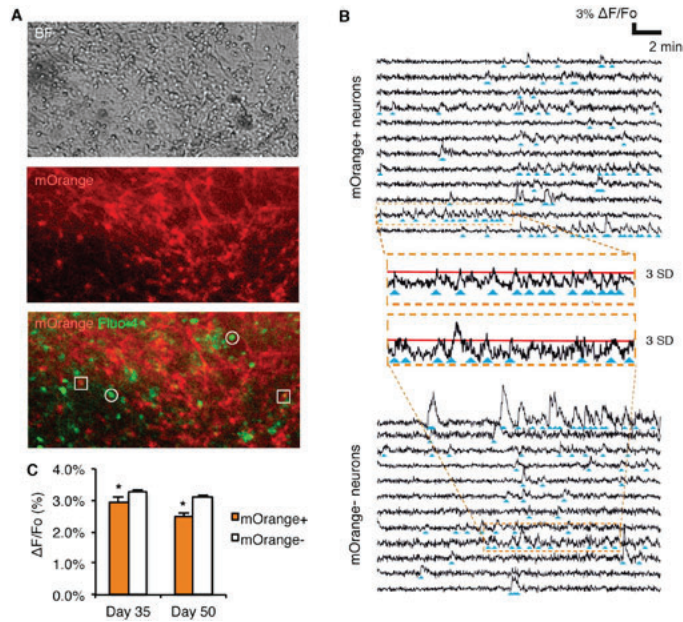


Figure 3. Ventral midbrain dopaminergic neurons show intrinsic electrical properties different from ventral midbrain non-dopaminergic neurons. (A) Live images in bright field (top picture) and the corresponding mOrange and Fluo-4 AM (middle and bottom pictures) fluorescent signal of differentiated neurons (Day 50) during calcium imaging. Squares in the bottom picture point to mOrange⁻ non-dopaminergic neurons whereas circles point to mOrange⁺ dopaminergic neurons in which oscillations of Fluo-4 AM fluorescence are measured. (B) Calcium traces of selected mOrange⁺ and mOrange⁻ neurons confirm electrophysiological activity. Blue arrowheads point to neuronal firing events. Insets show in detail calcium traces from individual mOrange⁺ or mOrange⁻ neurons. Red line represents an increase in fluorescence equivalent to 3 standard deviations (SD) of the mean of the baseline noise. (C) Quantification of the average amplitude of the firing events of mOrange⁺ and mOrange⁻ after 35 and 50 days of differentiation. Data show the average \pm S.E.M. of two or three independent experiments. At day 35, 130 mOrange⁺ and 1187 mOrange⁻ cells from 3 independent experiments. At day 50, 124 mOrange⁺ and 1034 mOrange⁻ cells from 2 independent experiments. Asterisk denotes statistically significant differences (* $p < 0.05$).

Here, we used CRISPR/Cas9-based gene editing to generate an iPSC reporter line carrying a copy of mOrange under control of the endogenous *TH* promoter. The mOrange fluorescent construct was preceded by a self-excitable 2A peptide sequence and was fused to the last exon of the endogenous *TH* gene. The engineered reporter system was shown to work successfully using two different DAN differentiation protocols. First, using a differentiation protocol for floor plate progenitors⁵, we demonstrated the colocalization of the reporter protein in A9 DAN, which are the most vulnerable cells during PD pathogenesis. Secondly, fluorescent DAN were obtained after differentiating TH-mOrange hiPSCs to NPCs using dual SMAD inhibition¹⁸. Since earlier attempts to visualize living dopaminergic cells were unsuccessful¹⁹, we believe the success of our strategy is based on the exceptional brightness of the mOrange protein.

Our ability to identify live dopaminergic neurons allowed us to quantify their electrophysiological activity, an important dynamic phenotype. By calcium imaging, we could distinguish very subtle differences in firing patterns between mOrange⁺ and mOrange⁻ neurons. Specifically, we observed that mOrange⁺ neurons exhibited bursts of higher amplitude, which directly corresponds to a higher overall activity given the correlation between the fluorescence amplitude $\Delta F/F_0$ and the number of elicited action potentials²⁰. Accordingly, the ability to sample a specific neuronal subtype should help to minimize the variability associated with the differentiation procedure. This is crucial when probing subtle and cumulative phenotypes typical of late onset disease such as PD.

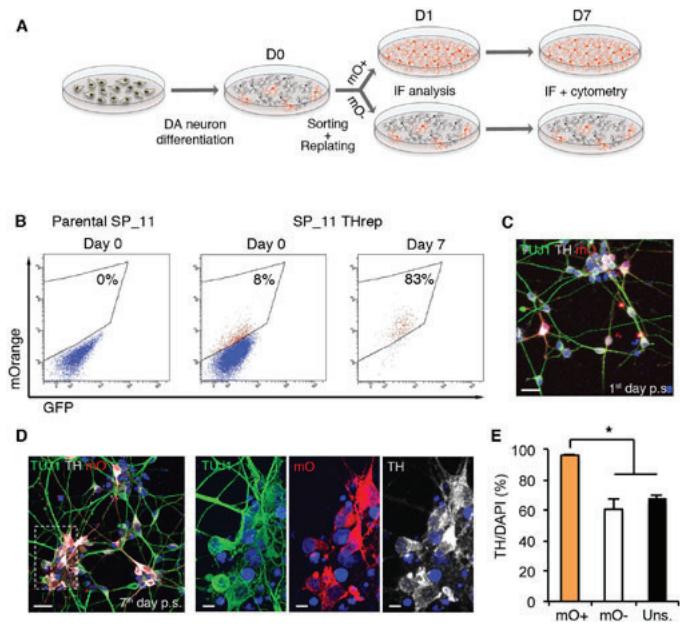


Figure 4. mOrange⁺ DA neurons are amenable to FACS-mediated purification and survive after sorting. (A) Experimental procedure followed for FACS-sorting and subsequent re-plating of mOrange⁺ DAn. (B) Cytograms from FACS of mOrange⁺ cells from differentiated TH-mOrange iPSC. Purified cells were seeded after sorting and re-analyzed after 7 days. Cytograms are representative of 2 independent experiments. (C,D) Immunofluorescence analysis of mOrange⁺ DAn sorted and reseeded on Matrigel for 1 (C) and 7 (D) days. One day post-sorting, living neurons were first imaged and then fixed and stained with antibodies against TUJ1 (green), TH (grey) and mOrange (red). The same combination of antibodies was used to stain neurons cultured for 7 days after sorting. Nuclei were counterstained with DAPI. Scale bars, 20 μ m and 10 μ m for the large image and the inset, respectively. (E) Quantitative analysis of the percentage of cells staining positive for TH 7 days after sorting. Data is the average \pm S.E.M. of two or three independent experiments. Sorted mOrange⁺ cells, 1232 cells from 2 independent experiments; sorted mOrange⁻ cells, 1020 cells from 3 independent experiments; unsorted cells, 679 cells from 2 independent experiments. Asterisk denotes statistically significant differences (* $p < 0.05$).

Our novel genetic TH reporter system enabled us to successfully isolate and purify mOrange⁺ DAn and later resume *in vitro* culture while preserving their dopaminergic identity. Post-sorted DAn successfully attached to plates and extended new neurites in a manner similar to that observed when generating primary neuronal cultures from fetal brain. The discordance in TH⁺ neuron number estimation using cytometry or immunofluorescence is likely due to the reduced sensitivity of the former, and the absolute expression of the TH gene would allow for the observation of those neurons with the highest TH expression. However, a counterweight to this limitation is the standardization of the sampled (or isolated) neurons, since they most likely represent a defined maturation stage.

In conclusion, we here developed an efficient method for generating TH reporter iPSCs that can be differentiated and sorted to obtain pure dopaminergic neuronal populations without the commonly observed heterogeneity of iPSC-derived dopaminergic cultures. We believe that our novel TH reporter tool will facilitate future research on the processes associated with specific DAn biology and disease.

Experimental Procedures

Cell culture. The previously generated SP_11 iPSC line (from a healthy control subject) was used, and cells were cultured as described². Briefly, hiPSC were cultured on Matrigel-coated plates (Corning, NY) and maintained in human embryonic stem cell medium consisting of KnockOut (KO)-DMEM supplemented with 20% KO-Serum Replacement (Gibco/Invitrogen, Carlsbad, CA), 2 mM ultraglutamine, non-essential amino acids and

1% penicillin/streptomycin (all from Lonza), 50 μ M 2-mercaptoethanol (Gibco/Invitrogen) and 10 ng/ml bFGF (PeproTech, Rocky Hill, NJ), at 37°C, 5% CO₂. The medium was preconditioned overnight by irradiated mouse embryonic fibroblasts.

Generation of CRISPR/Cas9 plasmids and donor template for homology-directed repair. The CRISPR/Cas9 plasmid pSpCas9(BB)-2A-GFP (PX458) was a gift from Dr. Feng Zhang (Broad Institute, MIT; Addgene plasmid #12345)³¹. The original pCbh promoter was exchanged for the full-length pCAGGS promoter to achieve higher expression levels in hiPSCs. Custom guide RNAs were cloned into the BbsI sites as annealed oligonucleotides. The donor template for HDR was generated using standard molecular cloning procedures. Briefly, for *TH* donor template, homology arms were amplified from genomic DNA and verified by Sanger sequencing. Resulting sequences matched those of the reference genome GRCh38. The homology arms were inserted into the KpnI-ApaI (5'HA) and SpeI-XbaI (3'HA) sites of pBS-SK (-). The sequence coding for the P2A peptide was added to mOrange with the primers used to amplify the gene and the PCR product was inserted into the ApaI-XhoI sites of the pBS-5'HA-3'HA plasmid. Finally, pRex1-Neo-SV40 was inserted between the XhoI and SpeI of the plasmid.

Gene edition in iPSC. To generate the TH-mOrange hiPSC reporter cell line, cells were transfected with the HDR template and a Cas9- and gRNA-encoding plasmid; the latter overlapping the *TH* gene stop codon. In total, 800,000 iPSCs were seeded in 10 cm plates the day before transfection. iPSCs were co-transfected with 6 μ g of CRISPR/Cas9 plasmid and 9 μ g HDR template using FuGENE HD (Promega) at a 1:3 DNA to reagent ratio. Cells were plated in selection medium containing 50 μ g/mL G418 (Melford Laboratories Ltd., Ipswich, UK) and maintained for 2 weeks until resistant colonies could be screened. At that time, one-half of each resistant colony was manually picked and site-specific integration was verified by PCR.

To excise the selection cassette, edited iPSCs were transfected with a CRE recombinase-expressing plasmid, gifted from Dr. Michel Sadelain (Sloan Kettering Institute; Addgene plasmid #27546)³². At 48 hours post-transfection, cells were dissociated and seeded at clonal density on a feeder layer of irradiated human fibroblasts. When colonies attained a certain size, they were picked and subcultured in independent Matrigel-coated wells. Cells were sampled and checked for cassette excision by PCR and Sanger sequencing. Those clones in which the cassette was excised were expanded, cryopreserved and karyotyped.

Generation of iPSC-derived ventral midbrain dopaminergic neurons. For the derivation of vmdAN, we used a previously published protocol³ with minor modifications. Briefly, iPSCs were maintained in mTeSR-1 medium (StemCell Technologies, Vancouver, Canada) until they reached 80% confluence and were then cultured in serum replacement medium (day 0) (KO-DMEM, 15% KO serum, 1% non-essential amino acids, 1% GlutaMax and 1% penicillin/streptomycin) for an additional 5 days. After that, iPSCs were grown in neurobasal medium 1% N2 (17502-048; Gibco/Invitrogen), 2% B27 (17054-044; Gibco/Invitrogen) (N2B27) without vitamin A and with 1% penicillin/streptomycin. At day twelve, N2 was removed from the medium until the end of the differentiation. The medium was supplemented with SB-431542 (10 mM; day 0–day 5; Sigma-Aldrich, St Louis, MI), LDN193189 (100 nM; day 0–day 12; Miltenyi Biotec Inc., San Diego, CA), CHIR99021 (3 mM; day 3–day 25; Miltenyi), pumorphamine (2 mM; day 1–day 5; Stemgent, Cambridge, MA), Smoothened agonist (1 mM; day 1–day 5; Tocris, Bristol, UK), brain-derived neurotrophic factor (BDNF) (20 ng/ml; from day 12; Miltenyi), glial cell-derived neurotrophic factor (GDNF) (20 ng/ml; from day 12; Miltenyi), DAPT (10 mM; from day 12; Tocris), db-cAMP (500 mM; from day 12; Sigma-Aldrich), TGF β 3 (1 ng/ml; from day 12; Miltenyi) and ascorbic acid (AA, 200 mM; from day 12; Sigma-Aldrich). On day 20, cells were dissociated using Accutase (Merck, Kenilworth, NJ), re-plated at 0.75 \times 10⁵ cells per cm² on dishes pre-coated with polyornithine (15 μ g/ml), laminin (1 μ g/ml) and fibronectin (2 μ g/ml), and cultured in neurobasal medium with 2% B27 without vitamin A and with 1% penicillin/streptomycin and trophic factors (GDNF, BDNF, TGF β 3, AA, db-cAMP and DAPT) until analysis. Quantification of neurons (at day 35, 50 and 80) was assessed by confocal microscopy using anti-FOXA2, anti-MAP2, anti-TH and anti-GIRK2 antibodies.

Generation of human neural progenitor cells. For the generation of NPCs, we followed a previously published protocol¹⁸. Briefly, hiPSC colonies were gently disaggregated from the culture plate and plated for 6 hours in non-adherent conditions in DMEM/F12 (Gibco/Invitrogen), 2% B27, 1% N2, 10 μ M Y-27632 (Miltenyi-Biotec), 100 nM LDN-193189 (120-10-C; PeproTech), 10 μ M SB431542 (S4317-5MG; Sigma-Aldrich) and 2 ng/ml bFGF. Cells were then plated for 10 days on Matrigel-coated dishes in this medium before being detached with accutase and re-plated on Matrigel-coated dishes and cultured in neural induction medium: 1:1 DMEM/F12:neurobasal medium supplemented with 2% B27, 1% N2, 1% ultraglutamine, 10 ng/ml Epidermal Growth Factor (EGF; AF-100-15 Peptide) and 10 ng/ml bFGF. Culturing cells in this neural induction medium generates homogenous cultures of NSCs (>95% of the cells).

NPC differentiation to dopaminergic neurons. NSCs were grown at high confluence (70%) for 7 days on Matrigel-coated dishes in N2B27 medium supplemented with 200 ng/ml Sonic Hedgehog and 100 ng/ml FGF8 (100-25; PreproTech). This first culture step was required to pattern NPCs as DAN progenitors. For terminal differentiation, DAN progenitors were plated on polyornithine/laminin-coated dishes in N2B27 medium supplemented with 20 ng/ml BDNF (450-02, PeproTech), 20 ng/ml GDNF (450-10, PeproTech), 0.5 mM db-cAMP (A6885-25MG, Sigma-Aldrich) and 5 μ M DAPT (565770; Calbiochem, San Diego, CA) for the indicated time points.

Immunofluorescence. Cells were fixed with 4% paraformaldehyde in PBS at room temperature for 15 min and permeabilized for 15 min in 0.3% Triton X-100 in TBS. Cells were then blocked in Triton X-100 with 5% donkey serum for 2 h. The following antibodies were used: goat anti-Nanog (R&D Systems, Minneapolis, MI; AF1997; 1:50), mouse IgM anti-Tra-1-81 (Merck-Millipore; MAB4381; 1:200), mouse anti-OCT4 (Santa Cruz

Biotechnology, Santa Cruz, CA; sc-5279; 1:30), rat IgM anti-SSEA-3 (Developmental Studies Hybridoma Bank [DSHB] Iowa City, IA; MC-631; 1:10), mouse-SOX2 (R&D Systems; MB2018; 1:50), mouse anti-SSEA-4 (DSHB; MC-813-70; 1:100), mouse anti-NESTIN (Santa Cruz; sc-23927; 1:300action), rabbit anti-LMX1A (Millipore; ab10533; 1:1000), goat anti-EN1 (Santa Cruz; sc-46101; 1:200), mouse anti-TUJ1 (BioLegend, San Diego, CA; 801202; 1:500), chicken anti-MAP2ab (Abcam ab5392; 1:1000) goat anti-FOXA2 (R&D Systems; AF2400; 1:50), rabbit anti-TH (Santa Cruz Biotechnology; sc-14007; 1:500), sheep anti-TH (Pel-Freez Biologicals, Rogers, AR; P60101-0 1:500), rabbit anti-mRFP (Abcam, Cambridge, MA; ab34771; 1:400), rabbit anti-GIRK2 (Sigma-Aldrich; P8122; 1:40). Secondary antibodies used were the Alexa Fluor Series from Jackson ImmunoResearch Europe (Newmarket, UK) (all 1:500). Images were taken using a Leica SP5 confocal microscope. To visualize nuclei, slides were stained with 0.5 µg/ml DAPI (4',6-diamidino-2-phenylindole) and then mounted with polyvinyl alcohol with DABCO® (SIGMA).

Calcium Imaging. At days 35 and 50 of differentiation vMDan were incubated with the calcium indicator Fluo-4 AM (Invitrogen) for 30 minutes, with gentle shaking at room temperature. Spontaneous neuronal activity was monitored for 20 minutes with a CMOS fluorescence camera (Hamamatsu Orca Flash v4; Hamamatsu Photonics, Tokyo, Japan) at a rate of 20 images/s and a spatial resolution of 2.3 µm/pixel, which allowed for the identification of single neuronal bodies. Data acquisition was controlled through the software Hokawo 2.10 (Hamamatsu). Data analysis was carried out with the software NETCAL²³, which registers the variation of the fluorescence signal for each neuron as a function of time, and is directly related with calcium uptake and release. The fluorescence signal for each neuron was expressed as $\Delta F/F_0$ (%) = $100 \cdot (F - F_0)/F_0$, where F_0 is the average fluorescence value of the neuron at rest.

Neuronal fluorescence traces were next analyzed with NETCAL to infer the timing of neuronal activations. The Schmitt trigger method²⁴ was used for inference. This method scans the fluorescence traces for events that first pass a high threshold and then remain elevated above a second lower threshold for at least a certain minimum duration. In our analysis, we used +3 standard deviations (SD) of the mean of the baseline noise as the high threshold, +2SD as the low threshold, and 200 ms as the minimum event length.

The series of detected activity events were further contrasted with the fluorescence signal to determine the amplitude A of each activity event. The distribution of amplitude values for mOrange⁺ and mOrange⁻ was then computed and the mean and SD values of the distributions finally evaluated.

Statistical analysis. Differences among groups were evaluated by one-way analysis of variance, and comparisons between two groups by Student's *t*-test, using Prism (Mac OS X). Error bars represent mean ± SEM. A *p*-value less than 0.05 was considered significant.

Study approval. All methods were performed in accordance with the relevant guidelines and regulations. The subject from whom iPSC were obtained, gave written informed consent prior to their participation in the study. The Commission on Guarantees for Donation and Use of Human Tissues and Cells of the Instituto de Salud Carlos III (ISCIII) and the local ethics committee at the Hospital Clinic de Barcelona approved the study, in full compliance with Spanish and European laws and regulations.

References

- Sulzer, D. & Surmeier, D. J. Neuronal vulnerability, pathogenesis, and Parkinson's disease. *Mov. Disord.* **28**, 41–50 (2013).
- Sánchez-Danés, A. *et al.* Disease-specific phenotypes in dopamine neurons from human iPSC-based models of genetic and sporadic Parkinson's disease. *EMBO Mol. Med.* **4**, 380–95 (2012).
- Nguyen, H. N. *et al.* LRRK2 mutant iPSC-derived DA neurons demonstrate increased susceptibility to oxidative stress. *Cell Stem Cell* **8**, 267–80 (2011).
- Arenas, E., Denham, M. & Villaescusa, J. C. How to make a midbrain dopaminergic neuron. *Development* **142**, 1918–36 (2015).
- Kirkeby, A. *et al.* Generation of Regionally Specified Neural Progenitors and Functional Neurons from Human Embryonic Stem Cells under Defined Conditions. *Cell Rep.* **1**, 703–714 (2012).
- Kriks, S. *et al.* Dopamine neurons derived from human ES cells efficiently engraft in animal models of Parkinson's disease. *Nature* **480**, 547–51 (2011).
- Cooper, O. *et al.* Differentiation of human ES and Parkinson's disease iPSC cells into ventral midbrain dopaminergic neurons requires a high activity form of SHH, FGF8a and specific regionalization by retinoic acid. *Mol. Cell. Neurosci.* **45**, 258–266 (2010).
- Sánchez-Danés, A. *et al.* Efficient Generation of A9 Midbrain Dopaminergic Neurons by Lentiviral Delivery of LMX1A in Human Embryonic Stem Cells and Induced Pluripotent Stem Cells. *Hum. Gene Ther.* **23**, 56–69 (2012).
- Kajiwara, M. *et al.* Donor-dependent variations in hepatic differentiation from human-induced pluripotent stem cells. *Proc. Natl. Acad. Sci.* **109**, 12538–12543 (2012).
- Kyttälä, A. *et al.* Genetic Variability Overrides the Impact of Parental Cell Type and Determines iPSC Differentiation Potential. *Stem Cell Reports* **6**, 200–212 (2016).
- Lee, C.-T. *et al.* Functional consequences of 17q21.31/WNT3-WNT9B amplification in hPSCs with respect to neural differentiation. *Cell Rep.* **10**, 616–32 (2015).
- Haavik, J. & Toska, K. Tyrosine hydroxylase and Parkinson's disease. *Mol. Neurobiol.* **16**, 285–309 (1998).
- Bardy, C. *et al.* Predicting the functional states of human iPSC-derived neurons with single-cell RNA-seq and electrophysiology. *Mol. Psychiatry* **21**, 1573–1588 (2016).
- Marchetto, M. C. N. *et al.* Non-cell-autonomous effect of human SOD1 G37R astrocytes on motor neurons derived from human embryonic stem cells. *Cell Stem Cell* **3**, 649–57 (2008).
- Cui, J. *et al.* Quantification of dopaminergic neuron differentiation and neurotoxicity via a genetic reporter. *Sci. Rep.* **6**, 25181 (2016).
- Xia, N. *et al.* A Knockin Reporter Allows Purification and Characterization of mDA Neurons from Heterogeneous Populations. *Cell Reports* **18**, 2533–2546 (2017).
- Shaner, N. C. *et al.* Improved monomeric red, orange and yellow fluorescent proteins derived from *Drosophila* sp. red fluorescent protein. *Nat. Biotechnol.* **22**, 1567–1572 (2004).
- Chambers, S. M. *et al.* Highly efficient neural conversion of human ES and iPSC cells by dual inhibition of SMAD signaling. *Nat. Biotechnol.* **27**, 275–280 (2009).

19. Borgs, L. *et al.* Dopaminergic neurons differentiating from LRRK2 G2019S induced pluripotent stem cells show early neurotic branching defects. *Sci. Rep.* **6**, 33377 (2016).
20. Weir, K., Blanquie, O., Kilb, W., Luhmann, H. J. & Sinning, A. Comparison of spike parameters from optically identified GABAergic and glutamatergic neurons in sparse cortical cultures. *Front. Cell. Neurosci.* **8**, 460 (2015).
21. Ran *et al.* Genome engineering using the CRISPR-Cas9 system. *Nat. Protoc.* **8**, 2281–2308 (2013).
22. Papapetrou, E. P. *et al.* Genomic safe harbors permit high β -globin transgene expression in thalassemia induced pluripotent stem cells. *Nat. Biotechnol.* **29**, 73–78 (2011).
23. Yamamoto, H. *et al.* Impact of modular organization on dynamical richness in cortical networks. *Sci. Adv.* **4**, eaau4914 (2018).
24. Lee, D., Huang, T.-H., De La Cruz, A., Callejas, A. & Lois, C. Methods to investigate the structure and connectivity of the nervous system. *Fly* **11**(3), 224–238 (2017).

Acknowledgements

The authors thank Yvonne Richaud-Patin for her participation in the generation of the original iPSC line and for technical support, and Marta Cañizares for performing immunofluorescence staining. We are grateful to the Advanced Fluorescence Microscopy Unit of the Institute of Biomedicine of the University of Barcelona (especially to Elena Rebollo Arredondo). Research from the authors' laboratories is supported by the European Research Council-ERC (2012-StG-311736-PD-HUMMODEL), the European Union's Horizon 2020 Program (MESOBRAIN project; grant agreement No 713140), the Spanish Ministry of Economy and Competitiveness-MINECO (SAF2015-69706-R; BFU2017-83066-P; and BFU2016-80870-P), Instituto de Salud Carlos III-ISCIII/FEDER (Red de Terapia Celular - TerCel RD16/0011/0003 and RD16/0011/0024; PIE12/00061), AGAUR (2017-SGR-899 and 2017-SGR-1061), and CERCA Program/Generalitat de Catalunya. C.C. is supported by the PD-HUMMODEL European Research Council (ERC)- Ideas PhD fellowship. G.C. is partially supported by predoctoral fellowship from Spanish Economy and Competitiveness-MINECO (BES-2014-069603). The authors declare that they have no competing interests.

Author Contributions

This project and the initial idea were conceived and originated by C.C., A.C., A.R.; Experiments were performed by C.C., G.C., I.F.-C., M.V., S.J., M.D.; Calcium imaging studies were supervised by J.S.-F. and J.G.-S.; Validation, A.C. and A.R.; Writing – Original draft, C.C.; Writing – Review & Editing, C.C., A.C. and A.R.; Resources, J.S.-F., J.G.-C., A.C. and A.R.; Funding Acquisition, A.C.; A.R.; Supervision, A.C. and A.R.

Additional Information

Supplementary information accompanies this paper at <https://doi.org/10.1038/s41598-019-43080-2>.

Competing Interests: The authors declare no competing interests.

Publisher's note: Springer Nature remains neutral with regard to jurisdictional claims in published maps and institutional affiliations.



Open Access This article is licensed under a Creative Commons Attribution 4.0 International License, which permits use, sharing, adaptation, distribution and reproduction in any medium or format, as long as you give appropriate credit to the original author(s) and the source, provide a link to the Creative Commons license, and indicate if changes were made. The images or other third party material in this article are included in the article's Creative Commons license, unless indicated otherwise in a credit line to the material. If material is not included in the article's Creative Commons license and your intended use is not permitted by statutory regulation or exceeds the permitted use, you will need to obtain permission directly from the copyright holder. To view a copy of this license, visit <http://creativecommons.org/licenses/by/4.0/>.

© The Author(s) 2019

Enhancing glycolysis attenuates Parkinson's disease progression in models and clinical databases

Rong Cai,^{1,2} Yu Zhang,³ Jacob E. Simmering,⁴ Jordan L. Schultz,⁵ Yuhong Li,² Irene Fernandez-Carasa,⁶ Antonella Consiglio,^{6,7} Angel Raya,^{8,9} Philip M. Polgreen,¹⁰ Nandakumar S. Narayanan,¹¹ Yanpeng Yuan,¹ Zhiguo Chen,¹ Wenting Su,² Yanping Han,¹ Chunyue Zhao,¹² Lifang Gao,² Xunming Ji,^{1,2} Michael J. Welsh,¹³ and Lei Liu^{2,12}

¹Institute of Hypoxia Medicine, Xuanwu Hospital and Key Laboratory for Neurodegenerative Diseases of the Ministry of Education, and ²Center of Stroke, Beijing Institute for Brain Disorders, Capital Medical University, Beijing, China. ³State Key Laboratory of Membrane Biology, School of Life Sciences, Peking University, Beijing, China. ⁴Department of Internal Medicine and ⁵Departments of Pharmaceutical Care and Neurology, Carver College of Medicine, University of Iowa, Iowa City, Iowa, USA. ⁶Department of Pathology and Experimental Therapeutics, Bellvitge University Hospital-IDIBELL, Hospital de Llobregat and Institute of Biomedicine of the University of Barcelona (IBUB), Barcelona, Spain. ⁷Department of Molecular and Translational Medicine, University of Brescia, Brescia, Italy. ⁸Center of Regenerative Medicine in Barcelona (CMRB) and Networking Biomedical Research Center in Bioengineering, Biomaterials and Nanomedicine (CIBER-BBN), Hospital Duran i Reynals, Hospital de Llobregat, Barcelona, Spain. ⁹Institució Catalana de Recerca i Estudis Avançats (ICREA), Barcelona, Spain. ¹⁰Departments of Internal Medicine and Epidemiology and ¹¹Department of Neurology, Carver College of Medicine, University of Iowa, Iowa City, Iowa, USA. ¹²Beijing Advanced Innovation Center for Big Data-Based Precision Medicine, Beihang University, Beijing, China. ¹³Howard Hughes Medical Institute, Departments of Internal Medicine, Neurology, and Molecular Physiology and Biophysics, Carver College of Medicine, University of Iowa, Iowa City, Iowa, USA.

Parkinson's disease (PD) is a common neurodegenerative disease that lacks therapies to prevent progressive neurodegeneration. Impaired energy metabolism and reduced ATP levels are common features of PD. Previous studies revealed that terazosin (TZ) enhances the activity of phosphoglycerate kinase 1 (PGK1), thereby stimulating glycolysis and increasing cellular ATP levels. Therefore, we asked whether enhancement of PGK1 activity would change the course of PD. In toxin-induced and genetic PD models in mice, rats, flies, and induced pluripotent stem cells, TZ increased brain ATP levels and slowed or prevented neuron loss. The drug increased dopamine levels and partially restored motor function. Because TZ is prescribed clinically, we also interrogated 2 distinct human databases. We found slower disease progression, decreased PD-related complications, and a reduced frequency of PD diagnoses in individuals taking TZ and related drugs. These findings suggest that enhancing PGK1 activity and increasing glycolysis may slow neurodegeneration in PD.

Introduction

Parkinson's disease (PD) is the second most common neurodegenerative disease. It is estimated to affect approximately 6 million people worldwide, and its prevalence will increase further as populations age (1). Patients with PD suffer debilitating motor symptoms as well as nonmotor symptoms including dementia and neuropsychiatric abnormalities (2, 3). Dopamine neurons in the substantia nigra pars compacta (SNc) and their projections into the striatum are especially susceptible to disruption in PD (4). Loss and impaired function of dopamine neurons cause the motor abnormalities that are a hallmark feature of PD. Although current treatments can sometimes relieve PD symptoms, no therapies prevent the neurodegeneration (5).

PD may have a number of different causes, and several pathogenic mechanisms have been proposed to contribute to the apoptotic death of neurons (6–10). In the majority of cases, the etiologies are unknown and probably complex. Aging, environmental toxins, and genetic mutations are all risk factors. In many cases, energy deficits and decreased ATP levels are observed in PD (11).

First, aging, the major risk factor for PD, impairs cerebral glucose metabolism, reduces mitochondrial biogenesis, and decreases ATP levels (12). Second, glycolysis and mitochondrial function are decreased in individuals with PD (13, 14). Third, mitochondrial toxins (1-methyl-4-phenyl-1,2,3,6-tetrahydropyridine [MPTP], rotenone, paraquat) induce PD and PD-like phenotypes in cells and animals, including humans (15). Fourth, mutations associated with familial PD (e.g., *PINK1*, *LRRK2*, α -synuclein, parkin, *DJ-1*, *CHCHD2*) disrupt various aspects of energy metabolism (16). It is also hypothesized that SNc dopaminergic neurons may be particularly susceptible to PD neurodegeneration, because their highly branched, unmyelinated axonal arbor, their many neurotransmitter release sites, and their rhythmic firing engender a large metabolic burden (17). These considerations suggested that impaired bioenergetics and reduced ATP levels might contribute to the pathogenesis of PD, might modify the risk of developing PD in the face of PD risk factors, and/or might modify the course or severity of the disease.

We recently discovered that terazosin (TZ) binds and activates phosphoglycerate kinase 1 (PGK1) (18), the first ATP-generating enzyme in glycolysis (Figure 1A). TZ is an α_1 -adrenergic receptor antagonist that can relax smooth muscle and is prescribed to treat benign prostatic hyperplasia and, rarely, hypertension (19). However, biochemical and functional studies show that the effects of TZ on PGK1 are independent of α_1 -adrenergic

Conflict of interest: The authors have declared that no conflict of interest exists.

Copyright: © 2019, American Society for Clinical Investigation.

Submitted: May 2, 2019; **Accepted:** July 23, 2019; **Published:** September 16, 2019.

Reference information: *J Clin Invest.* 2019;129(10):4539–4549.

<https://doi.org/10.1172/JCI129887>.

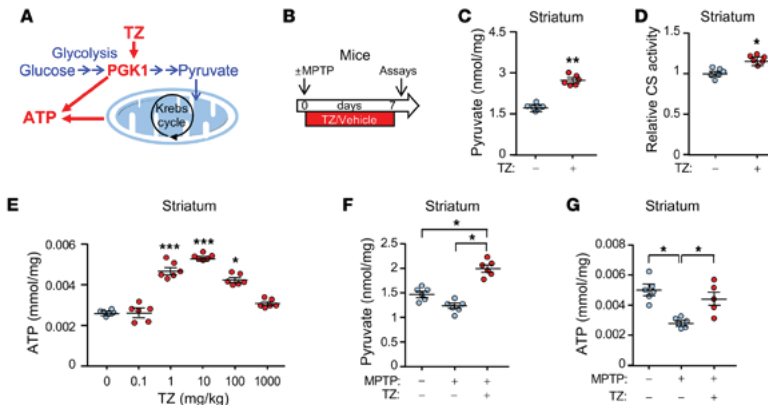


Figure 1. TZ enhances glycolysis in the mouse brain. Data points represent individual mice. Blue indicates controls and red indicates TZ treatment. (A) Schematic of ATP production by glycolysis and oxidative phosphorylation. (B) Schematic time course for experiments in C–G. Eight-week-old C57b1/6 mice were given MPTP (20 mg/kg i.p.) or vehicle 4 times at 2-hour intervals. Then, TZ (10 µg/kg) or vehicle was injected i.p. once a day for 1 week. Assays were performed on day 7. (C–E) Pyruvate levels (C), citrate synthase (CS) activity (D), and ATP levels (E) were measured in mouse striatum. TZ doses are indicated in E. $n = 6$. Statistical comparison was made versus no TZ treatment. (F and G) Pyruvate (F) and ATP (G) levels in the mouse striatal region. Supplemental Table 3 shows statistical tests and P values for all comparisons. Bars and whiskers indicate the mean \pm SEM. * $P < 0.05$, ** $P < 0.01$, and *** $P < 0.001$, by Mann-Whitney U test (C and D), Kruskal-Wallis with Dunn's test (E), and Kruskal-Wallis with Dwass-Steele-Critchlow-Figner test (F and G).

antagonism (18). The crystal structure of TZ with PGK1 revealed that the 2, 4-diamino-6, 7-dimethoxyisoquinazoline motif of TZ binds PGK1 adjacent to the ADP/ATP binding site. In cultured cells, TZ enhanced PGK1 activity, thereby increasing ATP levels, and inhibited apoptosis (18).

The impaired energy production in PD, together with the ability of TZ to increase PGK1 activity, led us to hypothesize that increasing glycolysis in vivo might slow or prevent the apoptotic neurodegeneration of PD. To test this hypothesis, we used models of PD in flies, mice, rats, and human cells, and we interrogated patient databases to learn whether TZ altered the course of disease.

Results

TZ increases brain ATP levels in vivo in mice. To determine whether TZ would enhance glycolysis in vivo, we administered the drug to mice. TZ increased the levels of pyruvate, the product of glycolysis, in the SNc and striatum as well as in cortex (Figure 1, B and C, and Supplemental Figure 1, A and B; supplemental material available online with this article; <https://doi.org/10.1172/JCI129987DS1>). Increased pyruvate enhances oxidative phosphorylation (20), and consistent with this finding, we observed that TZ increased citrate synthase activity, a marker of mitochondrial activity (Figure 1D and Supplemental Figure 1C). Correspondingly, we found that ATP levels increased (Figure 1E and Supplemental Figure 1D). Like previous in vitro data, the dose response was biphasic; our previous studies suggest that, at low but not high concentrations, TZ may enhance ATP release from PGK1 (18).

We also asked whether TZ would increase energy production in mice that received MPTP. MPTP causes PD in humans and is used to model PD in other animals (21, 22). Seven days after

administration of MPTP to mice, pyruvate and ATP levels fell (Figure 1, F and G, and Supplemental Figure 2, A–C), and administration of TZ prevented the fall in pyruvate and ATP levels. Mitochondrial content (assessed by the ratio of mitochondrial DNA to nuclear DNA and by VDAC and PHB1 levels) also fell (Supplemental Figure 2, D–F). TZ partially prevented the decrease. As previously suggested (23), the increased pyruvate levels may have stimulated mitochondrial biogenesis. It would be difficult to measure ATP specifically in neurons, however, we observed similar changes in human neuroblastoma cells (Supplemental Figure 3, A–E). These data indicate that TZ activates glycolysis in vivo. Together with measurements of brain TZ levels (Supplemental Figure 3F), they also indicate that TZ readily crosses the blood-brain barrier.

Although PGK1 produces ATP, oxidative phosphorylation is probably important for increasing ATP on the basis of the following: (a) pyruvate, the product of glycolysis and major substrate for the citric acid cycle, increased (Figure 1, C and F, Supplemental Figure 1B, Supplemental Figure 2B, and Supplemental Figure 3A); (b) citrate synthase activity, a marker of mitochondrial activity, increased (Figure 1D, Supplemental Figure 1C, and Supplemental Figure 3B); (c) the extracellular acidification rate, a measure of glycolysis, and the O_2 consumption rate, a measure of mitochondrial respiration, both increased (Supplemental Figure 3, D and E); and (d) mitochondrial content was partially maintained after MPTP (Supplemental Figure 2, D and F), which may have also contributed to the increased ATP content.

TZ decreases MPTP-induced neurodegeneration in mice. MPTP can model aspects of dopamine neuron loss in mice (21). To determine whether PGK1 stimulation would slow or prevent MPTP-mediated deficits, we administered MPTP to the mice, followed

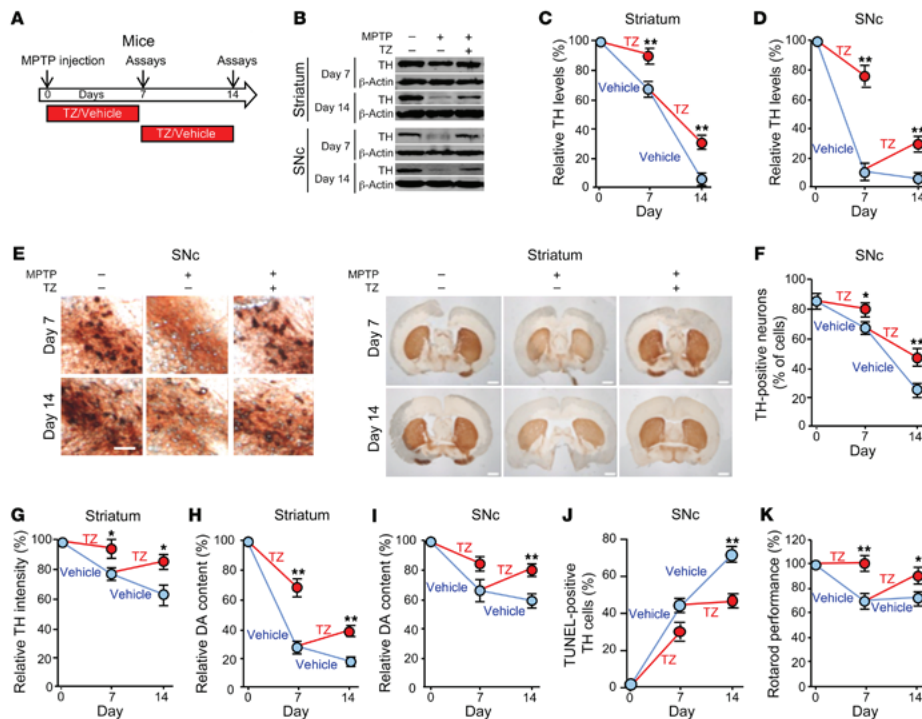


Figure 2. TZ improves dopamine neuron and motor function in MPTP-treated mice. (A) Schematic for experiments in panels B–K. Eight-week-old C57BL/6 mice received 4 i.p. injections of MPTP (20 mg/kg at 2-hour intervals) or vehicle on day 0. Mice were then injected with TZ (10 µg/kg) or vehicle (0.9% saline) once a day for 1 week, and assays were performed on day 7. Other mice began receiving daily TZ or vehicle injections beginning on day 7, and assays were performed on day 14. *n* = 6. (B–D) Example of Western blots with TH and β-actin (protein loading control) in striatum and SNc on days 7 and 14. (E) Example of immunostaining of TH in SNc and striatum. Scale bars: 100 µm (SNc) and 1 mm (striatum). Quantification of TH-positive neurons in SNc (F) and TH intensity in the striatum (G). *n* = 6. (H and I) Dopamine (DA) content in striatum and SNc. *n* = 6. (J) Percentage of TH-positive neurons that were positive for TUNEL staining. *n* = 6. (K) Behavioral response of mice in the rotarod test. Data reflect the duration that the mice remained on an accelerated rolling rod, normalized to mice on day 0. *n* = 8. Data represent examples and indicate the mean ± SEM. Blue indicates control and red indicates TZ treatment. **P* < 0.05 and ***P* < 0.01, by Mann-Whitney *U* test for days 7 and 14. Supplemental Table 3 shows *P* values for all comparisons.

by administration of TZ for the next 7 days, and an assay on day 7 (Figure 2A). Because individuals with PD present after the onset of neuron degeneration, we also asked whether delayed TZ administration would slow neuron loss and functional decline. Therefore, in some mice, we waited 7 days after delivering MPTP before starting the 7-day course of TZ treatment. We then performed an assay on day 14 (Figure 2A).

Over the course of 14 days, MPTP progressively decreased the levels of tyrosine hydroxylase (TH), the rate-limiting enzyme for generating dopamine. MPTP decreased TH levels in the SNc and striatum, reduced the numbers of TH-positive cells in the SNc, and decreased the intensity of TH immunostaining in the neuron projections into the striatum (Figure 2, B–G, and Supplemental

Figure 4, A and B). As a result, the dopamine, 3,4-dihydroxyphenylacetic acid (DOPAC) and homovanillic acid (HVA) content of the striatum and SNc decreased (Figure 2, H and I, and Supplemental Figure 4, C–F). MPTP also increased the percentage of TH-positive cells that were TUNEL positive, indicating increased apoptosis (Figure 2J and Supplemental Figure 4, G and H). Beginning TZ treatment at the time we administered MPTP attenuated all these defects on day 7. When TZ delivery was delayed for 7 days after MPTP administration, it improved the abnormalities on day 14. Consistent with these biochemical defects, TZ prevented deficits in motor function on day 7, and it improved motor performance on day 14 after delayed administration (Figure 2K and Supplemental Figure 4, I and J).

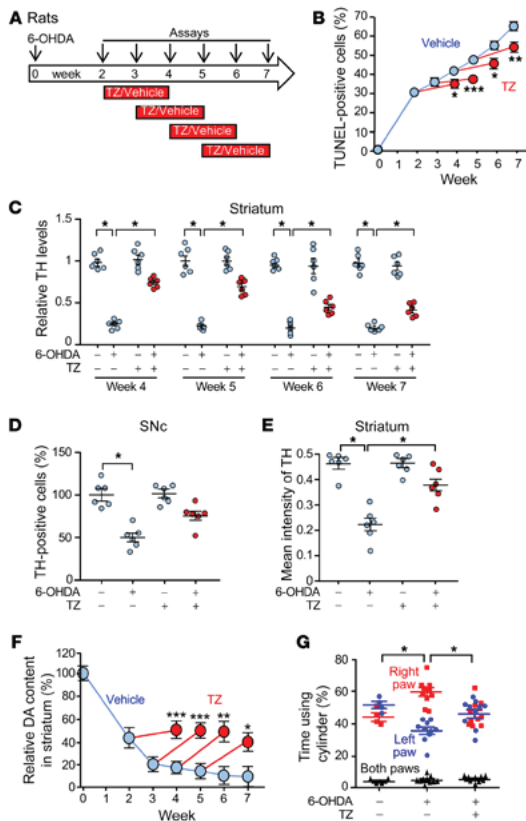


Figure 3. TZ slows neurodegeneration, increases dopamine, and improves motor performance in 6-OHDA-treated rats.

(A) Schematic for experiments in B–G. 6-OHDA (20 μ g) was injected into the right striatum of rats on day 0. TZ (70 μ g/kg) or saline was injected i.p. daily for 2 weeks, beginning 2, 3, 4, or 5 weeks after 6-OHDA injection. Assays were performed at 0 and 2–7 weeks. (B) Percentage of TUNEL-positive SNc cells. $n = 6$. (C) Quantification of TH protein levels assessed by immunoblotting in the striatum, normalized to control. $n = 6$. (D and E) Percentage of SNc cells positive for TH immunostaining (D) and intensity of TH immunostaining in striatum (E) 7 weeks after 6-OHDA injection. TZ treatment was administered from week 5 to week 7. $n = 6$. (F) Dopamine content in the right striatum relative to the left (control) striatum. $n = 6$. (G) Results of the cylinder test. 6-OHDA was injected into the right striatum, impairing use of the left paw. The assay was performed 7 weeks after 6-OHDA injection. TZ treatment was given from week 5 to week 7. $n = 4$ for control group and $n = 10$ for the two 6-OHDA groups. In C, D, E, and G, data points represent individual rats, and bars and whiskers indicate the mean \pm SEM. Blue indicates controls and red indicates TZ treatment. Supplemental Table 3 shows statistical tests and P values for all comparisons. * $P < 0.05$, ** $P < 0.01$, and *** $P < 0.001$, by Mann-Whitney U test (B and F), Kruskal-Wallis with Dwass-Steels-Critchlow-Fligner test (C, D, and E), and Friedman with Dunn's test (G).

These *in vivo* results in mice suggest that TZ slows or prevents MPTP-induced neurodegeneration, partially restores TH and dopamine levels, and improves motor function.

TZ enhancement of *PGK1* activity slows neurodegeneration in 6-OHDA-treated rats. The compound 6-hydroxydopamine (6-OHDA) is delivered to rats to produce a model of dopamine neuron degeneration in PD (24). Previous studies have shown progressive cell death and injury between 2 and 12 weeks after administration of 6-OHDA (25–27). Therefore, we chose a 7-week course of observation. We injected 6-OHDA into the right striatum of rats, waited 2–5 weeks, and then initiated a 2-week course of TZ treatment (Figure 3A). In vehicle-treated rats, evidence of SNc cell apoptosis progressively increased from 2 to 7 weeks (Figure 3B and Supplemental Figure 5, A and B). However, irrespective of the delay before the start of treatment, we observed that TZ attenuated further cell loss. 6-OHDA also progressively decreased TH levels in the striatum and SNc (Figure 3C and Supplemental Figure 5, C–F). The percentage of TH-positive cells in the SNc and the intensity

of TH immunostaining in the striatum also decreased (Figure 3, D and E). TZ partially reverted these abnormalities toward control values. 6-OHDA progressively decreased dopamine, DOPAC, and HVA content, and TZ partially prevented the reduction (Figure 3F and Supplemental Figure 5, G and H). Seven weeks after injection of 6-OHDA into the right striatum, we observed that use of the left forepaw had fallen (Figure 3G), however, when the rats received TZ between weeks 5 and 7, they used both forepaws equally.

Previous studies have shown that MPTP and 6-OHDA can rapidly reduce TH expression (21), and consistent with this finding, we observed that TH levels, TH-positive neurons, TH intensity in the striatum, and dopamine content decreased rapidly after administration of MPTP and 6-OHDA to mice and rats, respectively (Figures 2 and 3 and Supplemental Figures 4 and 5). Cell death was also apparent. However, not all the damaged cells were rapidly killed, as cell death continued to progress for at least 14 days in MPTP-treated mice and for 7 weeks in 6-OHDA-treated rats (Figure 2J and Figure 3B). Accordingly, TH levels, TH-positive

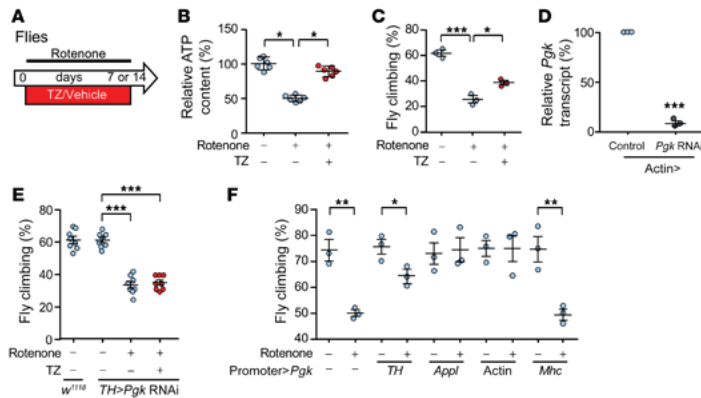


Figure 4. TZ enhances Pdk activity to attenuate rotenone-impaired motor performance. (A) Schematic for experiments in panels B–F. Flies received rotenone (125 or 250 μM in food) with TZ (1 μM) or vehicle for 7 or 14 days. (B) Relative ATP content in the brains of *w¹¹¹⁸* flies that received 250 μM rotenone with or without TZ for 14 days. $n = 6$, with 200 fly heads for each treatment in each trial. (C) Climbing behavior of flies after 250 μM rotenone with TZ (1 μM) or vehicle for 7 days. Data show the percentage of flies that climbed up a tube (see Methods). $n = 3$, with 200 flies tested for each treatment in each trial. (D) Knockdown of *Pdk* in offspring of *actin-Gal4* crossed with *UAS-Pdk* RNAi flies. Offspring of *actin-Gal4* crossed with *y1 v1 P [CaryP] attP2* were used as a genetic background matched control. $n = 3$, with RNA collected from 30 fly heads for each sample. (E) *Pdk* was knocked down in TH neurons by crossing *UAS-Pdk* RNAi flies with flies carrying the TH neuron-specific promoter (*TH-Gal4*) to produce *TH>Pdk* RNAi flies. Rotenone (250 μM) and TZ were administered as indicated for 7 days. Climbing behavior was measured on day 7. $n = 8$, with 200 flies tested for each treatment in each trial. (F) *Pdk* (*UAS-Pdk*) overexpression was driven by a dopaminergic neuron promoter (*TH-Gal4*), a pan-neuronal promoter (*Appl-Gal4*), a pan-cell promoter (*Actin-Gal4*), and a muscle-specific promoter (*Mhc-Gal4*). Rotenone (250 μM) was administered for 7 days, and climbing behavior was measured on day 7. $n = 3$, with 200 flies tested for each treatment in each trial. Data points represent individual groups of flies, and bars and whiskers show the mean \pm SEM. Blue indicates controls and red indicates TZ treatment. Supplemental Table 3 shows statistical tests and P values for all comparisons. * $P < 0.05$, ** $P < 0.01$, and *** $P < 0.001$, by Kruskal-Wallis with a Dwass-Steele-Critchlow-Fligner test (B), 1-way ANOVA with Tukey's test (C and E), paired t test (D), and unpaired t test (F).

neurons, TH intensity in the striatum, and dopamine content also continued to decrease further with time. Administration of TZ, even after the onset of neurodegeneration, slowed cell death, and it increased TH levels, dopamine content, and motor performance compared with vehicle-treated controls (Figures 2 and 3 and Supplemental Figures 4 and 5).

After MPTP and 6-OHDA administration, apoptotic cell death continued for 14 days and 7 weeks, respectively. Delayed TZ administration (beginning on day 7 in MPTP-treated mice and in week 5 in 6-OHDA-treated rats) slowed or prevented further apoptotic cell death. In MPTP-treated mice, dopamine levels, behavioral performance, and in some cases TH levels on day 14 exceeded those on day 7. Likewise, in 6-OHDA-treated rats, dopamine and TH levels by week 7 exceeded those in week 5. PD neurons that have not yet undergone apoptotic cell death almost certainly have impaired metabolic function (28). Our results suggest that TZ improved the function of neurons that were impaired by MPTP and 6-OHDA but had not yet degenerated.

TZ enhances PGK activity to attenuate rotenone-induced neurodegeneration in flies. As an additional model of PD, we treated *Drosophila melanogaster* with rotenone, a mitochondrial complex I inhibitor implicated in sporadic PD (29). Rotenone exposure reduced brain ATP levels (Figure 4, A and B). It also disrupted motor function as tested by climbing behavior (Figure 4C). PGK is highly conserved in flies and mammals, and supplying TZ

together with rotenone minimized decrements in ATP content and motor performance.

Previous studies showed that TZ increases ATP by enhancing PGK1 activity (18, 30). We knocked down *Pdk* in *Drosophila* by expressing RNAi and found that it abolished the protective effect of TZ on motor performance (Figure 4, D and E, vs. Figure 4C). Conversely, overexpression of PGK1 in *Drosophila* TH neurons, all neurons (*Appl* promoter), or all cells (*actin* promoter) made flies resistant to rotenone-induced behavioral defects (Figure 4F). In contrast, we found that expression in muscle was not protective. These results, together with earlier findings (18, 30), indicate that TZ protects TH neurons by activating PGK1.

TZ attenuates neurodegeneration in genetic models of PD. In addition to toxin-induced models, we tested fly, mouse, and human genetic models of PD. *PINK1* mutations cause PD in humans; we therefore tested the *Drosophila PINK1^Δ* mutant (31–33). We administered vehicle or TZ from day 1 after hatching to day 10. On day 10, nearly all *PINK1^Δ* flies exhibited wing posture defects (Figure 5A). TZ partially reversed this abnormality. Brain TH and ATP levels also decreased, and motor performance was impaired in *PINK1^Δ* flies (Figure 5, B–E, and Supplemental Figure 6). TZ partially corrected these defects. We also tested the *Drosophila LRRK^{ext}* mutant (34); *LRRK2* mutations cause autosomal-dominant, late-onset PD (35). TZ also attenuated motor deficits in that model (Figure 5F).

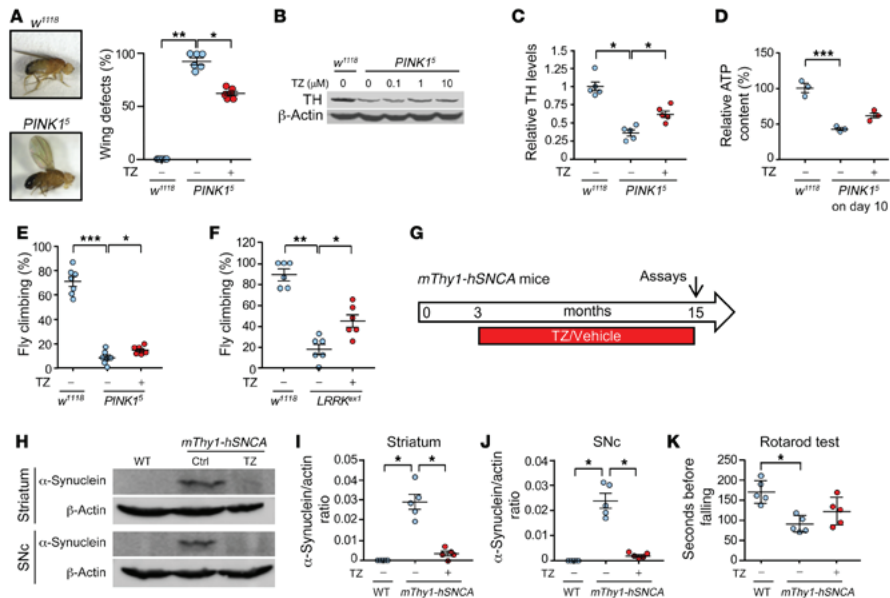


Figure 5. TZ improves TH levels and motor performance in genetic models of PD. Data points are from individual mice and groups of flies. (A–E) WT (w^{1118}) and $PINK1^{\Delta}$ flies received TZ or vehicle for 10 days beginning on the first day after eclosion. Day 10 assays included: (A) Example of wing posture defect and percentage of w^{1118} and $PINK1^{\Delta}$ flies with wing posture defects. $n = 6$, with 80 flies for each treatment in each trial. (B and C) Example of TH Western blot (B) and quantification of TH (C). $n = 5$, with 40 fly heads for each treatment in each trial. (D) ATP content in brains (relative to w^{1118}). $n = 3$, with 200 fly heads for each treatment in each trial. (E) Climbing behavior of flies. $n = 3$, with 100 flies for each treatment in each trial. (F) Climbing behavior of $LRRK2^{\Delta 1}$ male flies. $n = 6$, with 100 flies for each treatment in each trial. (G–K) TZ administration to $mThy1-hSNCA$ -transgenic mice. (G) Schematic behavior for experiments in panels H–K. (H) Example of Western blot of α -synuclein in striatum and SNc. (I and J) Quantification of α -synuclein in striatum and SNc. $n = 5$. (K) Duration that mice remained on an accelerating rotarod. $n = 5$. Data are from individual groups of flies (A–F) and individual mice (I–K). Bars and whiskers indicate the mean \pm SEM. Blue indicates controls and red indicates TZ treatment. Supplemental Table 3 shows statistical tests and P values for all comparisons. * $P < 0.05$, ** $P < 0.01$, and *** $P < 0.001$, by 1-way ANOVA with Tukey's test (D) and Kruskal-Wallis with a Dwass-Steel-Critchlow-Fligner test (A–C, E, F, and I–K).

Abnormal accumulation of α -synuclein, a major constituent of Lewy bodies, is a key feature of PD (36). Transgenic mice overexpressing WT human α -synuclein ($mThy1-hSNCA$) exhibit PD-like neurodegeneration at an advanced age (37). We began treating $mThy1-hSNCA$ mice at 3 months of age with vehicle or TZ. When they were 15 months old, the vehicle-treated mice had substantial expression of human α -synuclein in the striatum and SNc (Figure 5, G–J) and impaired motor performance on the rotarod and pole tests (Figure 5K and Supplemental Figure 7). TZ treatment partially prevented these abnormalities.

We also tested the effect of TZ on dopamine neurons differentiated from induced pluripotent stem cells (iPSCs). $LRRK2^{G2019S}$ is the most common $LRRK2$ mutation and is associated with approximately 4% of familial PD cases and approximately 1% of sporadic PD cases (38). Dopamine neurons derived from $LRRK2^{G2019S}$ iPSCs recapitulate PD features including abnormal α -synuclein accumulation (39). We studied such neurons generated from 2 patients.

After 30 days of differentiation, the dopamine neurons showed no overt signs of neurodegeneration (Supplemental Figure 8). However, approximately 60% of the $LRRK2^{G2019S}$ dopamine neurons had accumulated α -synuclein compared with approximately 15% of dopamine neurons from healthy individuals (Figure 6, A and B). Addition of TZ for 24 hours increased the ATP content and reduced the percentage of $LRRK2^{G2019S}$ dopamine neurons with elevated α -synuclein accumulation (Figure 6, A–C).

In the Parkinson's Progression Markers Initiative database, individuals with PD who were taking TZ had a reduced rate of progressive motor disability. In the past, assessment of whether an agent might affect PD has been largely limited to animal models. Three factors allowed us to assess efficacy in humans. First, TZ is a relatively commonly used drug. Second, availability of human clinical databases allowed us to test for a TZ effect. Third, tamsulosin can serve as a control for TZ. Like TZ, tamsulosin is an $\alpha 1$ -adrenergic antagonist, and, like TZ, tamsulosin is prescribed for benign pros-

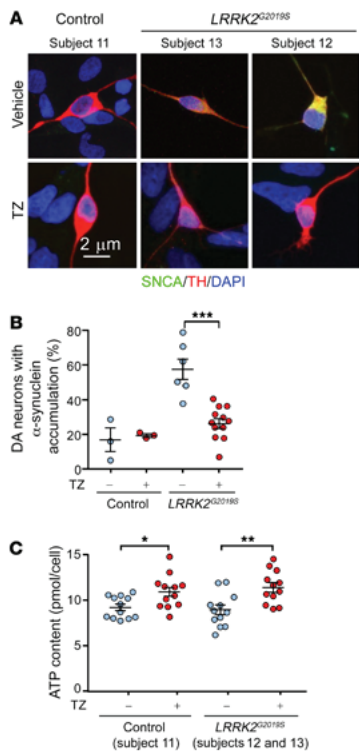


Figure 6. TZ increases ATP content and decreases α -synuclein accumulation in iPSC-derived dopamine neurons from patients with PD. (A) iPSC-derived dopamine neurons from 2 patients with PD (subjects 12 and 13) carrying *LRRK2*^{G2019S} mutations and a healthy control (subject 11). Thirty-day-old dopamine neurons were plated and were treated with TZ (10 μ M) 1 or 3 days later. The neurons were studied 24 hours after addition of TZ. We observed no difference between the 2 start dates and therefore combined the data. Representative immunofluorescence images of α -synuclein (SNCA, green), TH (red), and DAPI (nuclei, blue). (B) Percentage of TH-positive neurons with cytoplasmic accumulation of α -synuclein. $n = 12$. (C) ATP content in control and *LRRK2*^{G2019S} iPSC-derived dopamine neurons. $n = 12$. Bars and whiskers indicate the mean \pm SEM. Blue indicates controls and red indicates TZ treatment. Supplemental Table 3 shows statistical tests and P values for all comparisons. * $P < 0.05$, ** $P < 0.01$, and *** $P < 0.001$, by Mann-Whitney U test.

activity. Consistent with that possibility, doxazosin (DZ) and alfuzosin (AZ) increased glycolysis in M17 cells and tyrosine hydroxylase levels in MPTP-treated mice (Supplemental Figure 9, A and B). We identified 13 men in the PPMI database who were using TZ, DZ, or AZ (TZ/DZ/AZ) (Table 1). The progression of motor disability was slowed in those patients (Figure 7, Supplemental Figure 10, and Table 1).

In contrast to TZ, DZ, and AZ, tamsulosin lacks a quinazoline motif for binding to PGK1. Consistent with that, tamsulosin did not rescue tyrosine hydroxylase levels in MPTP-treated mice (Supplemental Figure 9B). Correspondingly, tamsulosin failed to slow the motor function decline of patients enrolled in the PPMI database (Figure 7 and Table 1). These data are also consistent with the conclusion that enhanced glycolytic activity and attenuation of cell death are mediated by the effect of TZ on PGK1 and not on $\alpha 1$ -adrenergic receptors.

The IBM Watson/Truven database shows that individuals with PD who used TZ/DZ/AZ had fewer PD-related diagnoses. To evaluate a larger number of individuals with PD and to use a different database and assessment methods, we interrogated the IBM Watson/Truven Health Analytics MarketScan Database for the years 2011 to 2016. The database includes longitudinal, deidentified diagnoses (ICD-9/ICD-10 codes) and pharmaceutical claims. We identified 2880 PD patients with PD taking TZ/DZ/AZ (4821 person years) (Table 2). For a comparison group, we chose patients with PD who were taking tamsulosin, which controlled for use of an α_1 -adrenergic antagonist and for the presence of benign prostatic hyperplasia. We identified 15,409 individuals with PD who were taking tamsulosin (21,409 person years). To obtain a list of diagnostic codes associated with PD, we first identified the 497 most common diagnostic codes in the group of individuals with PD. Then, 2 neurologists who care for patients with PD identified 79 potentially PD-related diagnoses (Supplemental Table 1).

Using a quasi-Poisson generalized linear model, we found that the relative risk (RR) of having any of the 79 PD-related diagnostic codes was 0.78 (95% CI: 0.74–0.82) for the TZ/DZ/AZ group relative to the individuals on tamsulosin ($P < 0.00001$). Of the 79 PD-related codes, we found a reduced risk in 69 codes among patients with PD who were taking TZ/DZ/AZ versus those taking tamsulosin (Figure 8A). Moreover, 41 diagnostic codes were statistically significantly decreased in the PD patients taking TZ/DZ/

tatic hyperplasia. However, in contrast to TZ, tamsulosin does not have a quinazoline motif that binds to and enhances PGK1 activity.

PD is common in older men, its incidence increases markedly after age 60, and the prevalence of the disease in men is approximately 1.5 times that in women (40). TZ is prescribed for benign prostatic hyperplasia, a disease that also affects older men. Therefore, we suspected that some patients with PD used TZ, and we hypothesized that they would have a reduced rate of disease progression. To test this hypothesis, we interrogated the Parkinson's Progression Markers Initiative (PPMI) database. This database enrolls patients with PD shortly after diagnosis and follows their motor function as determined by the Movement Disorder Society's Unified Parkinson's Disease Rating Scale Part 3 (41). Although this clinical database is small, it is relatively unique in assessing motor progression. We identified 7 men with PD who used TZ and compared them with 269 men not taking TZ. Compared with the controls, the patients who used TZ had a slower rate of motor function decline (Table 1). Although the difference was statistically significant, only 7 patients used TZ. We therefore sought a larger sample.

The crystal structure of TZ with PGK1 (18) suggested that related drugs with quinazoline motifs might also enhance PGK1

Table 1. Subjects from the PPMI database

	Controls	Tamsulosin	TZ	TZ/DZ/AZ
Number of PD patients	269	24	7	13
Dosage mg/d, mean \pm SD	NA	0.4 \pm 0.1	5.0 \pm 2.5	TZ 5.0 \pm 2.5 DZ 3.3 \pm 1.2 AZ 10.0 \pm 0.0
MDS-UPDRS Part 3 Baseline score, mean \pm SD	20.2 \pm 9.4	20.3 \pm 7.1	19.1 \pm 12.8	20.9 \pm 12.2
<i>P</i> (vs. controls)	NA	0.961	0.771	0.81
MDS-UPDRS Part 3 Slope of change/month, mean \pm SEM	0.54 \pm 0.05	0.39 \pm 0.14	0.01 \pm 0.25	0.02 \pm 0.20
<i>P</i> (vs. controls)	NA	0.301	0.038	0.013

TZ/DZ/AZ includes patients with PD taking TZ (*n* = 7), DZ (*n* = 3), or AZ (*n* = 3). When comparing TZ with controls, the 6 participants taking DZ and AZ were removed (as opposed to being considered part of the control group). Statistical analysis was performed using linear mixed-effects regression and is further described in the Supplemental Methods. MDS-UPDRS scores were obtained when the participants were not yet taking a PD medication or were in the practically defined OFF state (at least 6 hours after the last dose of levodopa or any other anti-PD medication).

AZ versus those on tamsulosin, whereas only 2 diagnostic codes were significantly increased in the TZ/DZ/AZ group.

To estimate PD-related benefits and risks attributable to TZ/DZ/AZ versus tamsulosin, we calculated the RR for clinically relevant groupings of the 79 PD-related codes. Relative to patients with PD taking tamsulosin, those on TZ/DZ/AZ had reduced clinic and hospital visits for motor symptoms (RR 0.77; 95% CI: 0.70–0.84), nonmotor symptoms (RR 0.78; 95% CI: 0.73–0.83), and PD complications (RR 0.76; 95% CI: 0.71–0.82) (Figure 8B, Supplemental Table 1, and Supplemental Table 2). Of note, dopamine analogs do not treat PD symptoms such as dementia and neuropsychiatric manifestations (3). However, the RR for these diagnostic codes was also less than 1.0.

These data suggest that under real-world conditions, TZ and related drugs that enhance PGK1 activity reduce PD signs, symptoms, and complications.

Individuals who used TZ/DZ/AZ had a decreased risk of PD diagnosis. We also used the Truven database to test whether TZ/DZ/AZ might reduce the frequency of PD diagnoses. We identified 78,444 PD-free enrollees who were taking TZ/DZ/AZ. During a follow-up duration of 284 \pm 382 days (mean \pm SD), a total of 118 individuals (0.15%) developed PD. In contrast, in an equal-sized cohort of PD-free enrollees taking tamsulosin and matched for age and follow-up duration (284 \pm 381 days), 190 individuals (0.25%)

Figure 7. TZ and related drugs slow the progression of motor defects for patients with PD enrolled in the PPMI database. Movement Disorder Society–Unified Parkinson's Disease Rating Scale (MDS-UPDRS) Part 3 (motor) scores for patients with PD in the PPMI database. Patients were taking TZ/DZ/AZ (blue, *n* = 13), tamsulosin (green, *n* = 24), or none of these drugs (red, *n* = 269). Data represent scores upon entry into the PPMI database through approximately 1 year and include all measures between those times. All patients taking these drugs were men prescribed TZ/DZ/AZ or tamsulosin, without breaks for benign prostatic hyperplasia or undefined urological problems. Lines are plotted from linear mixed-effect regression analyses. By maximum likelihood estimation, TZ/DZ/AZ differed from controls (*P* = 0.012).

developed PD. The HR from the Cox proportional hazards regression for the matched cohort was 0.62 (95% CI: 0.49–0.78; *P* < 0.0001).

Discussion

Our results indicate that in both toxin-induced and genetic models of PD in multiple animal species, enhancement of PGK1 activity slows or prevents neurodegeneration in vivo, thereby increasing dopamine levels and improving motor performance. Enhancement of PGK1 activity showed beneficial effects, even when begun after the onset of neurodegeneration. Moreover, interrogation of 2 independent databases suggested that TZ and related quinazoline agents slowed disease progression, reduced PD-related

complications in individuals with PD, and reduced the risk of receiving a PD diagnosis.

Evidence from our present and earlier experiments indicates that TZ elicits its beneficial effects in PD by enhancing the activity of PGK1 and not by inhibiting the α_1 -adrenergic receptor. Our earlier experiments and crystal structure showed that the quinazoline motif of TZ binds PGK1 near the nucleotide binding site (18). Studies with recombinant PGK1, studies using cultured cells, and measurements in brain following in vivo delivery all revealed a biphasic relationship between the concentration of TZ and ATP levels (18). In the present study, tamsulosin inhibited α_1 -adrenergic receptors, but its structure lacks a quinazoline group that binds PGK1, and it did not enhance glycolysis or prevent the reduction of tyrosine hydroxylase levels in MPTP-treated mice. In contrast, 2 drugs that have a structure similar to that of TZ (DZ and AZ) enhanced glycolysis in vitro and protected MPTP-treated mice.

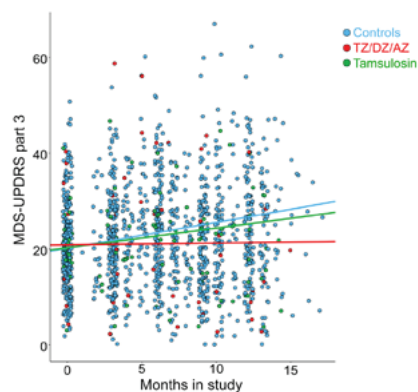


Table 2. Subjects from the Truven MarketScan database

	Tamsulosin	TZ	DZ	AZ	TZ/DZ/AZ
Number of enrollees	15,409	1173	1177	529	2879
Person-years of exposure	21,409	2046	1967	808	4821
Dosage mg/d, mean ± SD	0.4 ± 0.0	4.6 ± 3.1	3.9 ± 2.3	10	NA
Age (yr)					
Mean ± SD	77.2 ± 7.7	77.8 ± 7.4	77.6 ± 7.7	75.9 ± 8.0	77.4 ± 7.7

Summary of the number of enrollees, duration of exposure, and dose of drugs. Age refers to the age of the patient at the first observed medication-dispensing event. The first event can be the age of a patient at the time of a refill of a prescription that was begun prior to entry of the patient into the Truven database, or it can be the age at which the patient started the medication during the Truven observation period.

Knockdown of *Pgk1* in *Drosophila* TH neurons abolished the protective effect of TZ. Overexpression of PGK1 in flies, mice, and fish phenocopied the effects of TZ (18, 30). TZ was active in *Drosophila melanogaster*, which do not have α_1 -adrenergic receptors. Allosteric and covalent regulatory mechanisms have been identified for most glycolytic enzymes. For example, insulin-stimulated deacetylation increases PGK1 activity, and disrupting that regulation results in glycolytic insufficiency (42).

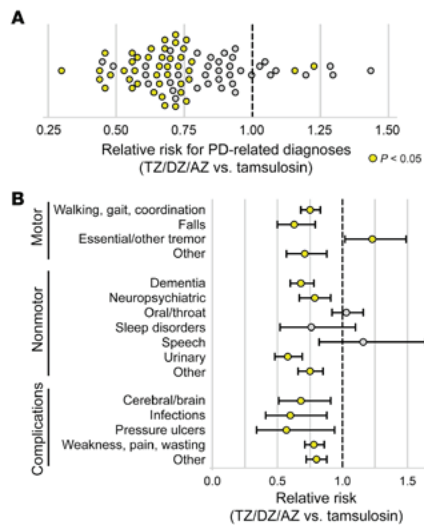
Previous work has identified numerous genetic mutations and several environmental factors that cause or predispose individuals to PD (11–16, 43). As indicated above, reduced energy metabolism and decreased ATP levels are a feature of many of these environmental and genetic factors, as is aging, the major PD risk factor. Therefore, enhancing glycolysis might slow progression in PD of several etiologies.

This study does not reveal how enhanced glycolysis slows neurodegeneration and progression in PD. However, the increased ATP levels produced by TZ may be key. ATP has properties of a hydrotrope; it can prevent aggregate formation and dissolve previously formed protein aggregates (44, 45). Moreover, the transition between aggregate stability and dissolution occurs in a narrow range at physiological ATP concentrations. We speculate that by elevating ATP levels, TZ facilitates the solubilization of aggregates, including α -synuclein, and prevents the neurodegeneration of PD. However, other mechanisms are also possible including ATP-dependent disaggregases and chaperones (such as hsp90) that reduce apoptosis (18, 44, 45).

Figure 8. TZ and related drugs reduce symptoms as assessed by diagnostic codes for patients with PD in the Truven/IBM Watson clinical database. Data are from the Truven Health MarketScan Commercial Claims and Encounters and Medicare Supplemental Databases for the years 2011–2016. Patients had a diagnosis of PD and were prescribed TZ/DZ/AZ or tamsulosin for at least 1 year. We assessed RRs for 79 previously identified PD-related diagnostic codes. (A) RR for 79 PD-related diagnostic codes for patients taking TZ/DZ/AZ versus tamsulosin. Yellow indicates a statistically significant difference in risk between TZ/DZ/AZ and tamsulosin ($P < 0.05$) determined by a generalized linear model with a quasi-Poisson distribution. (B) RR for the categories of PD-related diagnostic codes for patients taking TZ/DZ/AZ versus tamsulosin. Data represent the mean and 95% CIs.

This study also has limitations, including those for toxin-induced and genetic models of PD (46). Toxins such as MPTP and rotenone can cause PD in humans and PD-like disease in animals. Genetic defects also cause PD in humans and PD-like disease in animals. However, most PD is age related, with etiologies that remain unidentified and are likely complex. Moreover, no current model unequivocally or accurately predicts therapeutic benefit or pathogenesis. It is precisely for these reasons that we used multiple animal models of PD and that we sought out human data. A second limitation is that our analysis of human databases was limited to men, because

they are treated for benign prostatic hyperplasia. However, we expect that similar results would be obtained in women. Third, our data from humans are retrospective; however, these data provide compelling evidence that cannot be obtained from animal models alone. Fourth, our analysis of the PPMI and Truven databases compared patients on TZ/DZ/AZ with those on tamsulosin. Although all the drugs were prescribed for benign prostatic hyperplasia, we cannot exclude the possibility that some other factor might have influenced prescribing behavior. For example, orthostatic hypotension is a complication of both the autonomic dysfunction in PD and of the drugs, and there are reports suggesting that tamsulosin may elicit less orthostatic hypotension than TZ (47). However, such an effect would not explain the PPMI conclusions. Interestingly, the risk of orthostatic hypotension and falls was reduced, not increased, for patients with PD taking TZ/DZ/AZ versus those on



tamsulosin. In PD, neurons that have not yet degenerated almost certainly have compromised cellular function (28), and we speculate that TZ/DZ/AZ improved their functional integrity.

Results from this study, together with earlier data, led us to 3 additional speculations. First, TZ is already used clinically, and in this regard, it is interesting that several studies reported that TZ improved glucose metabolism in patients with diabetes (48, 49). That observation has gone unexplained. We speculate that stimulation of PGK1 activity might have been responsible. Consistent with that conjecture and with the conclusion that an α_1 -adrenergic receptor antagonistic effect was not responsible, we found that α_1 -adrenergic receptor antagonists structurally unrelated to TZ lacked that effect. In addition, disruption of the α_{1b} -adrenergic receptor in mice had an effect opposite of that induced by TZ (50). Second, loss-of-function *PGK1* mutations cause recessive hemolytic anemia, myopathy, seizures, and intellectual disability. However, other studies have reported Parkinsonism (51, 52), and the authors speculated that reduced ATP generation in the SNc may have been responsible. Third, PD occurs approximately 1.5 times more frequently in men than in women (53). Why males are more predisposed to PD is unknown. However, it may be worth noting that the *PGK1* gene is located on the X chromosome. Thus, the consequences of DNA sequence variations that could subtly reduce PGK1 levels or activity might more often manifest in men than in women.

Our findings that TZ increased glycolysis and prevented progressive neurodegeneration suggest that energy deficits might either be a pathogenic factor in the pathogenesis of PD or predispose individuals to PD in the presence of environmental or genetic etiologies (11, 16). These findings identify a protein and a pathway that might be targeted to slow or prevent neurodegeneration in PD and potentially other neurodegenerative diseases with altered energy balance (54).

Methods

The Supplemental Methods contain information on the materials, reagents, experimental procedures, and analysis methods used in this study.

Statistics. For experiments to quantify animal behavior and for sample collections, the experimenters were blinded to the genotype and intervention, and the studies were conducted by 2 different experimenters. The number of animals studied was based on our past experience and preliminary data. In all figures, data points are from individual mice and rats or groups of flies. We did not exclude any data points from this study. Data in the figures indicate the mean \pm SEM. Blue indicates controls, and red indicates TZ treatment. Statistical significance for comparisons between data sets was primarily done with nonparametric tests. For studies of fly motor performance, our previous studies showed that within a group of flies (15–50 flies for 1 data point), the data fit a Gaussian distribution. Moreover, data for multiple

groups of flies also fit a Gaussian distribution. Therefore, parametric tests were used to evaluate statistical significance in studies using flies, and ANOVA evaluations were 1 way. All statistical tests were 2 tailed. A *P* value of less than 0.05 was considered statistically significant. Supplemental Table 3 shows the statistical tests used for all data and the resulting *P* values for comparisons.

Study approval. All experiments using mice and rats were approved by the IACUC of Peking University in Beijing (approval nos. LSC-Liul-1 and LSC-Liul-2).

Author contributions

RC designed and performed many of the experiments and analyzed the data. YZ and YL performed fly and mouse studies. IFC and AC performed LRRK2 iPSC studies. AR designed the LRRK2-mutant iPSC studies. JES and PMP performed the analysis of the Truven database. YY, ZC, and WS performed parts of the animal behavior tests. JLS and NSN performed the PPMI database analysis. YH, CZ, and LG provided technical support and data analysis. XJ designed experiments. MJW designed experiments and analyzed data. LL designed and supervised experiments and analyzed data. RC, AR, MJW, and LL wrote the manuscript.

Acknowledgments

The authors thank Carles Calatayud (Center of Regenerative Medicine in Barcelona, Hospital Duran i Reynals, Hospital de Llobregat, Barcelona, Spain) for help and advice with iPSC cultures. We thank Andrew Thurman (Department of Internal Medicine, Carver College of Medicine, University of Iowa) for assistance with the statistical analysis. This work was supported by the National Natural Science Foundation of China (NSFC) (91649201 and 31771121, to LL) and Beijing Municipal Administration of Hospitals Clinical Medicine Development of Special Funding Support (ZYLX201706, to LL); the Spanish Ministry of Economy and Competitiveness (MINECO) (SAF2015-69706-R, to AR, and BFU2016-80870-P, to AC); and the Instituto de Salud Carlos III - ISCIII/FEDER (Red de Terapia Celular: TerCel RD16/0011/0024 and PIE14/00061, to AR). Additional support was provided by the European Research Council (ERC) 2012-StG (311736- PD-HUMMODEL, to AC); the AGAUR (Agency for Management of University and Research Grants (2017-SGR-899); the CERCA Programme/Generalitat de Catalunya (to AR); and the Roy J. Carver Charitable Trust and the Pappajohn Biomedical Institute (to MJW). MJW is an investigator at the Howard Hughes Medical Institute.

Address correspondence to: Michael J. Welsh, 169 Newton Road, 6332 PBDB, Iowa City, Iowa 52242, USA. Phone: 319.335.7619; Email: michael-welsh@uiowa.edu. Or to: Lei Liu, Beijing Institute for Brain Disorders and Beijing Tiantan Hospital, Capital Medical University, Youanmen, Beijing 100069, China. Phone: 010.8395.0371; Email: leiliu@ccmu.edu.cn.

1. GBD 2016 Neurology Collaborators. Global, regional, and national burden of neurological disorders, 1990–2016: a systematic analysis for the Global Burden of Disease Study 2016. *Lancet Neurol.* 2019;18(5):459–480.
2. Fahn S. The history of dopamine and levodopa in

- the treatment of Parkinson's disease. *Mov Disord.* 2008;23(Suppl 3):S497–S508.
3. Chaudhuri KR, Odin P. The challenge of non-motor symptoms in Parkinson's disease. *Prog Brain Res.* 2010;184:325–341.
4. Kalia LV, Lang AE. Parkinson's disease. *Lancet.* 2015;386(9996):896–912.

5. Maiti P, Manna J, Dunbar GL. Current understanding of the molecular mechanisms in Parkinson's disease: Targets for potential treatments. *Transl Neurodegener.* 2017;6:28.
6. Braak H, Del Tredici K. Neuropathological stag-

- ing of brain pathology in sporadic Parkinson's disease: Separating the wheat from the chaff. *J Parkinsons Dis.* 2017;7(1):S71–S85.
7. Hunn BH, Cragg SJ, Bolam JP, Spillantini MG, Wade-Martins R. Impaired intracellular trafficking defines early Parkinson's disease. *Trends Neurosci.* 2015;38(3):178–188.
 8. Johnson ME, Stecher B, Labrie V, Brundin L, Brundin P. Triggers, facilitators, and aggravators: Redefining Parkinson's disease pathogenesis. *Trends Neurosci.* 2019;42(1):4–13.
 9. Lunati A, Lesage S, Brice A. The genetic landscape of Parkinson's disease. *Rev Neurol (Paris).* 2018;174(9):628–643.
 10. Grünewald A, Kumar KR, Sue CM. New insights into the complex role of mitochondria in Parkinson's disease. *Prog Neurobiol.* 2019;177:73–93.
 11. Saxena U. Bioenergetics failure in neurodegenerative diseases: back to the future. *Expert Opin Ther Targets.* 2012;16(4):351–354.
 12. Hoyer S. Brain glucose and energy metabolism during normal aging. *Aging (Milano).* 1990;2(3):245–258.
 13. Hsu CC, et al. Risk factors for myopia progression in second-grade primary school children in Taipei: a population-based cohort study. *Br J Ophthalmol.* 2017;101(12):1611–1617.
 14. Schapira AH. Mitochondrial complex I deficiency in Parkinson's disease. *Adv Neurol.* 1993;60:288–291.
 15. Blesa J, Phani S, Jackson-Lewis V, Przedborski S. Classic and new animal models of Parkinson's disease. *J Biomed Biotechnol.* 2012;2012:845618.
 16. Schapira AH. Mitochondria in the aetiology and pathogenesis of Parkinson's disease. *Lancet Neurol.* 2008;7(1):97–109.
 17. Surmeier DJ. Determinants of dopaminergic neuron loss in Parkinson's disease. *FEBS J.* 2018;285(19):3657–3668.
 18. Chen X, et al. Terazosin activates Pgc1 and Hsp90 to promote stress resistance. *Nat Chem Biol.* 2015;11(1):19–25.
 19. Wilt TJ, Howe W, MacDonald R. Terazosin for treating symptomatic benign prostatic obstruction: a systematic review of efficacy and adverse effects. *BJU Int.* 2002;89(3):214–225.
 20. Compan V, et al. Monitoring mitochondrial pyruvate carrier activity in real time using a BRET-based biosensor: investigation of the Warburg effect. *Mol Cell.* 2015;59(3):491–501.
 21. Heikkilä RE, Hess A, Duvoisin RC. Dopaminergic neurotoxicity of 1-methyl-4-phenyl-1,2,5,6-tetrahydropyridine in mice. *Science.* 1984;224(4656):1451–1453.
 22. Przedborski S, et al. The parkinsonian toxin MPTP: action and mechanism. *Restor Neurol Neurosci.* 2000;16(2):135–142.
 23. Wilson L, Yang Q, Szustakowski JD, Gullicksen PS, Halse R. Pyruvate induces mitochondrial biogenesis by a PGC-1 alpha-independent mechanism. *Am J Physiol, Cell Physiol.* 2007;292(5):C1599–C1605.
 24. Ungerstedt U. 6-Hydroxy-dopamine induced degeneration of central monoamine neurons. *Eur J Pharmacol.* 1968;5(1):107–110.
 25. He Y, Lee T, Leong SK. Time course of dopaminergic cell death and changes in iron, ferritin and transferrin levels in the rat substantia nigra after 6-hydroxydopamine (6-OHDA) lesioning. *Free Radic Res.* 1999;31(2):103–112.
 26. Harms AS, et al. Delayed dominant-negative TNF gene therapy halts progressive loss of nigral dopaminergic neurons in a rat model of Parkinson's disease. *Mol Ther.* 2011;19(1):46–52.
 27. Yuan WJ, et al. Neuroprotective effects of edaravone-administration on 6-OHDA-treated dopaminergic neurons. *BMC Neurosci.* 2008;9:75.
 28. Braak H, Del Tredici K. Potential pathways of abnormal tau and alpha-synuclein dissemination in sporadic Alzheimer's and Parkinson's diseases. *Cold Spring Harb Perspect Biol.* 2016;8(11):a023630.
 29. Coulom H, Birman S. Chronic exposure to rotenone models sporadic Parkinson's disease in *Drosophila melanogaster*. *J Neurosci.* 2004;24(48):10993–10998.
 30. Boyd PJ, et al. Bioenergetic status modulates motor neuron vulnerability and pathogenesis in a zebrafish model of spinal muscular atrophy. *PLoS Genet.* 2017;13(4):e1006744.
 31. Clark IE, et al. *Drosophila pink1* is required for mitochondrial function and interacts genetically with parkin. *Nature.* 2006;441(7097):1162–1166.
 32. Tsai PI, et al. PINK1 Phosphorylates MIC60/Mitofilin to Control Structural Plasticity of Mitochondrial Crista Junctions. *Mol Cell.* 2018;69(5):744–756.e6.
 33. Yun J, et al. Loss-of-function analysis suggests that Omi/HtrA2 is not an essential component of the PINK1/PARKIN pathway in vivo. *J Neurosci.* 2008;28(53):14500–14510.
 34. Lee SB, Kim W, Lee S, Chung J. Loss of LRRK2/PARK8 induces degeneration of dopaminergic neurons in *Drosophila*. *Biochem Biophys Res Commun.* 2007;358(2):534–539.
 35. Zimprich A, et al. Mutations in LRRK2 cause autosomal-dominant parkinsonism with pleomorphic pathology. *Neuron.* 2004;44(4):601–607.
 36. Spillantini MG, Crowther RA, Jakes R, Hasegawa M, Goedert M. alpha-Synuclein in filamentous inclusions of Lewy bodies from Parkinson's disease and dementia with Lewy bodies. *Proc Natl Acad Sci U S A.* 1998;95(11):6469–6473.
 37. Rockenstein E, et al. Differential neuropathological alterations in transgenic mice expressing alpha-synuclein from the platelet-derived growth factor and Thy-1 promoters. *J Neurosci Res.* 2002;68(5):568–578.
 38. Lill CM. Genetics of Parkinson's disease. *Mol Cell Probes.* 2016;30(6):386–396.
 39. Nguyen HN, et al. LRRK2 mutant iPSC-derived DA neurons demonstrate increased susceptibility to oxidative stress. *Cell Stem Cell.* 2011;8(3):267–280.
 40. Driver JA, Logroscino G, Gaziano JM, Kurth T. Incidence and remaining lifetime risk of Parkinson disease in advanced age. *Neurology.* 2009;72(5):432–438.
 41. Goetz CG, et al. Movement Disorder Society-sponsored revision of the Unified Parkinson's Disease Rating Scale (MDS-UPDRS): scale presentation and clinimetric testing results. *Mov Disord.* 2008;23(15):2129–2170.
 42. Wang S, et al. Insulin and mTOR pathway regulate HDAC3-mediated deacetylation and activation of PGK1. *PLoS Biol.* 2015;13(9):e1002243.
 43. Zanon A, Pramstaller PP, Hicks AA, Pichler I. Environmental and genetic variables influencing mitochondrial health and Parkinson's disease penetrance. *Parkinsons Dis.* 2018;2018:8684906.
 44. Patel A, et al. ATP as a biological hydrotrope. *Science.* 2017;356(6339):753–756.
 45. Hayes MH, Peuchen EH, Dovichi NJ, Weeks DL. Dual roles for ATP in the regulation of phase separated protein aggregates in *Xenopus* oocyte nuclei. *Elife.* 2018;7:e35224.
 46. Dawson TM, Golde TE, Lagier-Tourenne C. Animal models of neurodegenerative diseases. *Nat Neurosci.* 2018;21(10):1370–1379.
 47. Dong Z, Wang Z, Yang K, Liu Y, Gao W, Chen W. Tamulosin versus terazosin for benign prostatic hyperplasia: a systematic review. *Syst Biol Reprod Med.* 2009;55(4):129–136.
 48. Kirk JK, Konen JC, Shihabi Z, Rocco MV, Summerson JH. Effects of terazosin on glycemetic control, cholesterol, and microalbuminuria in patients with non-insulin-dependent diabetes mellitus and hypertension. *Am J Ther.* 1996;3(9):616–621.
 49. Shionoiri H, et al. Long-term therapy with terazosin may improve glucose and lipid metabolism in hypertensives: a multicenter prospective study. *Am J Med Sci.* 1994;307(Suppl 1):S91–S95.
 50. Boyda HN, Procyshyn RM, Pang CC, Barr AM. Peripheral adrenergic receptors: the impetus behind glucose dysregulation and insulin resistance. *J Neuroendocrinol.* 2013;25(3):217–228.
 51. Sakaue S, et al. Early-onset parkinsonism in a pedigree with phosphoglycerate kinase deficiency and a heterozygous carrier: do *PGK-1* mutations contribute to vulnerability to parkinsonism? *NPJ Parkinsons Dis.* 2017;3:13.
 52. Sotiriou E, Greene P, Krishna S, Hirano M, DiMauro S. Myopathy and parkinsonism in phosphoglycerate kinase deficiency. *Muscle Nerve.* 2010;41(5):707–710.
 53. Wooten GF, Currie LJ, Bovbjerg VE, Lee JK, Patrie J. Are men at greater risk for Parkinson's disease than women? *J Neurol Neurosurg Psychiatry.* 2004;75(4):637–639.
 54. Yao J, Irwin RW, Zhao L, Nilsen J, Hamilton RT, Brinton RD. Mitochondrial bioenergetic deficit precedes Alzheimer's pathology in female mouse model of Alzheimer's disease. *Proc Natl Acad Sci U S A.* 2009;106(34):14670–14675.

